Diss. ETH No. 19830

Integrated Active Pulsed Reflector for an Indoor Local Positioning System

A dissertation submitted to

ETH Zurich

for the degree of
Doctor of Sciences

presented by

Silvan Wehrli

M.Sc. ETH
born 29 July 1980
citizen of Zürich ZH, Switzerland

accepted on the recommendation of

Prof. Dr. Heinz Jäckel, examiner
Prof. Dr. Robert Weigel, co-examiner
Dr. Andreas Ziroff, co-examiner

2011

Diss. ETH No. 19830

Integrated Active Pulsed Reflector for an Indoor Local Positioning System

First Edition 2011

Published by ETH Zürich, Switzerland

Acknowledgments

It is a pleasure to thank those who made this thesis possible and supported me during the whole time.

Sincere thanks are given to my advisor, Prof. Dr. Heinz Jäckel, for giving me the opportunity to write this thesis at the Electronics Laboratory at ETH Zurich, providing me with research facilities, infrastructure and supporting my work.

I am grateful to Prof. Dr. Robert Weigel from the Friedrich-Alexander-Universität Erlangen-Nürnberg and to Dr. Andreas Ziroff from Siemens AG, Munich, for agreeing to serve as co-examiners and for taking the time to evaluate this work.

A special thank you goes to Prof. Dr. Frank Ellinger, who encouraged me to start a PhD and initialized the EU project RESOLUTION. I appreciated to work with all project partners and enjoyed the fruitful discussions during the project meetings and the social events after the meetings. I wish to thank Siemens for the collaboration and for allowing me into their measurement facilities. I want to thank my fellow CMOS designers Dr. Marco Krcmar for the concert, party visits and Athens sightseeing and Dr. Jörg Carls for the enjoyable time in Munich.

I thank all the members of the Electronics Laboratory (IfE) for a pleasant work atmosphere. Especially, I would like to thank all my office mates for the constructive teamwork and the numerous technical and non-technical discussions: Dr. George von Büren, Dr. David Barras, Martin Kusserow, Dr. Urs Hammer and Adam Lauterbach.

Several master and semester theses accomplished within my research direction provided valuable inputs for this thesis. For that, I would like to thank Benjamin Sporrer, Andrin Maggi, Jelena Stamenkovic and Bin Yan.

I would like to express my gratefulness to Ruth Zähringer for her helpfulness on any non-technical problem, for spreading a good mood at the institute and for many encouraging words. Many thanks also go to our institute technicians Fredy Mettler and Urs Egger. I am also thankful to the system administrators Frank K. Gürkaynak and Beat Muheim from the design center. I would like to show my gratitude to Martin Lanz and Hans-Ruedi Benedikter for assistance in measurements, hardware support, building printed circuit boards (PCB) and bonding chips.

Finally, I would like to thank my parents, my brother Roger and my friends for their continuous support. Most of all, I thank my girlfriend Janine for her love and patience.

Zurich, July 2011 Silvan Wehrli

Contents

Abstract

In the last decade, global positioning entered our daily lives in form of car navigation systems, mobile phones and nowadays even photo cameras. Photos can be geotagged, the shortest route in a foreign city can be found, the nearest restaurant can be searched and tourists can explore tourist attractions or complete cities with GPS tours. Another large application is that automated guided vehicles know their position and can be controlled accordingly. However, the accuracy of standard GPS receivers is too low for certain applications and GPS cannot be used indoors.

A dedicated indoor positioning solution can solve these problems. The goal of this thesis was the development of an active reflector for an indoor positioning system. The indoor positioning system is based on a frequency modulated continuous wave (FMCW) radar, which measures the round-trip time-of-flight to the active reflector. One application of the active reflector is interactive guiding in museums. Therefore, the reflectors should be compact, cheap and power efficient and the indoor positioning accuracy (σ) should be in the order of 20 cm.

The active reflector is based on the phase coherent start-up of an oscillator, therefore the start-up of an oscillator was studied first. It could be shown that an oscillator preserves the phase of the incoming signal during start-up under certain conditions. The measurements on a real oscillator verified this start-up behavior. The received signal strength influenced the phase synchronicity of the oscillator. The phase synchronicity was below the measurement accuracy (0.73 rad), if the received signal was stronger than -46 dBm.

The positioning system was simulated with the verified start-up model of the oscillator. System simulations helped to identify the optimal design parameters. The accuracy of the distance measurement decreases from $\sigma_{\Delta d} = 0.74$ cm for distances below 10 m to $\sigma_{\Delta d} = 2.6$ cm for distances below 30 m due to lower signal-to-noise ratio. The largest influence on the positioning accuracy has multipath propagation. The simulation results with an UWB channel model demonstrated that the accuracy decreases to $\sigma_{\Delta d} = 25$ cm due to multipath propagation.

An active pulsed reflector was integrated in 0.18-μm CMOS technology. The reflector was tested outdoors and indoors. Outdoors, the functionality of the system could be verified up to distances of 24.8 m.

The accuracy for distances between 2.8 and 14 m is 22 cm. The measurements have a high repeatability, the consecutive measurements at the same position lead to the same results ($\sigma_{\Delta d}(d) = 1.4$ cm). The accuracy of the system decreases in a multipath environment. The accuracy of the distance measurements decreases to 26.6 cm and 74.21 cm with directional and omnidirectional antennas respectively. The accuracy could be improved by a simple weighted sliding window average to 7.17 cm and 32.88 cm.

The 3D positioning capability of the system could not be tested, because only one base station was available. In order to verify the applicability of the developed hardware, multipath propagation in a museum environment was simulated with ray tracing. The predicted positioning accuracies in horizontal directions ($\sigma_{\Delta x}$ and $\sigma_{\Delta y}$) were between 11 and 20 cm, while the vertical accuracy was lower ($\sigma_{\Delta z} \approx 30$ cm).

Zusammenfassung

Globale Navigationssysteme, wie z.B. GPS und Galileo, beeinflussen zunehmend unser tägliches Leben. Ein Navigationssystem im Auto hilft den kürzesten Weg zum Ziel zu finden, GPS im Mobiltelefon hilft bei der Suche nach einem Restaurant oder liefert Informationen über Sehenswürdigkeiten. Moderne digitale Kameras haben GPS Empfänger um den aufgenommenen Bilder geografische Koordinaten zuzuordnen. Ein anderes, grosses Anwendungsgebiet ist die Steuerung von fahrerlosen Transportfahrzeugen. Jedoch ist die Positionsbestimmung von normalen GPS Empfängern zu ungenau für gewisse Anwendungen und GPS kann nicht in Räumen verwendet werden.

Ein spezialisiertes Innenraumpositionierungssystem kann diese Probleme lösen. Das Ziel dieser Arbeit war die Entwicklung, Simulation und Integration eines aktiven Reflektors für ein Innenraumpositionsbestimmungssystem. Das Positionierungssystem basiert auf einem frequenzmodulierten Dauerstrichradar, welches die Zeitdifferenz zwischen ausgesendetem und des vom Reflektor zurückgesendeten Signals misst. Eine Anwendungsgebiete des aktiven Reflektors sind interaktive Führungen in Museen. Deshalb sollte der Reflektor kompakt, kostengünstig und stromsparend sein, die Positionsgenauigkeit (σ) sollte in der Grössenordnung von 20 cm sein.

Der aktive Reflektor enthält einen Oszillator, der phasenkohärent zum empfangenen Signal anschwingt. Deshalb wurde zuerst dieses phasenkohärente Anschwingen genauer untersucht. Es konnte gezeigt werden, dass ein Oszillator die Phase des empfangenen Signals unter bestimmten Bedingungen erhalten kann. Die Messungen an einem realen Oszillator bestätigten dieses Verhalten. Die empfangene Signalstärke beeinflusst die Phasensynchronizität des anschwingenden Oszillators. Die Synchronizität des Oszillators lag im Bereich der Messgenauigkeit (0.73 rad), falls das empfangene Signal stärker als -46 dBm war.

Das komplette Positioniersystem konnte anhand eines experimentell verifizierten Oszillatormodelles simuliert werden. Die Systemsimulationen halfen bei der Wahl der optimalen Parametern und zeigen einen Zusammenhang zwischen Messdistanz und Messgenauigkeit auf. Die Distanzmessgenauigkeit des Systems nimmt mit zunehmender Distanz von 0.7 cm (Distanzen unter 10 m) auf 2.6 cm ab (Distanzen unter 30 m), weil das Signal-Rausch-Verhältnis mit zunehmender Di-

stanz abnimmt. Mehrwegausbreitung beeinflusst die Messgenauigkeit am stärksten. Simulationen mit einem UWB Kanalmodell zeigten, dass die Genauigkeit mit Mehrwegausbreitung 25 cm ist.

Ein aktiver Reflektor wurde in einem 0.18-μm CMOS Prozess integriert. Der Reflektor wurde im Freien und drinnen getestet. Die Funktionalität des Reflektors konnte im Freien bis zu einer Distanz von 24.8 m verifiziert werden. Die Distanzgenauigkeit war 22 cm für Distanzen zwischen 2.8 und 14 m. Die Messungen konnten reproduziert werden, das mehrmalige Messen an einer bestimmten Stelle führte immer zum gleichen Resultat ($\sigma_{\Delta d}(d) = 1.4$ cm). Die Messgenauigkeit der Innenraummessungen war kleiner als draussen. Die Distanzgenauigkeit sank auf 26.6 cm mit direktionalen Antennen und 74.21 cm mit ungerichteter Antenne. Jedoch konnte die Genauigkeit mit einem einfachen gleitenden Mittelwert verbessert werden (7.2 cm und 32.9 cm).

Die 3D Positionierungsgenauigkeit des Systems konnte nicht getestet werden, da nur eine Basisstation zur Verfügung stand. Die Positionierungsgenauigkeit der entwickelten Hardware wurde anhand von Simulationen geschätzt. Die horizontale Genauigkeit ($\sigma_{\Delta x}$ und $\sigma_{\Delta y}$) in einer Museumsumgebung mit Mehrwegausbreitung ist zwischen 11 und 20 cm, die erreichbare vertikale Genauigkeit $\sigma_{\Delta z}$ ist 30 cm.

1

Introduction

1.1. Why Local Positioning and Indoor Navigation?

During the last decade, global positioning system (GPS) became omnipresent. GPS enabled many new applications, for example precision farming, car navigation or even GPS based tourist guides. But GPS has also its drawbacks. The accuracy is limited to about 1 m (neglecting highly specialized and expensive geodetic GPS). The accuracy is further reduced in urban canyons or indoor.

There are many potential applications for indoor positioning, where GPS based positioning is either not available or not accurate enough. Most applications can be assigned to one of the three categories:

- interactive guiding,
- industrial and
- security applications.

Interactive guiding summarizes all applications where people are guided. For example, indoor positioning can help shoppers finding the wanted goods in a shopping mall. Positioning could be used to suggest

products to the customer and for advertisement. Indoor navigation can help blind people to find their way in public buildings. Another application is interactive guiding in museums, visitors can retrieve information about an object based on the position, similar to the already existing GPS based city guides.

The second market is the industrial market. Autonomous guided vehicles (AGV) transport goods in industrial environments. AGVs can also include cranes and forklifts. It is important that AGVs are guided accurately and safely. An accurate positioning reduces the need of additional sensors such as gyroscopes. Most AGVs are guided either wired, by guide tape, with gyroscopes, laser target navigation [1], [2], by natural feature navigation based on camera images or laser scans. In outdoor scenarios, GPS improves the guiding. AGVs move shipping containers in the ports of Rotterdam and Hamburg [3].

The third potential field are security applications. The surveillance of fire fighters in burning buildings helps to save fire fighters in the case of an accident [4], [5], [6]. Alzheimer's patients or patients with a head injury in a hospital sometimes wander around disoriented. A local positioning system could help to track these patients and warn as soon as the patients move into an unsafe zone or leave a certain area [7], [8], [9]. It could also be possible to automatically lock doors. Also patients in emergency rooms could be tracked. Their position could be monitored together with blood pressure and heart rate. I know from my own experience that sometimes the doctors are looking for a patient, because somebody moved the patient into another room. Other scenarios in hospitals are the localization of important equipment (e.g. crash cart) or the surveillance of new borns in maternity wards to prevent baby swapping, mismatch or abduction.

All the above mentioned applications pose different challenges to the positioning system. In the case of interactive guiding, an accuracy of around 50 cm is good enough and an update rate of 0.5 to 1 Hz is fast enough, but the system has to be capable to track many people simultaneously. In industrial environments, only a few AGVs are operating simultaneously, but higher update rates ($\sim$ 10-100 Hz) and better accuracy (in the range of a few centimeters) are needed. There are also different requirements about the intelligence of the mobile station (MS). For most security applications, only the infrastructure has to know where the mobile stations are. But in many industrial applications, the position information is required at the mobile stations (e.g. AGVs).

1.2. Positioning Systems

As there is not one single specification for an indoor positioning system, there is also not one single system for indoor positioning. Many different systems for local positioning were presented at the Indoor Positioning and Indoor Navigation Conference (IPIN 2010) [10]. Each system has its specific purpose. In the following list, the most common local positioning systems are shortly discussed:

HS GNSS High sensitivity global navigation satellite system (GNSS) is based on satellite navigation, for example GPS or Galileo. Satellite positioning penetrated our live in the last decade. GPS is present in our everyday live. Most new mobile phones have a GPS sensor integrated and many cars have a GPS navigation system. Therefore, it is an obvious approach to try to improve the sensitivity. Although receiver sensitivity improved a lot over the past 10 years, robust positioning indoors has yet to be achieved [11]. One of the reasons is that the received signal is not a line-of-sight signal but a reflected signal. The length of the received multipath is measured and not the line-of-sight length. This can result in very large errors in the range of 20 to 50 m [12]– [14]. proceedings nehmen, systeme beschreiben mit referenzen....

Pseudolite Pseudolite is the short form of 'Pseudo-satellite'. Pseudolites were first used to emulate GPS before the start of the satellites for testing purposes of the GPS concept. LocataNet uses synchronized nodes [15]. Each node transmits a GPS-like signals. The mobile station calculates the time difference of arrival (TDoA) between the different base stations' signals similar to a GPS receiver. Another concept is to use GPS repeaters inside a building as pseudolites [16], [17]. This improves the positioning accuracy drastically to 2-3 m [18] .

Hybrid IMU Hybrid inertial measurement unit (IMU) consist of inertial sensors and an additional system, such as GPS or received signal strength (RSS). Only relative movements can be detected with inertial sensors, the absolute position is determined by another system (e.g. GPS). This approach is very interesting for smartphones [19]. Most smartphones have a GPS receiver, an acceleration sensor and the newest phones (such as IPhone 4) even have a gyroscope. The combination of GPS signals with inertial sensors improves the positioning at places with bad GPS

reception and multipath propagation. There exist many different hybrid IMU systems. One of the first system was developed by EPFL in 2002 [20]– [22]. The measured position error is below 10 m.

RF RSS TOF Two different techniques are summarized into one category, because they are often used together. The first technique is RF RSS and the second one is time-of-flight (ToF). The received signal strength is in free space proportional to the distance of the base station. The position can be estimated if signals from multiple base stations are received. The most common RF signals used for RSS measurements are wireless local area network (WLAN) (IEEE 802.11), Bluetooth and ZigBee (IEEE 802.15.4). In indoor scenarios, many multipaths lead to interferences and shading. Thus, the distances from RSS measurements aren't reliable. The positioning can be improved if fingerprinting is applied. In the case of fingerprinting, the mobile station measures the received signal strengths and compares it with a map containing previously measured signal strengths [23]. It is also possible to estimate the position by time-of-flight measurement. The base station transmits a time code, which is processed in the mobile station and returned to the base station. Most commercial WLAN cards work with an internal 40 MHz clock. Thus, the time-of-flight is quantized by 25 ns. This is equivalent to an error of 7.5 m. This value can be improved by averaging, but, to the author's best knowledge, submeter accuracy could not be demonstrated with commercial base stations. The implementation of a ToF system as a software definded radio on an FPGA in a smartphone is proposed by [24]. They measured the WLAN connectivity at the EPFL campus and simulated an RMS accuracy below 3 m on the university campus.

RFID Passive radio frequency identification (RFID) tags are very cheap. Positioning with RFID is possible. If many RFID tags (passive or active) are distributed over a building, then the position can be estimated with an RFID reader according to the tags the reader can detect. Or fixed installed RFID readers detect moving tags and compares it with reference tags. One of the first implementations is [25], 4 readers are placed in an approximately 24 m^2 room with 16 reference tags. The average error is 1 m and the worst case error is 2 m. The accuracy is limited by the

density of reference tags and on the few available power levels. A larger system based on distributed RFID tags and mobile readers was build by [26]. The 71 RFID tags are distributed in a building with 55 rooms covering 1600 m^2. A mean error of 1.7 m was achieved.

Ultrasound One of the earliest ultrasound localization system is Cricket [27]. Cricket consists of transmitters (called beacons) and receivers (called listeners). One beacon after the other transmit an RF trigger signal and at the same time an ultrasound pulse. The listeners receive the trigger signal and measure the time difference between the RF trigger signal and the ultrasound pulse. The time difference between the trigger signal and the acoustic pulse is directly proportional to the distance between beacon and listener. The position of the listeners is calculated by each listener individually. This has the advantage of higher privacy and also an unlimited number of listeners is possible. The cricket system can measure distances with an accuracy of 5 cm and a positioning accuracy of 10 cm. Active Bat [28] is similar to Cricket. A controller transmits an RF signal, which activates one mobile device (called Active Bat). Then, this device broadcasts an ultrasonic pulse. The fixed installed receiver measure the time difference between the received RF signal from the controller and the received ultrasonic pulse. The control computer collects all the measurements and calculates the position of the active bat. The achieved accuracy is 14 cm with a 95% confidence level. Newer systems are used in distributed sensor nodes. Each node is a beacon and listener at the same time. One node after the other transmits an RF signal and a ultrasonic pulse and all others measure its distance to the transmitting node. With this approach, fewer fixed references are needed [6], [29], [30].

Radar Radar is well known for detection and localization of ships, airplanes, land mines and rain clouds. Most applications are outdoors and covering a large range. But there exist a number of radar based approaches for local positioning. For example Symeo (formerly Siemens) offers a local positioning system called Local Positioning Radar (LPR). LPR-2D has a 2D accuracy up to ± 5 cm according to the data sheet [31]. Abatec has a system called Local Position Measurement (LPM) [32]. They claim an accuracy better than 10 cm within a covered range of 500 m in

square. However, no published indoor measurements with this system could be found (e.g. [33] and [34] only present outdoor measurements, even without accuracy). The product specifications state a relative measuring accuracy of ±5 cm (relative and outdoor) [35].

Although pulse based ultra-wideband (UWB) systems are also radar systems, we put them into their own category.

UWB As the name suggest, UWB has the advantage of a large available bandwidth between 3.1 GHz and 10.6 GHz with an equivalent isotropically radiated power (EIRP) density of -41.3 dBm/MHz according to the FCC regulations [36]. The UWB signal must have a -10 dB bandwidth larger than 500 MHz or larger than 20% of the center frequency, whichever is the larger value. Swept continuous frequencies, which occur in FMCW radars, can not be applied in UWB. Hence, UWB positioning systems are pulse based. Ubisense developed a pulse based UWB system. The system consists of one mobile transmitter and multiple base stations. When activated, the mobile device transmits a pulse, which all base stations receive. The position is then calculated with TDoA and angle-of-arrival (AoA). Ubisense claims in their product fact sheets [37] an accuracy of 15 cm in 3D (line-of-sight (LOS)) and an update rate of up to 33.75 Hz. The range of coverage of UWB systems is limited by the maximal power density.

Magnetic Magnetic positioning system rely on artificial magnetic fields. A magnetic sensor measures the field strength of at least three artificial magnetic fields and calculates its position. Ascension offers high precision magnetic tracking sensors. Their system is based on pulsed magnetic fields. The achieved accuracy is 1.4 mm for the mid-range ($d_{max} < 78$ cm) system TrakStar. The accuracy 'will be degraded if there are interfering electromagnetic noise sources or metal in the operating environment, which have not been identified and minimized' [38]. The FASTRAK product from Polhemus [39] achieves a static accuracy of 0.76 mm for a range of 76 cm, according to their product brochures. The range is limited to 1.5 m, but may be extended to 4.6 m with slightly reduced performance. The system with the largest found range has a range of 10 m [40], for larger ranges the accuracy decreases significantly due to noise.

Geodetic GNSS are used for geodetic measurements. Different error sources limit the accuracy of standard GNSS (e.g. GPS). GNSS have an inherent limitation due to the signal data rate. In GPS, the C/A code, for civilian use, transmits data at 1.023 million chips per second. The receiver calculates the distance to the satellite by correlating the received signal with an internal pseudo random code. The accuracy of modern correlators is in the range of 15 ns [41]. This is equal to a distance error of 4.5 m. The resolution can be improved by not only taking the received C/A code but also the carrier signal (L1=1.57542 GHz) into account. The carrier signal's frequency is 1500 times higher than the transmitted data. Thus, potentially a 1500 times higher resolution can be achieved. This approach is called real time kinematic (RTK) or carrier-phase enhancement. The height is the least reliable coordinate in GNSS . With RTK GPS the height accuracy (σ) can be improved to 1-3 cm [42].

The biggest error sources of GNSS are satellite clock errors, satellite ephemeris errors (difference between the actual satellite location and the predicted location using the satellite orbital data) and atmospheric effects (ionospheric and tropospheric errors) [43]. Two GPS receivers close to each other will see the same errors. This fact is utilized by differential GPS. A fixed reference station with exactly known position measures the error between detected position and real position and transmits this error to the mobile GPS receivers. The mobile GPS receivers then correct their position accordingly. The accuracy is strongly dependent on the distance of the reference station to the GPS receiver. The DGPS error (95%) is between 0.5 and 1 m and increases by approximately 0.2 m per 100 km from the reference station [43].

Optical All camera based positioning systems belong to this category. We exclude laser based positioning and distance measurement systems from this category, although they are also optical, we classified them under industrial metrology. One application of a camera based positioning is to control a robot to follow an object [44]. In robotics, simultaneous tracking and mapping with cameras is possible [45]. A camera continuously photographs the environment. The shift between two images is calculated by means of feature extraction (often in combination with inertial sensors). Camera based positioning is also applied in optical

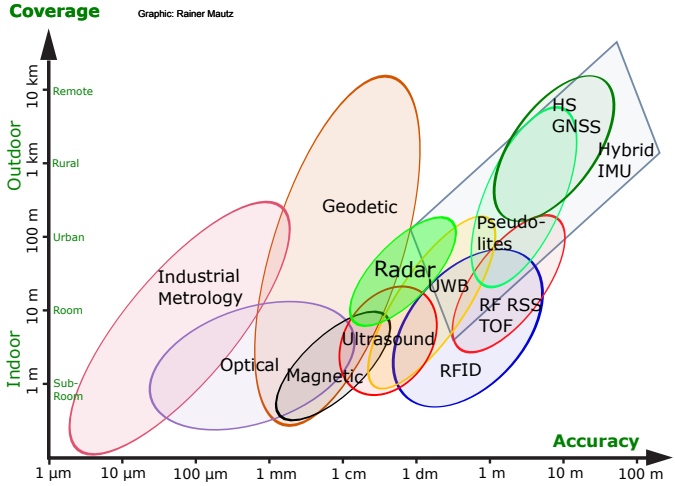

Figure 1.1. Comparison of the accuracy and coverage of different positioning systems. The comparison is based on all presentations of the indoor positioning and indoor navigation conference (IPIN 2010) and was compiled by Rainer Mautz [48].

industrial metrology. For example ProCam (Aicon) is an optical coordinate measuring machine (CMM) [46]. The measuring probe has an integrated high definition CCD camera. During measurement, the camera takes a picture of a field of control points that is located nearby. A computer evaluates the picture and calculates the position of the camera. Aicon specifies the accuracy of ProCam as ± 0.1 mm + 0.1 mm/m.

Industrial Metrology There exist a plethora of industrial measurement tools. One example for a system used in industrial metrology is indoor GPS (iGPS) [47]. It has nothing to do with real GPS, the system 'is a large volume frameless and distributed coordinate measurement machine that is made up of a network of rotary-laser automatic theodolites (R-LATs)' [47]. The system calculates the position of an object based on the automatically measured angles. Laser trackers not only measure angles but also distances, they are often seen on construction sites.

One of the organizers of the Indoor Positioning and Indoor Navigation Conference 2010 [10] went through all accepted papers and

drew the claimed accuracy and coverage into a plot. The most important commercial products were also taken into account. Afterwards, he classified the different systems into the above mentioned categories and summarized the individual points in ellipsoids which are plotted in Fig. 1.1. It seems that geodetic GNSS is the best technology, because it combines good accuracy with a large coverage range. However, this is only true if a line-of-sight to the satellites exist, which is very seldom in indoor scenarios. In addition to that, it is also very costly. Industrial metrology and optical systems are expensive and specialized solutions, which cannot be applied for interactive guiding in a crowded place. Ultrasound and magnetic systems have the drawback of limited coverage. It seems that radar, UWB and ultrasound are the best techniques for AGVs. The best solutions for interactive guiding, where accuracy in the order of 50 cm are required, are radar, UWB, pseudolites and RF RSS combined with ToF. Radar has the best compromise between accuracy, coverage and price. This is the reason why radar was chosen in this thesis.

1.3. Radar Principle

The word radar is an acronym of **ra**dio **d**etection **a**nd **r**anging [49] Either distances or velocity or both are measured by electro magnetic waves.

As early as 1904, Hülsmeyer patented a technique to identify the presence of metallic objects [50] by transmitting electromagnetic waves and if the receiver receives a signal, there must be a reflective object. Guglielmo Marconi also suggested the use of the reflective property of electro magnetic waves for detection of ships in 1922 [51]:

'As was first shown by Hertz, electric waves can be completely reflected by conducting bodies. In some of my tests I have noticed the effects of reflection and deflection of these waves by metallic objects miles away.

It seems to me that it should be possible to design apparatus by means of which a ship could radiate or project a divergent beam of these rays in any desired direction, which rays, if coming across a metallic object, such as another steamer or ship, would be reflected back to a receiver screened from the local transmitter on the sending ship, and thereby immediately reveal the presence and bearing of the other ship in fog or thick weather. One further great advantage of such an arrangement would be that it would be able to give warning of the presence

and bearing of ships, even should these ships be unprovided with any kind of radio.

I have brought these results and ideas to your notice as I feel – and perhaps you will agree with me – that the study of short electric waves, although sadly neglected practically all through the history of wireless, is still likely to develop in many unexpected directions, and open up new fields of profitable research.'

Just a month later, Taylor and Young made the first experiments with a continuous wave (CW) transmitter and a separate receiver. They were able to detect an approaching steamship on the Potomac river [52]. In a letter to the Bureau of Engineering Taylor suggested using this technology to detect passing ships in fog or darkness. The bureau did not fund further research and the use of CW signals for detection was shelved.

The next development step was stimulated by the ionosphere research. Appleton and Barnett's measurements [53] gave evidence for downward reflection from the ionosphere. Breit and Tuve wanted to prove the existence of the ionosphere and measure the height of the layer [54]. The measurement setup consists of a transmitiing station and a receiving station. The transmitting station sends a 'set of interrupted trains of waves', it is a pulsed radio transmitter. At the receiving end the signal is detected. They could measure two signals, the ground wave and a reflected wave. With the time delay of these two waves, the height of the ionosphere could be measured. The measurement equipment was developed by Taylor, Young and Gebhardt. This was probably the first pulse based radar.

Since the very beginning of radar, there exist the two approaches: continuous waves and pulse based radars. As a special case of continuous wave radar is the frequency modulated continuous wave radar. All radars are based on at least one of the following principles.

1.3.1. CW Radar

A nicely formulated definition for CW can be found on wikipedia: 'A CW is an electromagnetic wave of constant amplitude and frequency; and in mathematical analysis, of infinite duration.' [55] A CW signal is a sinusoidal signal of the form

$$y_{CW}(t) = B \sin(\omega t + \phi_0) \tag{1.1}$$

with a time independent amplitude B and a constant frequency ω.

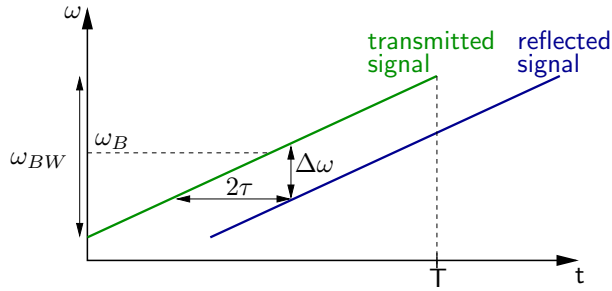

Figure 1.2. The radar station transmits a linear frequency ramp with sweep duration T, center frequency ω_B and sweep bandwidth ω_{BW}. The time delay between the transmitted signal and the reflected signal is calculated with the measured frequency difference $\Delta\omega$.

In CW radars, the speed of an object is measured by the Doppler frequency shift of the continuous, reflected electromagnetic wave

$$f_{rx} = f_{tx}\frac{1+\frac{v}{c}}{1-\frac{v}{c}} \tag{1.2}$$

where c is the speed of light and v is the velocity of the target. v is positive if the target moves towards the source. The beat frequency f_{beat} is the frequency difference between received signal f_{rx} and transmitted signal f_{tx}

$$f_{beat} = f_{rx} - f_{tx} = f_{tx}\frac{2v}{c-v}. \tag{1.3}$$

This frequency can be measured by mixing the transmitted and the received signal in a heterodyne receiver. The CW radar can be used to determine the speed of moving targets, but not for distance measurements.

1.3.2. FMCW Radar

By modulating the frequency of a CW signal, distance information can be obtained. A frequency modulated continuous wave (FMCW) signal is a CW signal with a modulated frequency:

$$y_{FMCW}(t) = B\sin\left(\int_0^t \omega(t)\mathrm{d}t + \phi_0\right) \tag{1.4}$$

with a time dependent frequency $\omega(t)$. Often, a linear frequency ramp is chosen as depicted in Fig. 1.2. The oscillation frequency $\omega(t)$ is

$$\omega(t) = \omega_B + \left(\frac{t}{T} - \frac{1}{2}\right)\omega_{BW}. \tag{1.5}$$

where ω_{BW} is the bandwidth, ω_B is the center frequency and T is the sweep duration. The radar station transmits a FMCW signal, which is reflected by the target object and received after the round-trip time-of-flight 2τ. The transmitted and the reflected frequency ramp are plotted in Fig. 1.2.[1] The two frequency ramp have different frequencies due to the time delay. The frequency difference $\Delta\omega$ between the transmitted and reflected signal is

$$\Delta\omega = \omega_{beat} = \frac{\omega_{BW}}{T}2\tau = \frac{\omega_{BW}2d}{cT} \tag{1.6}$$

Hence, the distance between the radar station and the object is given by

$$d = \frac{\Delta\omega T c}{2\omega_{BW}}. \tag{1.7}$$

The time-of-flight τ is not directly measured, but the frequency difference is proportional to τ.

1.3.3. Pulse Based Radar

Pulse based radars, in contrast to FMCW radars, measure the time-of-flight τ directly. The radar station transmits a pulse and the time is measured until the pulse is received. Two problems arise with the use of pulses. First, rectangular pulses give the best results, but they occupy a large bandwidth. Second, high distance resolution requires a high resolution in time, which is equal to a high sampling rate (1 GHz is equal to a spatial resolution of 30 cm). It is simpler to measure a small frequency difference than a small time difference, because a longer observation time results in a higher frequency resolution.

[1] For simplicity, only a rising frequency ramp is plotted and the Doppler frequency shift is neglected. In the case of a moving target, the received frequency ramp is shifted by the Doppler frequency. If the frequency difference for a rising ramp increases, then the frequency difference for a falling ramp decreases. The measured average frequency difference is proportional to the distance and the difference between the two measurements with rising and falling ramp is proportional to the velocity v.

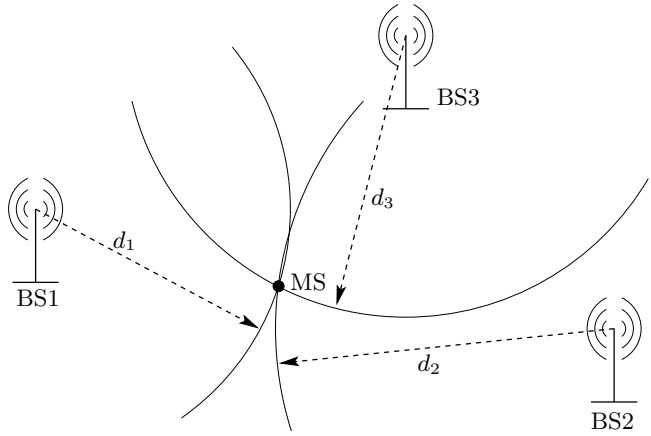

Figure 1.3. Positioning based on round-trip time-of-flight. Each base station i (BSi) measures the distance d_i to the mobile station (MS). The position of the MS is calculated by the intersection of the spheres around each base station.

1.4. Measurement Principle

Independent of the chosen radar principle, radar measures distances (and sometimes angles of arrivals) and not positions. The position of an object is calculated from the distance measurements either with round-trip time-of-flight (RToF) or with TDoA.

1.4.1. Round-Trip Time-of-Flight

RToF measurement is the original radar principle. The ground (or base station) transmits either an FMCW signal or a pulse. This signal is then either passively or actively reflected. The transmitting station receives the signal and calculates the time difference 2τ. The distance can be calculated with

$$d = \frac{\tau}{c} \tag{1.8}$$

with c as the propagation velocity.

Conventional air traffic surveillance radars use a rotating directional antenna. Thus by knowing the angle and the distance, the position of the aircraft can be calculated. The air traffic radar takes advantage of the free space propagation with direct LOS and the antenna has a very

high directivity. In indoor environments strong multipath propagation occurs, there are often objects blocking the LOS connection and the antennas must have a smaller directivity because of size limitations. Thus, multiple base stations are needed for an indoor 3D positioning system. Figure 1.3 illustrates the measurement principle. Each base stations measures the RToF to the mobile unit. Hence, the distance between the mobile unit and the base station is known. The possible positions of the MS are on a sphere of constant distance d_i. The intersection of the spheres around each base stations leads to position of the mobile unit. This method is also called trilateration.

1.4.2. Time Difference of Arrival

In some cases, not the RToF is measured, but only a time difference. For example the mobile station at position $\vec{x}_{MS}$ transmits a pulse and all base stations at $\vec{x}_{BSi}$ measure the arrival time. The exact time, when the pulse was transmitted is not known, the only known values are the time differences of arrival. The time difference τ_{ik} is equal to a distance difference Δd_{ik}. The locus of possible mobile station positions $\vec{x}_{MS}$ is a one half of a hyperboloid

$$\Delta d_{ik} = ||\vec{x}_{MS} - \vec{x}_{BSi}|| - ||\vec{x}_{MS} - \vec{x}_{BSk}||. \tag{1.9}$$

The intersection of all hyperboloids is the position of the mobile station. This approach is called hyperbolic positioning or multilateration. An example with 3 base stations and one mobile station is drawn in Fig. 1.4.

1.5. RESOLUTION Project

The work presented in this thesis was performed during an EU project called RESOLUTION [56], [57]. RESOLUTION stands for **Re**configurable **S**ystems for M**o**bile **L**ocal Comm**u**nication and Posi**tion**ing [58].

The aim of the RESOLUTION project is the development of an accurate indoor positioning system, which can fulfill different positioning needs due to the reconfigurability of its hardware. Industrial applications demand for an accuracy in the centimeter range, but with only few simultaneous mobile stations, whereas many mobile stations have to be positioned in interactive guiding, but with a smaller update rate (∼1 Hz) and lower accuracy (∼50 cm). In order to support a wide

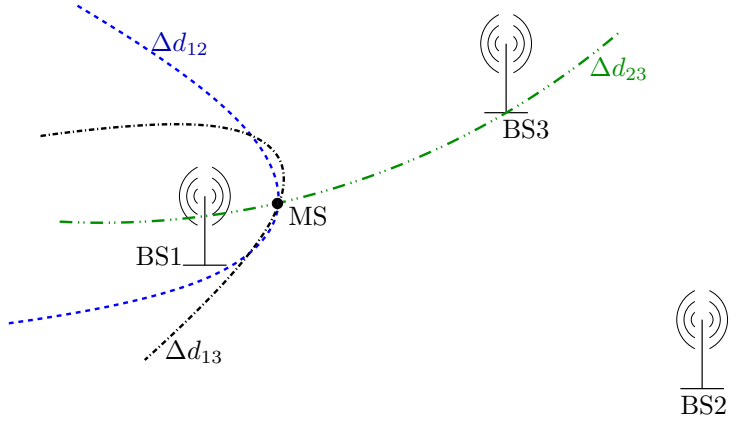

Figure 1.4. Positioning based on time difference of arrival. Only the differences (e.g. $\Delta d_{23} = d_2 - d_3$) are known. For each base station pair, the locus of the possible position is on one half of a hyperboloid (hyperbola in 2D). The solid line is the hyperbola for base station 1 and 2 (Δd_{12}), the dotted line is the hyperbola for base station 2 and 3 with $\Delta d_{23} = d_2 - d_3$ and the dashed for base station 1 and 3 (Δd_{13}).

field of potential applications, the RESOLUTION system is operating in the license-free industrial, scientific and medical (ISM) band at 5.8 GHz with an allocated bandwidth of 150 MHz. The design and application of proprietary RF ICs allow for power-efficient and potentially inexpensive hardware.

The main building block of the RESOLUTION system is the reconfigurable base station [59] depicted in Fig. 1.5. This base station consists of four parallel RF front-ends. Each front-end can either be configured for transmission or reception. Each reception path consists of an low-noise amplifier (LNA) [60], a mixer [61], variable gain amplifier (VGA) [62], base band filter and analog-to-digital converter (ADC). An field-programmable gate array (FPGA) processes the base band signals. The FPGA also controls a synthesizer [63] for transmitting linear frequency ramps. The four parallel front-ends enable many different positioning scenarios, beam-forming and even angle-of-arrival detection.

Due to the reconfigurability of the base stations, at least three different positioning scenarios are possible with the RESOLUTION system.

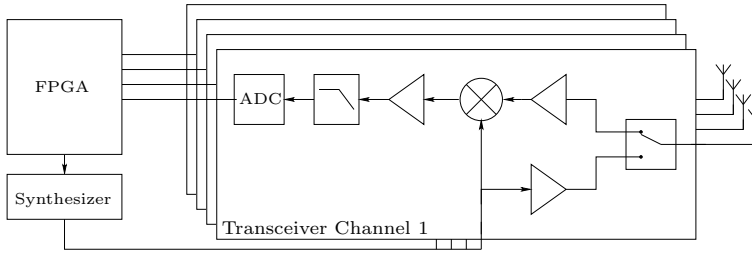

Figure 1.5. Block diagram of the RESOLUTION base station. The base station consists of four transceiver channels, an FPGA and a shared synthesizer. Each channel can be individually configured for transmission or reception.

- AGVs require accurate and real-time position information on the mobile station's side. Therefore, the positioning is performed at the mobile station and the approach is called 'self positioning'.
- In the second system topology, called 'tag localization', complexity of the mobile station is kept low. Base-band processing is completely performed on the infrastructure side, which reduces the mobile 'tag' to very small and power-efficient signal generators, controlled and interfaced by the host device (e.g. a smartphone).
- The third approach is the active reflector approach. The complexity of the mobile station is even lower than with the 'tag localization'. The signal processing and the ramp generation is performed on the base station side.

A detailed description of the three approaches can be found in the RESOLUTION deliverable D17 [64] and in [65]. Here, we give only a short overview of the three approaches.

1.5.1. Self Positioning

Main attribute of the self positioning concept is the fact that mobile stations are just receivers, which means they do not transmit signals to the infrastructure and hence do not occupy system capacity. The benefits are obvious: position update rate is independent of the number of mobile stations and no protocol managing the measurement process between the mobile stations and the infrastructure is required.

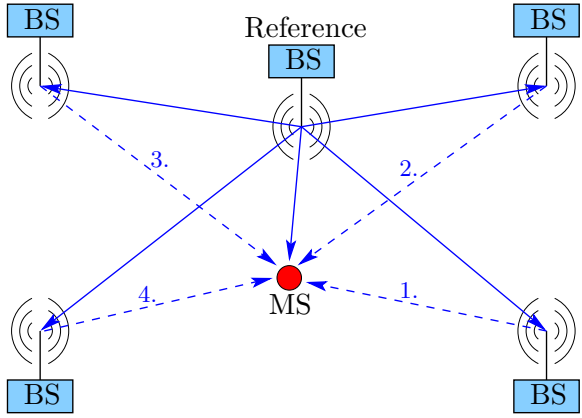

Figure 1.6. Self positioning: In a first step, the reference base station transmits a linear frequency ramp, which is received by all base stations (BS) and the mobile station. The base stations synchronize their internal frequency ramp to the received frequency ramp. In a second step, one base station after the other transmits synchronized radar signals to the mobile station (MS).

The system consists of at least 4 base stations (BSs), 1 reference station (RS) and an unlimited number of mobile stations. As with GPS, the base stations have to be synchronized. This task is done by a synchronization signal, which is periodically transmitted by the dedicated reference station as depicted in Fig. 1.6. All base stations and mobile stations receive this synchronization signal and adjust their own internal frequency ramp to the received signal. In a second step, one base station after the other transmit synchronized radar signals to the mobile stations. Each mobile station calculates its position based on the TDoA between the incoming signals. The reference station is only used to synchronize the base stations. Otherwise, the base stations had to be synchronized by cables or optical fibers. In this case, the exact propagation time of the synchronization signal to each base station has to be known precisely, because this directly influences the positioning accuracy. Therefore, each cable has to be measured and the system has to be calibrated, which makes the installation of the system very complex and time consuming. By adding a reference base station, the installation is simplified, because the reference base station synchronizes the other base stations. Hence, no additional synchroniza-

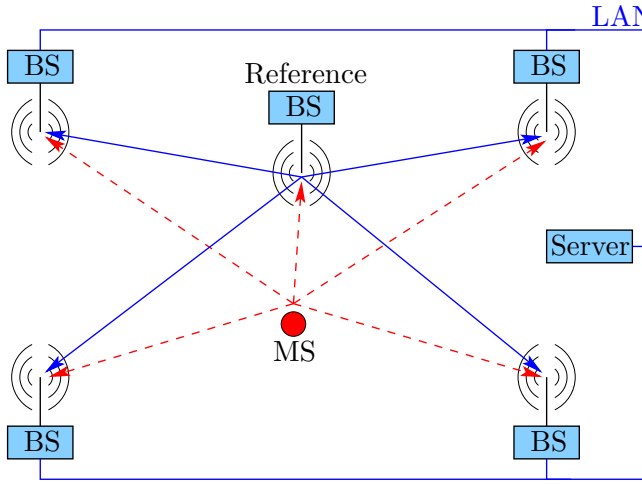

Figure 1.7. Tag localization: The mobile station (MS) transmits a radar signal, which is received by all base stations. Afterwards, the reference station with known position also transmits a radar signal. The server calculates the position of the MS based on TDoA between reference and mobile station's signals.

tion signal (and no cable) is needed. If the base station have wireless communication ability, then only a power plug is needed for each base station. One drawback of the reference base station is that each base station needs a LOS connection to the reference station, because each base station has to receive the synchronization signal.

The mobile station has the same architecture as the base stations, although the transmit path is not needed.

1.5.2. Tag Localization

The self positioning has the advantage that it is scale invariant in terms of number of mobile stations. The mobile stations do not compete for bandwidth, because they only receive. But the computational power needed for position calculation and the complete receive path are power consuming and the hardware is costly. Many applications, especially interactive guiding, set a tight limit on hardware costs and power consumption. Therefore, a second positioning concept called 'tag localization' is developed [66], [67]. Figure 1.7 illustrates the system consisting

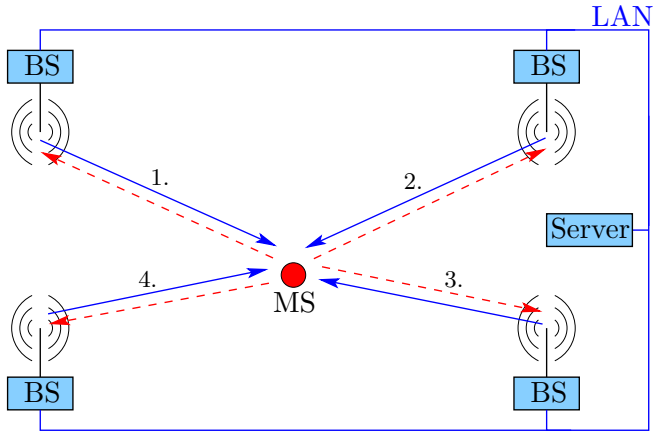

Figure 1.8. Active pulsed reflector system architecture. Each base station subsequently measures the RToF to the mobile station. The mobile station only acts as a reflector. The mobile station receives the radar signal, regenerates and modulates the signal.

of at least 1 MS, 1 RS and 4 BSs. In a first step, the location server addresses a specific mobile station over WLAN. This forces the selected mobile station to send a radar signal which is received by all base stations. Subsequently, the reference base station transmits a second radar signal. The base stations calculate the TDoA between the two radar signals and communicates this time to the location sever, where the position is calculated.

The mobile station is a simple tag without a receiver. It consists of a frequency ramp generator and a controller chip. The tag is connected to a host device (e.g. a smartphone). The server communicates with the host device and schedules the individual mobile stations, because only one mobile station can be measured simultaneously. The base station hardware for the 'tag localization' is equal to the base stations of the self localization approach, except that they are connected via local area network (LAN) to the location server. All except of the reference base station do not need a transmit path.

1.5.3. Active Reflector

The active reflector concept is the third positioning approach which is covered by the base station infrastructure. This is a RToF based

topology, where the mobile station functions as a reflector. Each base station subsequently measures the RToF to the mobile station. The mobile station regenerates the signal and transmits it back. Each base station calculates the distance to the mobile station and transmits this distance to the location server. An efficient way to regenerate, modulate and transmit the signal back is the active pulsed reflector approach [68], [69]. This approach allows for further optimization towards low power consumption, cheap hardware and a small form factor. This is the concept used in this thesis.

1.5.4. Comparison

The three possible localization schemes are compared in Table 1.1. The main difference between the 'self positioning' system and the 'tag localization' and 'active pulsed reflector' system is where the position is calculated. The position is calculated on the mobile device for 'self positioning' and on the base station side for the other two approaches. 'Self positioning' has the most complex mobile station, but at the same time the number of mobile stations is unlimited. The active pulsed reflector approach has the least complex mobile station, but in contrast to the 'tag localization' more than one mobile station can be simultaneously active. The active pulsed reflector is also the only one applying RToF measurements, which simplifies the synchronization of the base stations and no reference station is needed. Therefore, the system is better suited for indoor scenario with many rooms and hallways, because for the other systems many reference stations would be needed,.

1.6. Active Pulsed Reflector

Figure 1.9 illustrates the active pulsed reflector approach on a more detailed schematic level. For simplicity, only one base station is drawn, because each base station measures the distance individually (with time division multiple access (TDMA)). The base station generates a linear frequency ramp s_{tx} and transmits it. The signal is reflected and the received signal s_{rx} is mixed with the transmitted signal s_{tx}, filtered, sampled and the spectrum is calculated by a fast Fourier transform (FFT). This can be accomplished with the same base stations as before, because the base stations have 4 channels, which can be individually configured for transmission or reception. One channel is configured for transmission and between 1 and 3 channels for reception.

Table 1.1. Comparison of the three localization approaches 'self positioning', 'tag localization' and 'active pulsed reflector'.

Self positioning	+ unlimited number of mobile stations + simple infrastructure installation + high update rates possible	- complex and large mobile station - every BS needs a LOS connection to the reference station
Tag Localization	+ small, power efficient mobile stations + can be combined with mobile phones	- needs additional wireless communication - every BS needs a LOS connection to the reference station - low update rates
Active Pulsed Reflector	+ small, power efficient mobile stations + multiple mobile stations simultaneously + no synchronization of the base stations needed	- smaller range

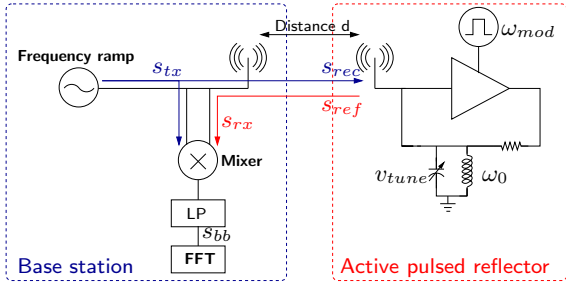

Figure 1.9. Active pulsed reflector radar system consisting of a base station and an active pulsed reflector. The base station is a conventional FMCW radar station, which is also used for tag localization and self positioning. The pulsed reflector is a periodically switched ω_{mod} oscillator with oscillation frequency $\omega_0 \gg \omega_{mod}$.

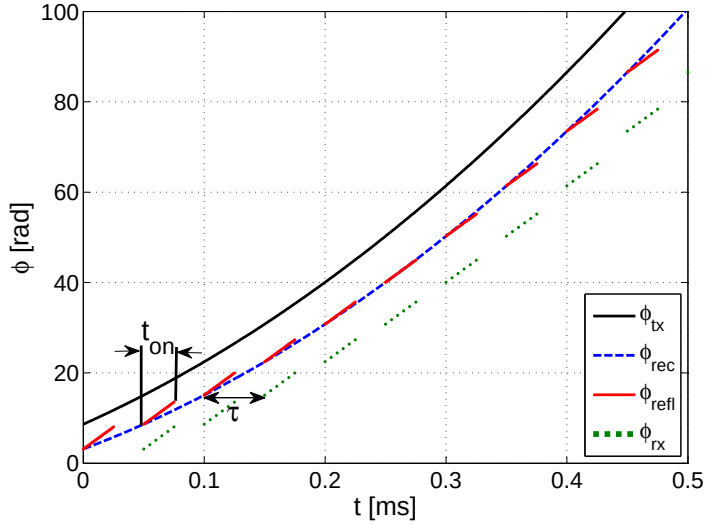

Figure 1.10. Phase behavior of the active reflector positioning system. ϕ_{tx} is the transmitted phase parabola (frequency ramp), which is delayed by the time-of-flight τ. The reflector receives the phase ϕ_{rec} and starts at the on-switching instant phase coherent to the incoming signal (ϕ_{refl}). The base station receives the phase from the reflector delayed by τ (ϕ_{rx}).

The active pulsed reflector actively reflects the received signal back to the base station as the name already indicates. Instead of just amplifying the signal, the reflector operates as an oscillator. The reflector is periodically switched on and off. During every start-up, the reflector starts to oscillate with a certain starting phase. It will be shown in Chapter 2 that this starting phase is equal to the incoming phase. But the oscillation frequency of the reflector ω_0 does not have to be identical to the incoming signal's frequency. We call this start-up behavior 'phase synchronous start-up'. Every time the reflector is switched on, the phase of the reflector is synchronized to the incoming signal. The active reflector 'samples' the phase of the incoming signal. This phase sampling characteristic is the key principle enabling the use of an active pulsed reflector for positioning. The positioning principle can be qualitatively understood by investigating the received phase ϕ_{rec} at the reflector and the resulting output phase ϕ_{refl} of the reflector. The transmitted phase parabola ϕ_{tx}, the received ϕ_{rec}, the output phase of the reflector ϕ_{refl} and the received phase ϕ_{rx} at the base station are depicted in Fig. 1.10. The transmitted signal is a linear frequency ramp, thus the phases ϕ_{tx} and ϕ_{rec} increase by t^2. Every time the reflector is switched on, this phase is sampled and transmitted back. Hence, a sampled phase parabola is transmitted back and the difference between the transmitted phase and the received phase at the base station depends on the time-of-flight τ. The gradient of the phase difference $\mathrm{d}(\phi_{rx}(t) - \phi_{tx}(t))/\mathrm{d}t$ is proportional to the time-of-flight τ and thus to the distance d. A constant phase error ϕ_e, e.g. if the reflector adds a constant phase to the incoming phase, does not affect the positioning, because the gradient is not affected

$$\frac{\mathrm{d}(\phi_{rx}(t) - \phi_{tx}(t)) + \phi_e}{\mathrm{d}t} = \frac{\mathrm{d}(\phi_{rx}(t) - \phi_{tx}(t))}{\mathrm{d}t} = \Delta\omega. \tag{1.10}$$

The phase parabolas are illustrated in Fig. 3.2 and the active pulsed reflector principle will be discussed in greater detail in Section 3.1.

The switching of the reflector is needed for the periodic sampling of the phase. But the switching also modulates the signal with the switching frequency ω_{mod}. The spectrum of a conventional, passive FMCW radar exhibits only one peak at the beat frequency f_{beat} as shown in Fig. 1.11. Due to the modulation, the spectrum with an active pulsed reflector exhibits two peaks at $f_{mod} \pm f_{beat}$. It is possible to identify different reflectors due to the different modulation frequencies. Thus, multiple reflectors can operate simultaneously (frequency division mul-

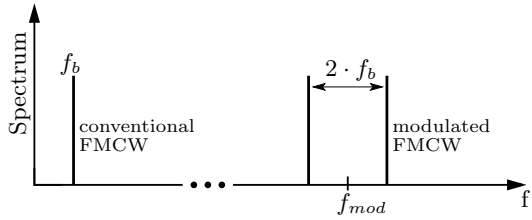

Figure 1.11. The base-band spectrum of a conventional, passive FMCW radar exhibits one peak at the beat frequency f_{beat}. The modulation of the reflector leads to two peaks around the modulation frequency f_{mod}.

tiple access (FDMA)). The number of nodes is limited by the available system bandwidth. Passive reflections from objects in the room or from walls are not modulated. Hence, they can be filtered more effectively.

The following list summarizes the advantages of the pulsed reflector approach:

- Active and passive reflections differ. Passive reflections can be filtered.
- Different modulation frequencies enable the detection of multiple reflectors simultaneously.
- Ideal range resolution after [70] increases. The ideal range resolution of a sawtooth linear FMCW homodyne radar is derived from (1.7). The beat frequency f_{beat} is measured in the spectrum. The frequency resolution Δf_{min} of an FFT is determined by the sampling duration T by

$$\Delta f_{min} = \frac{1}{T} \tag{1.11}$$

Inserting (1.11) into (1.7) results in the range resolution Δd_{min} of a linear FMCW radar

$$\Delta d_{min} = \frac{c}{2 f_{BW}} \tag{1.12}$$

The frequency difference for a linear FMCW radar is measured between zero and the first peak. The pulsed reflector modulates the signal around a frequency ω_{mod}. This modulation leads to a

peak above and one below the modulation frequency. The measured frequency difference is between these two peaks and thus twice as large as in the not modulated case. The frequency resolution Δf_{min} of the FFT is not affected by the modulation of the reflector. The range resolution of the active pulsed reflector is given by

$$\Delta d_{min} = \frac{c}{4 f_{BW}}. \tag{1.13}$$

The ideal range resolution of the active pulsed reflector is twice as good as for a linear FMCW radar without modulation.

- Each base station is independent. The frequency ramps must not be synchronized other than over Ethernet or WLAN.
- RToF measurements are less susceptible to multipath propagation as TDoA, because if one base station is affected by multipath propagation or non-line-of-sight (NLOS) condition, only one distance measurement is wrong. In the case of TDoA multiple distance differences are wrong. Thus, the potential error due to one NLOS path is smaller for RToF.

1.6.1. System Specifications

At the start of this work, only a few design parameters were known. The RESOLUTION hardware operates in the ISM band around 5.8 GHz. The available bandwidth is 150 MHz and the maximum allowed power level is 25 mW EIRP. The base station generates a frequency sweep with sweep duration T slightly above 0.5 ms. This value is a compromise between noise performance (longer measurement time improves noise performance) and measurement update rate.

The maximum measurable distance between a base station and an active reflector should be between 30 and 50 m. All other specifications are not obvious and have to be derived either from system simulations (Chapter 3) or from the theoretical start-up of the reflector (Chapter 2).

1.7. Motivation and Goal

There is a large market potential for a reliable indoor positioning system, which has small and power efficient mobile units. The integration

in CMOS may solve these challenges. The aim of this thesis is the development of an integrated active pulsed reflector in 0.18-μm CMOS. The main research contributions are:

- An active pulsed reflector has to start phase coherent. We study the start-up behavior, verify the phase coherent start-up and investigate the conditions and the circuit design needed for synchronicity.
- CMOS technology has the disadvantage of low quality factors Q of inductors and a low supply voltage. This thesis evaluates, if it is possible to integrate the active pulsed reflector approach in CMOS and what the effects of these limitations on the accuracy of distance measurements are.
- In indoor environments, multipath propagation influences the accuracy of positioning systems. The influence of multipath propagation on the positioning accuracy will be studied.
- The integration of the active reflector in CMOS. Challenges are the impedance matching and on-switching mechanism.
- Experimental characterization of the active reflector indoors and with different antennas.

1.8. Thesis Organization

The structure of the thesis is as follows:

Chapter 2: Oscillator Start-Up presents a theoretical analysis of the start-up behavior of an oscillator under the influence of a CW signal. The conditions for phase-coherent start-up are presented and the influences of different oscillator parameters on the phase behavior are simulated. The simulation results are verified by measurement of a real oscillator.

Chapter 3: Active Pulsed Reflector System provides a detailed description of the positioning system. The system is simulated with two different models, one is derived from the theoretical start-up model and the other one is a Simulink model. The system simulations reveal the influence of design parameters such as oscillator loop gain, quality

factor Q of the feedback filter, received signal strength, frequency drift, jitter and SNR on the positioning accuracy. Finally, the deterioration of system performance due to multipath propagation is simulated with an UWB channel model.

Chapter 4: Reflector Integration discusses the circuit implementation of the active pulsed reflector. The application-specific integrated circuit (ASIC) is discussed first including the switching mechanism and impedance matching. The switching mechanism is of great importance, because on-switching can influence the phase coherent start-up of the reflector. Next, the complete prototype is presented. Finally, the system is tested indoors in a challenging multipath environment.

Chapter 5: 3D Positioning deals with signal processing and algorithms for 3D positioning. Spectral peak detection algorithms and different positioning algorithms (least-squares, mass-spring models and linear minimization) are compared based on simulation results with a simple multipath model. The chapter closes with an estimation of the performance of the active reflector system in a small museum.

Chapter 6: Conclusion draws a summary of the thesis and provides concluding comments on the achieved results. A brief outlook on future work is given.

2

Oscillator Start-Up

The previously presented positioning system is based on the phase synchronous start-up of the active pulsed reflector. The active pulsed reflector is a periodically switched oscillator and the input signal is sinusoidal $y_{in} = B\sin(\phi(t))$. In this chapter, a theoretical analysis of the start-up of an oscillator is presented and verified by measurements.

For most use cases of an oscillator, only the steady state is of importance. It has to be ensured that the oscillator initially starts, thus the analysis of the start-up conditions are sufficient, but the evolution of the phase $\phi(t)$ and amplitude $B(t)$ during start-up is not important. For example the exact start-up behavior of a voltage-controlled oscillator (VCO) in a phase locked loop (PLL) is not of interest, because the initial settling time of the loop is much longer than the start-up time of the oscillator. Only the steady state is relevant.

However, the start-up behavior of oscillators is important for many applications, for example UWB transmitter and super-regenerative filters. For pulse generating in UWB transmitter [71] very fast oscillator start-up is of interest. The envelope $B(t)$ of a starting oscillator formed by a cross-coupled differential pair is calculated. The start-up time strongly depends on the initial conditions. Because the phase

$\phi(t)$ is not important for the pulse generation, fast start-up can be achieved by setting large initial conditions by adding a digital start-up circuit [72]. Barras et al. decouple the sources of the differential pair in a cross-coupled LC VCO and split the tail current source I_{tail} into two current sources $I_{tail}/2$ [71]. When the reflector is switched on, one of the two tail current sources is switched on earlier, leading to an imbalance, which decreases the start-up time. The second method is used for differential ring oscillators [72]. Initially, one of the differential signals is connected to a low potential and the other to a high potential. As soon as the oscillator is switched on, the signals are disconnected from the initial potential and oscillation starts.

The start-up time of an oscillator with or without an applied CW signal is important for super-regenerative receivers [73]. Super-regenerative receivers are basically pulsed oscillators. The oscillator's gain is periodically modulated. As soon as the loop gain is larger than 1, an oscillation starts. The growth of the amplitude over time depends on the power of the incoming amplitude modulated (AM) signal at start-up. For a stronger received signal, the oscillation reaches a larger amplitude until the oscillator is switched off again. The output of the oscillator is low-pass filtered and thus the AM signal is down-converted to the base-band. A detailed analysis of the super-regenerative principle is presented in [74] and a recent implementation of a 2.4 GHz super-regenerative receiver can be found in [75].

Only the amplitude $B(t)$ of the oscillator is important for the previously discussed applications. However, there exist scenarios, where the exact start-up behavior including phase $\phi(t)$ and amplitude $B(t)$ of an oscillator under the influence of an external signal is of importance, such as pulsed magnetrons [76] or in our case the active pulsed reflector approach [77] for local positioning FMCW radar system.

2.1. Theoretical Analysis

A generic oscillator can be represented as a feedback block diagram with an amplifying $A(\omega)$ and a passive part $F_{Filt}(\omega)$ as shown in Fig. 2.1. For the analysis of the start-up behavior, we assume a linear, frequency and time independent loop gain $A(\omega) = A$. The second order transfer function of the passive feedback is defined by the quality factor Q and the resonance frequency ω_0. Even ring-oscillators can be approximated

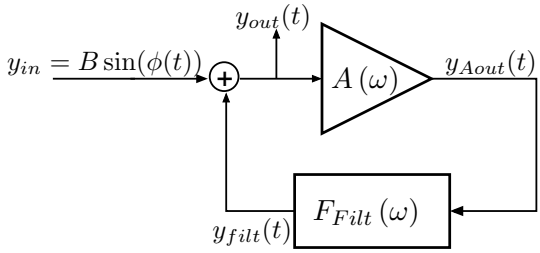

Figure 2.1. Simple reflector block model used for the theoretic analysis.

with this model [78]. The band-pass type feedback is

$$F_{Filt}(s) = \frac{\frac{\omega_0}{Q}s}{s^2 + \frac{\omega_0}{Q}s + \omega_0^2} \tag{2.1}$$

Thus, the closed loop transfer function F_{Osz} of the oscillator becomes

$$F_{Osz}(s) = \frac{1}{1 - A \cdot F_{Filt}} = \frac{s^2 + \frac{\omega_0}{Q}s + \omega_0^2}{s^2 + (1-A)\frac{\omega_0}{Q}s + \omega_0^2} \tag{2.2}$$

The closed loop transfer function has two zeros at

$$z_{1/2} = \frac{\omega_0}{2}\left(-\frac{1}{Q} \pm \sqrt{\frac{1}{Q^2} - 4}\right) \overset{Q>4}{\approx} \frac{\omega_0}{2}\left(-\frac{1}{Q} \pm 2i\right) \tag{2.3}$$

and two complex conjugate poles at

$$p_{1/2} = \frac{\omega_0}{2}\left(\frac{A'}{Q} \pm \sqrt{\frac{A'^2}{Q^2} - 4}\right) \tag{2.4}$$

with $A' = A - 1$. For $Q > 1/2$, both zeros lie in the closed left half of the complex plane. The stability criterion determines that both poles must lie in the closed right plane for instability. Thus, A' has to be equal or larger than zero, which leads to an open-loop gain $A \geq 1$, corresponding to the first Barkhausen criteria. The second Barkhausen criteria states that the open-loop phase shift around the loop has to be $k \cdot 2\pi$. This is fulfilled in this model due to the bandpass filter characteristic of the feedback.

The impulse response of this unstable system is an exponentially growing, oscillating function. This function is not integrable and its

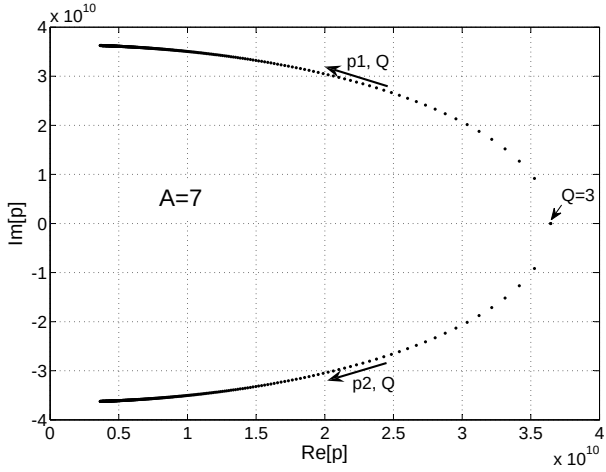

Figure 2.2. Root of the poles vs. Q for a fixed open loop gain A of 7. Q is swept from 3 to 30. When $Q = (A-1)/2$, both poles lie on the real axes. For higher Q, the poles move closer to the imaginary axis.

Fourier transform does not exist. Nevertheless, the convolution of the incoming signal with the impulse response leads to the time behavior of the system, because we modeled the oscillator as a linear, time invariant (LTI) system. The system is time-invariant, because all coefficients are time independent. And the system is linear, because saturation effects are neglected. In the Laplace domain, the convolution of the incoming signal with the impulse response of the system is a simple multiplication of the Laplace transform of the input signal and the transfer function. Often the input signal is only random noise. When the oscillator is used as a back scatter in an FMCW radar system, the input is a sinusoidal signal

$$y_{in}(t) = B \sin\left(\int_0^t \omega\,(t)\,\mathrm{d}t + \phi_0\right) \tag{2.5}$$

where $\omega(t) = \omega_B + (t/T - 1/2)\omega_{BW}$ is a linear frequency ramp with sweep duration T. As we will see later, the oscillator used as active pulsed reflector is periodically switched on and off and the on-time t_{on} is very short (13.3 ns). Since the on-time t_{on} is much shorter than the sweep duration T (0.65 ms), the incoming frequency is almost constant during one on-switching process (changes by roughly 3 kHz). For the

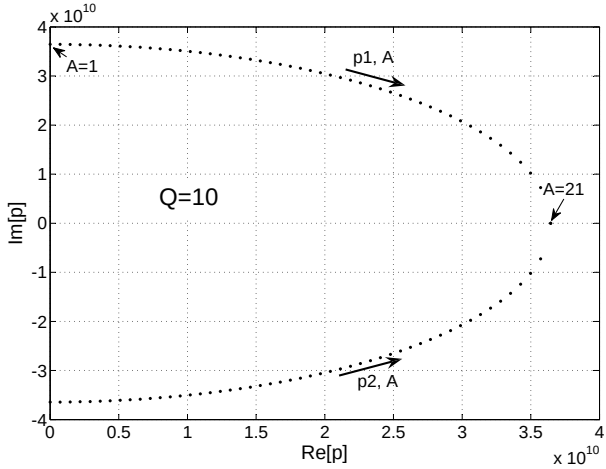

Figure 2.3. Evolution of critical pair of complex-conjugate poles against open-loop gain A for a fixed quality factor $Q = 10$. A is swept from 1 to 21. When A is equal to $2Q + 1$, both poles lie on the real axes. For smaller A, the poles approach the imaginary axis. When the open loop gain equals 1, both poles lie on the imaginary axis. In this case, the oscillator is in steady state operation.

start-up analysis, the incoming signal can therefore be simplified to

$$y_{in}(t) = B\sin\left(\omega t + \phi_0\right), \omega \approx \text{const.} \tag{2.6}$$

Initially, all signals and internal states of the oscillator are 0. The amplifier A attenuates the incoming signal completely, hence the signal is not received at the filter and the internal states of the filter remain all on 0. The oscillator is switched on at t_0 and from then on, the incoming signal y_{in} is amplified. This has the same effect as if the reflector is always on, but the incoming signal is switched on. Without an incoming signal, all internal states and signals remain on 0. The oscillator does not start before an input signal is applied (this is only true in a noiseless environment). In reality, the two cases, gain switching or incoming signal switching, are not exactly identical, because the filter is not perfectly isolated from the incoming signal when the reflector is switched off and the on-switching is not instantaneous. A more generic case is discussed in Appendix A.2. The switched incoming signal $y_{in,rs}(t)$

$$y_{in,rs}(t) = B\sin(\omega t + \phi_0)\Theta(t - t_0) \tag{2.7}$$

with the Heaviside step function $\Theta(t)$ defined as

$$\Theta(t) = \begin{cases} 0 & \text{if } t < 0, \\ 1 & \text{if } t \geq 0. \end{cases} \tag{2.8}$$

The on-switching moment t_0 can be chosen arbitrarily. In order to simplify the calculation, we chose $t_0 = 0$. This can be done without loss of generality, because this situation can be achieved with a simple coordination transfer ($\tilde{t} = t - t_0$). The unilateral Laplace transform of $y_{in,rs}$ for $t_0 = 0$ is

$$F_{in,rs}(s) = \frac{B(\omega\cos\phi_0 + s\sin\phi_0)}{s^2 + \omega^2} \tag{2.9}$$

Multiplying (2.2) with (2.9) gives

$$\begin{aligned} F_{out}(s) &= F_{in,rs}(s) \cdot F_{Osz}(s) \\ &= B\frac{\left(s^2 + \frac{\omega_0}{Q}s + \omega_0^2\right)(\omega\cos(\phi_0) + s\sin(\phi_0))}{\left(s^2 + (1-A)\frac{\omega_0}{Q}s + \omega_0^2\right)(s^2 + \omega^2)} \end{aligned} \tag{2.10}$$

The inverse Laplace transformation of $F_{out}(s)$ is

$$\begin{aligned} y_{out}(t \geq 0) = z(&x\sin(\omega t + \phi_0) + y\cos(\omega t + \phi_0) \\ &+ Ae^{\frac{(A-1)t\omega_0}{2Q}}(u(\phi_0)\sin(\omega_0' t) + v(\phi_0)\cos(\omega_0' t))) \end{aligned} \tag{2.11}$$

under the condition $4Q^2 > (A-1)^2$. $y_{out}(t)$ depends on the starting phase ϕ_0 at $t_0 = 0$. The terms u, v, x, y, z and ω_0' are given by the following expressions:

$$u(\phi_0) = \frac{(A-1)\,Q\omega\omega_0\left(\omega^2+\omega_0^2\right)\cos\phi_0}{\sqrt{\left|(A-1)^2-4Q^2\right|}} + \frac{\omega^2\omega_0^2\,(A-1)^2\sin\phi_0 + 2Q^2\omega_0^2\left(\omega_0^2-\omega^2\right)\sin\phi_0}{\sqrt{\left|(A-1)^2-4Q^2\right|}} \tag{2.12}$$

$$v(\phi_0) = \omega\omega_0\left(Q\cos\phi_0\left(\omega^2-\omega_0^2\right)+(A-1)\,\omega\omega_0\sin\phi_0\right) \tag{2.13}$$

$$x = Q^2\left(\omega^2-\omega_0^2\right)^2-(A-1)\,\omega^2\omega_0^2 \tag{2.14}$$

$$y = AQ\omega\omega_0\left(\omega_0^2-\omega^2\right) \tag{2.15}$$

$$z = \frac{B}{(A-1)^2\,\omega^2\omega_0^2+Q^2\left(\omega^2-\omega_0^2\right)^2} \tag{2.16}$$

$$\omega_0' = \omega_0\frac{\sqrt{\left|(A-1)^2-4Q^2\right|}}{2Q} \tag{2.17}$$

Equation (2.11) is the basis for phase synchronous start-up of the active pulsed reflector. The evolution of the phase after start-up is discussed later in this section. Equation (2.11) consists of two different oscillations. One oscillates with the incoming signal at ω and the other one with the detuned resonance frequency ω_0' of the reflector (see Equation 2.17). While the first oscillation has a constant amplitude over time, the second oscillation grows exponentially. In the case of an active reflector, the incoming signal is weak (≈-60 dBm). An active reflector amplifies the incoming signal before transmitting it back to the base station. This is achieved, if the second part of (2.11) grows exponentially. The two conditions (2.18) and (2.19) have to be satisfied to guarantee the exponential growth of $y_{out}(t)$

$$(A-1)^2 < 4Q^2 \tag{2.18}$$

$$0 < \frac{(A-1)\omega_0}{2Q} \tag{2.19}$$

Equation (2.19) can be simplified to $A > 1$. This is equal to the first Barkausen criterion that the loop gain has to be larger than 1 to start

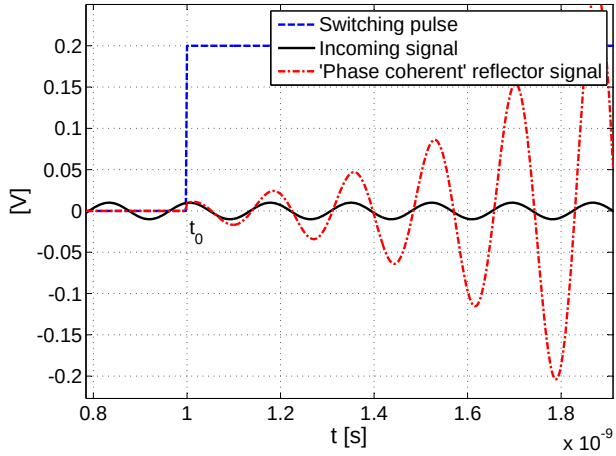

Figure 2.4. The reflector starts with the same phase as the incoming signal. Due to the different frequencies the two phases diverge.

an oscillation. The start-up of the oscillator with an applied sinusoidal signal is depicted in Fig. 2.4. The oscillation amplitude increases exponentially and the oscillator oscillates with a different frequency ω_0' than the incoming signal (ω). In addition, the oscillator starts with the same phase as the incoming signal.

2.1.1. Phase Synchronous Start-Up

The phase synchronous start-up is the most important property of the active reflector. The behavior of the phase can be best studied, if the oscillations are written in complex phasor notation. The incoming signal (2.6) can be expressed as

$$\vec{y}_{in}(t) = Be^{i\left(\omega t+\phi_0-\frac{\pi}{2}\right)} \tag{2.20}$$

The corresponding signal in the voltage domain is

$$y_{in}(t) = \text{Real}\left[\vec{y}_{in}(t)\right] = B\sin\left(\omega t+\phi_0\right) \tag{2.21}$$

The reflector output signal (2.11) in complex phasor notation is given as

$$\vec{y}_{out}(t) = z\Big(e^{i\left(\omega t+\phi_0-\frac{\pi}{2}\right)}(x+iy) + Ae^{\frac{(A-1)\omega_0 t}{2Q}} e^{i\left(\omega_0' t-\frac{\pi}{2}\right)}(u(\phi_0)+iv(\phi_0))\Big) \tag{2.22}$$

For a loop gain A larger than 1, the second part of (2.22) increases exponentially over time and becomes much larger than the first part of the equation (in reality a difference of ≈ 60 dB). The term $(u+iv)$ can be written in polar coordinates. The conversion of u and v to $B_{ref}e^{i\phi_{ref}}$ is illustrated in Fig. 2.5.

$$B_{ref}e^{i\phi_{ref}} = u(\phi_0)+iv(\phi_0) \tag{2.23}$$

with

$$B_{ref} = \sqrt{u^2+v^2} \tag{2.24}$$

$$\phi_{ref} = \angle(u(\phi_0)+iv(\phi_0)) \tag{2.25}$$

Equation 2.22 is rewritten as

$$\vec{y}_{out}(t) = zAe^{\frac{(A-1)\omega_0 t}{2Q}} e^{i\left(\omega_0' t-\frac{\pi}{2}\right)} B_{ref}e^{i\phi_{ref}} = r_{out}e^{i\phi_{out}} \tag{2.26}$$

The amplitude and the phase of the output signal are

$$r_{out}(t) = zAe^{\frac{(A-1)\omega_0 t}{2Q}} B_{ref} \tag{2.27}$$

and

$$\phi_{out}(t) = \omega_0' t + \phi_{ref} - \frac{\pi}{2} \tag{2.28}$$

respectively. The oscillator starts phase synchronous, if the output phase $\phi_{out}(t=0)$ is equal to the phase of the incoming signal $\phi_{in}(t=0)$. The phase error $\Delta\phi(t)$ is

$$\Delta\phi(t) = \phi_{in}(t) - \phi_{out}(t) = (\omega-\omega_0')t + \phi_0 - \phi_{ref} \tag{2.29}$$

and the starting phase error is the initial error $\Delta\phi(t=0)$ at start-up. Except of a special case, the starting phase error can only be calculated numerically. The results of the numerical calculation of the phase error under different conditions, such as $\omega \neq \omega_0'$ and loop gain A in the same order of magnitude as the quality factor Q, are discussed later. In a

first step, we prove that the reflector starts perfectly phase synchronous under certain conditions. Perfect phase synchronous start-up is equal to zero starting phase error $\Delta\phi(0) = 0$. The starting phase ϕ_{ref} must be equal to the input phase ϕ_0

$$\phi_{ref} = \phi_0. \tag{2.30}$$

This identity has to be proven. If the oscillator functions as a reflector in a FMCW radar, then the input signal is a linear frequency ramp $\omega(t) = \omega_B + \omega_{BW} \cdot (t/T - 1/2)$ and not a constant frequency ω. The center frequency is chosen as $\omega_B = \omega_0$. It happens that the incoming signal has exact the same frequency as the free running oscillator ($\omega = \omega_0$). Additionally, if we assume that the quality factor Q of the feedback filter is much larger than the loop gain A, then $u(\phi_0)$ (2.12) and $v(\phi_0)$ (2.13) are approximately

$$u(\phi_0) \approx (A-1)\omega^4 \cos(\phi_0) \tag{2.31}$$

$$v(\phi_0) \approx (A-1)\omega^4 \sin(\phi_0) \tag{2.32}$$

The calculations leading to this approximations can be found in Appendix A.1.1. The starting phase of the reflector ϕ_{ref} is

$$\phi_{ref} = \angle(u(\phi_0) + iv(\phi_0)) \approx \phi_0 \tag{2.33}$$

Therefore, the reflector starts with the phase of the incoming signal. Perfect phase synchronization at start-up is achieved.

The phase behavior during start-up without simplifications, such as $\omega = \omega_0$ and $Q \gg A$, is discussed in Section 2.1.3.

2.1.2. Start-Up Time t_{start}

An oscillator needs to fulfill two important characteristics, if it is used as an active pulsed reflector. The first property is the phase synchronous start-up discussed before. The second property is a fast start-up, because the on-time of the reflector is short ($t_{on} = 13.3$ ns). The on-time t_{on} is short, because the available bandwidth is large. This requirement is discussed later in Section 2.3. The model used for the analysis of the start-up behavior is a linear, small signal model. Therefore, the amplitude of the output signal exponentially grows to infinity. In a circuit implementation, this cannot happen. The non-linearities of real circuit components (especially transistors) limit the output amplitude to a steady state. Thus, the start-up time of a non-linear oscillator can

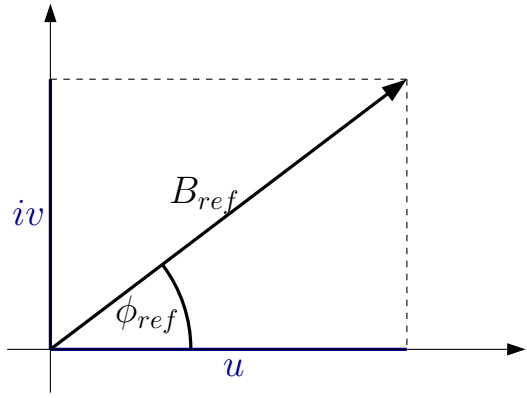

Figure 2.5. Illustration for the conversion from complex coordinates $u+iv$ to polar coordinates $B_{ref}e^{i\phi_{ref}}$.

be simulated numerically or the non-linearities can be approximated by a Taylor series [71]. But the start-up time t_{start} can be estimated based on the linear model. Figure 2.6 compares the start-up envelope of the linear model (grows exponentially) with a realistic envelope with saturation. Barras et al. [71] calculated the start-up envelope of a cross-coupled LC oscillator. The simplified single-ended equivalent schematic consists of a parallel RLC network and a transistor with transconductance g_m. The start-up envelope can be modeled as

$$\mathrm{env}(t) = \frac{2v_0}{\sqrt{1 + \left(\left(\frac{2v_0}{v(0)}\right)^2 - 1\right) e^{-\epsilon\omega_0 t}}}. \tag{2.34}$$

where v_0 is a normalizing factor

$$v_0 = 2V_{od}\sqrt{\frac{2}{3}\left(1 - \frac{G}{g_m}\right)}, \tag{2.35}$$

with V_{od} as the overdrive voltage of the transistor and G is the conductance of the parallel resistor R of the RLC resonator. ϵ is a damping factor

$$\epsilon = (g_m - G)\sqrt{\frac{L}{C}}. \tag{2.36}$$

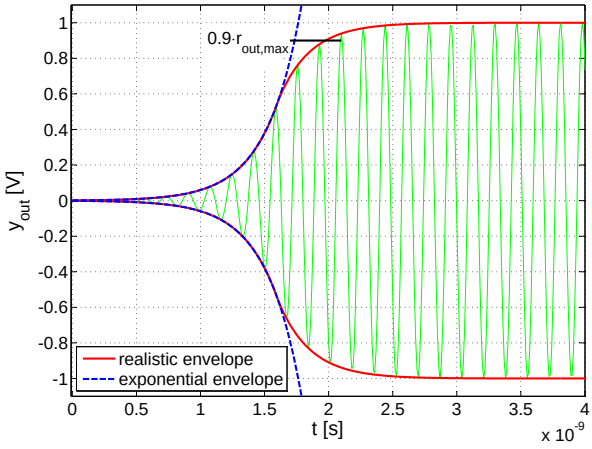

Figure 2.6. The output of an oscillator initially grows exponentially. The start-up time t_{start} is the time when 90% of the full amplitude is reached.

The start-up time is measured where the amplitude r_{out} reaches 90% of the steady state amplitude $r_{out,max}$. The start-up time is underestimated, but the error is around 15%. Since the values of the passive components (especially the Q-factor of inductances) have typically 5-20% tolerances an analysis with much greater accuracy is unnecessary for practical purposes [79].

The exponential growing amplitude $r_{out}(t)$ of the oscillator is given by (2.27). By taking the logarithm and rearranging, we obtain

$$t_{start} = \frac{2Q}{\omega_0 (A-1)} \ln\left(\frac{0.9 r_{out,max}}{Az\sqrt{u(\phi_0)^2 + v(\phi_0)^2}}\right) \tag{2.37}$$

where $r_{out,max}$ is defined as the steady state amplitude of the oscillator. z, $u(\phi_0)$ and $v(\phi_0)$ are given by (2.16), (2.12) and (2.13), respectively. The start-up time is directly related to the loop gain A and the quality factor Q. The amplitude of the incoming signal B has also a large influence on the start-up, because z is directly proportional to B. But this parameter B is determined by the base station's output power and the channel attenuation. There is also a weak influence of the phase ϕ_0 and the frequency ω of the incoming signal on the start-up time t_{start} due to the phase and frequency dependence of $u(\phi_0)$ and $v(\phi_0)$. The

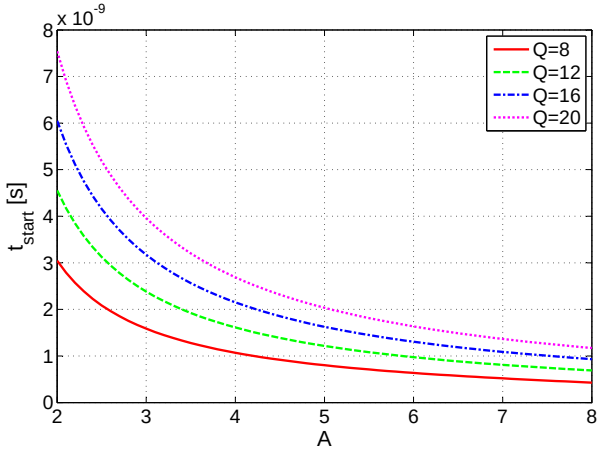

Figure 2.7. Start-up time t_{start} vs A and Q for an input power P_{in} of -63 dBm ($B = 224\ \mu$V) and an output power of 5 dBm. The phase and frequency of the received signal are $\phi_0 = \pi/2$ and $\omega = 2\pi 5.725e9$, respectively.

only two parameters that can be influenced by the design of the active reflector are the loop gain A and the quality factor Q. Figure 2.7 explores the design space for these two parameters. Integrated inductors in CMOS technology have a low Q_{ind}-factor, normally below 20. The loaded Q-factor Q_{load} is even lower. Therefore, the quality factor of the filter Q without Q-enhancement is also below 20. The oscillator starts reasonably fast ($\approx$4 ns$\ll t_{on} =$ 13.3 ns) for a loop gain A larger than 3. If the load resistance and the output swing remain constant, then a larger loop gain A needs more power. Thus, a loop gain of 3 is chosen for the subsequent simulations.

2.1.3. Start-Up Simulations

We showed in the previous section that the starting phase of the oscillator ϕ_{ref} is identical to the incoming phase ϕ_0. This is only true, if the loop gain A is much smaller than the quality factor Q and the incoming signal has the same frequency as the reflector ($\omega = \omega_0$). How does the phase behavior change if these simplifications are not fulfilled? In a first scenario, the quality factor Q is in the same order as the loop gain A, but the incoming signal has the same frequency as the free running oscillator ($\omega = \omega_0$). We are interested in the difference between an

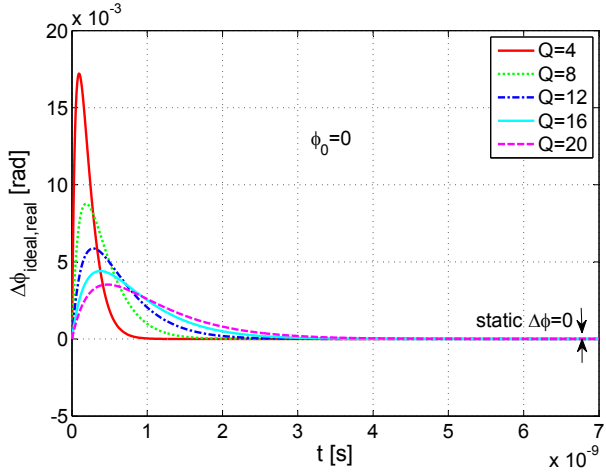

Figure 2.8. Simulated phase difference $\Delta\phi_{ideal,real}(t)$ between a reflector with ideal start-up and the theoretical model for a starting phase $\phi_0 = 0$, a loop gain of $A = 3$ and the incoming signal has the same frequency as the oscillator $f = f_0 = 5.8$ GHz. After the start-up, the oscillator is perfectly in sync with an ideal oscillator independent of Q.

ideal start-up and the actual start-up. The phase of the ideal start-up is

$$\phi_{ideal}(t) = \omega_0' t + \phi_0 - \frac{\pi}{2} \tag{2.38}$$

while the phase of the real start-up can be written as

$$\phi_{out}(t) = \angle\vec{y}_{out}(t) \tag{2.39}$$

where $(\vec{y}_{out}(t)$ is defined in (2.22). The phase error $\Delta\phi_{ideal,real}(t)$ between an ideal phase synchronous oscillator and the real start-up behavior is defined by

$$\Delta\phi_{ideal,real}(t) = \phi_{ideal}(t) - \phi_{out}(t) = \omega_0' t + \phi_0 - \frac{\pi}{2} - \angle\vec{y}_{out}(t) \tag{2.40}$$

Figure 2.8 illustrates the phase error $\Delta\phi(t)$ versus the quality factor Q for a starting phase $\phi_0 = 0$. The maximum difference between the ideal start-up and the real start-up is below 0.02 [rad] for a Q factor above 4. And is zero when the full-swing amplitude is reached

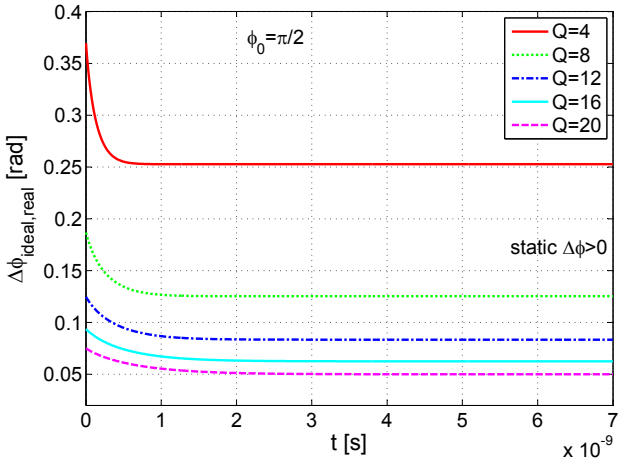

Figure 2.9. Simulated phase difference $\Delta\phi_{ideal,real}(t)$ between a reflector with ideal start-up and the theoretical model for a starting phase ϕ_0 of $\frac{\pi}{2}$ for a loop gain A=3 and the incoming signal has the same frequency as the oscillator $f = f_0 = 5.8$ GHz.

for $t > 3$ ns. This is only the case if the input phase ϕ_0 is either 0 or π, because the incoming signal is 0 when the oscillator is switched on. The simulation results for a starting phase $\phi_0 = \frac{\pi}{2}$ are depicted in Fig. 2.9. With a non-zero starting phase, the phase difference is smaller for a higher Q-factor. A higher Q-factor increases the start-up time, which also increases the time during which the oscillator is sensitive to the input signal. The influence of an external signal on the oscillator depends on the amplitude of the received signal and the amplitude of the oscillation [74], [80]. As soon as the oscillator's output is orders of magnitude larger than the incoming signal, the incoming signal has no substantial influence on the oscillation. This behavior can be analytically described by the sensitivity function (see Appendix A.2).

The oscillator needs about 1 to 3 ns until the final phase difference is reached. For the further study of the phase behavior, only the final phase difference $\Delta\phi_{ideal,real}(t > 3\ ns)$ is considered. The influence of the starting phase ϕ_0 on this final phase error $\Delta\phi_{ideal,real}(t > 3\ ns)$ is plotted in Fig. 2.10. The phase error decreases for a higher quality factor Q. But a high Q reduces the bandwidth of the bandpass filter, making the oscillator more selective. Up to now, the incoming signal's

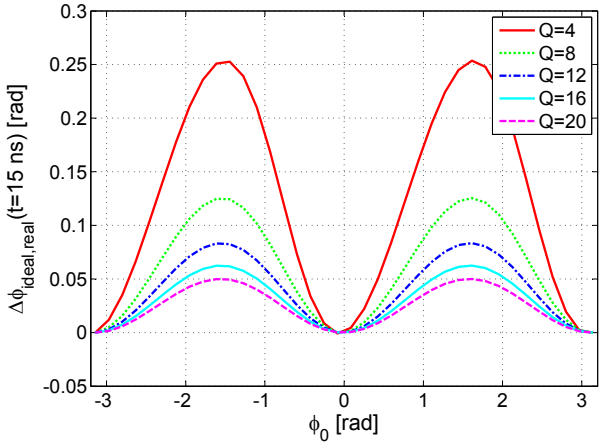

Figure 2.10. Final phase error $\Delta\phi_{ideal,real}(t = 15\ ns)$ vs. the starting phase ϕ_0, if the incoming signal and the oscillator oscillate with the same frequency ($f = f_0 = 5.8$ GHz).

frequency ω is exactly at the same frequency as the oscillator (ω_0). If this is not the case anymore, the phase error changes. Figure 2.11 shows the mean phase error $\Delta\phi_{ideal,real}(t = 15\ ns)$ and the maximum and minimum phase error for different Q-factors, and different incoming signal frequencies f. The phase error for a specific frequency f is the largest in the case of a low Q-factor. But the difference between the different input frequencies f is small. A higher Q-factor reduces the phase error for a specific frequency f, but increases the influence of the incoming signal. An explanation for this is that the higher Q-factor leads to a narrower bandwidth and thus the oscillator's start-up behavior is more sensitive to the incoming frequency f. The same simulations, but with a varying loop gain A instead, exhibits a similar behavior. The phase error is plotted in Fig. 2.12. The phase error is large for a large loop gain A, but almost independent of the incoming frequency f.

On the other hand, the variance of $\Delta\phi$ is small for a small loop gain, but the absolute phase error is strongly dependent on the incoming frequency f. The smallest overall phase error ($f \in [5.725, 5.875]$ GHz, $\phi_0 \in [0, 2\pi]$) is achieved by a loop gain A between 3 and 4 for a quality factor Q of 10.

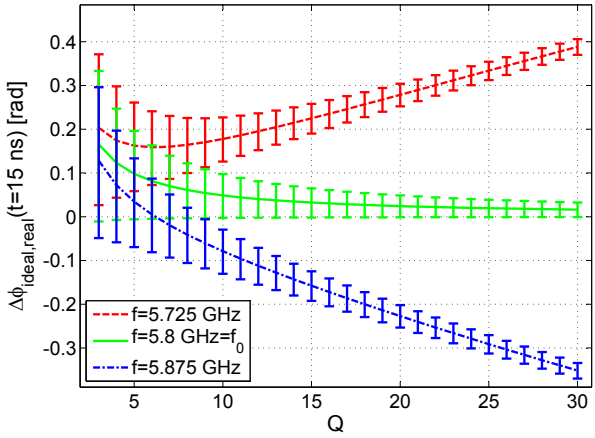

Figure 2.11. Phase error $\Delta\phi_{ideal,real}(t = 15\ ns)$ between ideal start-up behavior and calculated real start-up behavior after 15 ns for a loop gain A of 3.

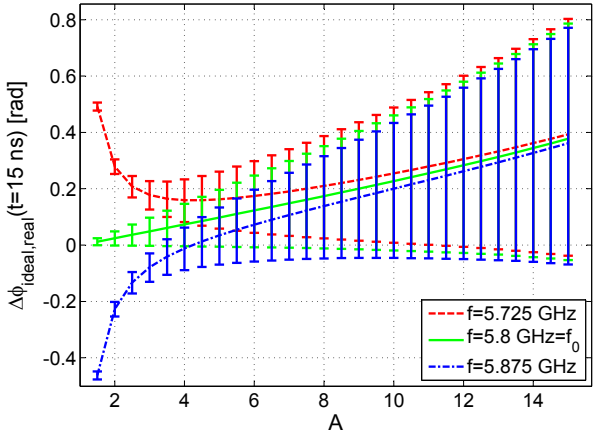

Figure 2.12. Phase error $\Delta\phi_{ideal,real}(t = 15\ ns)$ between ideal and calculated start-up behavior after 15 ns with a Q-factor of 10.

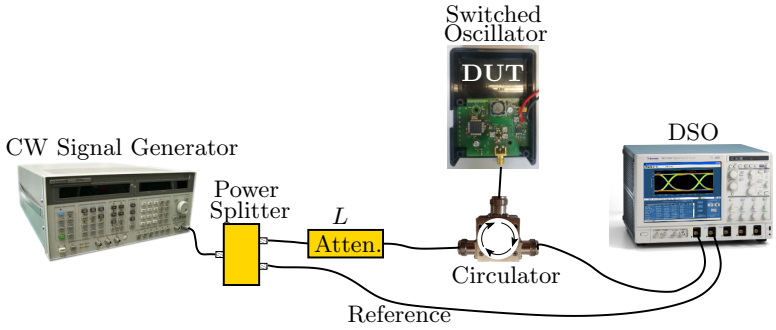

Figure 2.13. Measurement setup for the phase synchronous start-up. The signal generator generates a 5.8 GHz CW reference signal. This CW signal is fed through an attenuator to the oscillator (DUT) and is also sampled by a digital sampling oscilloscope (DSO). The output of the pulsed oscillator is also sampled by the DSO.

All the above mentioned characteristics are based on the calculated, theoretical model. In the next Section, the model has to be verified by measurements on a real oscillator. The theoretical model is later (Section 3.2.2) also compared to a Simulink model of an oscillator. Without anticipating this discussion too much, it can be stated that the theoretical model and the Simulink simulations agree well.

2.2. Measurement of the Phase-Synchronous Start-Up Behavior

In this Section, we discuss the measurements of the start-up behavior of a real oscillator, if a sinusoidal CW signal is applied to the input. The oscillator used for the measurements is an active reflector prototype. The active reflector prototype is extensively discussed in Chapter 3.6. For the moment, it is enough to know that the reflector consists of a periodically on and off-switched oscillator with a modulation frequency f_{mod} and a on-time t_{on}. The architecture of the oscillator is plotted in Fig. 4.1. The reflector architecture is very similar to the simplified theoretical model depicted in Fig. 2.1. The difference is that instead of an broad-band amplifier and a passive band-pass filter, two amplifiers with a band-pass characteristic are applied.

The measurement setup for the phase synchronous start-up behav-

ior is drawn in Fig. 2.13. The idea of the measurement is to measure the phase difference $\Delta\phi$ between the incoming signal and the oscillator's output. The input signal is a 5.8 GHz CW signal generated by a signal generator. This signal is attenuated by a variable attenuation L and then fed to the oscillator's input. The oscillator's output and the reference signal are sampled by a Tektronix digital sampling oscilloscope (DSO). The sampling frequency is 50 GS/s. The time difference between the falling edges of incoming and the outgoing signal can be measured. Unfortunately, the two paths have not the same length and thus, there is an unknown phase shift $\Delta\phi_{cable}$ between the two measured signals. This phase shift could be measured for each attenuation L, but for a high attenuation $L = -70$ dBm, the received signal at the DSO is weak and noisy and thus the phase shift measurement is not too accurate. However, we want to prove the phase synchronous start-up. If the reflector starts completely phase synchronous to the incoming signal ($\Delta\phi = 0$), then the two measured signals have a constant, but unknown phase difference ($\Delta\phi_{meas} = \Delta\phi + \phi_{cable} = \phi_{cable}$). A good measurement for the phase synchronicity of the reflector is the standard deviation $\sigma_{\Delta\phi}$ of the phase error $\Delta\phi$. $\sigma_{\Delta\phi_{meas}}$ is equal to $\sigma_{\Delta\phi}$, because the phase shift due to the cables (ϕ_{cables}) is constant.

2.2.1. Simulation Results of the Phase-Synchronous Start-Up Behavior

Before conducting the measurements, the phase synchronous start-up is simulated. The start-up of the reflector is modeled by Equation (2.11). The phase synchronous start-up is disturbed by noise. The noise here is modeled as an additional sinusoidal signal $y_{noise}(t) = N\sin(\omega t + \phi_{rand})$. For every start-up calculation, a random phase ϕ_{rand} is chosen and the two signals $y_{noise}(t)$ and $y_{in}(t)$ are added. It is assumed that the noise signal is not correlated to the incoming signal, because in the measurement setup we have a very clean incoming signal and the noise is mainly generated in the oscillator itself (e.g. supply noise, thermal noise, detoriation due to on-switching pulse). Therefore, the noise signal can be assumed to have a constant amplitude N. The weaker the incoming signal y_{in} is, the smaller is the signal-to-noise ratio (SNR) B/N. The phase difference $\Delta\phi$ is calculated by the time difference between the first zero crossing of the incoming signal and the reflected signal, when the amplitude of the reflected signal is the first time larger than 0.1 V.

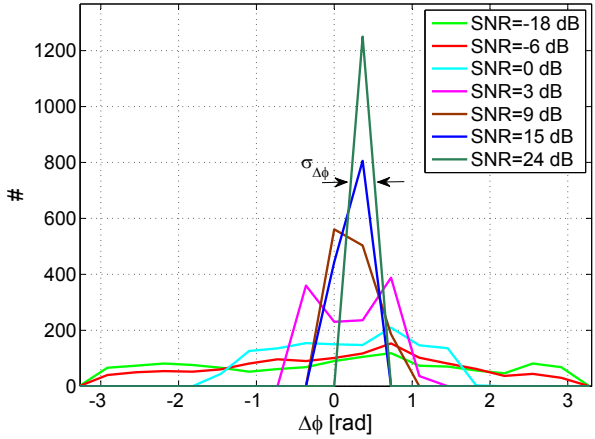

Figure 2.14. Simulated phase error $\Delta\phi$ between incoming signal and the output of the oscillator with added signal noise. The larger the SNR is, the smaller is the phase error distribution.

Because the standard deviation $\sigma_{\Delta\phi}$ is of interest, 1250 start-ups with varying input phases ϕ_{rand} and ϕ_0 are simulated for each SNR ratio. Figure 2.14 depicts the distribution of the phase errors $\Delta\phi$. The resolution of the simulation is 0.37 rad, because the simulation time step is 10 ps. The synchronization is best for a high SNR. The phase error is below the simulation resolution for a SNR above 18 dB. $\sigma_{\Delta\phi}$ is below 0.04 for a SNR above 24 dB. If the SNR decreases, the mean error $\overline{\Delta\phi}$ stays constant, but the standard deviation of the phase error increases with lower SNR. The phase error $\Delta\phi$ is almost equally distributed for a SNR of -18 dB and $\sigma_{\Delta\phi}$ is 1.7753. The standard deviation for a perfect equally distributed phase error is 1.814. Hence, we can conclude that the oscillator does not start phase synchronous anymore for a SNR below -18 dB. The influence of the SNR on the positioning accuracy is simulated in Section 3.3.7.

2.2.2. Measurement Results of the Phase-Synchronous Start-Up Behavior

The time domain measurement of the pulsed oscillator's output is shown in Fig. 2.15. The pulse frequency f_{mod} is 18.75 MHz and the on-time t_{on} is set to 13.3 ns. The reflector output for one on-switching

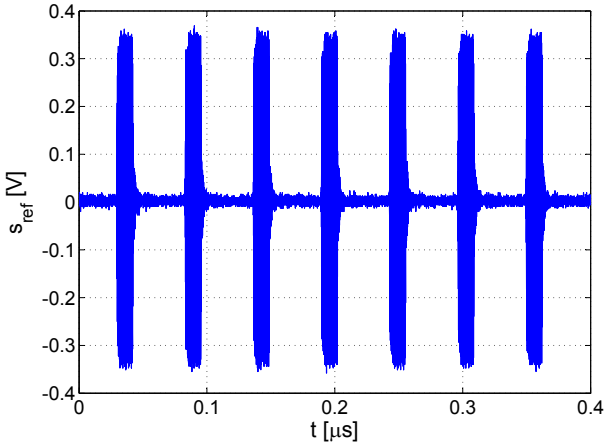

Figure 2.15. Measured output signal of a pulsed oscillator with a pulsing frequency f_{mod} of 18.75 MHz and a wanted on-time t_{on} of 13.3 ns. The input power P_{in} of the received CW signal is -66 dBm and the CW frequency f is equal to the oscillation frequency $f_0 = 5.8$ GHz

period is drawn in Fig. 2.16. The measured pulse length $t_{on} = 12.3$ ns is close to the derived 13.3 ns. The measured voltage swing is 0.37 V (equivalent to 1.4 dBm). The start-up time strongly depends on the ratio $(A-1)/(2Q) = 0.15$. This measured factor is 50% larger than in the previous simulations. This is either due to a too high gain A or a lower Q-factor.

The measurements prove that the oscillator can be pulsed fast enough and that the wanted, short on-time t_{on} of 13.3 ns can be achieved. The more important property of the oscillator is the phase synchronous start-up. The incoming signal y_{in} and the outgoing signal y_{out} are plotted in Fig. 2.17. The incoming signal power is -31 dBm. The input signal had to be slightly shifted, because there is a constant, but unknown path length difference ϕ_{cable} between the two measured signals. Hundreds of start-ups have to be measured for a quantitative description of the quality of the phase synchronization ($\sigma_{\Delta\phi}$).

The start-up behavior of the oscillator is analyzed using a Matlab script. The script analyzes the output signal and detects the individual start-ups. A start-up is detected, if the oscillator's output signal exceeds 0.1 V for the first time. From this point on, the next falling

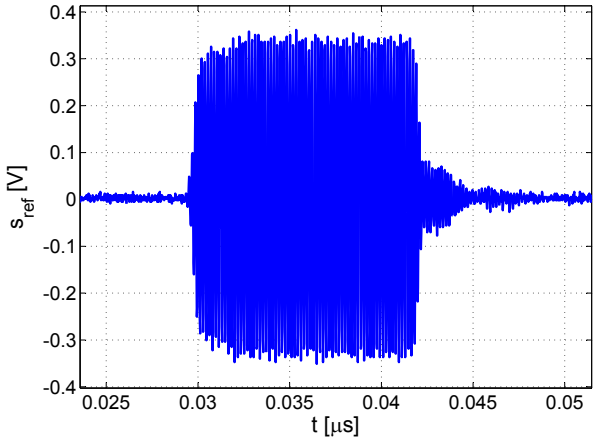

Figure 2.16. Measured single pulse of a pulsed oscillator (f_{mod} = 18.75 MHz, $P_{in} = -66$ dBm, $f = f_0 = 5.8$ GHz). The measured on-time t_{on} is with 12.3 ns shorter than the duration of the on-switching pulse the oscillator receives (13.3 ns). The reflector is not completely switched off, leading to a decaying oscillation after it is switched off.

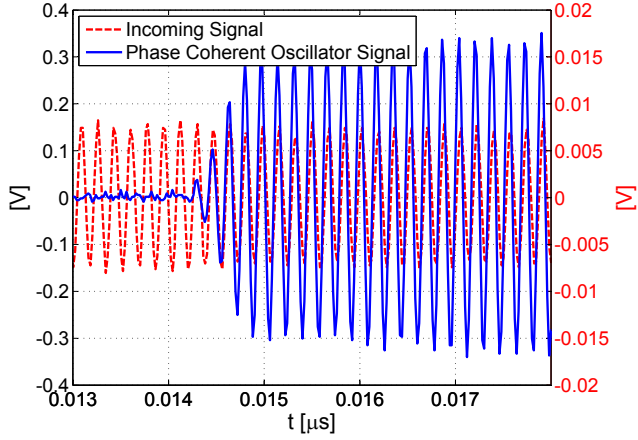

Figure 2.17. Measured start-up of the oscillator with an applied CW input signal ($P_{in} = -31$ dBm, $f = f_0 = 5.8$ GHz). The input signal is plotted as dashed line with a 20 times larger scale (on the right axes) than the oscillator signal.

zero crossings of the incoming and the outgoing signal are searched and the time difference between the two crossings are calculated. This time difference ($\Delta t_{meas} = \Delta\phi/\omega_0 + t_{cable} = t_{cable}$) is constant in the case of an ideal phase synchronous start-up ($\Delta\phi = 0$) and without noise. The mean time difference is given by the path difference t_{cable} between the two signals from the reflector to the measurement and is not important for the phase synchronous start-up. The more interesting property is the distribution of the measured phase differences $\Delta t_{meas}\omega_0$. The distributions are plotted in Fig. 2.18. The time resolution of the DSO is 20 ps, thus the phase resolution is only 0.73 rad. The measured distributions are comparable to the simulated distributions drawn in Fig. 2.14. The reflector and the input signal have a phase difference smaller than the phase resolution (0.73 rad) of the measurement, if the input power P_{in} is larger than -46 dBm. The measurement equipment limits the measurable accuracy of the phase synchronization. The distribution of the phase error Δ_ϕ widens for weaker input signals P_{in} and the simulation predicted that the distribution widens for a lower SNR. The standard deviation of the phase error $\sigma_{\Delta\phi}$ determines how wide the distribution is. The simulated and the measured standard deviations are compared in Fig. 2.19. For a fair comparison, the phase resolution of the simulation of 0.37 rad is reduced to the resolution of the measurement of 0.73 rad. The simulated standard deviation is plotted against the SNR and the measured standard deviations are plotted against the incoming signal power P_{in}. The main noise-sources in the measurement setup with a clean incoming signal are inside the reflector and are not correlated to the incoming signal. Hence, we assume a fixed, but unknown noise amplitude N. From Fig. 2.19, it can be seen that the measured and the simulated curves are equal, but shifted by 67 dB. Thus, an input power P_{in} of -67 dBm is equal to a SNR of 0 dB. The noise amplitude N must therefore be $\sim$-67 dBm. This measured equivalent noise amplitude N will be used later for system simulations, which determine how much noise is acceptable.

The sensitivity of the oscillator is defined as the input power P_{in} where the SNR is 0. Hence, the sensitivity of the measured oscillator is -67 dBm. Later on, we show that a higher sensitivity can be achieved. The reasons for the reduced sensitivity are that a high gain setting is chosen for the reflector and a high modulation frequency f_{mod} of 18.75 MHz. The reflector is switched on during one third of the time. The relatively short off time and the high loop gain result in a incompletely switched off reflector. This reduces the sensitivity. Only two

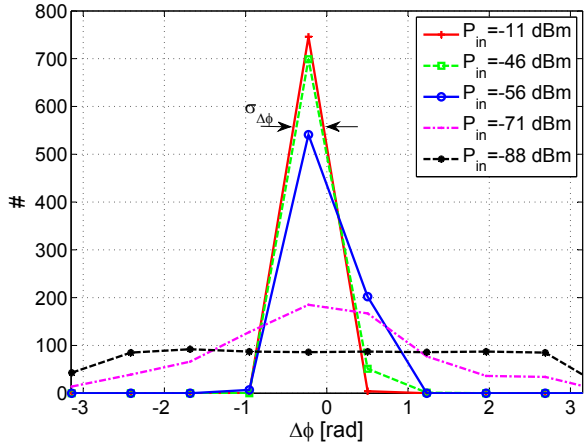

Figure 2.18. Measured distribution of the phase difference between incoming and outgoing signal ($\Delta\phi$). For a large input signal, the alignment of the incoming phase and the outgoing phase is very good.

measurements were conducted with the same gain setting but a lower pulse rate f_{mod} of 1.63 MHz, but the extrapolated sensitivity improved from -67 dBm to -69 dBm. In addition, the measurement setup adds error sources, such as the attenuators, imperfect matching and reflections. These error sources are observable if a stronger input signal and a larger attenuation is used. With a 10 dB larger reference signal and 10 dB higher attenuation, still the same input power is achieved. However, the standard deviation of the phase error increased (from 0.43 to 0.83 for $P_{in} = -61.1$ dBm and from 1.28 to 1.47 for $P_{in} = -71.1$). The jitter of the DSO sampling with 50 GS/s also adds to the phase error.

The simulation is based on the calculated start-up behavior of an oscillator. Because the simulation results agree with the measured results, it can be concluded that the calculated start-up is correct. An oscillator can start phase coherent to an incoming sinusoidal signal, even if the incoming frequency is different to the oscillator's resonance frequency.

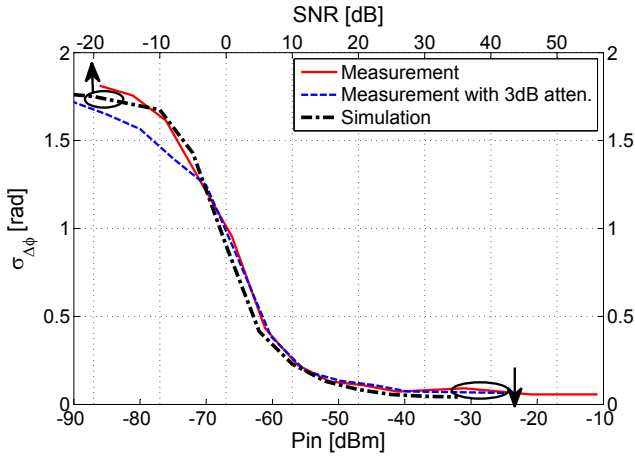

Figure 2.19. Measured phase synchronization accuracy $\sigma_{\Delta\phi}$ vs. simulated accuracy. Simulation and measurement results agree, if a SNR of 0 is equal to an input power P_{in} of -67 dBm.

2.3. Resulting Spectrum of a Pulsed Oscillator

Until now, only the start-up of the oscillator in the time domain was discussed. In this section, an interesting behavior of a the spectrum of a pulsed oscillator is covered: the phase synchronous start-up can be directly measured by the output spectrum.

The output signal $y_{out}(t)$ of an ideal phase synchronous oscillator can be written as

$$y_{out}(t) = s_{mod}(t)\sin(\omega_0 t), \tag{2.41}$$

where $s_{mod}(t)$ is the modulating pulse wave function

$$s_{mod}(t) = \sum_{n=-\infty}^{\infty} \mathrm{rect}\left(\frac{1}{t_{on}}\left(t - \frac{n}{f_{mod}}\right)\right) \tag{2.42}$$

The spectrum is calculated by the Fourier transform, the multiplication of two functions in the time domain is the same as the convolution of

the two Fourier transformed functions

$$y_{out}(t) \circ\!\!-\!\!\bullet\, Y_{out}(\omega) = \int_{-\infty}^{\infty} S_{mod}(\omega-\nu)\sqrt{2\pi}\frac{\delta(\nu-\omega_0)-\delta(\nu+\omega_0)}{2j}\mathrm{d}\nu$$
$$= \frac{\sqrt{2\pi}}{2j}\left(S_{mod}(\omega-\omega_0)-S_{mod}(\omega+\omega_0)\right) \qquad (2.43)$$

The Fourier transform of the pulse wave function is

$$s_{mod}(t) \circ\!\!-\!\!\bullet\, S_{mod}(\omega) = \frac{t_{on}}{\sqrt{2\pi}}\,\mathrm{sinc}\left(\frac{\omega t_{on}}{2\pi}\right)\sum_{n=-\infty}^{\infty} e^{-j\omega\frac{n}{f_{mod}}}. \qquad (2.44)$$

The resulting spectrum of an ideal phase synchronous oscillator is

$$Y_{out}(\omega) = \frac{t_{on}}{2j}\left(\mathrm{sinc}\left(\frac{(\omega-\omega_0)t_{on}}{2\pi}\right)\sum_{n=-\infty}^{\infty} e^{-j(\omega-\omega_0)\frac{n}{f_{mod}}}\right.$$
$$\left.+\,\mathrm{sinc}\left(\frac{(\omega+\omega_0)t_{on}}{2\pi}\right)\sum_{n=-\infty}^{\infty} e^{-j(\omega+\omega_0)\frac{n}{f_{mod}}}\right) \qquad (2.45)$$

The sum-term leads to equidistant peaks in the spectrum. The individual peaks are equidistant to each other with the modulation frequency f_{mod}. The spectrum is weighted by a sinc-shaped envelope, which is centered around the oscillation frequency ω_0. The resulting spectrum $Y_{out}(\omega)$ is depicted in Fig. 2.20. The width of the main lobe is $2/t_{on}$. Thus, the optimal on-time t_{on} is determined by the available bandwidth of the ISM band. For an optimal usage of the available 150 MHz bandwidth, the first zeros of the sinc function should lie at 5.725 and 5.875 GHz, respectively. The optimal on-time is

$$t_{on} = 2/f_{BW} = 2/150e6 = 13.3\ ns. \qquad (2.46)$$

The spectrum of the perfect rectangular signal leads to strong side lobes, which violates the ISM band requirements. The ISM band requires that the spectral power density outside the band has to be below -74.8 dBm/Hz [81]. However, the start-up and the off switching of the reflector is in reality not instantaneous as was assumed for the calculation of the spectrum. The other extreme would be Gaussian pulses instead of rectangular functions. The Fourier transform of a Gaussian pulse results in a Gaussian pulse. Therefore, the spectrum with Gaussian pulses fulfills the spectral mask as shown in Fig. 2.20. The real

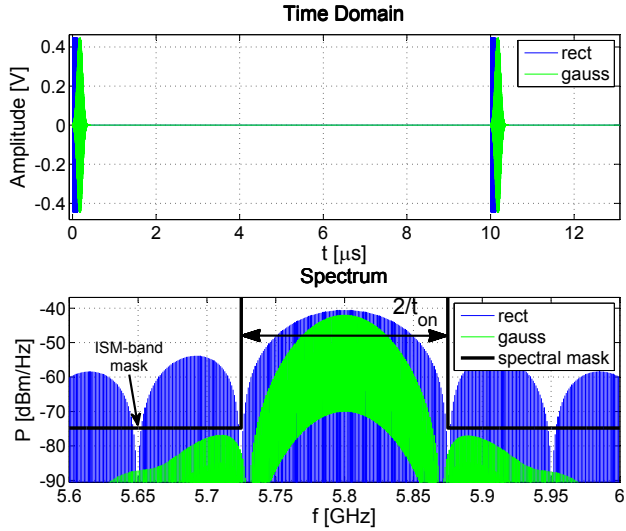

Figure 2.20. Noise free time domain signal and spectrum of the output signal of the reflector s_{rx} for $f_{mod} = 1$ MHz and $t_{on} = 13.3$ ns. The first zeros of the sinc envelope lie at the edge of the ISM band at 5.725 and 5.875 GHz, respectively.

start-up behavior is between these two cases, but the side lobes are further reduced due to the band-pass characteristics of the antenna.

The height of the individual peaks depends on the incoming signal. Without an incoming signal, the oscillator starts due to noise and thus with a random phase. The resulting spectrum has a sinc-envelope, but without any peaks because the individual start-ups have a random phase shift. Assuming a perfect start-up and no noise at all, the spectrum exhibits clean peaks every f_{mod} with a sinc-envelope. In reality, the spectrum is somewhere in between these two extremes, the oscillator starts phase synchronous but with a phase error $\sigma_{\Delta\phi}$. The simulated spectra for different SNR are plotted in Fig. 2.21. The simulation environment is the one used in Section 2.2.1 for the simulation of the phase error in the time domain. The simulation results revealed that the peak height is linearly proportional to the SNR. With this knowledge, it is possible to measure the sensitivity of the oscillator, as defined in Section 2.2.2, in the frequency domain. The advantage is that only a spectrum analyzer is needed instead of a high speed DSO and measuring one spectrum is much faster than sampling two signals and analyzing it statistically. Figure 2.22 depicts the measured spectra from the measurements of the phase synchronous start-up. With the spectral method, the sensitivity of the oscillator is -67.5 dBm with an additional 3 dB attenuator at the input and -65.6 dBm without a 3 dB attenuator. The time domain measurements showed a sensitivity of -67 dBm. Both measurement methods revealed almost the same result. Thus, the spectral method is chosen for future sensitivity measurements.

2.3.1. Influence of the On-Switching Pulse

In the previous section, we analyzed the influence of a random phase error $\sigma_{\Delta\phi}$ on the spectrum of the oscillator. The sources of the random phase error are for example thermal noise or supply noise. But it could also be that the on-switching itself influences the start-up of the oscillator. Without an input signal, oscillators start due to noise or due to disturbance from the on-switching. In a first step, the noise is neglected and only the on-switching pulse is taken into account. Without an input signal, the oscillator starts with a parasitic coupling of the on-switching pulse and thus the oscillator starts always with the same phase. The stronger the input signal is, the smaller is the influence of the on-switching. Hence, the on-switching directly influences the sensi-

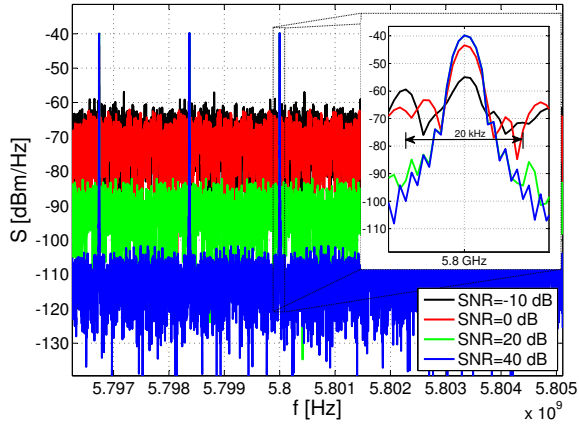

Figure 2.21. Simulated spectrum of the active reflector output with an applied noisy CW signal. The distance between the peaks and the noise floor increases proportional to the SNR of the CW signal.

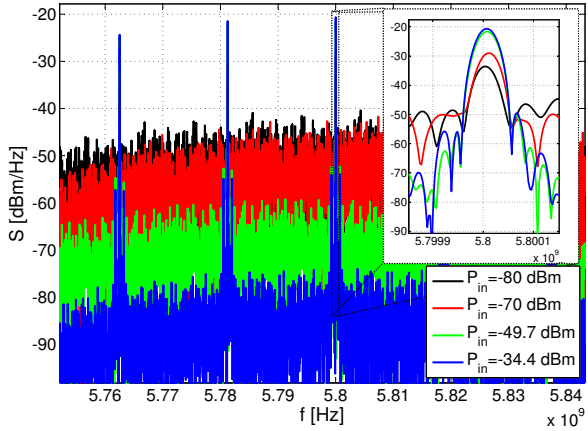

Figure 2.22. Measured spectrum of the active reflector output with an applied CW signal. The distance between the peaks and the noise floor increases directly with the signal power of the CW signal.

tivity of the oscillator. As a design goal, the influence of the switching on the starting phase has to be minimized by circuit design described in Section 4.1.2.

Many assumptions and simplifications are needed for the theoretical analysis of the influence of the switching pulse on the start-up. First of all, the on-switching pulse's shape has to be known and its coupling. The pulse is buffered on-chip by an inverter as illustrated in Fig. 4.12. The inverter drives a differential switching transistor. Without mismatch, the pulse only influences the common mode signal of the oscillator. Furthermore, the impedance of the circuit depends on the switching signal and thus changes during the switching process. This makes the theoretical analysis even more complicate.

The cause of the phase distortion is the transient pulse form and its influence on the oscillator. The transient pulse form strongly depends on the chosen topology and the oscillator parameters and can only be simulated after the circuit is designed. Simulations on circuit level will be presented in Section 4.1.2. But at the moment, we are more interested in the effect of the on-switching pulse. The previously mentioned circuit simulations revealed that the on-switching has the same influence as an additional input signal. The pulse has the same effect as if at each start-up time t_0 a sinusoidal signal $s_{det}(t)$ with constant, deterministic starting phase ϕ_{det} is added to the input signal

$$y_{in,detphase}(t) = Be^{i(\omega t+\phi_0)} + V_{det}e^{i(\phi_{det}+\omega_0(t-t_0))}, \tag{2.47}$$

with V_{det} as the length of the phasor and ϕ_{det} as the phase. V_{det} is the amplitude of the equivalent sinusoidal signal at the input of the oscillator. It is not obvious that the on-switching pulse has the same effect as an external signal s_{det}. A more detailed explanation is given on transistor level in Section 4.1.2. V_{det} and ϕ_{det} cannot be calculated analytically, but it can be found from circuit simulations (Section 4.1.2).

The on-switch pulse changes the start-up behavior over two mechanism. First, the starting phase changes from ϕ_0 to

$$\phi_{start}(t_0) = \angle\left(Be^{i(\phi_0+\omega t_0)} + V_{det}e^{i\phi_{det}}\right). \tag{2.48}$$

Secondly, the amplitude of the input signal is changed from B to

$$B_{start}(t_0) = \left|Be^{i(\phi_0+\omega t_0)} + V_{det}e^{i\phi_{det}}\right|. \tag{2.49}$$

Hence, the oscillator starts faster, if the input signal and the switching pulse have the same phase and slower, if the phases are shifted by π.

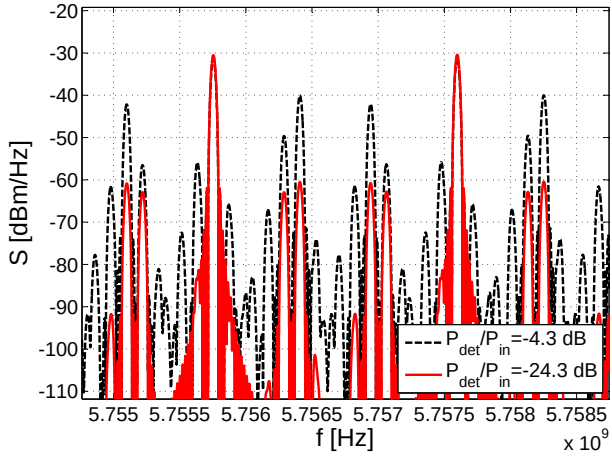

Figure 2.23. Spectrum of a pulsed oscillator with an unwanted deterministic starting phase with power $P_{det} = V_{det}^2/R_{load}$.

The spectrum of the pulsed oscillator with the disturbance of the on-switching pulse is plotted in Fig. 2.23. Instead of the ideal peaks, which are separated by f_{mod}, additional peaks between these ideal peaks appear. Because V_{det} is constant for a specific circuit implementation, the influence of the on-switching reduces with stronger input signals.

2.4. Conclusion

The start-up behavior of an oscillator under the influence of CW signal with and without noise was studied analytically. The calculations proved that the oscillator can start phase synchronous to the incoming signal, meaning that the initial phase of the oscillator is equal to the incoming signal, if the incoming signal and the oscillator have the same frequency ($\omega = \omega_0$) and the loop gain is much smaller than the quality factor ($A \ll Q$). The evolution of the phase error over time depends on four main factors: the loop gain A, the quality factor Q, the received phase ϕ_0, the frequency difference between the incoming signal ω and the oscillation ω_0. The response of the system to a CW signal is a complex equation. Therefore, the system cannot be optimized analytically, but has to be simulated numerically. In the simulations, the phase evolution over time is only evaluated at discrete time intervals

and at certain phases. However, we have a linear oscillator, thus the phase and the signal of the oscillator are continuous. The theoretical start-up allowed the simulation of the response of a pulsed reflector to a noisy CW signal. The synchronization process depends on the SNR. This behavior was verified by measurements.

The phase synchrony is the main principle of the positioning system presented in this thesis. With the verified model, it is now possible to conduct system simulations. The system simulations will give information on the requirements of the oscillator. For example, the optimal value of the Q factor is not yet known. The phase synchronization improves for higher Q-factors, but the influence of the frequency difference increases at the same time and the start-up time is increased. How does this effect the positioning system? What are the possible error sources and which accuracy can be achieved? These questions are discussed in the next chapter.

3

Active Pulsed Reflector System

3.1. Active Pulsed Reflector Principle

The phase synchronous start-up of an oscillator, as described in the previous chapter, is usable for the design of a backscatter in an FMCW radar system. This idea was originally described by [82]. They called the approach 'switched injection locked oscillator', although it is not real injection locking. In injection locked oscillators, the oscillator's frequency is captured by the incoming frequency. In the case of the 'switched injection locked oscillator', the oscillator's frequency is not affected, only the starting phase is synchronized during start-up as discussed in the previous chapter. The concept is better described as a phase resynchronization. Figure 3.1 illustrates a radar system based on the active pulsed reflector. It consists of a base station (BS) and an active pulsed reflector.

The base station generates a FMCW signal s_{tx} with a linear frequency ramp with sweep bandwidth ω_{BW} and sweep time T. The

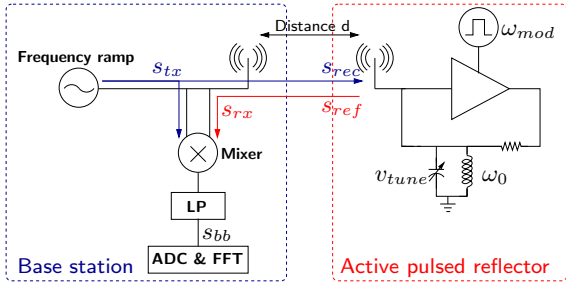

Figure 3.1. FMCW radar system consisting of a base station and an active pulsed reflector.

signal is received at the reflector. The reflector is periodically switched on with frequency f_{mod} and starts phase coherent to the incoming signal, as discussed in Chapter 2. The reflected signal is received at the base station (s_{rx}) and mixed with the transmitted signal s_{tx}. The base station is almost identical to a standard FMCW base station, but the reflector is different. Firstly, we will explain the working principle of the system qualitatively for a rough understanding of the principle. Secondly, the resulting base band spectrum for a FMCW radar system with an active pulsed reflector is derived analytically.

The principle of the active pulsed reflector can be qualitatively understood by investigating the phase ϕ_{tx} of the transmitted signal s_{tx} and ϕ_{rx} of the received signal s_{rx} at the BS. The base station transmits a linear frequency ramp like a conventional FMCW radar, thus the phase of the signal s_{tx} increases quadratically with time. Figure 3.2(a) illustrates the phase of the transmitted signal versus the sweep time T. The active pulsed reflector receives this signal with a delay $\tau = d/c$. Every time the reflector is switched on for a time t_{on}, an oscillation of duration t_{on} is generated with the initial phase condition $\phi_{rec}\,(t = T_{mod} \cdot n)$ imposed by the received signal. The reflector starts oscillating with a determined phase ϕ_{ref}, ideally $\phi_{ref} = \phi_{rec}$, and a frequency ω_0, which is not necessarily the same frequency as the received signal. Thus, the phase of the reflector is synchronized to the incoming signal and the phase information is transmitted back to the base station. The difference of the transmitted and reflected phase $\Delta\phi_{tx,rx}(t) = \phi_{tx} - \phi_{rx}$ at the BS is plotted in Fig. 3.2(b). Ideally, the

phase difference for a linear frequency ramp is

$$\Delta\phi_{tx,rx}(t) = \phi_{tx}(t) - \phi_{rx}(t) = \phi_{tx}(t) - \phi_{tx}(t - 2\tau) \tag{3.1}$$

$$= t\frac{\tau\omega_{BW}}{T} + \phi_{const}. \tag{3.2}$$

The phase difference $\Delta\phi_{tx,rx}(t)$ increases linearly over time and the gradient is directly dependent on the time-of-flight τ, thus a constant phase shift ϕ_{const} does not affect the positioning accuracy. Every time the reflector is switched on, the phase of the reflector is synchronized to the incident phase ϕ_{rec} owing to the phase coherent start-up. Furthermore, the switching also modulates the reflected signal with the switching frequency ω_{mod} and allows the distinction between reflectors with different ω_{mod} and between reflectors and passive reflections.

The following calculation summarizes the resulting base-band signal for this FMCW radar system with an active pulsed reflector. The base station transmits a linear frequency ramp given as

$$s_{tx}(t) = A_{tx}\sin\left(\int_0^t (\omega_B + \omega_{SW}(t))\mathrm{d}t + \phi_0\right). \tag{3.3}$$

with the amplitude A_{tx}. The angular frequency ω_B is the center frequency and ϕ_0 is the initial phase of the transmitter at $t = 0$. The time dependent linear ramp ω_{SW} is defined as

$$\omega_{SW}(t) = \omega_{BW}\left(\frac{t}{T} - \frac{1}{2}\right) \tag{3.4}$$

where ω_{BW} is the sweep bandwidth and T the frequency ramp duration. This signal is received at the reflector after the time-of-flight $\tau(d) = d/c$ and has been attenuated by $\alpha(d)$. The incoming signal s_{rec} at the reflector can be written as

$$s_{rec}(t) = \alpha(d)A_{tx}\sin(\phi_{rec}(t)). \tag{3.5}$$

Assuming the reflector is switched on at time $t_0 = T_{mod} \cdot n$, the phase of the received signal $s_{rec}(t)$ at t_0 is

$$\phi_{rec}(t_0) = \phi_{tx}(t_0 - \tau) = \phi_0 + \int_0^{t_0-\tau} (\omega_B + \omega_{SW}(t))\,\mathrm{d}t \tag{3.6}$$

$$= \phi_0 + \left(\omega_B - \frac{\omega_{BW}}{2}\right)(t_0 - \tau) + \frac{\omega_{BW}}{2T}(t_0 - \tau)^2 \tag{3.7}$$

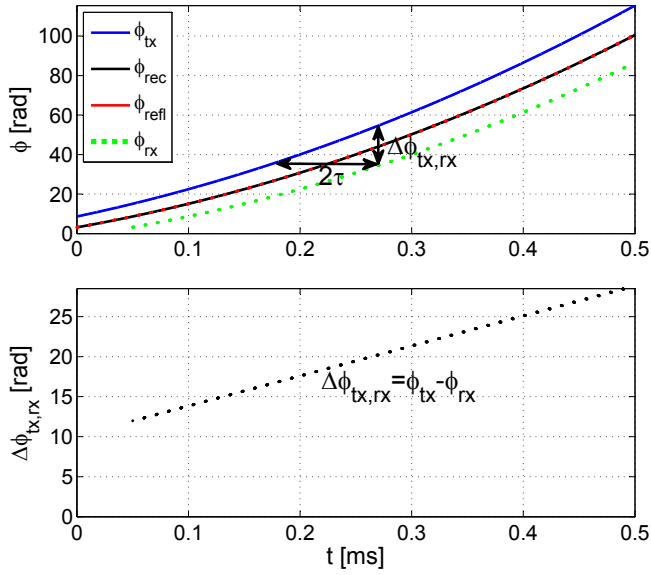

Figure 3.2. Phase relation between incoming and outgoing signal:
(a) The phase ϕ_{tx} of the transmitted linear frequency ramp increases quadratically. This phase is received at the active reflector. Every time the reflector is switched on at $t = T_{mod} \cdot n$, the reflector synchronizes its phase ϕ_{refl} to the phase ϕ_{rec} of the incoming signal. The sweep time T is much larger than the on-time t_{on} and T_{mod}.
(b) The phase difference between the transmitted and reflected signal $\Delta\phi_{tx,rx}(t) = \phi_{tx} - \phi_{rx}$ increases linearly. The first derivative $\mathrm{d}\Delta\phi_{tx,rx}/\mathrm{d}t$ depends on the time-of-flight τ.

The start-up behavior of the reflector is discussed in Chapter 2. Since the exact start-up of the reflector, as formulated in Equation (2.11), is too complicated for the following calculation, an ideal start-up behavior is assumed. The influence of the complex start-up is studied by means of simulations in Section 3.3. In case of an ideal start-up behavior, the reflector starts to oscillate with the same phase as the received signal but with the constant and different oscillation frequency ω_0 of the oscillator.

$$s_{ref}(t) = A_{refl} \sin\left(\omega_0 \cdot (t - t_0) + \phi_{rec}(t_0 - \tau)\right) \tag{3.8}$$

The start-up envelope is neglected, the reflector instantly oscillates with the full amplitude A_{refl}. The reflector output signal s_{ref} is transmitted back to the base station and delayed by the time-of-flight (TOF) τ and attenuated by factor α. The signal is received at the time $t_0 + \tau$. Therefore, the received signal at the base station is given by

$$s_{rx}(t) = \alpha s_{ref}(t - \tau) = \alpha A_{refl} \sin\left(\omega_0 \cdot (t - t_0 - \tau) + \phi_{rec}(t_0 - \tau)\right) \tag{3.9}$$

with ϕ_{rec}, defined in (3.6), which represents the deterministic phase of the signal s_{rec}. We are interested in the resulting base-band signal, when the reflector is switched on once at t_0 with the emission duration t_{on}. The frequency ramp duration T of the radar is much longer than the time t_{on} during which the reflector is on ($2\pi/\omega_{mod}, t_{on} << T$), thus $\omega_{SW}(t)$ can be approximated during t_{on} with the constant value

$$\omega_{SW,t_0+\tau} \approx \frac{\omega_{BW}}{T}(t_0 + \tau) - \frac{1}{2}\omega_{BW}. \tag{3.10}$$

Thus, the frequency $\omega_{tx}(t)$ of the transmitted signal s_{tx} is approximated by

$$\omega_{tx}(t) \approx \omega_{tx,t_0+\tau} = \omega_B - \frac{1}{2}\omega_{BW} + \frac{\omega_{BW}}{T}(t_0 + \tau). \tag{3.11}$$

The phase of the frequency ramp at the time $t_0 + \tau$ is

$$\phi_{tx} = (t_0 + \tau)\left(\omega_B - \frac{1}{2}\omega_{BW}\right) + \frac{\omega_{BW}}{2T}(t_0 + \tau)^2 + \phi_0. \tag{3.12}$$

The transmitted signal is then written as an approximation

$$s_{tx} = A_{tx} \sin\left(\omega_{tx} \cdot (t - t_0 - \tau) + \phi_{tx}\right) \tag{3.13}$$

The received signal s_{rx} (3.9) and the transmitted signal s_{tx} (3.13) are mixed in the base station:

$$\begin{aligned} s_{mix}(t) &= s_{rx}(t) \cdot s_{tx}(t) && (3.14)\\ &= A \sin\left(\omega_0 \cdot (t - t_0 - \tau) + \phi_{rec}(t_0 - \tau)\right) \\ &\quad \cdot \sin\left(\omega_{tx} \cdot (t - t_0 - \tau) + \phi_{tx}\right) && (3.15)\\ &= \frac{A}{2}(\cos\left(\phi_{rec} - \phi_{tx} + (t - t_0 - \tau)(\omega_{ref} - \omega_{tx})\right) \\ &\quad - \cos\left(\phi_{rec} + \phi_{tx} + (t - t_0 - \tau)(\omega_{ref} + \omega_{tx})\right)). && (3.16) \end{aligned}$$

The variable A is the amplitude of the signal, depending on A_{refl}, A_{tx}, the attenuation factor α as well as the antenna, LNA and mixer gain G_{rx}. s_{mix} has a low frequency component and a high frequency component at $\omega_{ref} + \omega_{tx}$. The mixed signal s_{mix} is low-pass filtered, hence, the sum frequency component can be neglected. The simplest form of a low-pass filter is an integrator. The pulse arrives at $t_0 + \tau$ and is on for the on-time t_{on}, thus the filtered down-converted signal s_{filt} for one pulse length of the active pulsed reflector (APR) can be written as

$$\begin{aligned} s_{filt}(t_0) &= \int_{t_0+\tau}^{t_0+\tau+t_{on}} s_{tx}(t) \cdot s_{rx}(t)\,\mathrm{d}t && (3.17)\\ &= \frac{A}{2(\omega_{ref} - \omega_{tx})}\big(\sin\left(\phi_{rec} - \phi_{tx} + t_{on}(\omega_{ref} - \omega_{tx})\right) \\ &\quad - \sin\left(\phi_{rec} - \phi_{tx}\right)\big). && (3.18) \end{aligned}$$

The calculation can be further simplified by setting $\omega_0 = \omega_B$, this can be achieved by tuning the oscillation frequency ω_0 with the tuning voltage V_{tune}. This simplification is needed for the analytical analysis, simulations for different oscillation frequencies ω_0 are presented in Section 3.3.4. Inserting equations (3.11), (3.6) and (3.12) into (3.18) and rearranging the equation leads to

$$\begin{aligned} s_{filt}(t_0) = \frac{At_{on}}{2} \cos\Bigg(t_0 \frac{\omega_{BW}}{T}\left(2\tau + \frac{t_{on}}{2}\right) + \tau\Bigg(\frac{t_{on}\omega_{BW}}{2T} \\ + \omega_B - \omega_{BW}\Bigg) - \frac{t_{on}\omega_{BW}}{4}\Bigg) \\ \cdot \operatorname{sinc}\left(\frac{\omega_{BW} t_{on}}{2T}\left(t_0 + \tau - \frac{T}{2}\right)\right) \end{aligned} \quad (3.19)$$

The value $s_{filt}(t_0)$ is a constant value, which depends on the time t_0 when the reflector has been switched on. By repeating this process

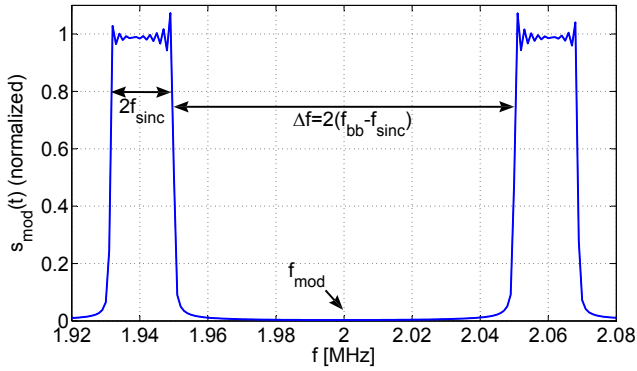

Figure 3.3. Ideal spectrum of the down-mixed signal $s_{bb}(t)$ for $T = 0.5$ ms, $t_{on} = 33$ ns, $T_{mod} = 0.5$ μs and $d = 2.5$ m.

periodically with the frequency ω_{mod}, we obtain an up-converted base-band time domain signal s_{bb}

$$s_{bb}(t) = \sum_{i=0}^{\omega_{mod}T} s_{filt}\left(\frac{i}{\omega_{mod}}\right) \tag{3.20}$$

$$= \frac{At_{on}}{2}\cos\left(\omega_{bb}(\tau)\cdot t + \phi_{bb}(\tau)\right) \cdot \operatorname{sinc}\left(\omega_{sinc}\cdot\left(t+\tau-\frac{T}{2}\right)\right) \cdot \left(\operatorname{sign}\left(\sin\left(\omega_{mod}\cdot t\right)\right)+1\right) \tag{3.21}$$

with

$$\omega_{bb}(d) = \frac{\omega_{BW}}{T}\left(2\tau(d)+\frac{t_{on}}{2}\right), \tag{3.22}$$

$$\phi_{bb}(d) = \tau\left(\frac{t_{on}\omega_{BW}}{2T}+\omega_B-\omega_{BW}\right)-\frac{t_{on}\omega_{BW}}{4} \tag{3.23}$$

and

$$\omega_{sinc} = \frac{\omega_{BW}}{T}\frac{t_{on}}{2}. \tag{3.24}$$

The spectrum $S_{mod}(\omega)$ of the base-band signal $s_{bb}(t)$ around the fundamental frequency ω_{mod} is depicted in Fig. 3.3. The sinc envelope

of the $s_{bb}(t)$ signal leads to rectangular peaks in the spectrum. The frequency difference $\Delta\omega = 2\pi\Delta f$ of the inner edges of these peaks is

$$\Delta\omega = 2(\omega_{bb} - \omega_{sinc}) = 4\frac{\omega_{BW}}{T}\tau(d) \tag{3.25}$$

The measured frequency difference $\Delta\omega$ is proportional to the time-of-flight τ. Hence, the distance between the base station and the reflector can be calculated from $\Delta\omega$

$$d = \frac{\Delta\omega cT}{4\omega_{BW}}, \tag{3.26}$$

with c as the propagation velocity. It is possible to detect multiple reflectors at the same time by using different modulation frequencies f_{mod} for every reflector. The square function $(\text{sign}(\sin(\omega_{mod}t)) + 1)/2$ modulates the base-band signal. Thus, the two peaks in the spectrum can be seen around the fundamental frequency f_{mod}, but also around the higher harmonics $n \cdot f_{mod}$. Therefore, to identify multiple reflectors at the same time, the lowest modulation frequency $f_{mod,low}$ and twice this frequency $2f_{mod,low}$ limits the available frequency space. The highest usable f_{mod} is determined by the sampling frequency of the ADC in the BS. The case of multiple simultaneous reflectors is studied in Section 3.4

An ideal start-up behavior was assumed for the previous calculation. The influence of a non-ideal start-up and also the influence of phase noise and SNR can only be simulated. Sections 3.3 discusses the influences of various design parameters on the positioning accuracy..

3.1.1. Link Budget

The power received at the reflector can be calculated in free space by the Friis transmission equation

$$\frac{P_r}{P_t} = G_t G_r \left(\frac{\lambda}{4\pi d}\right)^2 \tag{3.27}$$

with λ as the wave length, d as the distance, P_r and P_t as the received and the transmitted power, respectively. G_r and G_t are the antenna gains of the receiver and the transmitter. The Friis transmission equation can be used, because the wanted signal for radar localization is the LOS signal. The free space loss $\alpha(d)$ at 5.8 GHz over the operation

range of 30 m is

$$\alpha(d) = 20 \log \left(\frac{\lambda}{4\pi d} \right) = -77 \; dB. \tag{3.28}$$

The output power of the base station after the antenna is set to 10 dBm, the ISM band regulations limit the maximum output power to 14 dBm. We chose a smaller value to be on the safe side. The reflector uses a directional or omnidirectional antenna with an antenna gain between 3 and 14 dBi, thus the received power of the reflector is larger than −64 dBm.

The required output swing of the reflector is calculated using the same assumptions. The base station has a receiver sensitivity of −70 dBm according to the RESOLUTION system specifications and an antenna with at least 6 dBi gain. Therefore, in order to compensate the transmission loss, the signal at the reflector antenna has to be above 1 dBm. With an antenna gain of larger than 3 dBi, the reflector has to be able to transmit more than −2 dBm equaling to 0.18 V_{RMS}.

3.2. Simulation Models

The previous calculation of the base-band signal $s_{bb}(t)$ assumed an ideal start-up without transient. Furthermore, the reflector oscillates exactly at the center frequency of the base-band and the phase of the base station is linearized during one on-time t_{on} ($t_{on}, T_{mod} \ll T$). Simulations are needed to verify the calculated behavior in the case of a realistic transient start-up and to simulate the influence of different design parameters and noise and multipath propagation.

3.2.1. Analytical Start-Up Model

For the simulation of the realistic active pulsed reflector system, the start-up of the reflector has to be known. The analysis of the start-up behavior of a linear oscillator under the influence of a sinusoidal input signal is covered in Section 2.1. The reflector's output signal in the time domain is described by Equation (2.11). The first half of (2.11) oscillates with the same frequency as the incoming signal. The second half of the equation represents an exponentially growing sinusoidal function oscillating with ω_0'. From (2.11), the start-up time and the non-ideal phase behavior can be calculated. The evolution of the phase error $\Delta\phi(t)$ is correctly modeled as was verified by measurement. However,

the equation does not model gain saturation and thus the amplitude of the oscillation grows infinitely large. Therefore, the amplitude is limited to $\pm v_{sat}$ for the system simulations. If the amplitude is larger than the limit v_{sat}, then it is normalized to v_{sat}. Although this is not perfectly correct, because the oscillation frequency changes slightly if the oscillator is saturated, simulations showed no recognizable deviation between this idealized behavior and the non-idealized Simulink model. The Simulink model is discussed in the next section.

The start-up behavior depends on the incoming phase ϕ_0 and the incoming frequency ω. For the calculation, it was assumed that the reflector starts at time $t_0 = 0$. The comparison with the Simulink-model (Section 3.2.2) verified that the start-up behavior is the same for the same parameters, independent of the on-switching time t_0. This analytic start-up model simulates fast. The influence of received power, loop gain, phase noise, and also the influence of SNR can be simulated. However, it is not possible to simulate the interactions of multiple reflectors and the behavior in a multipath environment with this model, because the analytical start-up assumes a sinusoidal input signal and calculates the start-up based on the phase at time t_0 and the frequency $\omega(t_0)$. The modeled reflector is immune to disturbances after the on-switching time.

3.2.2. Simulink-Model

A time-domain Simulink model is needed to simulate disturbances occurring during or after the start-up of the reflector like multipath effects. The Simulink model is, like the analytical model, based on the feedback model of the oscillator (Fig. 2.1). The forward path contains an amplification A_v and a voltage limiter. Figure 3.4 illustrates the voltage gain characteristic used in the Simulink model. An RLC-bandpass filter is used in the feedback path. The RLC-filter as depicted in Fig. 3.1 assumes a perfect LC tank without losses. Without losses, the oscillation in the LC tank is not attenuated and would continue even if the loop gain is switched off. At the next on-switching time, the internal oscillation is as strong as at the off-switching time and much stronger than the incoming signal. A real circuit always has losses, thus an LC tank is never perfect. By adding a resistor R_1, the two reactances C and L are decoupled from each other and the internal oscillation decays after the oscillator is switched off. The schematic of the filter is plotted in Fig. 3.5. Adding a resistor R_1 does not make the

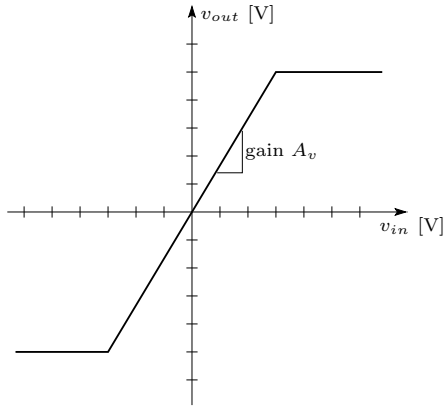

Figure 3.4. Voltage gain of the oscillator feedback loop. The maximum output voltage v_{out} is limited to $v_{out,sat}$ due to saturation effects.

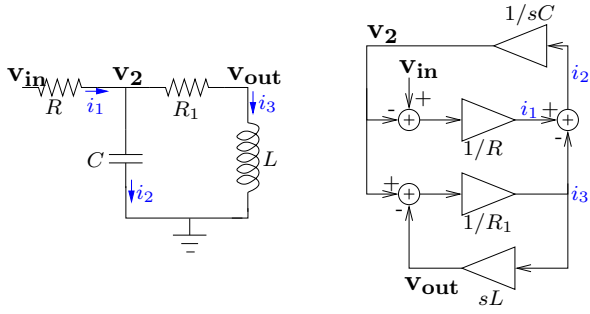

Figure 3.5. Filter and signal graph. The signal graph can be implemented in Simulink.

simulation less realistic, on contrary, this resistor emulates the Q-factor of the inductor or the parasitic resistance of the interconnects and the vias. The transfer function of the filter changes from

$$F_{Filt,ideal}(s) = \frac{v_{out}}{v_{in}} = \frac{sL}{s^2LCR + sL + R} = \frac{s\frac{\omega_0}{Q}}{s^2 + s\frac{\omega_0}{Q} + \omega_0^2} \tag{3.29}$$

to

$$F_{Filt,S}(s) = \frac{s\frac{1}{RC}}{s^2 + s\frac{R_1RC+L}{RLC} + \frac{R+R_1}{RLC}} = \alpha_S \frac{s\frac{\omega_{0S}}{Q_S}}{s^2 + s\frac{\omega_{0S}}{Q_S} + \omega_{0S}^2}. \tag{3.30}$$

The added resistor R_1 influences the transfer function. The new quality factor Q_S, oscillation frequency ω_{0S} and the additional attenuation α_S due to the resistor R_1 are

$$\omega_{0S} = \sqrt{\frac{R + R_1}{RLC}} \tag{3.31}$$

$$Q_S = \frac{\omega_{0S}RLC}{R_1RC + L} \tag{3.32}$$

$$\alpha_S = \frac{L}{R_1RC + L}. \tag{3.33}$$

The bode plots of the transfer function (3.30) with and without the resistor R_1 are compared in Fig. 3.6.

It is very helpful to draw a signal graph and then implement this signal graph to Simulink. The signal graph can be drawn using the following equations

$$i_1 = \frac{v_{in} - v_2}{R} \tag{3.34}$$

$$i_3 = \frac{v_2 - v_{out}}{R_1} \tag{3.35}$$

$$i_2 = i_1 - i_3 \tag{3.36}$$

$$v_2 = \frac{i_2}{sC} \tag{3.37}$$

$$v_3 = i_3sL. \tag{3.38}$$

The resulting signal graph is plotted on the right side in Fig. 3.5. This signal graph has the advantage that the internal states can be controlled. Thus the starting conditions can be set. The simplest way to switch off a differential filter is to shorten the differential signals. Thus, i_2, i_3, v_2 and v_{out} are all 0.

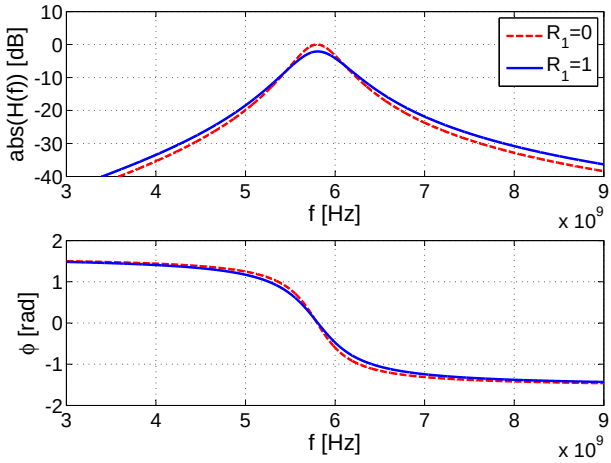

Figure 3.6. Bode plot of the filter transfer-function with R_1=0 and R_1=1 [Ω] respectively. See (3.30)

The Simulink model and the analytical start-up result in almost the same output waveform. The two are compared in Fig. 3.7. The main difference lies in the way the saturation is handled. The Simulink model limits the output amplifier, which alters the output waveform from a sinusoidal signal to a more trapezoidal waveform. This adds higher harmonics but does not change the fundamental frequency. In the case of the theoretical start-up, the phase is calculated and the amplitude is limited. With this approach no higher harmonics exist. The truth lies somewhere between these two extreme cases. The Simulink model is closer to reality, because the reflector is still sensitive to incoming signals after the initial start-up. But without unwanted signals present, the calculated phases of both models are identical. The theoretical model has the advantage that the simulation is orders of magnitude faster than the Simulink model.

3.3. Evaluation of Important Design Parameters

In this section, the influences of the most important design parameters on the positioning accuracy are simulated. These parameters include the loop gain A, the quality factor of the filter Q, phase noise performance, received signal strength and signal-to-noise ratio (SNR). All

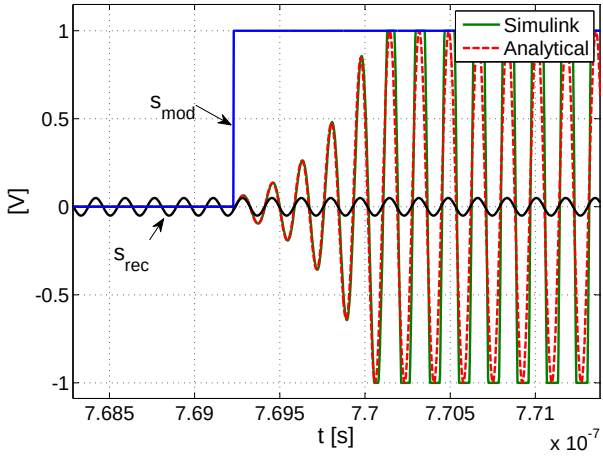

Figure 3.7. Comparison between the reflector's output signals resulting from the Simulink model and the analytical Matlab model with the analytical start-up.

the simulations in this section 3.3 are conducted with the analytical start-up model.

3.3.1. Influence of the Loop Gain A

The two major design parameters in an oscillator are the amplification A and the quality factor Q. The highest quality factor Q_L of integrated inductors at 5.8 GHz in the available 0.18-μm CMOS technology is around 25 [83]. The quality factor of a loaded LC-tank Q_{LC} is even lower, because the capacitor has also a finite quality factor Q_C and the output resistance of the transistor decreases the quality factor further. The transfer function of a loaded LC-tank, the transfer function of the implemented reflector and the simulated transfer function are compared in Appendix A.3. A realistic assumption of the loaded Q is around 10. The loop gain A is not limited by the technology, thus the gain can be chosen almost freely. For an oscillation to start, the loop gain has to be larger than 1. The complex poles of the oscillator are calculated by Equation (2.4). The poles are complex conjugate if the loop gain $(A-1)$ is smaller than $2Q$. This sets the upper limit for A.

As discussed in Section 2.3, the on-time of the reflector t_{on} is 13.3 ns

for an optimal usage of the available bandwidth. During this time, the oscillator must start-up completely, so that the oscillation reaches the final amplitude. The output power must be larger than -2 dBm according to the link budget (Section 3.1.1). Assuming a minimum output power of 0 dBm, the maximum output swing is

$$V_{p-p} = 2\sqrt{2P_{out}R_{out}} = 0.632\ [V] \tag{3.39}$$

where R_{out} is the antenna load of 50 Ω. The minimum loop gain A to reach this full swing after t_{on} can be calculated with Equation (2.11)

$$t_{start} = \frac{2Q}{\omega_0\,(A-1)} \ln\left(\frac{V_{p-p}/2}{Az\sqrt{u(\phi_0)^2 + v(\phi_0)^2}}\right) = 1.3. \tag{3.40}$$

The oscillator has to be able to drive the 50 Ω load. Thus, if the loop gain increases, also the power consumption increases. Thus, only loop gains between 1.5 and 10 are considered in the simulations. Figure 3.8 depicts the spectra for different loop gains. The peak is small for a loop gain A of 1.5. This is because the reflector starts too slow and thus the width of the peak is reduced. By increasing the loop gain, the peaks initially start to get wider and above a loop gain of 3 the height of the peaks reduces. This is counter intuitive. If the loop gain increases, the reflector starts faster and thus more energy is received at the base station. Hence, the peaks should increase. We can simulate the influence of the start-up envelope. An ideal phase-synchronous start-up is assumed with varying envelopes. The envelope is modeled with a Gaussian function with standard deviation $\sigma = c_g$

$$env_{start} = e^{-\frac{(t-3c_g)^2}{2c_g^2}} \tag{3.41}$$

for start-up and also a Gaussian function for the off-switching process

$$env_{off} = e^{-\frac{(t+t_{on})^2}{2c_{g,off}^2}} \tag{3.42}$$

with $c_{g,off} = 13/20$ ns. When the start-up is modeled with a Gaussian curve, the start-up time is approximately 3σ. Four different envelopes are simulated, the envelopes correspond to a loop gain A of 1.4, 2, 3 and 4.5. The envelopes are shown in Fig. 3.9. The resulting spectra are plotted in Fig. 3.10. For a slow start-up, the peak is smaller and the detected distance is too large (10.5485 m instead of 10 m). With

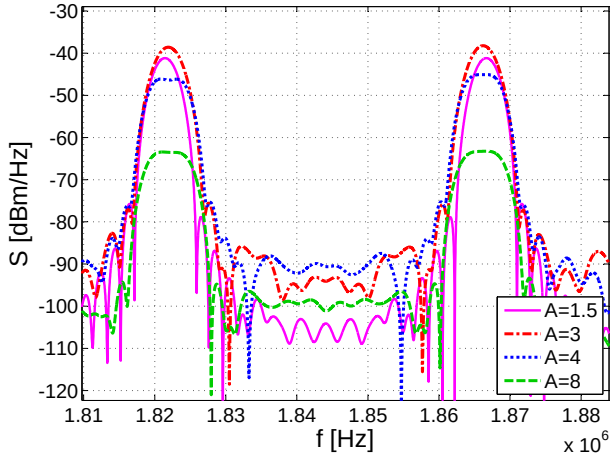

Figure 3.8. Simulated baseband spectrum for different loop gains A.

Table 3.1. Simulated detected distances vs. loop gain A for d=10 m and Q=10.

A	1.5	2	3	4	6	8	10
dist [m]	10.335	10.152	9.982	9.432	9.135	9.112	9.118
Δd [cm]	33.5	15.2	-1.8	-56.8	-86.5	-88.8	-88.2

faster start-up, the shape of the spectrum gets closer to the ideal spectrum with almost rectangular peaks. Thus, the change in the envelope explains the change of the peaks for low loop gains between 1.5 and 3. However, the lower peak height for higher loop gains cannot be explained by the envelope.

The decrease in the peak height is due to worse phase synchronization. Figure 2.12 illustrates the synchronization error $\Delta\phi_{ideal,real}$ for different loop gains A. The larger the loop gain A is, the larger is the synchronization error. The smallest synchronization error is achieved for a loop gain A between 3 and 4. This agrees well with the base band spectra in Fig. 3.8. High peaks have the advantage that they are better detectable, thus loop gains A between 2 and 4 give the best results.

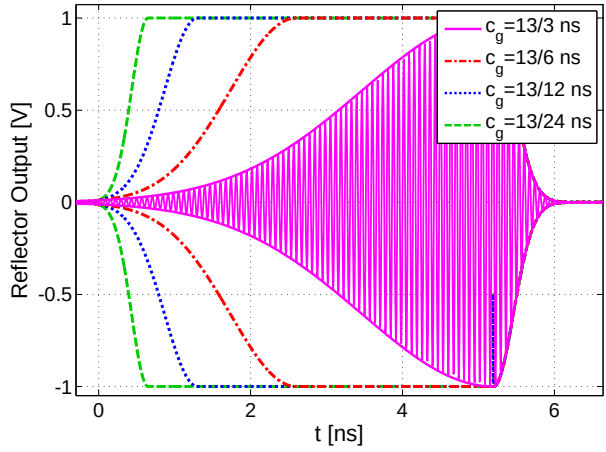

Figure 3.9. Output signals of the active reflector with different start-up time c_g corresponding to loop gain A of 1.4 ns ($c_g = 13/3$ ns), 2 ns ($c_g = 13/6$ ns), 3 ns ($c_g = 13/12$ ns) and 4.5 ns ($c_g = 13/24$ ns). In this simulation, only the envelope changes, but not the behavior of the phase of the signal. The off switching slope is the same for each envelope.

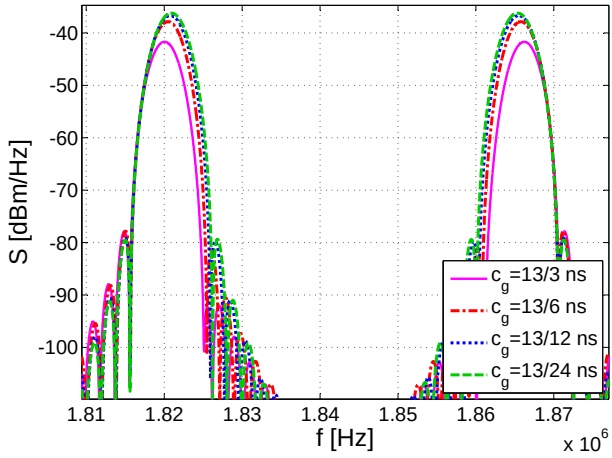

Figure 3.10. Spectrum for different start-up times of the reflector, which is modeled as a Gaussian function $\exp\left(-\frac{(t-3c_g)^2}{2c_g^2}\right)$ with the parameter cg.

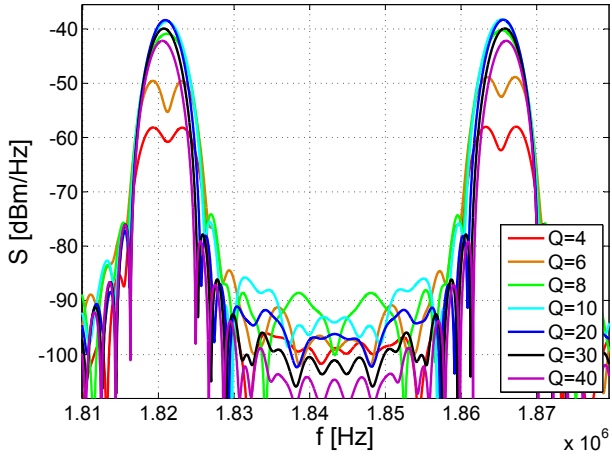

Figure 3.11. Spectrum depending on the quality factor Q.

3.3.2. Influence of the Quality Factor Q

As stated in the previous Section, the quality factor of a loaded LC tank is in the order of 10. The influence of the quality factor Q of the active reflector on the positioning accuracy is studied here. The simulated Q's are between 4 and 20. A quality factor above 20 is not realistic for an integrated circuit. The loop gain A is chosen to be 3 due to the simulation results in Section 3.3.1. Table 3.2 lists the simulation results for some selected Q-values. The detected distance changes by 69 cm when the quality factor Q increases from 4 to 8, but only by 25 cm for a change from 9 to 20. The system is less sensitive to changes in the quality factor for Q values above 9. This can be verified by looking at the resulting base-band spectra for different Q in Fig. 3.11. The peaks are less affected for quality factors above 9. For high quality factors, the the peaks get thinner because of a slower start-up and the different phase synchronization behavior as depicted in Fig. 2.11. The phase error increases, if the oscillation frequency ω_0 and the incoming signal's frequency ω are strongly detuned, but at the same time it has a smaller weight, because of the steeper band-pass characteristic of the oscillator.

An increasing quality factor Q has a similar effect as a decreasing loop gain A. The start-up behavior and thus the peak form is related

Table 3.2. Detected, simulated distances vs. quality factor Q for d=10 m and A=3.

Q	4	6	8	9	10	15	40
dist [m]	9.084	9.225	9.772	9.850	9.913	10.022	10.335
Δd [cm]	-91.61	-77.53	-22.81	-14.99	-8.74	2.20	33.47

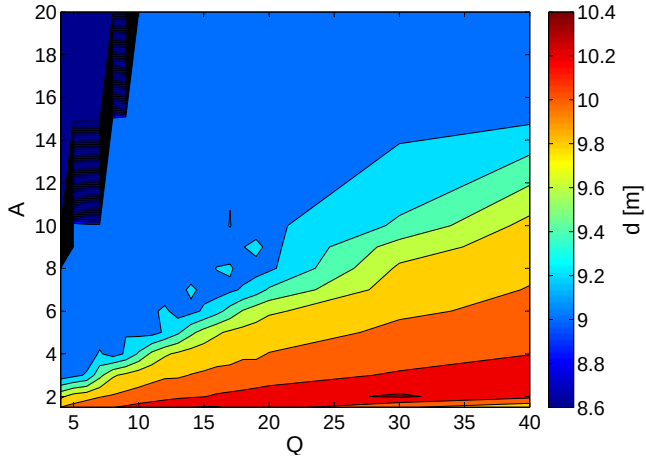

Figure 3.12. Detected distances d for various Q and A. The reflector does not oscillate if $(A-1)/(2Q) > 1$ (in the upper left corner).

to the ratio $(A-1)/(2Q)$. Figure 3.12 illustrates the detected distances d for various Q and A. The detected distances are equal if the $(A-1)/(2Q)$ ratio is equal. The simulated spectra for the same ratio are congruent.

3.3.3. Influence of the Received Signal Strength

Besides the two main design parameters quality factor Q and loop gain A, the amplitude B of the received signal (2.6) also has a large influence on the start-up. As can be seen from (2.11), the amplitude B defines the starting amplitude. The stronger the received signal is, the faster the oscillator starts, but it does not affect the phase. The spectra in

Fig. 3.10 show that the detected distance is dependent on the envelope of the pulse.

The power received at the reflector can be calculated by the Friis transmission equation

$$\frac{P_r}{P_t} = G_t G_r \left(\frac{\lambda}{4\pi d}\right)^2 \tag{3.43}$$

with λ as the wave length, d as the distance, P_r and P_t as the received and the transmitted power, respectively. The Friis transmission equation is valid even in a multipath environment, because the wanted signal for radar localization is the line of sight (LOS) signal.

In the simulations, the input power is swept from -30 dBm (d =0.6 m) to -120 dBm (d = 18.4 km). Realistic are power levels between -30 dBm and -70 dBm (d = 58 m), lower power levels are possible, if the LOS is attenuated by a thin wall. The loop gain A is set to 3 and the quality factor Q is 10 for the simulations. The spectra of the resulting base-band signals are shown in Fig. 3.13. The inner edges are affected by the input power. For smaller input power, the oscillator start-up is slower and thus the envelope flatter. This leads to a similar effect as a low loop gain A. Figure 3.14 illustrates the error of the detected distance error (Δd) dependent on the distance d. The detected distance increases for larger distances, because the received power is smaller. The error decreases linearly with the logarithmic input power. For 1 dB higher attenuation, the detected distance increases by 0.36 cm. This simulation takes only the slower start-up into account and neglects that the phase is possibly asynchronous due to a smaller SNR and also due to the stronger influence of the on-switching pulse if the received signal is weak. The deterioration due to a smaller SNR is studied in Section 3.3.7.

3.3.4. Oscillator Frequency ω_0

The oscillator ideally consists of a frequency independent loop gain A and a frequency dependent loop filter. The influence of the quality factor Q of the loop filter was studied earlier. Up to now, the resonance frequency ω_0 of the filter was fixed to the center frequency ω_B of the ISM band. What happens if the oscillator's frequency is detuned?

The calculation of the theoretical start-up of the reflector in Chapter 2 revealed that the oscillator starts oscillating at a slightly lower frequency ω_0' than its resonance frequency ω_0 of the LC tank. For a loop

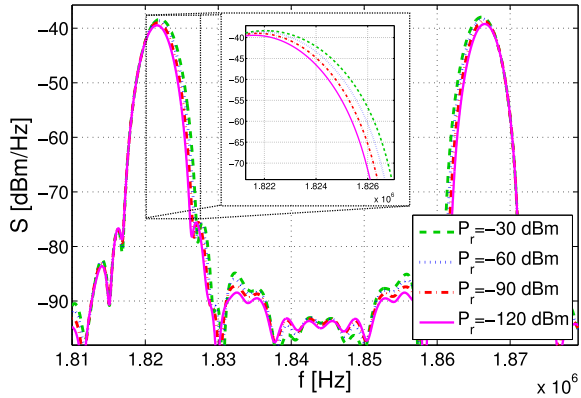

Figure 3.13. Peaks of the down-mixed-spectrum dependent on the received signal power P_r at the reflector.

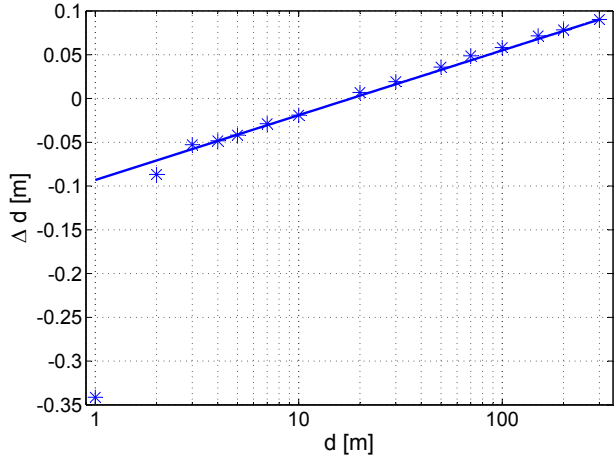

Figure 3.14. Error of the detected distance dependent on the distance d. The detected distance depends linearly on the input power in dBm and thus logarithmic on the distance.

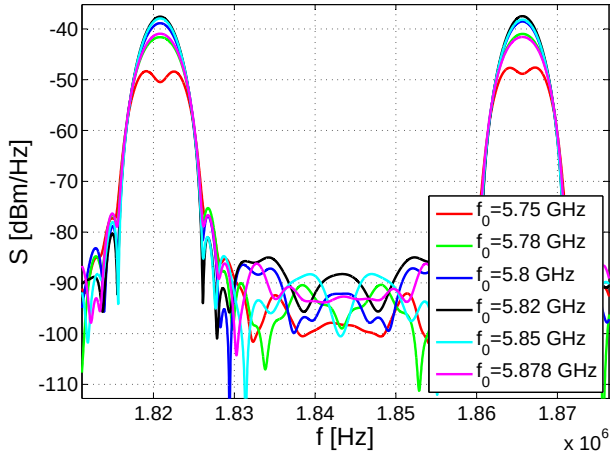

Figure 3.15. Spectrum dependent on the resonance frequency f_0 of the active reflector.

gain A of 3 and a quality factor Q equal to 10, a resonance frequency ω_0 of 5.829 GHz is equal to an oscillation frequency of 5.800 GHz. The simulation results for different resonance frequencies are depicted in Fig. 3.15. The highest peaks occur when ω_0 is 5.829 GHz, which is equal to a starting frequency of 5.8 GHz. For higher and lower frequencies, the height of the peaks reduce. This is because the mean phase error $\overline{\Delta\phi}_{ideal,real}$ increases, if the reflector and the incoming signal do not oscillate at the same frequency, as discussed in Section 2.1.3. A second influence is the slower start-up of the reflector. The start-up is slower when the difference between the incoming signal and the oscillation signal is larger, which is due to the band-pass characteristic of the feedback filter.

The detected distances are listed in Table 3.3. A frequency offset of 20 MHz results in a distance error of 3.1 cm. Thus, a slightly wrong oscillation frequency does not influence the positioning accuracy. However, an accurate oscillation frequency is wanted to fulfill the spectral mask as can be seen by Fig. 2.20

3.3.5. Oscillation Frequency Drift

The active reflector is a free-running oscillator. Hence, it is possible that the frequency drifts during one distance measurement. One of the main sources for oscillator drift is the drift due to temperature changes [84]. Even though the operating temperature can change drastically after the device is switched on, the temperature is going to settle around a certain temperature. Simulations for an LC-tank consisting of hyper-abrupt junction varactors and a differential inductor in 0.18-μm CMOS technology yield a high temperature dependency. The resonance frequency f_0 changes by 201 ppm/$^\circ C$ due to the temperature sensitive varactors. Appendix A.4 discusses the temperature coefficient in greater detail.

Different frequency drifts are simulated: a rising and a falling linear frequency drift and completely random frequencies. Linear frequency drifts occur by linearly rising or falling temperatures. Table 3.3 summarizes the results for linear frequency drift. Because the system only measures during one rising frequency ramp, the simulation results differ for rising and falling frequency drifts. In the case of a frequency drift of ± 10 [MHz/measurement], the detected distance changes from 9.9193 m to 9.8568 m. Thus, a frequency drift influences the positioning accuracy. However, one measurement takes below 1 ms. A frequency drift of 10 MHz in 1 ms is equal to a temperature drift of 8.5 °C/ms. It is very unlikely that such a fast temperature rise occurs and even if this happened, the positioning system still works but with a slightly worse accuracy (± 6 cm).

It could also be that the drift is completely random due to noise on the supply rails and bias voltages. In the simulation, the oscillation frequency is randomly changed at every start-up in a range of ± 10 MHz of the center frequency. A uniform distribution is chosen for the oscillation frequency. But even with this drastic random drift, the distance error is below 4 cm.

3.3.6. Impact of the Phase Jitter J_{rms} of the Modulation Signal s_{mod} on the Positioning Accuracy

Up to now, the different design parameters and deterministic errors are simulated. These errors lead to a deterministic positioning error. Many of these errors can be eliminated by calibration of the base stations and the reflectors. The more important error sources are non-deterministic effects, such as phase noise of the reflector, jitter of the modulation

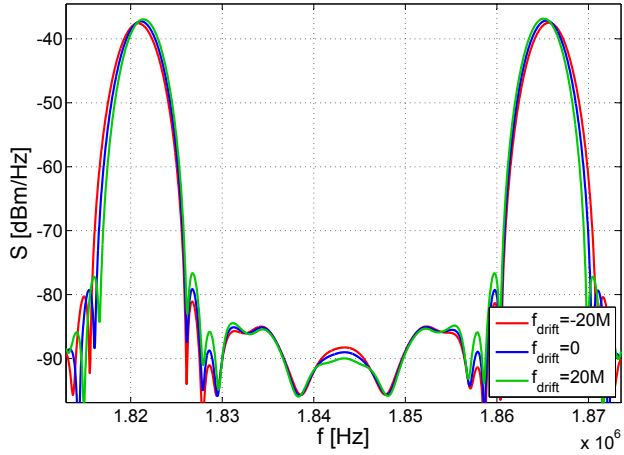

Figure 3.16. Spectra for different linear frequency drifts ω_{drift}

Table 3.3. Simulated distances vs. f_0 and frequency drift.

f_0 [GHz]	f_{drift}=-20M	-10M	0	10M	20M
5.75	9.4656	9.4030	9.3405	9.3092	9.2466
5.78	9.8568	9.8098	9.7785	9.7472	9.7160
5.8	9.9819	9.9506	9.9193	9.8568	9.8255
5.82	10.0445	9.9976	9.9506	9.8881	9.8411
5.85	10.0289	9.9819	9.9350	9.8724	9.8255
5.878	9.8568	9.8098	9.7785	9.7472	9.7003

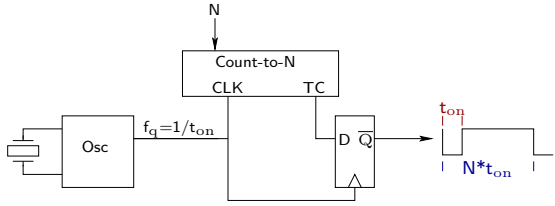

Figure 3.17. The modulation signal s_{mod} is generated by a programmable counter, which divides the reference frequency f_q.

signal s_{mod} and SNR. The following sections investigate the influence of these effects on the positioning accuracy. The non-deterministic effects do not lead to an absolute distance error but to a random error. This random error can be quantified by the standard deviation of multiple simulations.

The reflector is periodically switched on and off with a rectangular modulation signal. This signal is defined by the modulation frequency f_{mod} and the on-time t_{on}. There are many ways to generate such a signal. A simple way is to use a quartz oscillator with an oscillation frequency equal to $f_q = 1/t_{on} = 75$ MHz as shown in Fig. 3.17. A programmable counter is used to divide the quartz frequency to the wanted modulation frequency $f_{mod} = f_q/N$. The output of the counter is high only when its state is zero. This allows to change the modulation frequency, without changing the on-time t_{on}. The circuit generating the pulse signal is further described in Section 4.2.1.

This method has the advantage that the modulation signal has the precision of a quartz oscillator. It is a simple and smaller solution than a dedicated fractional-N PLL. However, the quartz oscillator has phase jitter which directly influences the modulation frequency f_{mod}. The modulation frequency f_{mod} up-converts the base-band signal s_{filt} (see Equation 3.20). Because the modulation frequency has phase noise, also the up-converted peaks exhibit phase noise. This leads to wider peaks in the base band spectrum, thus it directly influences the positioning accuracy.

For most quartz clocks, the exact phase noise behavior is not available from the data sheet. Instead, the only given value is often the RMS jitter. The reason for this is the missing standard for jitter measurement [85]. For the simulation. the phase jitter is assumed to be Gaussian. This assumption is made based on published jitter measure-

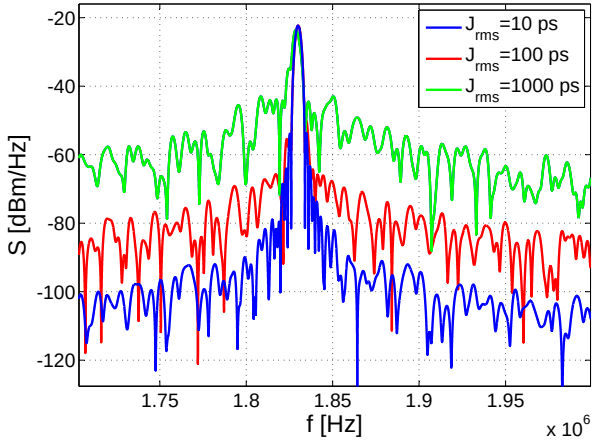

Figure 3.18. Spectrum of the modulation signal s_{mod} with added RMS jitter J_{rms}.

ments [86]. The simulations uses a 75 MHz clock, but with a normal distributed random period. The standard deviation of the period is equal to the RMS jitter J_{rms}. Due to the constant time increments in the simulation, this jitter is quantized into 6.25 ps steps. This reduces the accuracy of the simulations for small jitter values. For large jitter values (e.g. 1000 ps) the influence of the quantization is small. Furthermore, the jitter of one period $1/f_{mod}$ is the sum of N clock cycles and is only at the end quantized, this reduces the quantization error. Figure 3.18 depicts the spectrum of the modulation signal s_{mod} with added RMS jitter. 20 simulations were conducted for different jitter values. The standard deviation due to the clock jitter is shown in Fig. 3.19. The standard deviation of the detected distance is below 1 cm for J_{rms} below 400 ps and below 10 cm for a jitter value of 1 ns. Typical crystal oscillators for 75 MHz have a RMS jitter between 1 and 10 ps. Therefore, the influence of the jitter of the modulation frequency f_{mod} on the positioning accuracy is far below 1 cm.

3.3.7. Dependency on the SNR

In Section 2.3, the sensitivity of a pulsed reflector is presented. The sensitivity to continuous wave (CW) signals is -67 dBm as depicted in Fig. 2.22. If the input signal is -67 dBm, the reflector behaves as

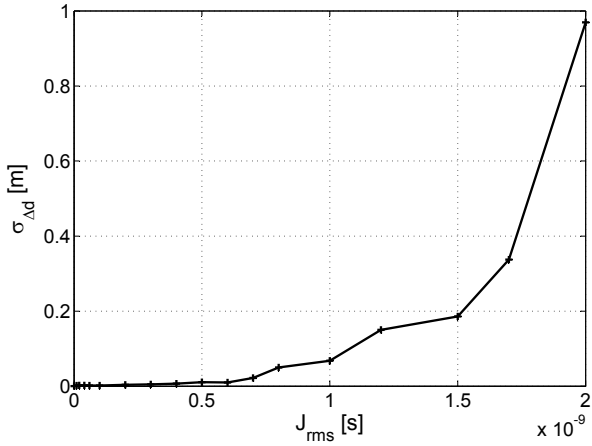

Figure 3.19. Standard deviation of the detected distance versus the RMS jitter J_{rms}.

if a signal with the same amplitude and frequency, but with a random phase, is added to the received signal. Hence, an input power of -67 dBm is equivalent to a SNR of 0 dB, when the noise is simulated as a single frequency noise. The comparison between the simulation results (Fig. 2.21) and the measurement results (Fig. 2.22) showed that this approximation emulates the measured behavior. By using this model and the measured sensitivity of -67 dBm, the influence of the SNR on the detection accuracy is simulated. 20 simulations are carried out for each SNR. The simulation results are summarized in Table 3.4 and the spectra of the base-band signal are plotted in Fig. 3.20. The confidence interval for the simulated standard deviation is discussed in Appendix A.5. The 95% confidence interval is between $0.76{\cdot}\sigma$ and $1.46{\cdot}\sigma$.

The SNR has two influences. First, the mean distance increases with lower SNR and second, the standard deviation increases with lower SNR. The increased detected distance due to a lower input signal is discussed in Section 3.3.3. The standard deviation increases due to the larger synchronization error as shown in Section 2.2.1. The starting phase of the reflector is more accurate for a high SNR, and thus the standard deviation of the detection error is smaller.

The positioning accuracy is still below 5 cm for an input signal

Table 3.4. Simulated mean distance $\overline{d}$ and $\sigma_{\Delta d}$ for different SNR values.

SNR [dB]	$\overline{d}$ [m]	$\sigma_{\Delta d}$ [cm]
-9	9.3915	231.1734
-6	9.9999	88.4562
-3	10.3000	10.9824
0	10.3031	5.8736
3	10.3164	3.0832
6	10.2976	1.6632
9	10.3074	1.3688
12	10.2991	0.7364
18	10.2996	0.3415
24	10.2993	0.1710

strength of -67 dBm. However, the heights of the peaks reduces with lower SNR. If multipath propagation occurs, the height of the peaks will further reduce as presented in Section 5.4. Thus, it is advantageous to have high peaks, because they are better detectable, especially in strong multipath environments..

3.3.8. Deterioration due to Switching

In Section 2.3.1 the influence of the on-switching pulse on an oscillator is discussed. The on-switching has a similar effect as noise, but it is deterministic. In this Section, the influence of the on-switching on the positioning accuracy is simulated.

The analytical start-up model (Section 3.2.1) calculates the start-up transient depending on the following parameters: loop gain A, quality factor Q, received signal amplitude B, phase ϕ_{start} of the received signal and the frequency of the incoming signal ω. The on-switching is modeled according to (2.48) and (2.49) as a constant phasor which is added to the input signal. This is similar to the simulation dependent on the phase noise with the difference that the phasor has a constant phase instead of a random phase. The phasor has a certain amplitude v_{switch} which can be transformed to a power level $P_{det} = v_{det}^2/R_{load}$.

Figure 3.22 shows the resulting base band spectra for a distance of 10 m with varying switching power levels P_{det}. The simulation results are summarized in Table 3.5. The peak height is above 30 dB for a distance of 10 m and a switching level P_{det} of -63 dBm. This is equal to a signal to P_{det} ratio of 8.3 dB. If the distance d is increased to 50 m,

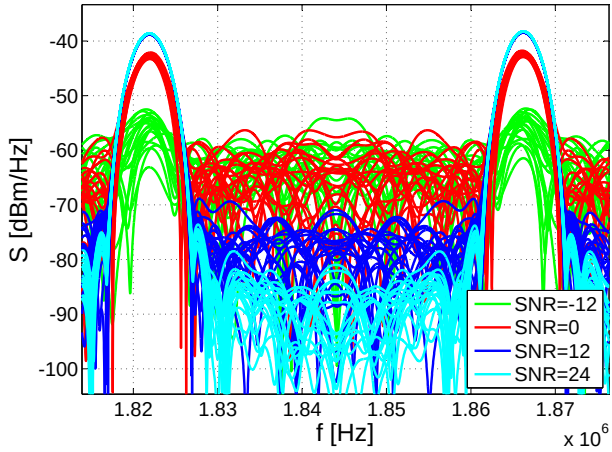

Figure 3.20. Spectrum vs. SNR between a SNR of -12 dB, equivalent to an input signal of -79 dBm (sensitivity=-67 dBm), and a SNR of 24 dB, equivalent to an input signal of -43 dBm.

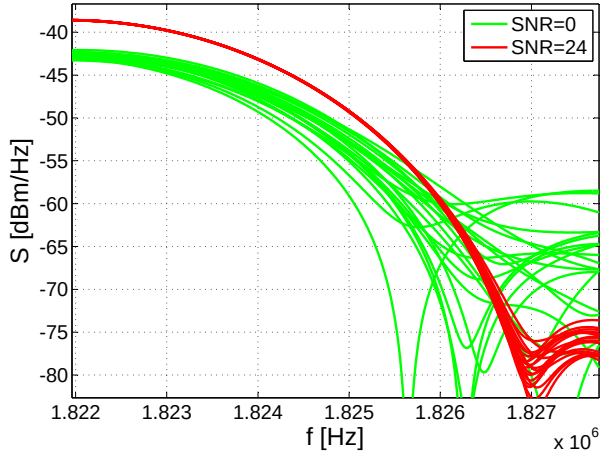

Figure 3.21. Spectrum vs. SNR for a SNR of 0 dB and a SNR of 24 dB. Only the inner edge of the left peak is visible. With a lower SNR, the edge has a larger variance and thus the positioning accuracy decreases.

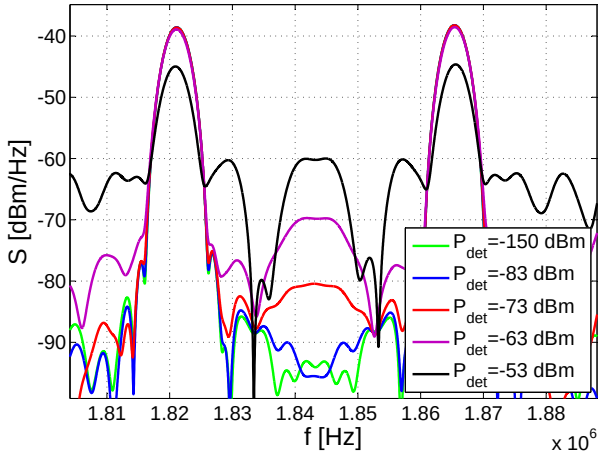

Figure 3.22. Resulting baseband spectrum with a deterministic starting phase ϕ_{det}. The stronger the deterioration P_{det} due to the switching is, the smaller is the peak height.

the received signal is weaker and thus the switching influence P_{det} has to be smaller (-78 dBm). The ratio of the signal P_{in} to P_{det} is 9.3 dB. From this, it can be stated that a ratio of P_{in}/P_{det} above 8.3 dB is sufficient for the pulsed reflector system.

3.3.9. Positioning Accuracy vs. Phase Noise

Like every FMCW radar system, the active pulsed reflector is susceptible to phase noise of the base station and the reflector. The influence of the phase noise of the active reflector is discussed in this section.

The phase noise characteristic $\mathcal{L}(\Delta\omega)$ of an oscillator is often approximated by the Leeson formula [87]:

$$\mathcal{L}(\Delta\omega) = 10\log\left(\frac{2FkT}{P_{out}}\left(1+\left(\frac{\omega_0}{2Q\Delta\omega}\right)^2\right)\left(1+\frac{\Delta\omega_{1/f^3}}{|\Delta\omega|}\right)\right) \quad (3.44)$$

with the empirical noise factor F, the Boltzman constant k, the temperature T and the output power P_{out}. Close to the carrier ($|\Delta\omega| < \Delta\omega_{1/f^3}$), the up-converted 1/f noise dominates, which decays 30 dB per decade. The feedback noise dominates in the range $\Delta\omega_{1/f^3} < |\Delta\omega| < \omega_0/(2Q)$ and decays 20 dB per decade. The phase

Table 3.5. Simulation results for different on-switching values P_{det}.

P_{det} [dBm]	Δd [cm] d=10	d=30 m	d=50 m
-150	-0.92	1.92	4.77
-88	-0.92	3.48	4.77
-83	-0.92	3.48	4.77
-78	-0.92	3.48	4.77
-73	-0.92	3.48	4.77
-68	-0.92	6.61	7.89
-63	-0.92	15.99	15.71
-58	0.64	36.32	-1835.47
-53	5.33	8091.47	8632.16
-48	14.71	8091.47	5989.85

noise of the active reflector can be simulated with Cadence. Figure 3.23 compares the phase noise characteristic based on the Leeson formula with the simulated phase noise characteristic. The Cadence simulation predicts a phase noise of -117.3 dBc/Hz at 1 MHz offset.

The influence of the phase noise on the positioning accuracy is simulated with the same model as the influence of the SNR. The phase noise can only accumulate during one on-switching time t_{on}, because at every start-up, the phase is resynchronized. The phase noise is added to the theoretical start-up model numerically with an algorithm from Bar-Guy [88]. The algorithm is a simple VCO phase noise model based on an oscillator output signal

$$V(t) = V_0 \cos(\omega_0 t + \phi_n(t)), \tag{3.45}$$

where V_0 is the amplitude and $\phi_n(t)$ is defined as the phase noise. In cases of small noise sources ($\phi_n(t) \ll 2\pi$), the following approximations can be used to express the oscillator output:

$$\begin{aligned} V(t) &= V_0 \cos(\omega_0 t + \phi_n(t)) && (3.46)\\ &= V_0 (\cos(\omega_0 t)\cos(\phi_n(t)) - \sin(\omega_0 t)\sin(\phi_n(t))) && (3.47)\\ &\approx V_0 (\cos(\omega_0 t) - \sin(\omega_0 t)\,\phi_n(t)). && (3.48) \end{aligned}$$

This result shows that the phase noise is mixed with the carrier to produce sidebands around the carrier. This assumption is used in the phase noise model. Additive white Gaussian noise (AWGN) is shaped in the frequency domain with the wanted phase noise characteristic.

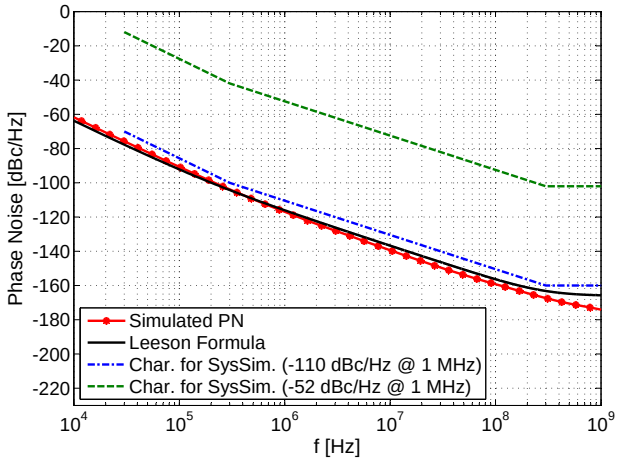

Figure 3.23. Comparison of the phase noise spectra of the integrated reflector circuit, simulated with Cadence (Simulated PN), the calculated phase noise based on the Leeson formula and the best and worst case phase noise characteristic used in the system simulations.

The applied phase noise characteristic are plotted in Fig. 3.23. An inverse discrete Fourier transform (DFT) then leads to the time-domain signal $\phi_n(t)$. This phase noise is then up-converted with the carrier signal $V_0 \sin(\omega_0 t)$ and added to the reflector signal $(V_0 \cos(\omega_0 t))$. In the case of the active pulsed reflector, the phase noise is added to each on-switching pulse separately, because the reflector is switched off in between and the phase is resynchronized during each on-switching process. Thus, slowly varying phase noise does not affect the reflector. The close to carrier phase noise can be neglected due to this resynchronization process.

The resulting simulated base-band spectra for a distance of 10 m are plotted in Fig. 3.25. The width of the peaks is not influenced by increasing phase noise, but the height of the peaks is reduced. The peaks vanish for a phase noise of -40 dBc/Hz @ 1 MHz offset. The simulation results are summarized in Table 3.6. The main influence of a higher phase noise is the higher standard deviation of the detected distance d.

The implemented active reflector has a phase noise of -116 dBc/Hz @ 1 MHz, which is below the simulated best case of -110 dBc/Hz @

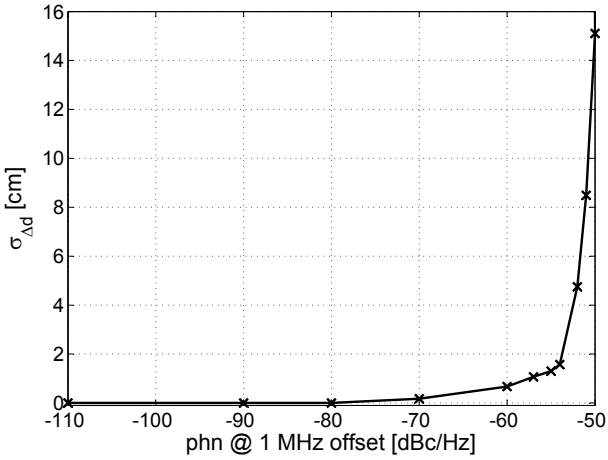

Figure 3.24. Standard deviation $\sigma_{\Delta d}$ versus the phase noise @ 1 MHz offset.

1 MHz offset. The positioning accuracy is not influenced for phase noise below -80 dBc/Hz @ 1 MHz, and even a phase noise of -54 dBc/Hz @ 1 MHz results in a standard deviation $\sigma_{\Delta d}$ of 1.57 cm. Therefore, the limitations on the positioning system due to phase noise of the reflector are small. This simplifies the design of the reflector, because the loop gain A and the quality factor Q can be chosen more freely.

3.3.10. Positioning Accuracy vs. the Distance

Until now, the influence of the input power P_{in}, the SNR and the phase noise were simulated separately. But, if the distance between the reflector and the base station increases, then the received signal is weaker and the SNR decreases. The simulated reflector's phase noise performance is -116 dBc/Hz @ 1 MHz offset. The sensitivity of the reflector was presented in Section 2.2 and is -67 dBm. Each distance is simulated 50 times, which increases the confidence in the simulated standard deviation.

The mean error $\overline{\Delta d}$ and the standard deviation $\sigma_{\Delta d}$ are depicted in Fig. 3.27 The simulations revealed that the mean value of the positioning error increases with larger distance as described in Section 3.3.3. The standard deviation increases as well due to the lower SNR. The

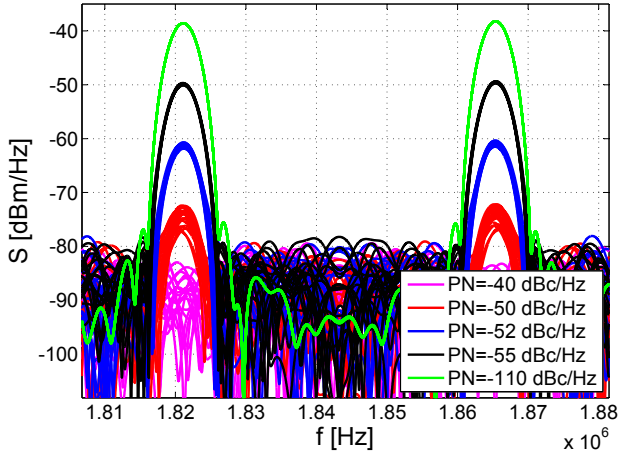

Figure 3.25. Spectrum vs. phase noise @ 1 MHz offset. The spectrum is not affected for phase noise better than -80 dBc/Hz @ 1 MHz offset.

Table 3.6. Simulation results for different phase noise characteristics. The standard deviation $\sigma_{\Delta d}$ increases for higher phase noise.

Phase noise @ 1MHz offset [dBc/Hz]	$\overline{d}$ [m]	$\sigma_{\Delta d}$ [cm]
-40	5.341	840.67
-50	10.028	15.11
-52	9.993	4.75
-54	9.998	1.57
-55	9.997	1.30
-57	9.991	1.07
-60	9.993	0.67
-70	9.992	0.17
-80	9.993	0.00
-90	9.993	0.00
-110	9.993	0.00

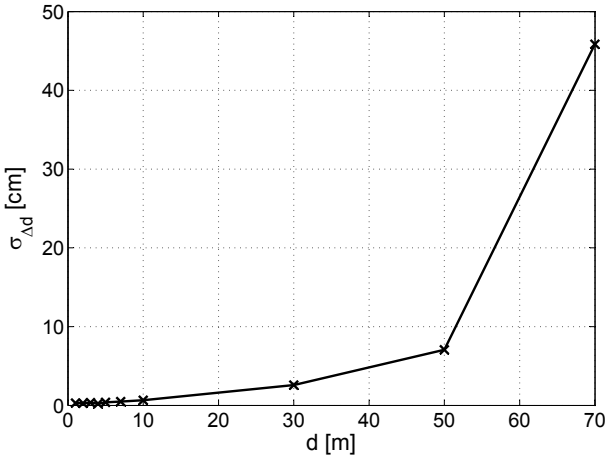

Figure 3.26. Standard deviation of the positioning error vs. the distance. The positioning system with an active pulsed reflector, which has a sensitivity of -67 dBm, has a positioning range of up to 50 m. The accuracy decreases drastically for distances above 50 m.

standard deviation of the distance error $\sigma_{\Delta d}$ is below 0.74 cm for distances between 1 and 10 m and below 2.6 cm for distances below 30 m as plotted in Fig. 3.26. The positioning accuracy decreases drastically for distances above 50 m. Larger distances are possible, for a better sensitivity, e.g. if the sensitivity increases by 6 dB, the possible distance doubles.

3.4. The Simultaneous Operation of Multiple Reflectors

One of the big advantages of the active pulsed reflector approach is the ability to measure multiple reflectors simultaneously. Multiple reflectors can be identified using their modulation frequencies f_{mod}.

The number of reflectors which can be detected depends on the width of the spectrum of one reflector and the available base-band bandwidth. The base-band bandwidth is limited by the sampling frequency of the ADC (f_{ADC}) which samples the base-band signal as depicted in Fig. 3.1. The spectrum of the base-band signal for one reflector can be seen in Fig. 3.3. The width of the peaks is independent of the distance,

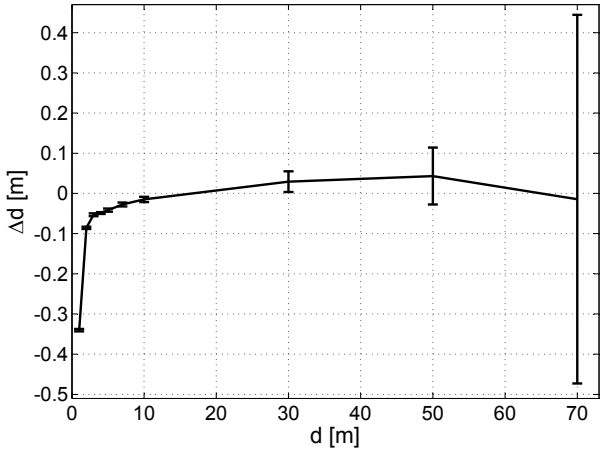

Figure 3.27. Error of the detected distance dependent on the distance d. The detected distance depends linearly on the input power and thus logarithmic on the distance. The errorbars indicate the standard deviation $\sigma_{\Delta d}$.

and thus are constant

$$f_{peak} = 2f_{sinc} = \frac{f_{BW}}{T} t_{on} = 4\ [kHz], \tag{3.49}$$

where T is the ramp duration (≈0.5 ms), f_{BW} is the sweep band-width (150 MHz) and the on-time t_{on} (13.3 ns). The distance between the peaks Δf is dependent on the round-trip time-of-flight (RToF) $\tau = d/c$:

$$\Delta f = 2\left(f_{bb} - f_{sinc}\right) = 4\frac{f_{BW}}{T}\tau = 4\frac{f_{BW}\, d}{Tc} = d \cdot 4000 \ \left[m \cdot \frac{Hz}{m}\right]. \tag{3.50}$$

Thus, the maximum base-band bandwidth occupied by one reflector is

$$f_{occupied}\left(d\right) = 2f_{peak} + \Delta f\left(d\right) \tag{3.51}$$

Figure 3.28 illustrates the base-band spectrum for multiple reflectors. One reflectors occupies a certain bandwidth $f_{occupied}$ in the base-band. This bandwidth, derived in (3.51), depends on the maximum

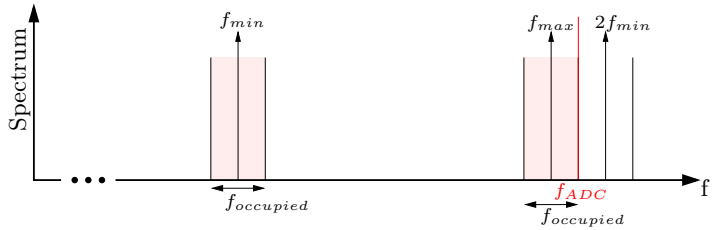

Figure 3.28. Base-band spectrum in the case of multiple reflectors. Each reflector occupies a bandwidth $f_{occupied}$. The highest modulation frequency f_{max} is limited by the ADC f_{ADC}. The second harmonic of f_{min} has to be larger than the highest modulation frequency f_{max} for an non-overlapping spectrum.

detectable distance d_{max} and can be rewritten as

$$f_{occupied}\left(d_{max}\right) = 2\frac{f_{BW}}{T}\left(t_{on} + 2\frac{d_{max}}{c}\right). \tag{3.52}$$

The maximum detectable distance d_{max} varies for different scenarios. In an indoor environment, the largest distance is limited by the room size. The detectable distance is larger outdoors. In order to calculate the number of simultaneous reflectors, the available bandwidth has to be known. The highest modulation frequency f_{max} is limited by the sampling speed of the ADC in the base station f_{ADC}. The highest modulation frequency f_{max} must be half the occupied frequency $f_{occupied}$ below f_{ADC}

$$\begin{aligned} f_{max} &= f_{ADC} - \frac{f_{occupied}\left(d_{max}\right)}{2} \\ &= f_{ADC} - \frac{f_{BW}}{T}\left(t_{on} + 2\frac{d_{max}}{c}\right). \end{aligned} \tag{3.53}$$

If f_{max} was higher, only one of the two peaks would be sampled.

The reflector is modulated with an rectangular signal, thus the peaks are visible around the modulation frequency f_{mod}, but also at multiples of the modulation frequency $n \cdot f_{mod}$. Two times the lowest modulation frequency has to be larger than the highest modulation frequency f_{max} plus $f_{occupied}$, otherwise the spectrum of f_{max} and $2f_{min}$

overlap. Thus, the lowest modulation frequency f_{min} is

$$\begin{aligned} f_{min} &= \frac{f_{max} + f_{occupied}\,(d_{max})}{2} \\ &= \frac{f_{ADC}}{2} + \frac{f_{BW}}{2T}\left(t_{on} + 2\frac{d_{max}}{c}\right). \end{aligned} \tag{3.54}$$

Hence, the usable bandwidth in the base-band is

$$f_{BB} = f_{max} - f_{min} = \frac{f_{ADC}}{2} - \frac{3f_{BW}}{2T}\left(t_{on} + 2\frac{d_{max}}{c}\right). \tag{3.55}$$

The number of simultaneous detectable reflectors is

$$\#reflectors = floor\left(\frac{f_{BB}}{f_{occupied}\,(d_{max})}\right) + 1 \tag{3.56}$$

Figure 3.29 plots the number of reflectors vs. the available bandwidth. In the implemented system, the f_{ADC} is 3.125 MHz, the used bandwidth f_{BW} is 150 MHz, sweep time T is 0.5 ms and the maximum distance d_{max} is 50 m. This leads to a maximum of 7 simultaneous detectable reflectors.

The base-band signals from the different reflectors are received simultaneously. The signal from near reflectors is much stronger than the signal from reflectors which are far away. The ADC resolution determines, what the smallest detectable signal is. The worst case scenario is, if 6 reflectors are close to the base station ($d \approx 1$ m) and one at the maximum distance $d = 50$ m. The received signal's amplitude differs by a factor of 50. It is possible that the 6 nearest reflectors interfere constructively and the amplitude adds up. Therefore, the weakest amplitude may be 300 times smaller than the maximum amplitude. In order to analyze the weakest signal with a reasonably good accuracy, at least 3 bits are needed for the weak signal. The total needed ADC resolution is at least 12 bit.

3.4.1. Simulations with 4 Simultaneous Reflectors

The simple theoretical start-up model (Section 3.2.1) cannot be used for the simulation of simultaneous reflectors, because it cannot simulate the influence of an external signal on the reflector after the start-up. Thus, the Simulink model (Section 3.2.2) is chosen. In the simulation scenario, the reflectors are randomly spread in a room with size 10x10

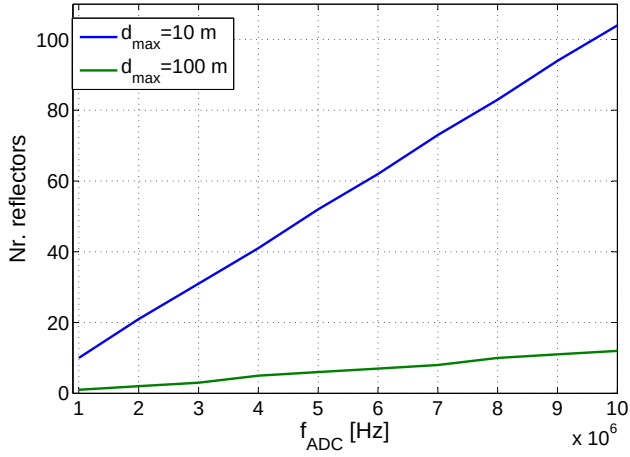

Figure 3.29. Number of simultaneously detectable reflectors vs. the sampling frequency f_{ADC}.

Table 3.7. Simulation results for 4 reflectors.

f_{mod} [MHz]	Distance [m]	Detected distance [m] w. coupling	Detected distance [m] w/o coupling	Diff. due to coupling [cm]
1.6245	3.2109	3.1755	3.1755	0
1.8723	6.6093	6.6167	6.6128	0.39
2.1201	8.4856	8.5032	8.5032	0
2.3679	9.6916	9.7141	9.7102	0.39

m^2. For each reflector, the line-of-sight (LOS) component is calculated. Each reflector couples into every other reflector, because the reflectors have omni-directional antennas. The delays and the attenuations are calculated by the distance between the reflectors.

Table 3.7 summarizes the simulation results. The largest distance error due to the coupling between the reflectors is 0.39 cm, which corresponds to the resolution of the interpolating zoom FFT. Thus, the coupling has a small influence on the positioning error for 4 reflectors.

Table 3.8. Frequency of 7 reflectors for a f_{ADC} of 3.125 MHz, and a maximum distance d_{max} of 50 m..

ref	f_{mod} [MHz]	
1	f_{min}	1.6144
2	$f_{min} + f_{occupied}$	1.8222
3	$f_{min} + 2f_{occupied}$	2.0301
4	$f_{min} + 3f_{occupied}$	2.2378
5	$f_{min} + 4f_{occupied}$	2.4457
6	$f_{min} + 5f_{occupied}$	2.6534
7	$f_{min} + 6f_{occupied}$	2.8613

3.4.2. Simulations with 7 Simultaneous Reflectors

The implemented system is capable to distinguish between 7 reflectors. Table 3.8 lists the different modulation frequencies f_{mod} of these reflectors. With more reflectors, the chance that two or more are transmitting at the same time is larger. If more than one reflector is on at the same time, it is possible that they couple into each other. For each reflector, the probability that at least one other reflector is on is around 10%.

As with 4 reflectors, the reflectors are randomly placed in a 10x10 m^2 room. One of the simulated scenario is shown in Fig. 3.31. In a first simulation campaign, the system is simulated with and without coupling between the reflectors. 4 simulations are conducted, each with different positions of the 7 reflectors. In a first simulation campaign, the reflections at the walls are neglected (no multipath propagation). Later, the reflections on the wall are introduced as a first multipath scenario. The resulting base-band spectrum is depicted in Fig. 3.30. The different reflectors are nicely separated. No significant influence of the coupling could be recognized. The standard deviation of the detection error and the mean value change less than 1%. The coupling does not reduce the positioning accuracy. One reason for this is that a fully oscillating reflector is not influenced by nearby reflectors, because of the large amplitude difference. The start-up behavior is only influenced, if the reflector during start-up receives a signal of another reflector in addition to the signal of the base station, because the reflector is only during start-up sensitive (the sensitivity curve is discussed in Appendix A.2). The simulation results of one of the four simula-

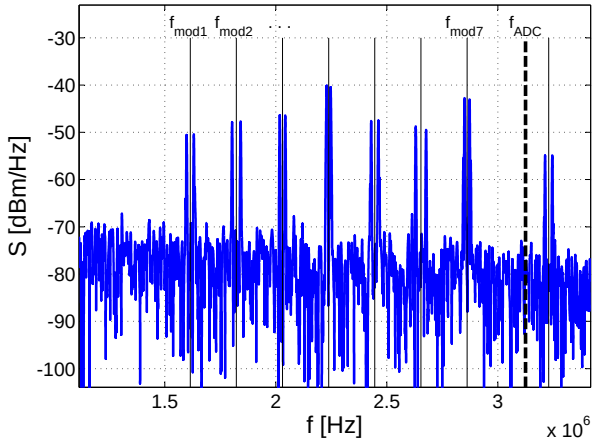

Figure 3.30. Simulated base-band spectrum with 7 reflectors with coupling. The ADC-bandwidth f_{ADC} is 3.125 MHz.

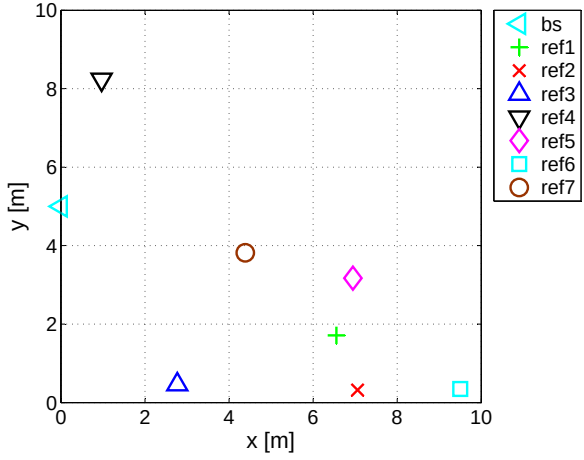

Figure 3.31. One of the simulated configurations of the 7 reflectors in a room of 10x10 m^2.

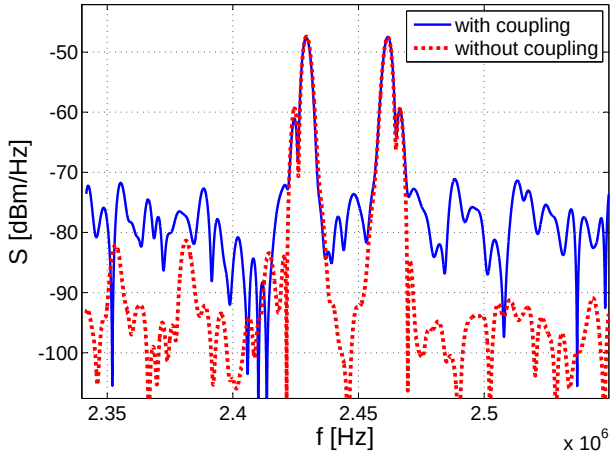

Figure 3.32. Simulated spectrum for 7 reflectors with and without coupling between the reflectors. Only the peaks of the reflector at $f_{mod2} = 2.446$ MHz are visible. This is the simulated reflector position with the shortest multipath. The multipath component leads to additional peaks close to the main peaks.

tions are listed in Table 3.9. The coupling does have an influence on the individual positioning, but it does not affect the overall accuracy (standard deviation and mean value not affected). The spectra with and without coupling between the reflectors are depicted in Fig. 3.32, including multipath propagation. With coupling, the height between the peaks and the noise floor is reduced. The simulation shows similar results as the SNR simulations with the theoretical start-up model (Section 3.3.7). Out of this agreement, two conclusions can be drawn. First, the theoretical start-up model and the Simulink model behave identical, which verifies the applicability of the models. Second, the coupling between the reflectors can be seen as additional noise and thus the SNR is reduced.

In indoor localization system, multipaths are the biggest challenge. A first approximation of the multipaths can be realized by taking the LOS component and the first multipath component (MPC). The first MPC is the multipath with the shortest path length and thus the strongest. Landron et al. [89] measured reflection coefficients Γ_r of limestone and brick walls. The values are between 0.03 and 0.6 for

Table 3.9. Results for 7 reflectors, configuration 2 without multipath propagation.

ref	dist [m]	w/o coupl. error [cm]	with coupl. error [cm]	Difference [cm]
1	5.2354	0.54	0.93	-0.39
2	5.3620	0.30	1.47	-1.17
3	7.8800	-0.60	-2.95	2.34
4	2.6009	5.03	4.64	0.39
5	3.8046	2.36	3.92	-1.56
6	10.4667	-0.90	1.05	-1.95
7	7.2433	-1.00	-2.56	1.56

limestone and 0.1 and 0.7 for brick walls, respectively. Table 3.10 summarizes the simulation results of 7 randomly placed reflectors in a 10x10 m^2 room. With coupling between the reflectors but without multipath propagation, the mean error is below 1 cm and the standard deviation is 2.9 cm. With a worst case reflection coefficient Γ_r of 1, the mean error increases to 53 cm and the standard deviation is close to 1 m. The simple multipath model revealed the urgent need for a more detailed analysis of multipath propagation.

Table 3.10. Simulation of 7 reflectors in a room with one MPC per reflector. Only the first MPC is simulated with different reflection coefficients Γ_r.

Γ_r	mean(Δd)	$\sigma_{\Delta d}$ [m]
0	0.0093	0.0290
0.3	0.0190	0.1172
1	-0.5309	0.9439

3.5. Multipath Propagation

The addition of one multipath component to the simulation with 7 reflectors in Section 3.4.2 manifests the need for a thorough study of the influence of multipath propagation effects on the positioning system. This section presents multipath simulations with a statistical wideband channel model.

3.5.1. Model

The development of an indoor positioning system requires a good understanding of the propagation characteristics of the transmission channel. An accurate channel model is needed for performance prediction and simulations. Different method exist to build a channel model. The most widespread method is to form a statistical model based on measurements. Many of these models exist for UWB channel in indoor environments [90] - [92].

One of the most complete UWB model is the channel model from the IEEE 802.15.4a channel modeling subgroup. The model is described in [93]. This UWB model covers the frequency range from 2 to 10 GHz and models indoor residential, indoor office, industrial and outdoor environments with a distinction between LOS and NLOS properties. Reference [94] provides MATLAB programs and numerical values for 100 impulse response realizations in each environment. Our indoor positioning system uses a bandwidth of 150 MHz around 5.8 GHz. This frequency range is covered by this channel model. For our positioning environment, the office LOS and the industrial LOS are the most relevant scenarios.

The channel model generates impulse responses. As described in [94], the generic channel model has the following key features

- model treats only the channel itself, while antenna effects, such as antenna characteristic and gain, are to be modeled separately
- frequency dependence of the pathloss
- modified Saleh-Valenzuela model:
  - arrival of paths in clusters
  - mixed Poisson distribution for ray arrival times
  - possible delay dependence of cluster decay times
  - some NLOS environments have first increasing and then decreasing power delay profiles
- Nakagumi-distribution of small-scale fading
- block fading: channel stays constant over data burst duration

The model does not include shadowing, or large scale fading. Shadowing S is defined as the variation of the pathloss G_{pr} around the local

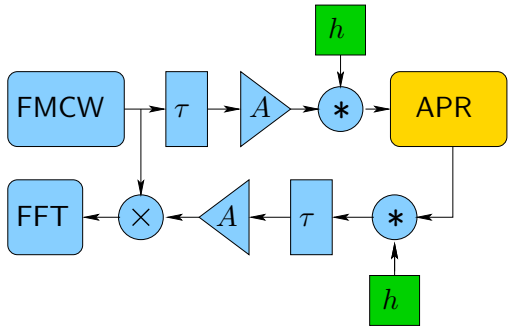

Figure 3.33. Multipath propagation environment: The multipath affected radar signal is generated in Matlab, while the reflector (APR) is simulated in Simulink.

mean

$$G_{pr} = G_{pr,0} + 10n \log_{10}\left(\frac{d}{d_0}\right) + S. \tag{3.57}$$

This does not affect the applicability of this model for the indoor positioning scenario, because a small change in the received power has a minimal influence on the positioning accuracy.

3.5.2. Implementation

Both Matlab and Simulink are used for the multipath propagation simulations. The multipath components are calculated in Matlab and the resulting signal is then applied to a Simulink model of the active reflector as depicted in Fig 3.33. The Simulink model of the reflector is described in Section 3.2.2. The output signal is then convoluted with the impulse response h of the transmission channel with MPC. And finally the transmitted and received signals are mixed.

The impulse response for different environments can be generated with the IEEE 802.15.4a channel model. The time resolution is defined by t_s. The Simulink model for the reflector uses a minimum sampling frequency of 25 GHz. The input signal for the radar model is generated by the discrete convolution of the impulse response h and the chirp signal x

$$y(n) = \sum_{\nu=-\infty}^{\infty} x(\nu)\, h(n-\nu), \tag{3.58}$$

thus both time resolutions should be equal ($t_s = 40ps$). The channel energy of the impulse response is normalized to 1, the path gain $G_{\mathrm{pr}}(d, f)$ and the delay $t_{\mathrm{d}}(d)$ of the line of sight path has to be calculated by

$$G_{\mathrm{pr}}(d, f) = G_{\mathrm{tx}}(f)\,\eta_{\mathrm{tx}}(f)\,G_{\mathrm{rx}}(f)\,\eta_{\mathrm{rx}}(f)\left(\frac{c_0}{4\pi f d}\right)^n \tag{3.59}$$

$$t_{\mathrm{d}}(d) = \frac{d}{c_0}, \tag{3.60}$$

where G_{tx} and G_{rx} are the antenna (power) gains for transmit and receive antenna respectively, and $\eta(f)$ is the antenna efficiency. c_0 is the speed of light, f is the considered frequency, and d is the distance between the antennas. Because the bandwidth of the planned RESOLUTION system is only 150 MHz, the path gain is approximately constant over the whole bandwidth, and usually described in dB by

$$G_{\mathrm{pr}}(d) = G_{\mathrm{pr},0} - 10n\log_{10}\left(\frac{d}{d_0}\right) \tag{3.61}$$

where the reference distance d_0 is set to 1 m, $G_{\mathrm{pr},0}$ is the path gain at the reference distance, and n is the propagation (path gain) exponent. LOS pathloss exponents in indoor environments range from 1 in a corridor to about 2 in an office environment. For the simulation, a worst case pathloss exponent n of 2 is chosen.

3.5.3. Simulation Results

Simulations are performed with two different channel models: Office LOS and Industrial LOS. The office LOS emulates an indoor environment with many multipath components, as plotted in Fig. 3.34, whereas the industrial line-of-sight scenario has only a few multipaths with a larger delay, as plotted in Fig. 3.35. In the industrial LOS model most of the energy is in the LOS path [95]. These two scenarios are chosen because they seem to be the environments, where the active reflector system will be used the most and because they have completely different channel characteristics. Therefore, small and large rooms are covered in the simulations.

The simulation results for the indoor office LOS scenario and the industrial LOS scenario are summarized in Table 3.11 and Table 3.12, respectively. Figure 3.36 shows the histogram of 100 simulations with

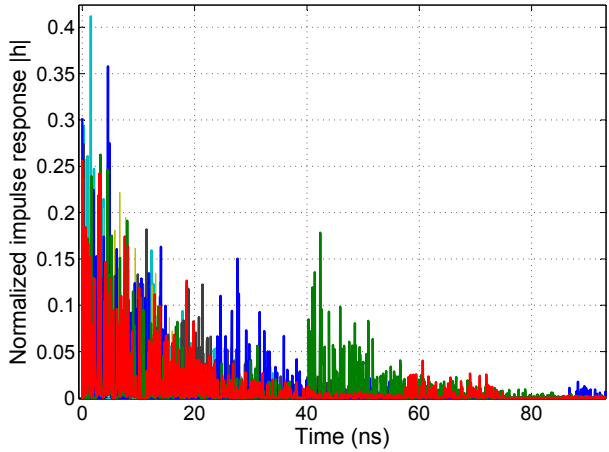

Figure 3.34. Impulse response of 6 realizations of the indoor office LOS channel model.

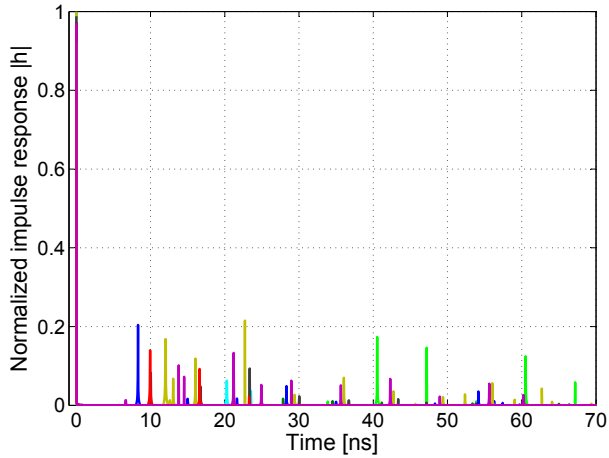

Figure 3.35. Impulse response of 6 realizations of the industrial LOS model.

Table 3.11. Simulation results of the indoor office LOS scenario for a distance of 3 m. Two different on-times $t_{on} = 15$ ns and 500 ns are simulated. For the two simulations $MPC_{ref \to BS}$ and $MPC_{BS \to ref}$ only one path is affected by multipath propagation. Multipath propagation has a larger influence on the path from the base station to the reflector ($BS \to ref$).

	#	mean(Δd) [m]	$\sigma_{\Delta d}$ [cm]
$t_{on} = 15$ ns	100	0.55	25.69
$MPC_{ref \to BS}$	100	0.40	11.43
$MPC_{BS \to ref}$	100	0.44	19.68
$t_{on} = 500$ ns	100	0.93	28.01

Table 3.12. Industrial LOS scenario results for a distance of 3 m.

	#	mean(Δd) [m]	$\sigma_{\Delta d}$ [cm]
$t_{on} = 15$ ns	100	0.40	25.07
$MPC_{ref \to BS}$	100	0.33	12.40
$MPC_{BS \to ref}$	100	0.37	19.03
$t_{on} = 500$ ns	100	0.78	27.23

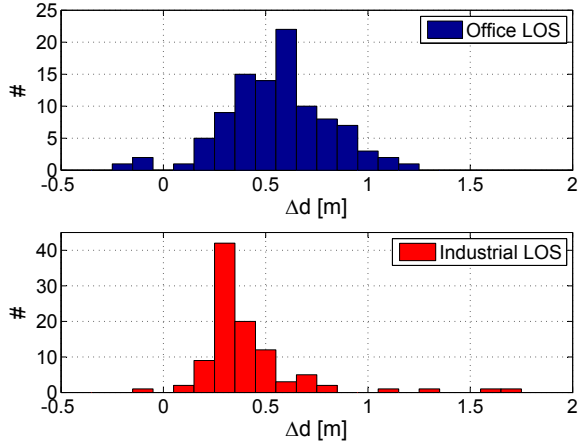

Figure 3.36. Histogram of 100 simulations with channel model 3 (indoor office LOS) and channel model 7 (industrial LOS)

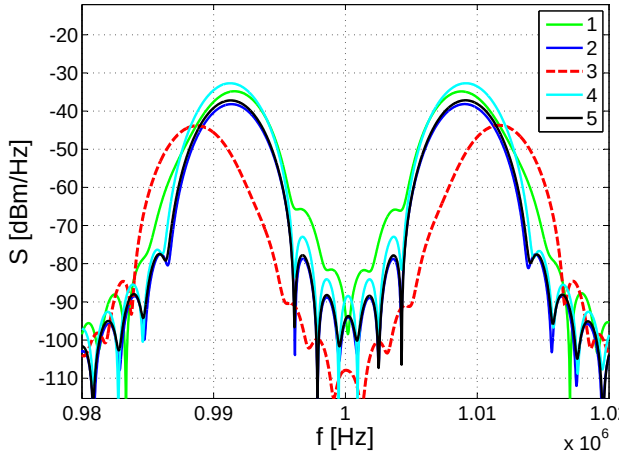

Figure 3.37. Base-band spectra for a distance of 3 m, with the industrial LOS channel model (5 realizations).

office indoor LOS and industrial LOS channel models. Although the standard deviation for the indoor office LOS (25.69 cm) is as large as for the industrial LOS model (25.07 cm), the number of detected positions with an absolute error smaller than 10 cm is higher for industrial LOS (67%) compared to 39% for office LOS. The simulations show that the active reflector concept performs better in an industrial environment with a few strong multipaths than with many multipaths. However, in a worst case, the system performance for the industrial LOS scenario degrades dramatically as depicted for channel realization 3 in Fig. 3.37.

The multipath simulations allow to test the influence of the on-time t_{on} on the positioning accuracy. With a larger t_{on}, the width of the main lobe of the sinc-envelope in the spectrum is reduced. Hence, the available bandwidth is not optmally used. A system with a narrower bandwidth is more susceptible to multipath propagation, because multipath propagation can lead to notches in the frequency band. Therefore, it is expected that the positioning system performs worse with a larger on-time. To investigate the influence of the on-time t_{on} in a multipath environment, two different on-times t_{on} of 15 ns and 500 ns are simulated. The corresponding widths of the main lobe are 133 MHz and 4 MHz according to (2.46). However, this only affects the path from the reflector to the base station. The other direction is not influenced by

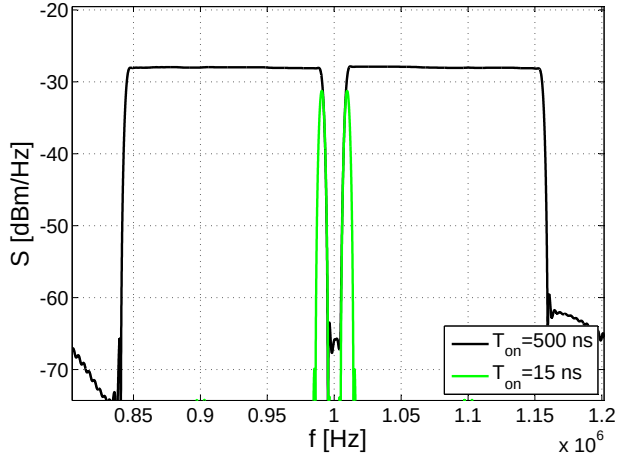

Figure 3.38. Spectra of the base-band signal for a distance of 3 m for a pulse width of 15 ns and 500 ns, respectively.

the on-time, because the base stations transmit unmodulated FMCW signals. The resulting base-band spectra for both t_{on} are plotted in Fig. 3.38. The inner edges of the peaks are identical. The standard deviation of the detected distance d for 100 simulations increases only from 25.07 cm to 27.23 cm for the longer pulse duration for the industrial LOS scenario and from 25.69 cm to 28.01 cm for the office LOS scenario. Thus, the system performs better for a shorter on-time t_{on}, but the influence is not as large as expected. This has two reasons: In most realizations of the channel model, the signal is attenuated over the complete bandwidth of 150 MHz. Second, the path from the base station to the reflector is for both on-times the same and it could be that this path is the more sensitive path. Which path is more susceptible to multipath propagation is studied in the next paragraph.

The base station transmits a frequency modulated continuous wave (FMCW) signal. This signal is a narrow-band signal for a short observation time. In the case of a deep notch in the channel transfer function, it may be possible that no signal is received at the reflector and thus the reflector starts with a random phase. The reflector on the other hand transmits a pulsed sine-wave. The pulsed sine-wave has a wide spectrum as long as the observation time is larger than one pulse width. The information of the reflector signal is spread and thus a

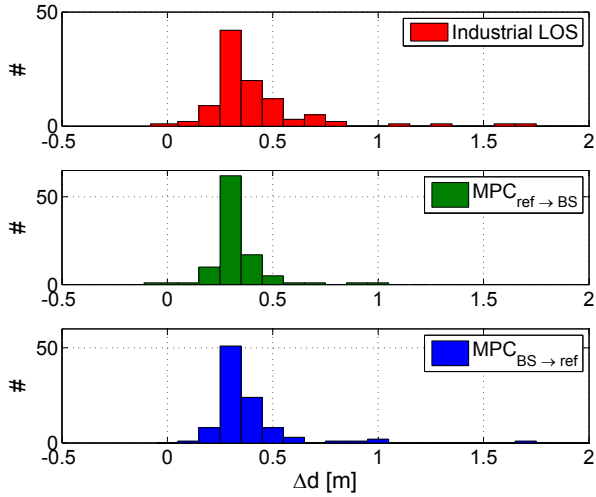

Figure 3.39. Histogram for the industrial LOS scenario. The first histogram shows the histogram of the detection error for 100 simulations with multipath propagation. The standard deviation of the distance error is smaller, if the multipath component from the base station to the reflector is neglected, as illustrated in the second plot.

notch in the transfer function influences the reflector signal less than the base band signal. The simulations confirm this explanation. The histograms of the positioning error Δd for the industrial LOS scenario are plotted in Fig. 3.39. For the case that multipath propagation only occurs on the path from the reflector to the base station ($MPC_{ref \rightarrow BS}$) the standard deviation of the detected distance d is only 11.4 cm and 12.4 cm for the office LOS and the industrial LOS scenario respectively. In the opposite case, when multipath propagation occurs from the base station to the reflector ($MPC_{BS \rightarrow ref}$), the standard deviation is significantly larger (19.7 cm for office LOS and 19.0 cm for industrial LOS). Therefore, the multipath propagation from the reflector back to the base station has a smaller influence on the overall standard deviation. This is also the reason, why the on-time t_{on} has a small influence on the detection accuracy.

For the previous simulations, the distance between the reflector and the base station is always assumed to be 3 m. However, this distance has only a small influence on the positioning accuracy, because of the

way the impulse responses are generated by the applied UWB model. The impulse responses are generated based on measurements, but with 0 delay for the LOS path. The distance information is added at the end by delaying the impulse response and attenuating the signal. Thus, for a larger distance, the impulse response does not change for our model except of the additional delay and attenuation. Furthermore, phase noise and SNR are neglected in the multipath simulations. Thus, the distance does not influence $\sigma_{\Delta d}$ in these simulations but only the mean value. This is verified by 24 simulations for a distance of 30 m (Table 3.13). The influence of the lower SNR and the phase noise was simulated in Section 3.3.10, the accuracy ($\sigma_{\Delta d}$) is 2.8 cm for a distance of 30 m. The influence of multipath propagation on the accuracy is much larger than the influence of phase noise and SNR for distances below 50 m.

Table 3.13. Indoor office LOS 3 m vs 30 m for 24 simulations.

	#	$\overline{\Delta d}$ [m]	$\sigma_{\Delta d}$ [cm]
3 m:	24	0.52	16.35
30 m:	24	0.71	16.13

3.6. Conclusion

In this chapter we have discussed the active pulsed reflector principle and the distance measurement between one base station and one or multiple reflectors. The resulting base-band spectrum is calculated and it is shown that the distance between the reflector and the base station is directly dependent on the frequency Δf between the peaks in the base-band spectrum by

$$d = \frac{\Delta\omega cT}{4\omega_{BW}}. \tag{3.62}$$

Two different simulation models of the active reflector have been presented. Both models verified the calculated behavior. Furthermore, the influence of different system parameters showed that

- a loop gain A of 3 gives the highest spectral peaks.
- the peaks do not change significantly for Q factors above 9.

- a small deviation in the oscillation frequency ω_0 has no influence on the positioning accuracy.
- the influence of the jitter of the modulation signal is very small and can be neglected for typical quartz oscillators.
- the reflector's phase noise performance should be better than -70 dBc/Hz at 1 MHz offset
- and the standard deviation of the detected distance $\sigma_{\Delta d}$ increases for larger distances due to the lower SNR.

The active pulsed reflector has the advantage that multiple reflectors can be simultaneously positioned. The number of reflectors increases for a higher ADC sampling frequency. Up to 7 reflectors are possible for our system with an ADC sampling frequency of 3.125 MHz. If a larger number of reflectors is needed and the sampling frequency cannot be further increased, time-division multiplex has to be applied.

Multipath simulations with the UWB channel model from the IEEE 802.15.4a channel modeling subgroup revealed that it influences the positioning accuracy the most. The standard deviation $\sigma_{\Delta d}$ is around 25 cm for the indoor office LOS and the industrial LOS scenario. The path from the base station to the reflector has a larger influence than the path from the reflector back to the base station. One reason for this is that the signal on the way back is modulated and thus uses a larger bandwidth. The modulation of the signal helps to improve the positioning accuracy. All simulations only consider one base station and only a distance measurement.

Finally, the reflector has to be positioned in two or three dimensions for a local positioning system. The 3D positioning and the needed algorithms are discussed in Chapter 5 and a path through a realistic museum environment is simulated, which verifies that the positioning system is accurate enough for interactive guiding.

4

Reflector Integration

The active reflector principle has been discussed in Chapter 3. System simulations helped to identify the main design parameters such as loop gain A and quality factor Q. The overall requirements for an active reflector are summarized in Section 3.6.

In this chapter, the circuit implementation of the active reflector ASIC is described in detail. Thereafter, the active reflector prototype and the base stations are presented, followed by the measurement results.

4.1. Active Pulsed Reflector ASIC

Based on the localization principle described in Chapter 3, an active pulsed reflector was designed in 0.18-μm CMOS technology. The schematic of the implemented analog, tunable reflector is illustrated in Fig. 4.1. The reflector is a fully differential oscillator and consists of an input amplifier, an output amplifier driving the antenna and a differential on-off-switching circuit. An external low frequency, quartz stabilized pulse generator ω_{mod} controls the switching and modulates the reflected signal. The single ended antenna is connected through an

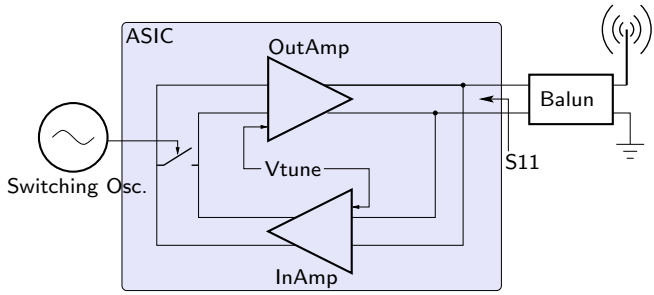

Figure 4.1. The fully differential analog tunable reflector ASIC consists of two tunable amplifiers and a switching network. The modulation signal is generated off-chip on the PCB.

external balun, thus the reflector has to be matched to a 50 Ω load. The reflector must be tunable in order to compensate process variations and has to be impedance matched to the antenna over the complete tuning range.

Two amplifiers are needed to isolate the switch from the antenna. Otherwise, the impedance matching to the antenna is strongly affected by the switch. Because the reflector has to be tunable, at least one of the amplifiers must be tunable. If only the output amplifier is tunable, the input amplifier has to have a wide bandwidth. A wide-band amplifier adds a frequency dependent phase shift, while a narrow-band amplifier has zero phase shift at maximum gain. Because the input amplifier would add a phase shift, the output amplifier has to compensate this phase shift. The reflector does not anymore oscillate at the frequency where the highest loop gain is achieved, but at a slightly lower frequency. In addition, the matching to the antenna worsens due to this oscillation frequency shift and the tuning range decreases. Furthermore, the efficiency of a wide-band amplifier is lower than a narrow-band amplifier. Two tunable amplifiers have the additional advantage that the overall Q-factor is higher if both frequencies are equal. Hence, two tunable narrow-band amplifiers are chosen.

The complete circuit is depicted in Fig. 4.2. Both input and output amplifier use almost the same differential structure shown in Fig. 4.3. This circuit consists of a differential pair with a tunable LC load. The output and the input amplifiers act as band-pass filters. The center frequency determines the oscillation frequency $\omega_0 = 1/\sqrt{L_{O1}C_{var}} =$

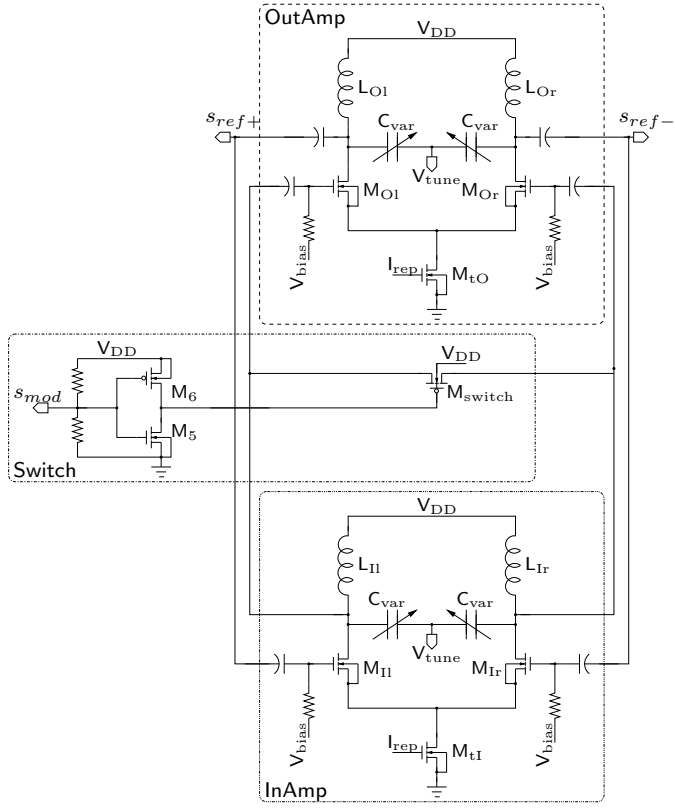

Figure 4.2. Active pulsed reflector circuit consisting of an input amplifier (InAmp), an output amplifier (OutAmp) and the on-off switch (Switch). The replica bias (I_{rep}) is not drawn.

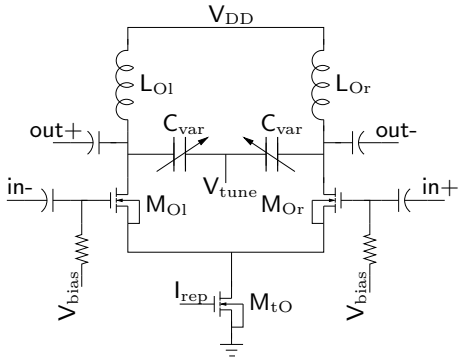

Figure 4.3. Tunable, fully differential output amplifier OutAmp.

$1/\sqrt{L_{I1}C_{var}}$ and can be tuned with two hyper-abrupt junction varactors. The individual building blocks are discussed later in this chapter.

On-off switching of the reflector can be achieved in many ways. Four different solutions are discussed here.

Supply switching The most obvious choice is to switch the supply voltage V_{DD} or a bias voltage. The required on-time t_{on} is small (only 13.3 ns) and thus the switching voltage cannot be stabilized by a capacitance, which leads to a noisy supply or bias voltage. In addition, the on-switching of a supply voltage leads to large common-mode signals. Mismatch in the circuit transform common-mode disturbances to a differential-mode signal. And this differential mode signal distorts the phase synchronous start-up. Switching supply voltages is only an option for applications, where long on-switch times are tolerable and the phase at start-up is not of importance.

Transmission gate The loop can be disconnected by adding two transmission gates between the input amplifier *InAmp* and the output amplifier *OutAmp*. The main disadvantage of the transmission gates is that both transmission gate have to switch exactly at the same time. A small time delay leads to a differential signal disturbing the phase synchronous start-up. In addition, the PMOS and NMOS transistor in a transmission gate do not switch at exactly the same time and the switching signal couples over the gate capacitances to the common-mode voltage.

Transistor A single PMOS transistor shorts the differential signals and thus decreases the loop gain. This is the approach drawn schematically in Fig. 4.1. The drain and the source of the transistor can be drawn symmetrically. When the reflector is switched off, the transistor is open and the DC voltage of the drain and source of the PMOS transistor are identical. The on-switch pulse closes the transistor. The channel charge is pushed symmetrically to drain and source and the capacitive coupling to the differential signals is also identical because the gate-source capacitance $C_{gs,swi}$ and the gate-drain capacitance $C_{gd,swi}$ are equal. The on-switch pulse only influences the common-mode signal. And this influence can be minimized by correctly designing the driving inverter ($M5$ and $M6$ in Fig. 4.12).

Mixer The last presented approach is to use a double-balanced mixer as a switch. A double-balanced mixer (e.g. Gilbert cell) has two differential input signals and a differential output signal. If one differential input is zero, then the currents through both branches are equal, and thus the output is zero. If the differential input signal at one port is a DC voltage ($\neq 0$), the output signal is equal to the RF input signal at the other port. Hence, a double-balanced mixer can be used as a switch. Although a double-balanced mixer is fully differential, a common-mode disturbance occurs when the switching state is changed. The disturbance occurs because the switching signal is a large signal which is applied to a differential pair. One of the two transistors forming a differential pair leaves the saturation region, which influences the common-mode voltage of the output signal. The common-mode signal influences the phase synchronous start-up, if there is a mismatch in the circuit. Circuit simulations of a Gilbert cell used as a switch confirmed the common-mode disturbance. The resulting common-mode signal due to switching is larger than for the single transistor approach ($\sim$ factor 3). Additional disadvantages of the double-balanced mixer are the additional power consumption and the additional phase shift added to the oscillation loop.

All four switching approaches induce a common-mode disturbance. The supply switching disturbs the common-mode signal the most. The transmission gate approach may introduce a differential disturbance in addition to a common-mode disturbance, which is even worse. A double-balanced mixer and the shortening transistor introduce a

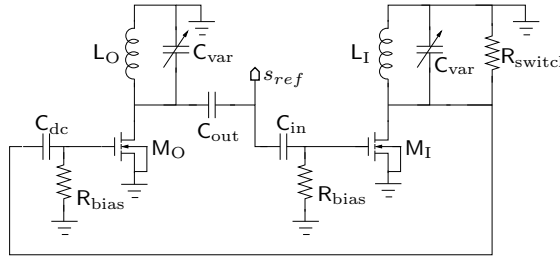

Figure 4.4. Differential mode half circuit of the active reflector.

common-mode distortion in the same order of magnitude, but the mixer is more complex, has a higher power consumption and adds an additional phase shift. Hence, a single transistor shortening the differential signal is chosen.

Figure 4.4 depicts the differential mode half circuit of the analog tunable reflector. The switching transistor is approximated by a resistor. The gate source capacitance $C_{gs,swi}$ is neglected for the differential mode, because $C_{gs,swi}$ is parallel to C_{var}. When the reflector is switched off, the transistor is open and shorts the differential signals. Therefore, the resistor R_{switch} has a low value when the reflector is switched off and reduces the gain of the first stage. Both transistors M_I and M_O have the same bias voltage V_{bias}. C_{dc} blocks the DC voltage from the first stage. Thus, the second transistor has a constant bias voltage independent of the reflector's state. Hence, the output resistance r_{dsO} of transistor M_O is the same if the reflector is switched on or off. This is important for the matching of the reflector as will be shown later. The two capacitances C_{in} and C_{out} DC decouple the antenna from the two amplifiers.

The small signal equivalent is shown in Fig. 4.5. The chosen small-signal transistor model neglects the gate-drain capacitance C_{gd}, simplifying the calculation of the voltage gain A_v and the input impedance Z_{in}. The impedance R_1 is the parallel equivalent of the output resistance r_{dsI} of transistor M_I and the switch resistance R_{switch}. The equivalent capacitance of the series connection of capacitances are in-

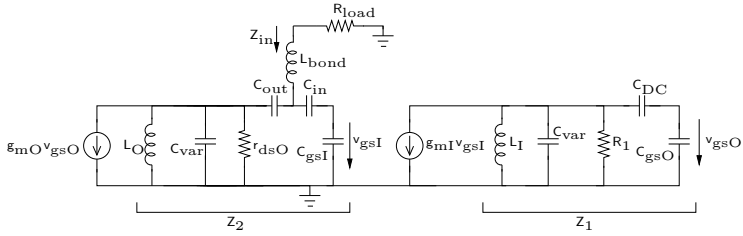

Figure 4.5. Small signal equivalent of the active reflector including the bond wire L_{bond} and the 50 Ω antenna load R_{load}.

troduced as additional variables C_{eq1} and C_{eq2}

$$R_1 = r_{dsI} \parallel R_{switch} \tag{4.1}$$

$$C_{eq1} = \frac{C_{in} C_{gsI}}{C_{in} + C_{gsI}} \tag{4.2}$$

$$C_{eq2} = \frac{C_{DC} C_{gsO}}{C_{DC} + C_{gsO}} \tag{4.3}$$

and the equivalent impedance Z_{eq} of the load R_{load} with the bond-wire L_{bond} in parallel to C_{eq1} is

$$Z_{eq1} = \left(sC_{eq1} + \frac{1}{sL_{bond} + R_{load}} \right)^{-1}. \tag{4.4}$$

For the following calculations, the impedance of the two RLC circuits are named Z_1 and Z_2. Z_1 includes $C_{var} + C_{eq2}$, R_1 and L_I, Z_2 includes C_{var}, Z_{eq1}, C_{out}, C_{eq3}, r_{dsO} and L_O.

$$Z_1 = \left(\frac{1}{R_1} + \frac{1}{sL_I} + s\left(C_{var} + C_{eq2}\right) \right)^{-1} \tag{4.5}$$

$$Z_2 = \left(\frac{1}{r_{dsO}} + \frac{1}{sL_O} + sC_{var} + \left(\frac{1}{sC_{out}} + Z_{eq1} \right)^{-1} \right)^{-1} \tag{4.6}$$

The voltage loop gain A_v is

$$A_v(\omega) = g_{mI} Z_1 \frac{C_{DC}}{C_{DC} + C_{gsO}} g_{mO} Z_2 \frac{sC_{out} Z_{eq1}}{1 + sC_{out} Z_{eq1}} \frac{C_{in}}{C_{in} + C_{gsI}} \tag{4.7}$$

The two Barkhausen criteria for oscillation are a loop gain $|A_v(\omega_0)| > 1$ and a phase shift $\angle A_v(\omega_0) = k \cdot 2\pi$. Hence, the loop gain at the oscillation frequency ω_0 has to be a real positive number. The loop gain is a real number, if both $Z_1(\omega_0)$ and $Z_2(\omega_0)\, sC_{out}Z_{eq1}/(1+sC_{out}Z_{eq1})$ are real numbers. From these relationships, the inductor values L_I and L_O can be calculated

$$L_I = \frac{1}{\omega_0^2 (C_{var} + C_{eq2})} \tag{4.8}$$

$$0 = \Im\left[\left(\frac{1}{r_{dsO}} + \frac{1}{j\omega_0 L_O} + j\omega_0 C_{var} + \left(\frac{1}{j\omega_0 C_{out}} + Z_{eq1}\right)^{-1}\right)^{-1} \cdot \frac{j\omega_0 C_{out} Z_{eq1}}{1 + j\omega_0 C_{out} Z_{eq1}}\right]. \tag{4.9}$$

The off-switching only influences the real part of $Z_1(\omega_0)$ and thus the phase shift criteria is fulfilled even when the oscillator is switched off. Hence, the loop gain is always a real number. Ideally the small signal loop gain $A(\omega_0)$ is 0 when the reflector is switched off and about 3 when the reflector is switched on (see Section 3.3.1). The two DC-block capacitances C_{DC} and C_{in} are an order of magnitude larger than C_{gsO} and C_{gsI}. Thus, both capacitive dividers introduce only a small attenuation

$$A_{divCin} = \frac{C_{in}}{C_{in} + C_{gsI}} \approx 0.8 - 0.95 \tag{4.10}$$

$$A_{divCdc} = \frac{C_{DC}}{C_{DC} + C_{gsO}} \approx 0.8 - 0.95. \tag{4.11}$$

Inserting (4.8) and (4.9) into (4.7) yields the loop gain at the resonance frequency

$$A_v(\omega_0) \approx A_{divCin} A_{divCdc} g_{mI} g_{mO} \frac{r_{dsO}}{2} (r_{dsI} \parallel R_{switch}) \tag{4.12}$$

This equation helps to dimension the transistors. The overall voltage gain of the active reflector $A_v(\omega_0)$ has to be around 9.5 dB according to the system simulations in Section 3.3.1. Both stages can deliver gain, but the first stage has a higher load resistance and thus higher gain can be achieved with a lower current consumption. When the reflector is switched off, the signal has to be attenuated around the loop. The attenuation should be larger than -6 dB, otherwise the off-switching is

too slow. Hence, the difference in loop gain between on and off state has to be at least 15.5 dB.

Transistor simulations revealed that the ratio in the switch resistance R_{switch} between off and on is almost independent of the transistor size. A wider transistor has a smaller on resistance, but also a smaller off resistance. The factor between $R_{switch,off}$ and $R_{switch,on}$ is always in the range of 8.5 ($R_{switch,off}$ is the resistance of the switch, if the reflector is switched off, meaning the switching transistor is on). For a thick-oxide transistor with 16 fingers, each 15 μm wide and 320 nm long the differential on-resistance is 24 Ω, and the off-resistance is 200 Ω. The single ended equivalent resistance R_{switch} changes therefore from 12 to 100 Ω. Hence, the maximum change in the loop gain A_v is 18 dB. For a large change in the loop gain, it is important that the output resistance r_{dsI} of the transistor M_I is large compared to the value of $R_{switch,off}$. At the same time, we would like to have gain in the first stage, thus g_{mI} must be larger than $1/\left(r_{dsI} \parallel R_{switch,on}\right)$. The results of transistor level simulations of the input amplifier gain A_{vi} for different input transistor (M_I) widths w_{MI} and switch transistor widths w_{switch} are plotted in Fig. 4.6. The tail current for this simulation is kept constant at 7 mA. A wider input transistor M_I results in a larger g_{mi} and thus in a larger voltage gain A_{vi}, at the same time the capacitive load C_{gsI} of the previous stage is increased, which reduces the tuning range. A wider switch transistor M_{switch} reduces the switch resistance $R_{switch,on}$, which reduces the voltage gain A_{vi}. But it also reduces the switch resistance when the reflector is switched off ($R_{switch,off}$) and thus a larger gain difference between the off and on state results as depicted in Fig. 4.7. A good compromise between loop gain and and on-off loop gain ratio is to chose an input transistor width w_{MI} of 140 μm and a switch with w_{switch} of 240 μm. This is equal to an on-off loop gain ratio of 17.3 dB and an input amplifier gain A_{vi} of 5.6 dB.

Because the input amplifier achieves 5.6 dB voltage gain, the output stage's voltage gain A_{vo} must be 4 dB. A good starting point for the design of the output amplifier is the calculation of the needed tail current i_{tail}. The tail current can be estimated via the output power requirement P_{out}. The lowest acceptable output power for a maximum range of 30 m is -2 dBm (see Section 3.1.1). A larger detection range would be favorable and a safety margin is needed as well, because the PCB and the connection to the antenna will introduce additional losses. Thus, the goal is set to achieve an output power of P_{out}=6 dBm=4 mW,

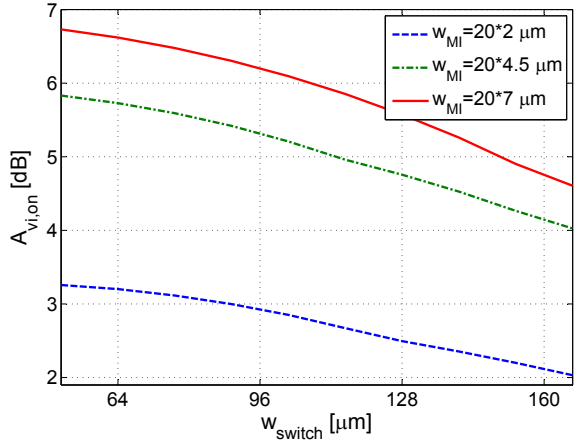

Figure 4.6. Input amplifier gain A_{vi} versus the width of transistor M_{switch} (W_{switch}) and M_I (W_{MI}).

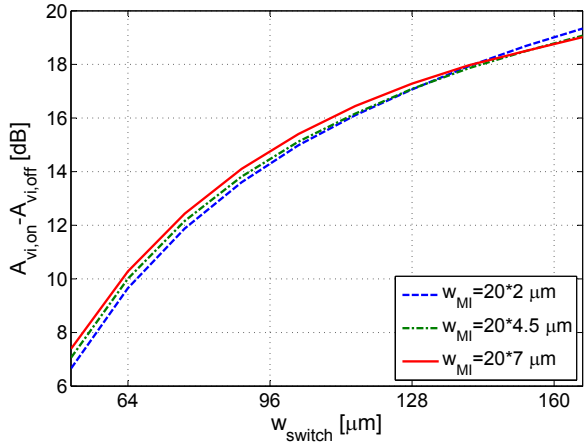

Figure 4.7. Difference between the input amplifier gain A_{vi} between the on- and off-state as a function of the width of the switching transistor ($w_{Mswitch}$).

this is equal to a single ended power $P_{out,se}$ of 2 mW. The single ended voltage swing at the load is

$$V_{pp,se} = \sqrt{P_{out,se} 8 R_{load}} \approx 0.89\ V. \tag{4.13}$$

The output stage is a differential class A amplifier. The ideal efficiency of a single ended class A amplifier is 50 %. The efficiency of a differential amplifier is further reduced due to the voltage drop v_{tail} over the tail current-source by

$$\eta_{diff} = \eta_{single} \frac{v_{dd} - v_{tail}}{v_{dd}}, \tag{4.14}$$

where v_{tail} is the voltage drop over the tail current source. The single ended efficiency η_{single} of an integrated amplifier is further reduced by the low Q-factor of the inductances and parasitic resistances. Published class AB PAs using a similar CMOS technology and similar frequencies have obtained an efficiency η_{single} of 13 % [96], 27.1 % [97] and 32.9% [98]. A good target of η_{single} for a class A amplifier is around 25 %. This results in a differential efficiency η_{diff} of 16.6 %. Thus, the power consumption of the output amplifier is roughly 24 mW. The current through each branch of the output stage is 6.7 mA. This is a good starting point for the calculation of transistor sizes of the output stage. For the size of the differential pair, the same trade-off as for the differential pair in the input stage exists: Too wide transistors reduce the tuning range, because the input stage sees the gate-source capacitance of the output stage C_{gsO} as a shunt capacitance to the varactor C_{var}. Too small transistors reduce the output swing and are difficult to match, because the output resistance r_{dsO} is large. The transistor sizes are optimized by numerical circuit simulations. Another important point is the value of the bias voltage v_{bias} of the differential pair. Figure 4.8 depicts the simulated output power P_{out} depending on the bias voltage v_{bias}. The optimum bias voltage v_{bias} is found to be at 1.2 V. The transistors leave the saturation region for very low bias voltages ($v_{bias} < 0.7$ V) and thus the output power is reduced. For high bias voltages, the common mode voltage v_{tail} increases, which decreases the voltage swing. The simulation with the extracted circuit including the wiring parasitics has a 1 dB lower output power than the schematic simulation (P_{out} is 5 dBm instead of 6 dBm).

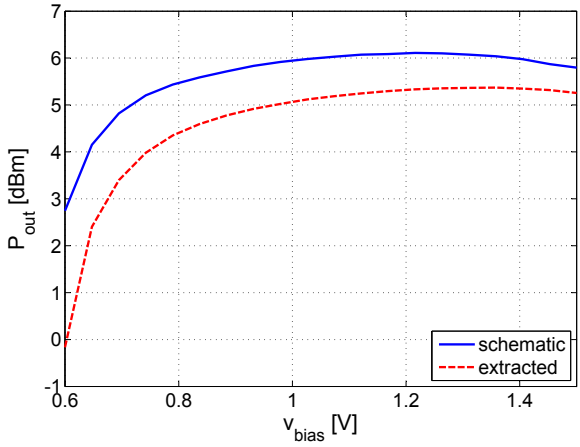

Figure 4.8. Simulated reflector output power vs. the bias voltage v_{bias} for schematic and extracted simulations.

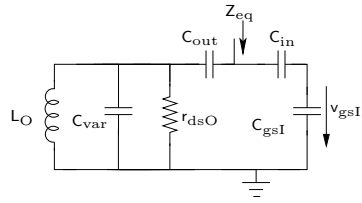

Figure 4.9. Small signal equivalent of the input impedance Z_{eq} without feedback and without bond wire.

4.1.1. Impedance Matching

The matching of the circuit to the antenna has to be considered for the design of the output stage. The matching between the off-switched reflector and the antenna is important for a good start-up sensitivity, because the incoming signal has to be present during the on-switching. A good matching is achieved if S_{11} is below -10 dB. The impedance matching is calculated with the single ended, simplified circuit in Fig. 4.4. The input impedance Z_{in} of the reflector is

$$Z_{in}(\omega) = \frac{Z_{eq}}{1 - A_v} + sL_{bond}. \tag{4.15}$$

where L_{bond} is the inductance of the bond wire. The equivalent input impedance Z_{eq} is the input impedance of the reflector without feedback as illustrated in Fig. 4.9

$$Z_{eq}(v_{tune}) = \left(sC_{eq1} + \frac{1}{\frac{1}{sC_{out}} + \left(\frac{1}{r_{dsO}} + \frac{1}{sL_O} + sC_{var}(v_{tune}) \right)^{-1}} \right)^{-1}. \tag{4.16}$$

C_{var} is the capacitance of the varactor diode. The value of C_{var} is dependent on the tuning voltage v_{tune}. The model and simulation results for the available hyperabrupt (HA) junction varactor diode of the chosen process are listed in the Appendix A.6. The input reflection coefficient S_{11} is calculated by

$$S_{11} = \frac{Z_{in}(Z_{eq}, A_v, L_{bond}) - 50}{Z_{in}(Z_{eq}, A_v, L_{bond}) + 50}. \tag{4.17}$$

The matching is optimal for the case

$$\frac{Z_{eq}\,(f_{refl})}{1 - A_v} = 50\ \Omega - sL_{bond}. \tag{4.18}$$

The inductance of the bond-wire L_{bond} is given by the length of the bond-wire and is approximately 0.8 nH. C_{eq1} is dominated by the gate-source capacitance C_{gsI} of transistor M_I. The main design parameters for optimal matching are C_{out} and r_{dsO}. The calculated $S_{11}\,(v_{tune})$ is drawn in a Smith chart in Fig. 4.10. The Smith chart illustrates that Z_{in} is larger than 50 Ω. The matching could be improved by reducing the output resistance r_{dsO} of the transistor M_O. However, decreasing

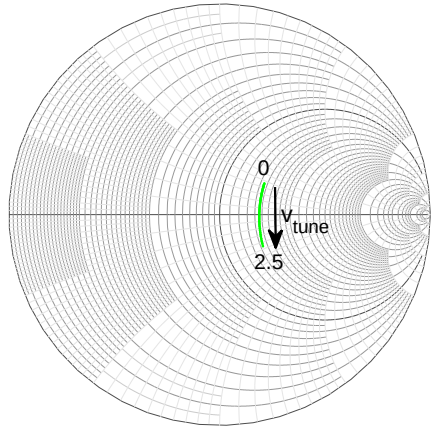

Figure 4.10. Calculated S_{11} vs v_{tune} for the simplified small-signal model.

the output resistance increases the current consumption of the output stage, which decreases the efficiency of the output stage.

The matching behavior is verified by simulating the extracted, final differential implementation of the circuit (Fig. 4.11). The oscillation frequency f_{refl} is tunable from 6.77 to 5.67 GHz. The input matching S_{11} to the 50 Ω antenna follows the oscillation frequency as shown in Fig. 4.11. The output matching is better than -9 dB over the complete tuning range and the output amplifier is capable of directly driving the equivalent load of the antenna. The simulated open loop transfer function can be found in Appendix A.3, the achieved quality factor Q of the feedback circuit, including all parasitics, is 8.1.

4.1.2. On-Off-Switch

The active reflector is based on the 'phase synchronous' start-up behavior described in Chapter 2. A deterministic, constant starting phase is unwanted as the system simulation results in Section 3.3.8 confirmed. The main source for a starting phase, which is synchronous to the modulation signal, is the on-switching process. Thus, the main challenge in the design of the switch is to minimize the influence of the external switch control signal on the start-up phase of the reflector. This Section describes the design of the switch and the modulation signal buffer and analyzes the influence of the starting phase if mismatch exists.

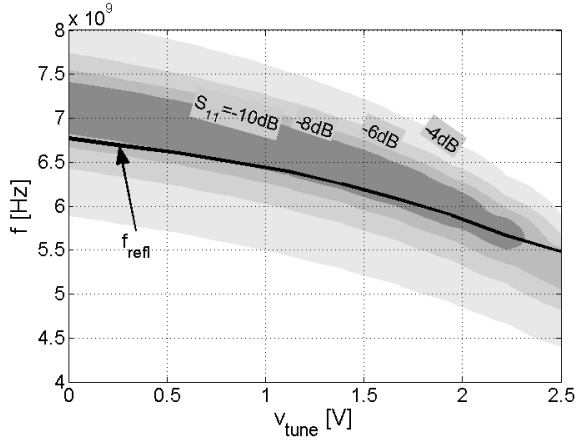

Figure 4.11. Simulated behavior of the input matching S_{11} and the oscillation frequency f_{refl} depending on v_{tune}.

As discussed earlier in this chapter, a fully differential topology is chosen for the reflector, because the on-switching signal distorts the phase coherent start-up less. The schematic of the switch is depicted in Fig. 4.12. The external modulation signal s_{mod} is buffered by an inverter. Its output v_{switch} is connected to a PMOS transistor M_{switch}. When the gate voltage of M_{switch} is on 0 V, then the transistor is on, the differential signal is shorted and the reflector is switched off. When the gate voltage is at 1.8 V, the transistor is off and the reflector is on $(R_{switch,on})$.

The switching signals are depicted in Fig. 4.13. The modulation signal s_{mod} used in the simulation is the measured modulation signal s_{mod} which is generated by the prototype PCB presented in Section 4.2.1. The inverter together with the capacitive load of M_{switch} determines how fast the reflector can be switched on. The slew rate SR is given by

$$SR = \frac{I_{ds,M6}}{C_{Mswitch}}, \tag{4.19}$$

where $C_{Mswitch}$ is the gate source and gate drain capacitance of transistor M_{switch}. The signal v_{switch} influences the signals OutAmp $in+$ and OutAmp $in-$ via two mechanism. One is the path from the modulation signal s_{mod} through R_{svdd} to the supply voltage V_{DD} and then influences the common mode. In the simulation, the supply voltage

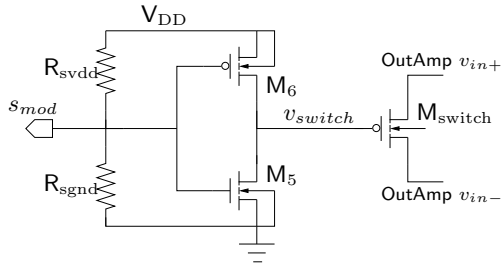

Figure 4.12. Schematic of the switch. The modulation signal s_{mod} is buffered on-chip by an inverter which controls the switching transistor M_{switch}.

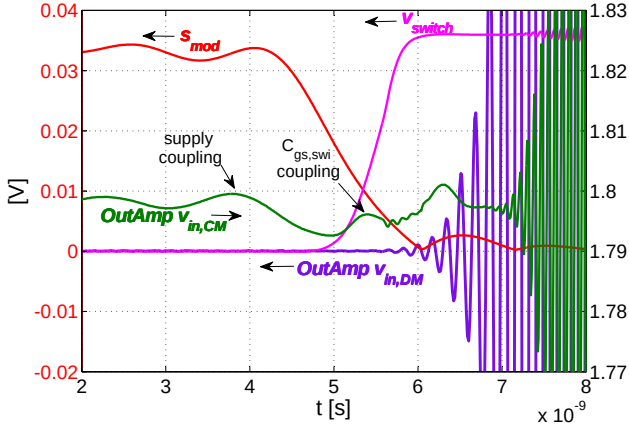

Figure 4.13. Simulation result of the on-switching process, s_{mod} and v_{switch} are scaled by a factor of 1/50 for better visibility. The input signal s_{mod} is taken from measurement and fed into Cadence. v_{switch} is the buffered, inverted signal, OutAmp $v_{in,CM}$ is the common mode signal $((v_{in+}+v_{in-})/2$ and $v_{in,DM}$ is the differential signal. The on-switching influences the common mode voltage OutAmp $v_{in,CM}$, but not the differential signal.

is not ideal, the inductance from the bond wire is also taken into account (L_{bond} = 800 pH). The supply voltage influences the common mode voltage of the two signals OutAmp $in+$ and $in-$. The coupling through the supply voltage is the reason for the common mode variation in Fig. 4.13 for the first 6 ns. The increase in the common mode voltage right after 6 ns is due to capacitive coupling of the v_{switch} signal through the gate source and gate drain capacitance of M_{switch}. The PMOS transistor M_{switch} is fully symmetrical, drain and source are identical and thus the channel charge is also pushed symmetrically to both nodes v_{in-} and v_{in+}. The switching voltage v_{switch} only affects the common mode voltage. The common mode equivalent of the active reflector is drawn in Fig. 4.14. The switching signal is coupled into the loop over $C_{gs,swi}$ (the gate source capacitance of M_{switch}). The transfer function from the switching signal to the input voltage of the output amplifier v_{in} is

$$H_{switch}(s) = \frac{v_{in}}{v_{switch}} \approx \frac{s^2 L_I C_{gs,swi}}{s^2 L_I (C_{gs,swi} + C_{var}) + \frac{sL_I}{r_{dsI}} + 1}, \qquad (4.20)$$

if the gate source capacitance C_{gsO} and R_{bias} are neglected. The transfer function has a high-pass characteristic with a peak at $\omega = 1/\sqrt{L(C_{gs,swi} + C_{var})}$. Higher frequency components are attenuated by a constant factor $C_{gs,swi}/(C_{gs,swi}+C_{var})$. If the input signal v_{switch} is a step-function, the signal is high-pass filtered from v_{switch} to v_{in} and then amplified by the two amplifiers and fed back. The amplifiers have a band-pass characteristic. Therefore, the resulting signal if the input v_{switch} is a step-function is approximately a sinusoidal signal. The common mode voltage could be unstable, but the source degeneration of transistors M_I and M_O by the tail current source M_{tI} and M_{tO} respectively, reduces the loop gain substantially. Hence, the signal is attenuated around the loop.

For a perfectly symmetrical circuit, supply coupling and capacitive coupling are identical and both resulting signals OutAmp $in+$ and $in-$ are the same. Hence, only the common mode is influenced by the on-switching and not the differential signals. The common mode signal is approximately a damped harmonic signal. Unfortunately, the final fabricated circuit will not be perfectly symmetrical due to random factors in production. Due to mismatch, the two signal $in+$ and $in-$ are not equally attenuated and thus a differential signal is generated. In Section 2.3.1, we claimed that the distortion due to on-switching is equal to an additional harmonic signal at the input. The start-up pulse is

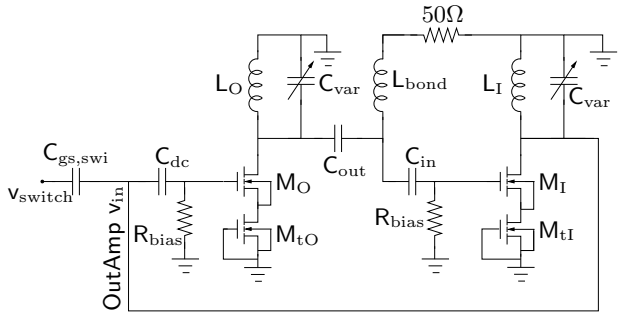

Figure 4.14. Common mode equivalent of the reflector. The transistors M_I and M_O are source degenerated by the tail transistor M_{tI} and M_{tO}, and thus the loop gain is attenuated.

modeled as if an external signal s_{det} is applied during start-up with a constant phase ϕ_{det} and a certain amplitude v_{det}

$$s_{det}(t_0) = v_{det} e^{i(\phi_{det} + \omega_0 (t - t_0))}. \tag{4.21}$$

We cannot prove this claim analytically from first principles, but it can be shown that this is a good approximation. The common mode signal (OutAmp $v_{in,CM}$) is approximately a damped harmonic signal and the difference between two unequally attenuated harmonic signals is a harmonic signal. Circuit simulations support the claim. Figure 4.15 compares the start-up behavior, if a threshold mismatch v_{th} in the input amplifier occurs, with the start-up behavior without mismatch, but with a deterministic input signal s_{det}. Both start-up are identical for an amplitude V_{det} of 20.5 μV and a phase $\phi_{det} = \pi$ is chosen.

Mismatch can influence the start-up of the active reflector and deteriorate the phase synchronization, thus the acceptable mismatch has to be studied. System simulations based on the equivalent deterministic signal in Section 3.3.8 predict that the acceptable ratio of incoming signal to the deteriorating on-switch signal s_{det} is P_{in}/P_{det} >8.3 dB. The input power P_{in} for a distance of 50 m is -68.7 dBm according to (3.43). The goal is to determine the equivalent power P_{det} of the on-switching pulse. The disturbance due to mismatch is acceptable, if P_{det} is smaller than -77 dBm. The following simulations should help to quantify the influence of different mismatch effects on the start-up phase.

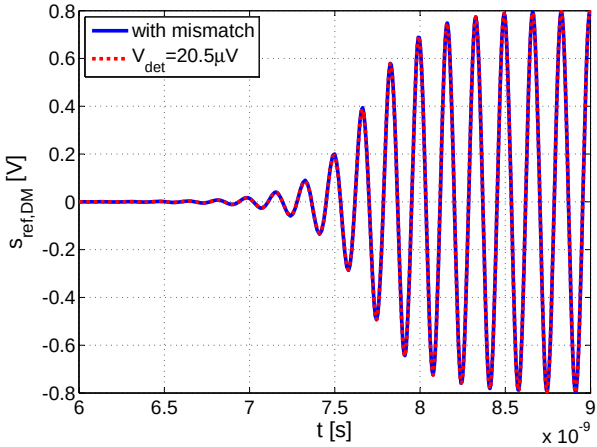

Figure 4.15. The active pulsed reflector is simulated on transistor level. The solid, blue line is the resulting output signal $s_{ref,DM}$, if one of the input transistors has a 35 mV higher threshold voltage v_{th}. The mismatch converts the common mode signal to a differential mode signal, which influences the start-up. The dotted line is the simulation result without mismatch, but with an equivalent deterministic signal $s_{det} = V_{det}e^{i(\phi_{det}+\omega_0(t-t_0))}$. The reflector behaves identically, if a mismatch occurs or if an additional deterministic signal is applied at the input.

Capacitive Mismatch $C_{mismatch}$

The start-up behavior is simulated on a schematic, transistor level in Cadence. The measured on-switching waveform $s_{mod}(t)$ is fed into the simulation as in the previous section. Multiple simulations with different starting phases $\phi_{i,n} = n \cdot \pi/12$ are conducted and the phase differences of the output between consecutive input phases are evaluated ($\Delta\phi_{ref,n} = \phi_{ref,n+1} - \phi_{ref,n}$). If the reflector starts perfectly phase synchronous, then the phase difference of the reflector output ($\Delta\phi_{ref,n} = \phi_{ref,n+1} - \phi_{ref,n}$) between the different input phases is equal to the difference of the respective input phases ($\Delta\phi_{i,n} = \phi_{i,n+1} - \phi_{i,n}$). The upper plot in Fig. 4.16 illustrates the reflector output s_{ref} (differential signal) for different input phases $\phi_{i,n}$. The reflector's phase differences ($\Delta\phi_{ref,n} = \phi_{ref,n+1} - \phi_{ref,n}$) between the different input phases are equally distributed without mismatch. In a real circuit, there are two main sources of mismatch. One is the mismatch between transistors, which will be discussed later, and the other one is mismatch due to asymmetric wiring, asymmetric inductors and capacitances. The mismatch due to asymmetric wiring and capacitors can be introduced into the simulation by adding an additional capacitance $C_{mismatch}$ to node labeled OutAmp $in+$ in Fig. 4.12. The on-switching pulse v_{switch} has now different transfer functions to the differential nodes OutAmp $in+$ and $in-$. The resulting differential signal influences the start-up of the reflector. This is well visible in the lower plot in Fig. 4.16, the phases of the reflector's output waveform are not evenly separated anymore. Figure 4.17 shows the start-up behavior of the reflector for four different input phases with a $C_{mismatch}$ of 300 fF. The reflector starts slower than without mismatch for an input phase ϕ_i of 100° and faster for 280°. This simulation verifies the model used in Section 2.3.1. According to Equation (2.49), the input signal can be calculated by the superposition of the received signal with an equivalent deterministic on-switching signal s_{det}. The amplitude of the resulting input signal is influenced by the on-switching and is minimal, if the input phase ϕ_i is 180° shifted to the on-switching phase ϕ_{det}, because the differential signal, which results from the common mode signal due to mismatch, counteracts the incoming signal. If the input phase ϕ_i is in phase with the on-switching phase ϕ_{det}, the two signals interfere constructively and the reflector starts faster. From the simulations, it can be concluded that the equivalent switching phase ϕ_{det} is approximately 280°.

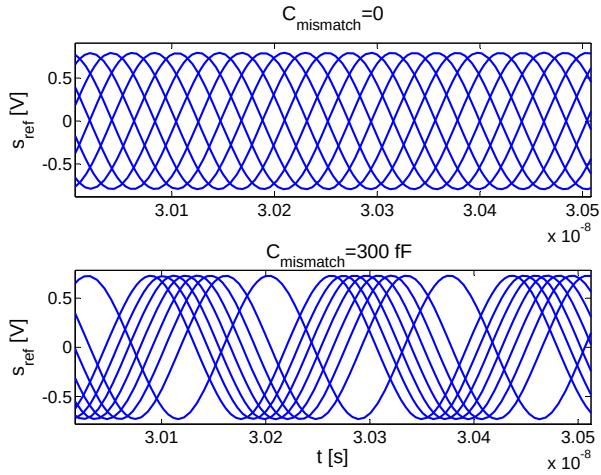

Figure 4.16. Differential reflector output (Cadence simulation) with an input signal of -73 dBm, with and without an added mismatch capacitance of 300 fF. Eight different input phases $\phi_{i,n} = n\pi/4$ are simulated. Without mismatch, the resulting outputs have a phase difference of 45°. This is not true for a large mismatch. In this case, the on-switching signal s_{mod} influences the start-up phase.

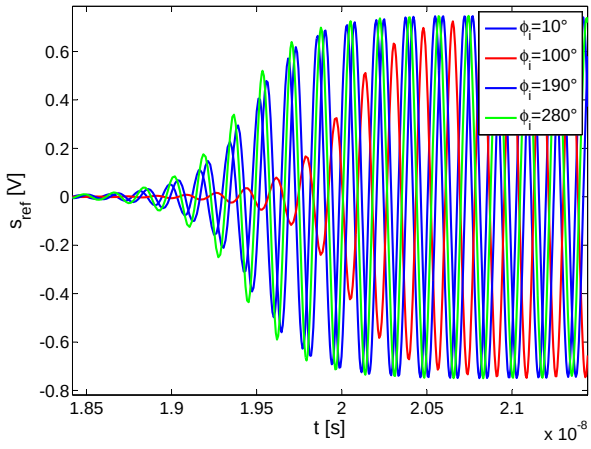

Figure 4.17. Start-up behavior of the reflector with mismatch ($C_{mismatch}$ = 300 fF). The reflector starts the fastest with an input phase $\phi_i = 280°$ and the slowest with $\phi_i = 100°$.

The relative phase errors

$$\Delta\phi_{ref,rel} = \frac{\Delta\phi_{ref,n} - \Delta\phi_{i,n}}{\Delta\phi_{i,n}} = \frac{\phi_{ref,n+1} - \phi_{ref,n} - (\phi_{i,n+1} - \phi_{i,n})}{\phi_{i,n+1} - \phi_{i,n}} \tag{4.22}$$

between consecutive input phases are printed in Fig. 4.18. In the case of an ideal phase synchronous start-up, the value is always zero. If the reflector starts always with the same phase (not sensitive to the incoming signal at all), all values are on -1 ($-\Delta\phi_i/\Delta\phi_i$, except for one large peak ($(2\pi - \Delta\phi_i)/\Delta\phi_i$. The flatter the curve is, the better is the synchronous start-up. A good measure for the flatness of the curve is to use the standard deviation of the relative phase error. With this measure, the equivalent P_{in} to P_{det} ratio can be found. The conversion characteristic is plotted in Fig. 4.19. The two curves for $P_{in}/P_{det} = 8.3$ dB and for $C_{mismatch} = 200$ fF have the same standard deviation and as can be seen match each other pretty well. The curve $P_{in}/P_{det} = 8.3$ dB is the worst, but still acceptable disturbance used in our system simulations.

The simulation results for different $C_{mismatch}$ are listed in Tab. 4.1. The highest acceptable mismatch $C_{mismatch}$ is 200 fF, if the largest

Table 4.1. P_{in}/P_{det} ratio for cadence simulation with different mismatch capacitances $C_{mismatch}$ for P_{in}= -68.7 dBm. A mismatch of up to 200 fF is acceptable.

$C_{mismatch}$	P_{in}/P_{det} [dB]
0 fF	>30
30 fF	>30
50 fF	21.6
100 fF	15.6
150 fF	11.4
200 fF	8.8
250 fF	6.8
300 fF	5.2

distance between base station and reflector is 50 m. In this case P_{det} is -77.5 dBm. For a higher coverage range, less mismatch is tolerable. The capacitance of the varactor C_{var} is 857 fF for a tuning voltage v_{tune} of 1.8 V. Adding a $C_{mismatch}$ of 200 fF equals a varactor mismatch of 23%, meaning that one varactor is 23% larger than the other. The model reference guide [83] does not state the mismatch of the chosen HA varactors, but the MIM capacitor have a mismatch smaller than 0.4%. The model guide predicts an maximum absolute error of 20%, but the relative error between adjacent varactors is much smaller. The mismatch of adjacent varactors in 0.18-μm CMOS is studied by [99]. The found values for MOS varactors and vertical p^+/n-well junction diode varactor (JVAR) are below 0.2% and below 0.3% respectively. This is almost two orders of magnitude below the acceptable mismatch. And simulations showed that even adding a second mismatch capacitance to the output does not increase the influence of the on-switching pulse. In the best case, it even compensates the influence of the first mismatch capacitance partially.

Transistor Mismatch

The identically designed MOS transistors in a differential pair often display variations in device characteristics due to non-uniformity and random factors in processing [100]. Sources for the mismatch can be varying oxide layer thickness t_{ox} or substrate doping concentration as well as geometric properties. The transistors forming a differential pair can be subject to mismatch. This influences the symmetry and

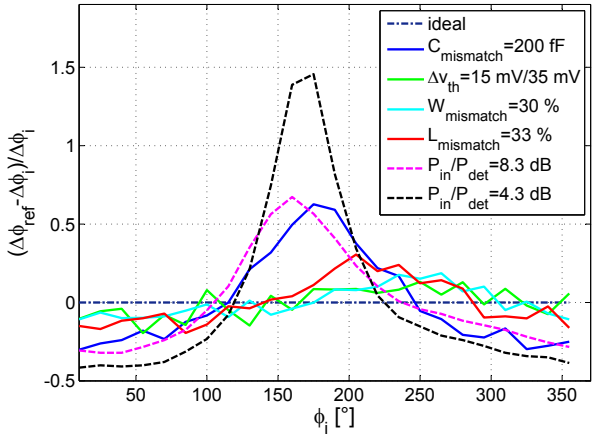

Figure 4.18. Plot of the relative phase error $(\Delta\phi_{ref} - \Delta\phi_i)/\Delta\phi_i$. A flat curve equals perfect phase synchronous start-up. The maximum tolerable synchronization error is $P_{in}/P_{det} = 8.3$ dB.

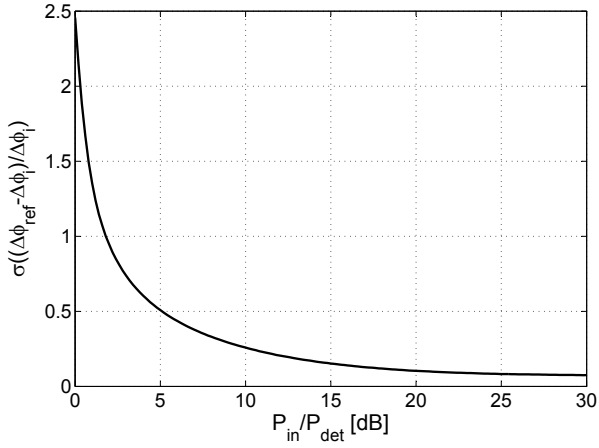

Figure 4.19. The standard deviation of the phase error between different input phases plotted against P_{det} is used for the conversion of the simulated reflector performance to a P_{det} value which can be used in the system simulations.

thus a common mode signal can be transformed to a differential signal. One possibility to reduce mismatch is to maximize transistor area WL and to increase the ratio L/W [101]. This is not an option, because longer transistors reduce the speed and wider transistors increase the capacitive load on the previous stage and hence reduce the tuning range. The mismatch can be reduced by splitting each transistor up into two separate transistors and placing the transistors of a differential pair in a common centroid structure. The influence of geometric mismatch and of a mismatch in the threshold voltage v_{th} is presented in the next two paragraphs.

Geometric Mismatch Both the width W and the length L of the transistors can be affected by mismatch. In reality, both parameters are simultaneously subject to mismatch. In the first simulation campaign, only the width W of the transistor is affected and in the second campaign only the length L is varied. For the simulations, the width W varies up to $\pm 30\%$. The very large mismatch in the width is chosen as a worst case scenario. The largest influence of the mismatch happens, when one transistor of the output stage is 30% larger than the designed value and one transistor of the input stage is 30% smaller than the designed value. Even with such an unrealistic large mismatch, the value $\sigma\left(\left(\Delta\phi_{ref} - \Delta\phi_i\right)/\Delta\phi_i\right)$ is 0.111. The relative phase error is plotted in Fig. 4.18. The curve is almost flat compared to the curve $P_{in}/P_{det} = 8.3$ dB used in system simulations. The equivalent P_{in} to P_{det} ratio is 18.8 dB. This is more than 10 dB above the acceptable limit found by system simulations in Section 3.3.8. In the second simulation campaign, the length L of one transistors of one differential pair is increased by 33%. The largest error occurs if the length of one transistor of the input stage is increased. The $\sigma\left(\left(\Delta\phi_{ref} - \Delta\phi_i\right)/\Delta\phi_i\right)$ is 0.1554, which equals to a P_{in} to P_{det} ratio of 15.2 dB. P_{det} is 9 dB below the acceptable limit despite the unrealistic large mismatch.

Hence, realistic geometric transistor mismatch does not influence the start-up behavior of the transistor noticeably.

V_{th} Mismatch Another source of mismatch is that the two transistors in a differential stage have a slightly different oxide thickness' t_{ox} or a variation in the doping of the material and thus different threshold voltages v_{th}. The maximum threshold voltage difference between two adjacent NMOS transistors is $\Delta v_{th} = 15$ mV according to the design manual [102]. In the available BSIM 3.3 model, the sigma of the

threshold voltage is given by

$$\sigma\left(v_{th}\right) = \frac{k_{vth}}{\sqrt{\left(W - k_{vthw}\right) nf \left(L - k_{vthl}\right)}} v_{th0}. \tag{4.23}$$

k_{vth}, k_{vthw} and k_{vthl} are process specific constants. nf is the number of fingers of the transistor, W is the width and L is the length. v_{th0} is the nominal threshold voltage of the transistor. The resulting $\sigma(v_{th})$ for the input M_I and output transistors M_O are 1.447 mV and 1.196 mV respectively. The mismatch is emulated by the addition of a voltage source to the source of one transistor of the differential pair. This reduces the overdrive voltage $v_{ov} = v_{gs} - v_{th}$ and v_{ds}. Reducing the overdrive voltage is the same as an increased threshold voltage v_{th}. The reduced v_{ds} does not influence the circuit behavior, because the transistors are in saturation. In a first simulation scenario, the two transistors forming a differential pair have a threshold voltage of $v_{th0} + 3\sigma(v_{th})$ and $v_{th0} - 3\sigma(v_{th})$. This transistor mismatch is added to the input and the output amplifier. All possible combinations are simulated. The largest resulting disturbance of the start-up is $\sigma\left(\left(\Delta\phi_{ref} - \Delta\phi_i\right)/\Delta\phi_i\right) = 0.0573$. This is smaller than the disturbances simulated in the system simulations and therefore, the accuracy of the system is not affected by a $3\sigma(v_{th})$ mismatch. Even a worst case mismatch of 15 mV between adjacent transistors and 35 mV between non-adjacent transistors result in a small distortion equal to a P_{in} to P_{det} ratio of 21.8 dB.

From these simulations, it can be concluded that the designed circuit is relatively immune to transistor mismatch and no auto-calibration to prevent mismatch is needed.

4.1.3. Measurement Results of the ASIC

The active pulsed reflector ASIC was integrated in a 0.18-μm CMOS process. The die photomicrograph of the reflector circuit is shown in Fig. 4.20. The die area is 0.85 mm^2. All inputs and outputs are ESD protected except the differential connection to the antenna and the tuning voltage v_{tune} input. The differential outputs are not ESD protected, because ESD protection adds additional capacitive load, which reduces the tuning range. The pad where the tuning voltage v_{tune} is applied is not protected in order to have a larger range of possible tuning voltages.

For the characterization of the ASIC, the ASIC is wire-bonded on a PCB build from a high-frequency laminate. The basic characteristics

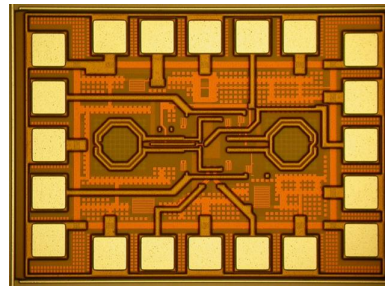

Figure 4.20. Chip micrograph of the implemented active reflector ASIC: chip size 0.85 mm x 1 mm.

for the active reflector ASIC are summarized in Table 4.2. The active reflector has an oscillation rise time below 4 ns and a fall time below 3 ns. This allows the usage of a modulation signal with short pulses with an on-time t_{on} of 13 ns.

The simulated and measured tuning range of the ASIC are in good agreement. The simulation of the circuit with extracted parasitics predicts a tuning range of 1.1 GHz, the measured tuning range is 1.24 GHz. The simulated output power is between 3.5 dBm and 7 dBm, while the measured output power varies from 2.17 dBm to 6.11 dBm depending on the oscillation frequency ω_0. The phase noise at 1 MHz offset is -116 dBc/Hz. The system simulations in Section 3.3.9 predict no measurement error due to this low phase noise performance. The measurement accuracy starts to decrease drastically for a phase noise above -100 dBc/Hz @ 1 MHz offset. The active reflector is not sensitive to close to carrier phase noise, due to the short on-time t_{on} and the synchronization process at every start-up.

4.2. Active Pulsed Reflector Prototype

Two different prototypes are built. The first one focuses on the primary functions: pulsing of the reflector and supplying all needed supply voltages for the ASIC and a balun for the antenna. This prototype is presented in [103] and [104]. The first prototype works well, but the modulation frequency f_{mod} is given by the used quartz and thus cannot be changed without exchanging the quartz. The on-time t_{on} is determined by a feedback delay of a asynchronously reseted flip-flop. The feedback delay can be slightly adjusted by adding capacitance to the

Table 4.2. Simulation results vs. measurement results for the analog tunable reflector ASIC.

Parameter	Specs	Simulated	Measured
V_{DD} [V]	1.8	1.8	1.8
I_{DC} [mA]	<30	26	30
f_{osc} [GHz]	5.8	5.67-6.77	5.45-6.69
tuning range [GHz]	>0.58	1.1	1.24
P_{out} [dBm]	>0	3.5-7	2.17-6.11

feedback. This is a reasonable approach for first measurements, but each prototype has to be adjusted manually and thus is not suitable if many reflectors are needed. Based on the experience with the first prototype, an advanced prototype was developed during a semester thesis [105]. The advanced prototype allows configuring the modulation frequency f_{mod} and includes a battery supply with under voltage lock-out (UVLO) and a commercial available case. The focus in this section lies on this second reflector prototype.

4.2.1. Pulse Generation

The most important function of the PCB is the generation of the modulation signal s_{mod}. The goal is to generate a rectangular modulation signal with a fixed on-time $t_{on} = 13.3$ ns (see Section 2.3) and a programmable modulation frequency f_{mod}. If multiple reflectors are detected at the same time, then every reflector needs a different modulation frequency f_{mod}, but the pulse width t_{on} is the same for every reflector.

In the first prototype, a quartz oscillator generates the modulation frequency f_{mod}. This signal is applied to a flip-flop with asynchronous reset. The delay in the reset path determines the pulse width. The delay can be adjusted by the capacitive load of the feedback path, but it has to be manually adjusted and soldered. With the asynchronously reseted flip-flop it is possible to generate the desired pulse length. However, the modulation frequency f_{mod} is determined by the crystal quartz and thus can only be changed by exchanging this quartz.

The second prototype solves this problem with digital logic. The schematic of the digital logic is drawn in Fig. 4.21. A quartz oscillator

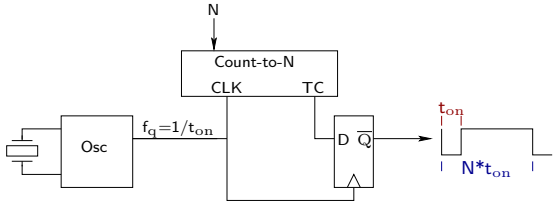

Figure 4.21. Counter solution with a quartz oscillator and a programmable counter, which generates output pulses with length t_{on}.

generates a frequency f_q. This frequency is related to the on-time t_{on} by $f_q = \frac{M}{t_{on}}$. A counter with programmable length N is driven by this clock signal. The output named TC (terminal count) delivers M times in a row a logic 1 every time the counter has counted to N. The other $N-M$ times a logic 0 will result. The output of the counter is buffered and inverted by a D-type flipflop. This improves the jitter performance. The jitter is then determined only by the jitter of the quartz oscillator.

The modulation frequency f_{mod} can be programmed with the counter length N

$$f_{mod} = \frac{f_q}{N} = \frac{1}{t_{on}} \frac{M}{N} \tag{4.24}$$

and the on-time is

$$t_{on} = \frac{M}{f_q}. \tag{4.25}$$

The on-time has to be 13.3 ns, this limits the choice of the oscillator frequency f_q. The lowest possible frequency is 75 MHz and $M = 1$. This frequency is chosen, because it lowers the speed requirements of the counter and flip-flops and reduces the length N of the counter, thus the power consumption is decreased. A higher oscillation frequency f_q allows for a better resolution of the possible frequencies f_{mod}. With $M = 1$, the available frequencies are limited, but it is still possible to have 7 reflectors for a baseband bandwidth of 3.125 MHz. The optimal modulation frequencies f_{mod} for a maximum distance of 50 m can be calculated according to Section 3.4. The best programmable modulation frequencies are listed in Table 4.3. The frequencies are not evenly spaced anymore and the maximum distance is reduced from 50 m to $d_{max} = 45.9$ m. If larger distances occur in adjacent frequency bands, the spectral peaks overlap and the distance is not correctly measured.

Table 4.3. The possible, programmable modulation frequencies (prog. f_{mod}) are limited by f_q/N. The ideal modulation frequencies f_{mod} are calculated according to Section 3.4.

N	f_{mod} [MHz]	prog. f_{mod} [MHz]
46	1.6145	1.6304
40	1.8223	1.8750
36	2.0301	2.0833
32	2.2379	2.3438
29	2.4457	2.5862
27	2.6535	2.7778
25	2.8613	3.0000

If larger distances occur in non-adjacent bands, the distances are still correctly identified.

Such a programmable divider in the needed frequency range is not available as an off-the-shelf component and thus either has to be assembled from flip-flops and logic gates or programmable logic can be used, which has a better reconfigurability. The counter and the control interface for the selection of the channel are implemented in a complex programmable logic device (CPLD). This CPLD can be reprogrammed on the PCB if different modulation frequencies are needed (e.g. if a larger coverage range is needed).

4.2.2. PCB and Case

The reflector prototype is powered by batteries. A switch mode DC/DC converters generates the needed supply voltage for the LEDs and the crystal oscillator. This voltage is further down-converted by two LDOs. These LDOs generate the supply voltage for the digital part and for the reflector ASIC. LDOs are preferred, because they generate a cleaner supply voltage. An under voltage lock-out (UVLO) circuit protects the batteries from discharging too much (especially important if LiPo accumulators are used).

The modulation frequency f_{mod} can be changed with a switch. A series of LEDs indicate which channel is chosen and if the reflector is on. The PCB and the batteries are fitted in a commercial available package. The open case is depicted in Fig. 4.22. The running reflector

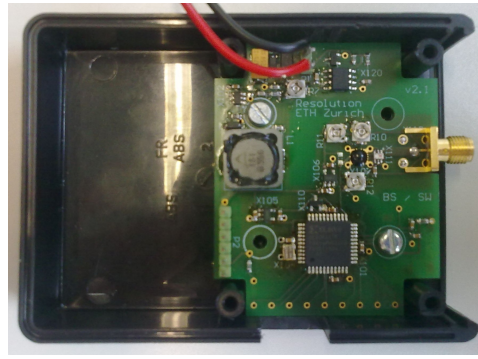

Figure 4.22. Open reflector case without battery pack.

Figure 4.23. Top view of the case with the LEDs indicating the chosen modulation frequency f_{mod}.

with the LEDs and the switches can be seen in Fig. 4.23.

4.3. Base Stations

The APR has been tested using the base station hardware depicted in Fig. 4.24. This hardware was developed by Siemens in the framework of the RESOLUTION project. A pseudo-monostatic front-end is employed in order to achieve a good receiver noise figure of 3.5 dB. RF shielding on the front-end board and sufficient spacing ($\sim$ 0.5 m) of the TX and RX antennas have been provided to avoid receiver saturation by the transmitter. The positioning accuracy of a FMCW radar

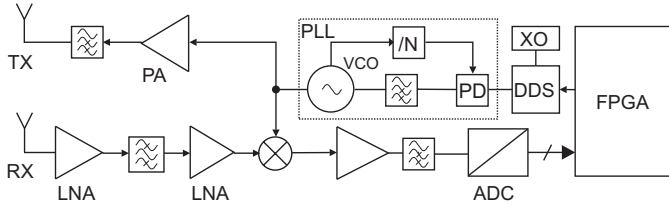

Figure 4.24. Base station architecture with one receive and one transmit path.

depends on the linearity of the frequency ramp. The influence of a sinusoidal nonlinearity was studied in [70]. A sinusoidal non-linearity does not add a variance, but only a distance dependent offset. The influence of a sinusoidal non-linear frequency ramp together with noise is discussed in [106]. A linear frequency ramp can be generated by a fractional-N PLL [107], [108] with a constant reference frequency. The divider ratio is changed over time with a sigma-delta modulator. This is the best choice, if very high sweep bandwidths f_{BW} are needed. The base stations presented here rely on a direct digital synthesizer (DDS), which can only be used for low sweep bandwidths ($f_{BW} \leq 500$ MHz). A 1 GS DDS generates a linear frequency ramp from a reference quartz oscillator (XO). The frequency ramp uses the available 150 MHz bandwidth and the ramp duration T is 0.65 ms. The chosen ramp duration is a compromise between high update rate and achievable positioning range. The frequency ramp is up-converted by a 5.8 GHz PLL, amplified by a power amplifier (PA) and transmitted over the TX antenna.

The reflected signal is received over the RX antenna and is amplified by a LNA and mixed with the transmitted frequency ramp. The down-converted signal is amplified by a variable-gain amplifier. The low-pass filtered IF signal is sampled by a 14-bit analog-digital converter. The raw sampled data is transmitted to a host computer over an Ethernet connection, because different windowing functions and spectral peak detection algorithms can be tested. The Virtex 4 FPGA is in the measurements not used for signal processing, but it has enough computation power for additional filtering and decimation of the signal. The FPGA will be utilized as soon as the optimal discrete Fourier transform (DFT) and spectral peak detection algorithm are found.

4.4. Measurement Results

A DC DC converter generates to 3.3 V for the quartz oscillator. The converter accepts supply voltages between 3.6 V and 9.8 V. The large voltage range leafs a large choice for the batteries. A supply voltage between 3.6 and 9.8 V can be achieved with 3, 4 or even up to 8 NiMH accumulators (∼3.6, 4.8 or 9.6 V) or by taking 1 or 2 LiPo accumulators (∼4.5 or 9 V). The overall power consumption of the active reflector prototype, including the clock, LEDs, voltage regulators, CPLD and the active reflector ASIC is 58.7 mA for a 4.2 V supply. Thus, the power consumption is 250 mW. This equals an operation time of 20 hours with 4 NiMH accumulators, if the reflector is always on. The quartz oscillator alone dissipates 66 mW. The active reflector ASIC draws a supply current of 30 mA from a 1.8 V supply, but because the 1.8 V supply is generated by a linear, low drop-out voltage regulator (LDO) from a 3.3 V voltage, the active reflector ASIC together with the LDO dissipates around 100 mW. The power consumption can be further reduced. If a CPLD and a quartz oscillator with 1.8 V supply is used, only one voltage converter is needed and the voltage drop over the LDO is reduced.

4.4.1. S11 Measurement

The impedance matching to the antenna is important for a high sensitivity. The active reflector ASIC is connected to the antenna via a balun. Thus, the matching to the antenna depends on the ASIC, but also on the balun and the transmission line on the PCB.

Figure 4.25 depicts the S11 measurement of the active reflector prototype including the SMA connector, the transmission line, the balun and the ASIC. The matching is between 5.76 and 5.88 GHz better than -10 dB. The peak matching exceed the simulation results. However, the bandwidth is narrower than the simulation of the ASIC alone predicted. But the simulation neglects the influence of the balun, connector and transmission line.

4.4.2. Sensitivity of the APR to CW Signal

Figure 4.26 depicts the output spectrum of the active pulsed reflector. The influence of an input signal and the resulting phase synchronous start-up is well visible. The reflector behaves as predicted in Section 2.3. Without a synchronizing input signal, only a sinc function is visible.

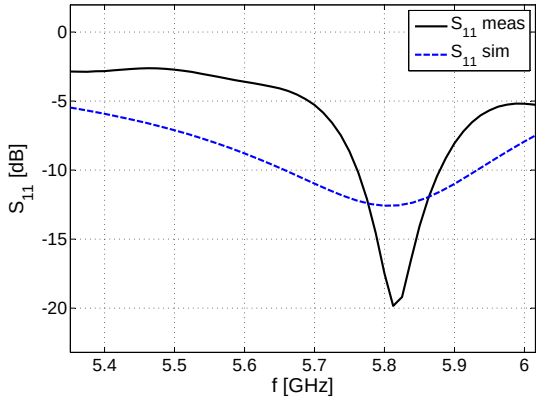

Figure 4.25. Measurement of the input matching of the active reflector prototype.

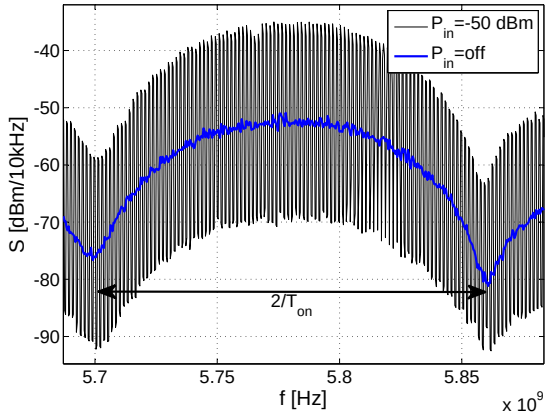

Figure 4.26. Measured spectrum of the active reflector with and without an applied input signal. The oscillator starts due to noise if no input signal is applied.

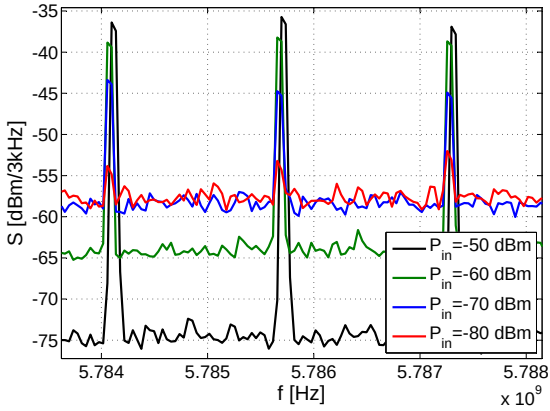

Figure 4.27. Measured spectrum of the active reflector with applied input signal. RBW=3 kHz

The phase synchronous start-up results in peaks separated by f_{mod}. The on-time t_{on} of the reflector can be indirectly measured by the width of the sinc envelope. The envelope is with a width of 159 MHz slightly larger than the wanted 150 MHz. This means that the on-time t_{on} is slightly too short (12.58 ns instead of 13.3 ns). The reason for the shorter on-time t_{on} is that the reflector's start-up time is longer than the time needed to switch the reflector off. This could be improved, either by increasing the off-switching time or by increasing the on-time t_{on} of the generated pulse. The off-switching time can be increased by decreasing the width of transistor M_5 in the inverter controlling the switch transistor M_{switch} in Fig. 4.12. To implement this fine-tuning, a new ASIC would have to be produced. The simpler solution is to reduce the frequency of the quartz oscillator $f_q = 70$ MHz, which increases the on-time t_{on} of the generated pulse. One disadvantage of the lower quartz frequency $f_q = 70$ is that the number of possible modulation frequencies $f_{mod} = f_q/N$ further reduces.

The sensitivity of the active pulsed reflector to CW signals is a good measure for the coherent start-up of the reflector as discussed in Section 2.3. The simulated output spectrum of the APR with an perfect phase synchronous start-up is plotted in Fig. 2.20, with the center frequency at ω_0 and the distance between the peaks is equal to ω_{mod}. When the external signal strength reduces, the SNR decreases

and the starting phase of the oscillator is influenced by the noise. This leads to a noisy output spectrum. When no input signal is applied, the oscillator starts each time with a random phase, the peaks in the spectrum vanish and only a noisy sinc envelope is visible as can be seen in Fig. 4.26. In simulations, the behavior of the peak height in the spectrum was analyzed (Fig. 2.21). The peak height in the spectrum increases linearly with higher input SNR. If the received power of the input signal P_{in} decreases, the SNR decreases as well, because the main noise sources are on chip or on the PCB and are not related to the received power. The measured spectra of the active reflector with different input powers P_{in} are shown in Fig. 4.27. The resulting peak heights, which can be compared to the simulation results, are summarized in Table 4.4.

These measurement results prove that the peak height decreases linearly if the applied CW signal power P_{in} increases. For an input power of -80 dBm, the peak to noise distance is 9 dB. A peak height S_{p-n} of 21 dB is equivalent to a SNR of 0 dB. Thus, the reflector starts phase coherent to an input power of -67.4 dBm. For the operation range of 50 m, the received signal at the reflector is -68.7 dBm, thus the equivalent SNR is -1.3 dB. System simulations in Section 3.3.7 revealed a positioning error of almost 6 cm for a SNR of 0 dB. The accuracy increases for smaller distances, the accuracy $\sigma_{\Delta d}$ is below 3.1 cm for a distance d of 30 m, below 1.7 cm for d =20 m and below 0.74 cm for d =10 m.

The spectrum of a switched oscillator with a constant starting phase is plotted in Fig. 2.23, the deterministic starting phase causes additional peaks in between the modulated peaks. These unwanted peaks are not visible in the measured spectrum, thus the influence of the on-switching pulse could be kept low and has only a minor influence on the positioning accuracy.

4.4.3. Distance Measurement

The positioning system is tested in different multipath environments and with directional and omnidirectional antenna. Figure 4.34 and Fig. 4.31 display the measurement setup in two measurement labs of Siemens Munich with partially metallic walls representing strong multipath scenarios.

Table 4.4. Peak height S_{p-n} of the measured spectrum and the equivalent simulated signal-to-noise ratio (SNR).

P_{in} [dBm]	S_{p-n} [dB]	SNR [dB]
-50	40.4	19.4
-60	29.4	8.4
-65	23.4	2.4
-70	17.9	-3.1
-75	13.4	-7.7
-80	9.0	-12

Outdoor Measurement

By measuring outdoors and with a directional 14 dBi antenna, the number of existing multipaths is kept very low and the excess delays are larger. The TX and RX antennas of the base station are mounted on a tripod and the active reflector, connected to an antenna, is mounted on a movable sledge. In this favorable environment, good positioning accuracy could be achieved. Figure 4.28 depicts the measured distances for a distances between 3.9 and 6.5 m, which is given by the length of the moving sledge. The standard deviation of the measurement error over all measurements (later called overall standard deviation) $\sigma_{all\Delta d}$ is 15 cm and the values are well reproducible. By measuring at the same position 50 times, the average standard deviation $\overline{\sigma_{\Delta d}(d)}$ of all measurements at the same distance d is only 4.37 cm, the highest measured standard deviation $\sigma_{\Delta d}(d)$ is 10.46 cm, the smallest is 1.4 cm.

The influence of the distance on the positioning accuracy is studied with the reflector mounted on a tripod. Six distances between 2.8 and 24.8 m are measured, each 50 times. The measured distance error is shown in Fig. 4.29. The measured local standard deviation $\sigma_{\Delta d}(d)$ is plotted in Fig. 4.30. The local standard deviation $\sigma_{\Delta d}(d)$ is large (0.81 m) for a distance d of 24.8 m. The system is more accurate for smaller distances: The overall standard deviation of the measurement error $\sigma_{all\Delta d}$ is below 22 cm from 2.8 m up to 14 m.

Indoor Measurement

The focus of the positioning system lies on indoor positioning and thus the system has to be measured indoors. The reflector is measured

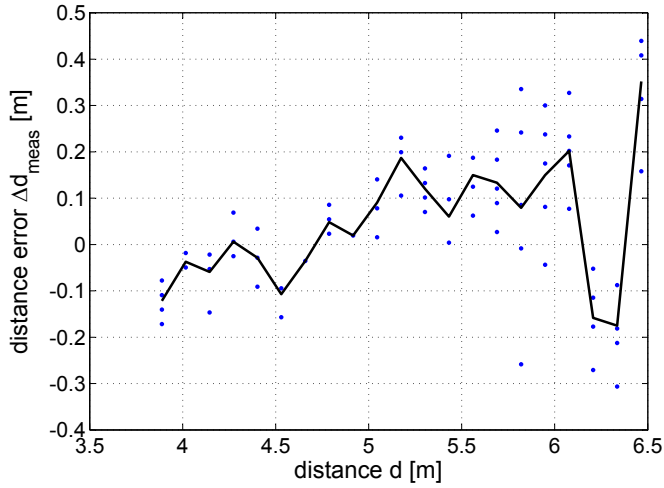

Figure 4.28. Plot of the measured distance error Δd_{meas} for outdoor measurements. Each dot represents one position measurement. The solid line represents the averaged position.

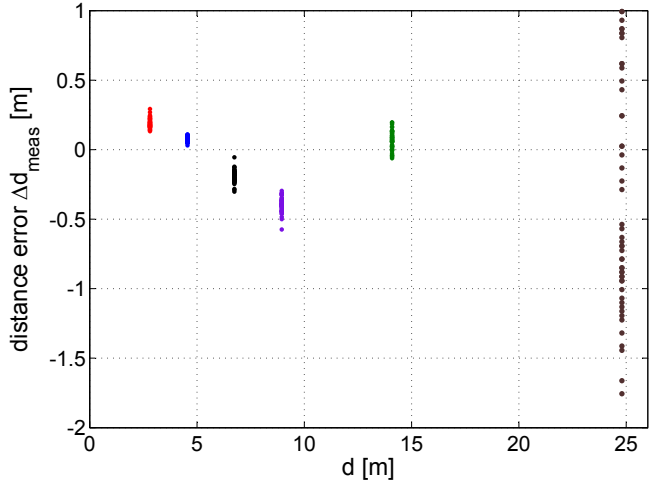

Figure 4.29. Measured distance error Δd for distances between 2.8 and 24.8 m outdoors. Each distance is measured 50 times.

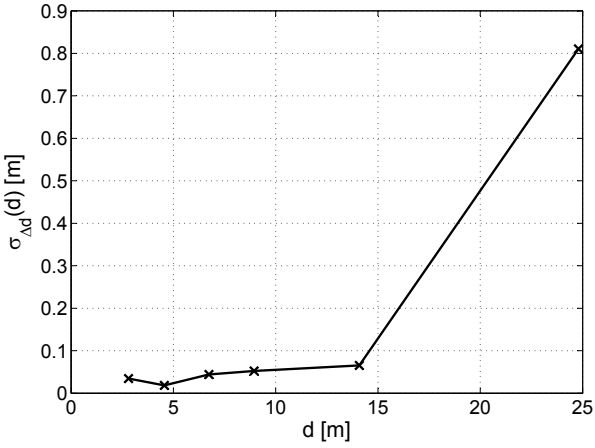

Figure 4.30. Measured local standard deviation $\sigma_{\Delta d}(d)$ (outdoor). The positioning accuracy decreases for increasing distances.

indoors in two different rooms. The first room is a wide room, whereas the second room is a narrow room representing a strong multipath environment.

The measurement setup in the first room is depicted in Fig. 4.31. The active reflector is tested with a directional 14 dBi antenna at 5 different distances between 1.2 and 6.4 m. For each position between 100 and 200 measurements are taken. The distance error $\Delta d = d_{meas} - d_{real}$ is plotted in Fig. 4.32. The overall accuracy $\sigma_{all\Delta d}$ is 18.42 cm and 8.13 cm without the smallest distance (d=1.2 m). The local accuracy $\sigma_{\Delta d}(d)$ is between 0.85 (for d =1.2 m) and 4.36 cm (for d = 6.4 m). For the second measurement campaign an E-shaped patch antenna is chosen. Figure 4.33 depicts the measured distance errors with this E-shaped patch antenna. The local accuracy $\sigma_{\Delta d}(d)$ decreases for the highest distance (d=5.45 m) to 32.4 cm. the overall accuracy is 20.02 cm. The decreased local accuracy for the largest distance could be due to three causes. The most obvious is that the patch antenna has a smaller antenna gain and thus the received signal strength is lower and the reflector starts less phase synchronous. The patch antenna has a lower directivity and thus the reflector receives additional multipath components, which disturbs the start-up. The last cause could be that the last position (the position depicted in Fig. 4.31) is a position where

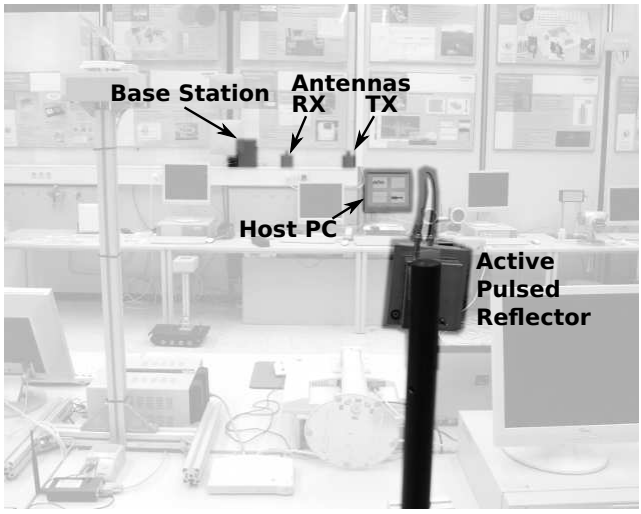

Figure 4.31. Indoor measurement setup in the demonstration lab at Siemens Munich.

LOS and multipath component interfere destructively.

Further measurements are needed to study the influence of the position on the accuracy. A smaller room is selected, because multipath propagation is more severe in small rooms. This second room (visible in Fig. 4.34) has partially metallic walls and contains measurement equipment. The active reflector is mounted on a movable sledge. The first data are recorded with a 14 dBi directional antenna. If only the distance is of interest (e.g. for a movable crane), directional antennas can be applied. For a 14 dBi directional antenna, only the multipath components close to the line-of-sight (LOS) affects the positioning accuracy. For this indoor scenario 260 positions are measured and for each position 10 measurements are carried out. The overall standard deviation $\sigma_{all\Delta d}$ increases to 26.6 cm. Figure 4.35 compares the measured distance error against the real distance. The measurements at most positions are accurate and have a small standard deviation $\sigma_{\Delta d}(d)$, while at a few position $\sigma_{\Delta d}(d)$ is very large (minimum: 0 cm, average: 5.96 cm, maximum: 122.5 cm). This clearly indicates that the measurement error is due to multipath components and not due to the larger distance. The biggest discrepancy occurs at 3.53 m. There, the error is due to a multipath component, which is stronger than the line-

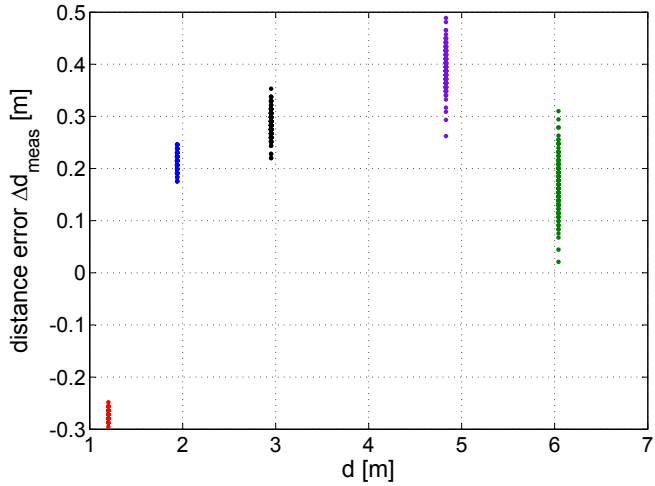

Figure 4.32. Measured distances indoor in the first room with a directional 14 dBi antenna.

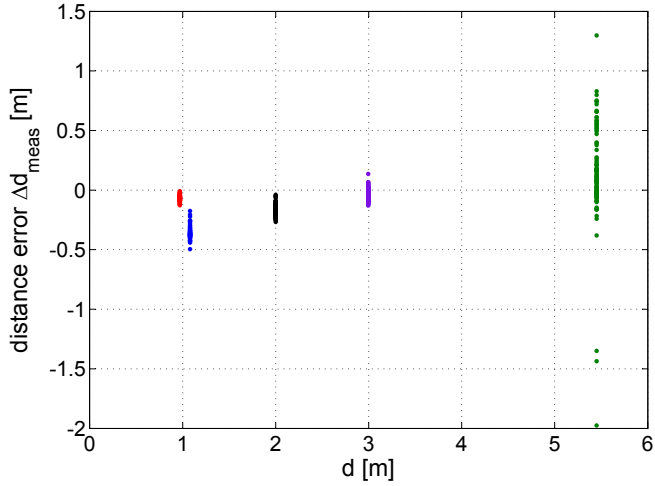

Figure 4.33. Measured distances indoor in the first room with an E-shaped patch antenna.

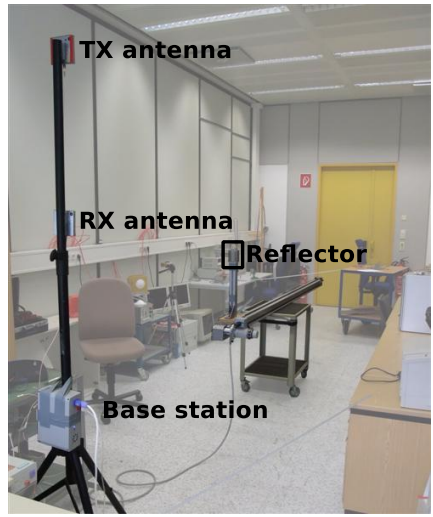

Figure 4.34. Indoor measurement setup in a high multipath environment.

of-sight component. Through the additional delay additional peaks are formed. In Fig. 4.36 the LOS and the NLOS component lead to overlapping peaks in the base-band spectrum. Hence, the detection algorithm is mislead and detects the wrong edge. The overall standard deviation $\sigma_{all\Delta d}$ without the two areas with the worst multipath condition is 9.1 cm.

In a 2D localization system, highly directional antennas cannot be used for the reflector. If the mobile reflector uses a whip antenna with 6 dBi antenna gain, more multipaths components are received and the positioning accuracy decreases. In Fig. 4.37, the spectra of an outdoor measurement, an indoor measurement with directional antenna and with an omni-directional, 6 dBi antenna are depicted. The outdoor measurement shows clearly distinct peaks unaffected by multipath components. For the indoor measurement with directional antenna, the disturbance due to multipath is already visible. In Fig. 4.38, the measured distances with the whip antenna are plotted. The standard deviation $\sigma_{all\Delta d}$ increases from 26.6 cm (14 dBi antenna) to 74.21 cm (6 dBi whip antenna), and the repeatability of the measurement at a single position decreases (minimum: 4 cm, mean: 26 cm, maximum: 139 cm). For a few positions of the reflector, the peaks are almost not visible in the base-band spectrum. This indicates that, at this point,

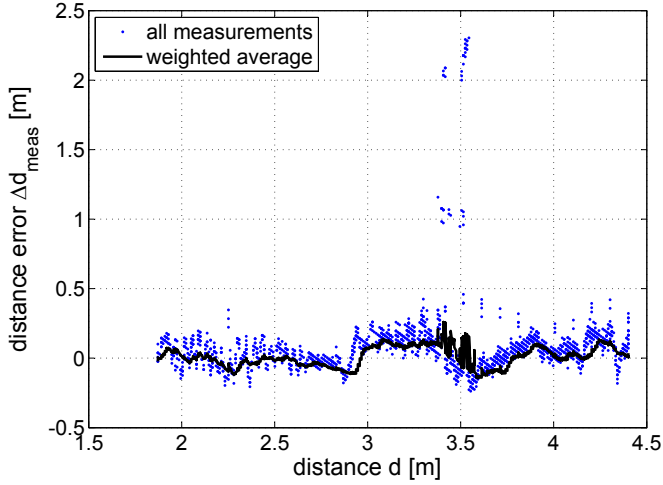

Figure 4.35. Plot of the measured distance error Δd_{meas} for 2600 indoor measurements with a 14 dBi antenna. The standard deviation for consecutive measurements at the same position is only 5.96 cm. The distance error is dominated by multipath propagation. The solid line is the weighted average of the measurement. With the weighted average, the standard deviation over the whole range decreases from 26.6 cm to 7.17 cm.

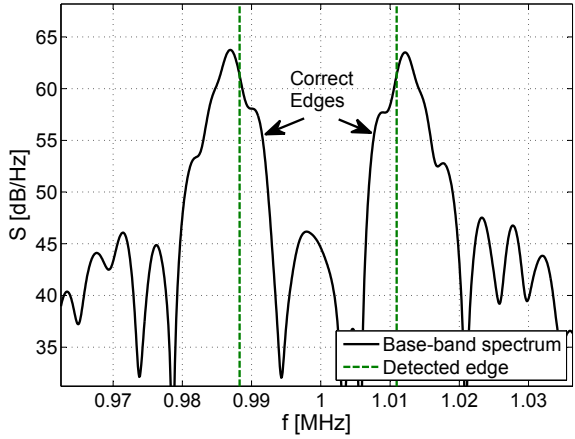

Figure 4.36. Strong multipath propagation leads to strong additional peaks in the spectrum. If the excess delay between the LOS and multipath component is small, the corresponding peaks overlap and the detection mechanism detects the wrong edge.

the line-of-sight component and the first multipath component (MPC) interfere destructively. This problem can be reduced by improving the edge detection algorithm and filtering as described in the following sections.

4.4.4. Edge Detection Algorithm

Two different edge detection algorithm were studied. The first studied detects the peak of the spectrum and then searches the edge, which is -3 dB below this peak. This algorithm works well for outdoor measurements with almost no multipath propagation. However, with strong multipaths, it is possible, that the MPC leads to a higher peak than the line-of-sight component and thus the wrong -3 dB point is detected. The second detection algorithm searches for the steepest edge in the spectrum by searching the peak in the derivative of the spectrum. This method in most cases detects the right edge even for overlapping peaks with a few exceptions (e.g. for the spectrum plotted in Fig. 4.36). The overall standard deviation $\sigma_{all\Delta d}$ as well as the local standard deviation $\sigma_{\Delta d}(d)$ improved with the steepest edge detection as depicted in Fig. 4.39. However, if the peaks are split into two peaks, sometimes

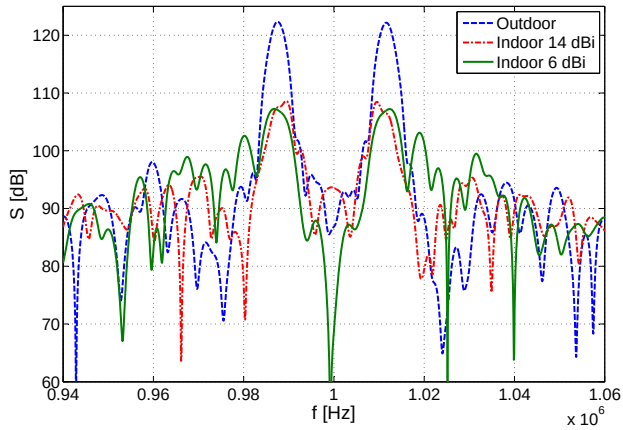

Figure 4.37. Measured spectrum for a distance of 3.83 m for outdoor, indoor with a directional 14 dBi antenna and indoor also with a whip antenna with 6 dBi gain. The measured spectrums agree with the theory. The peaks are well visible and detectable when only a few, weak multipaths exist. In a strong multipath environment, the inner edges of the peak can be better identified than the peaks.

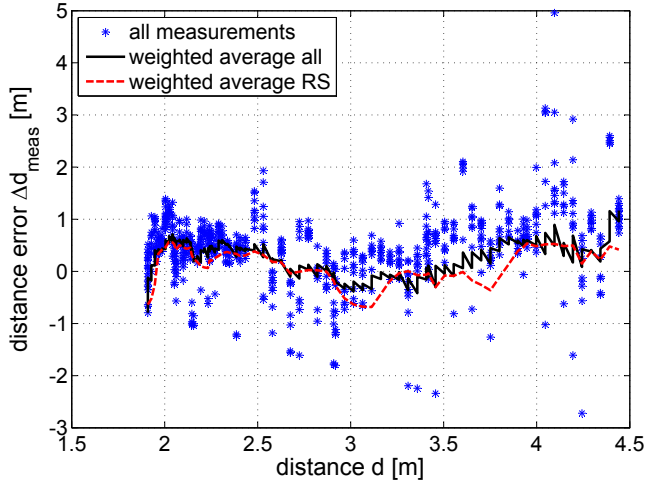

Figure 4.38. Plot of the measured distance error Δd_{meas} for 830 indoor measurements with a 6 dBi whip antenna. The standard deviation of all measurements is 74.21 cm. The solid line represents the weighted average of all measurements and results in a standard deviation of 32.88 cm. The dashed red line was calculated by randomly selecting only one measurement per distance and then calculating the weighted average. The standard deviation in this case is 33.38 cm, which shows that multiple measurements at the same position does not significantly improve the accuracy.

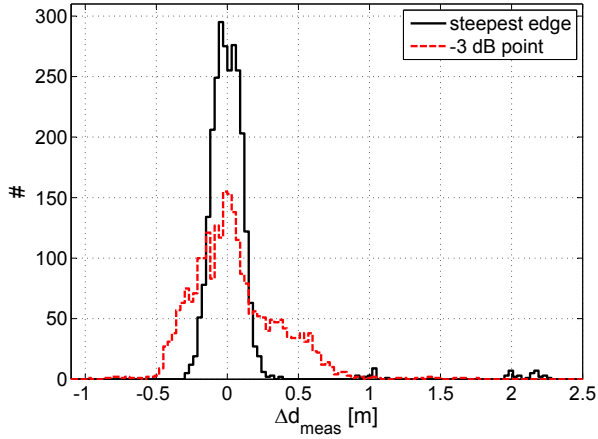

Figure 4.39. Plot of the measurement error distribution for 2600 indoor measurements for a distance between 1.75 and 4.3. The dashed curve is the distribution if the point which is -3 dB below the peak is searched. The solid curve illustrates the measurement error distribution for steepest edge detection algorithm.

the second edge was detected leading to a large, positive measurement error.

The two edge detection algorithm are further studied in Section 5.4.

4.4.5. Distance Measurement Filtering for Moving Targets

In indoor environments with strong multipaths, there are places with severe multipath conditions and this leads to a large measurement error. In a non-static environment, the multipath conditions always change. In such an environment, the overall accuracy can be improved by using a filter. The best solution is to use a Kalman filter, which is fitted to the specific application [109]. In this thesis, only a sliding window averaging is applied for simplicity instead of a Kalman filter. The distance is measured periodically ($k \cdot T_{distmeas},\ k = 0, 1, 2, \dots$). If the target does not move at all, the accuracy improves if more measurements are taken, because errors due to noise are averaged. If the target moves, only the average over the last L measurements is taken. The length L of the sliding window averaging depends on the measurement period $T_{distmeas}$ and the speed of the target. If the distance measurement

has a high repetition rate $1/T_{distmeas}$ and the target moves slowly, a long sliding window average can be used. The position is calculated from the weighted sliding window average $d_{avg}(k)$ and the measured distance $d_{meas}(k)$ by

$$d(k) = p \cdot d_{avg}(k) + (1-p) \cdot d_{meas}(k). \tag{4.26}$$

The variable p determines how much weight the sliding window average has compared to the real measured distance $d_{meas}(k)$. p is chosen small for very fast and irregularly moving object but large for a constant moving object such as a robot.

The measurement results showed that strong multipath conditions can cause large distance errors. The large errors enter the average and reduce the accuracy. One way to prevent this is to weight the data by the variance of the measured data

$$\begin{aligned} \mathrm{var}_d(i) = \mathrm{var}\Bigg(\Big[&d_{meas}(i-2), d_{meas}(i-1), \\ &\ldots, d_{meas}(i+2)\Big]\Bigg). \end{aligned} \tag{4.27}$$

For the weight var_d, the actual measured positions $d_{meas}(k)$ are taken into account and not the filtered results $d(k)$. If the index i of d_{meas} is smaller than 1 or larger than k, the measured position is not available and therefore not taken into account. If one measurement is wrong, it has a large variance var_d and thus is weighted weakly. One drawback is that the points next to the wrong measurements are also weakly weighted.

The sliding window average is weighted by the variance of the data var_d to reduce the influence of the points with strong multipath conditions. The sliding window average of length L is

$$d_{avg}(k) = \left(\sum_{i=k-L}^{k} \frac{d_{meas}(i)}{\mathrm{var}_d(i)}\right) \frac{L+1}{\sum_{j=k-L}^{k} \mathrm{var}_d(j)}. \tag{4.28}$$

with the previously introduced weight var_d.

With this filter, the standard deviation for our indoor measurements with a 14 dBi antenna improved from 26.6 cm to 7.17 cm. For the 6 dBi antenna, the standard deviation improved from 74.21 cm to 32.88 cm. For both cases, each distance was measured several times, which is only the case for a slowly moving target. Realistic is that

each position is only measured once. By randomly selecting one measurement at each position and filtering leads to a standard deviation of 33.38 cm (instead of 32.88 cm). Thus, multiple measurements at the same position do not significantly improve the accuracy. Therefore, it is not necessary to measure the same position several times, which reduces the requirements of the repetition rate $1/T_{distmeas}$.

4.4.6. Comparison between Simulation and Measurement Results

In Fig. 4.37 the base-band spectra for indoor and outdoor measurements are plotted. For the outdoor measurement, the peak heights are around 30 dB. This is equal to the system simulation results with an SNR of 9 to 12 dB (Section 3.3.7). A SNR of 9 dB leads to a positioning error $\sigma_{\Delta d}$ of 1.4 cm. This is comparable to the measured best case standard deviation $\sigma_{\Delta d}(d)$ of 1.4 cm. The local standard deviation increases for larger distances. This is expected, because the received signal power decreases with distances and thus the SNR decreases as well. In addition to the SNR, the positioning accuracy is also influenced by the base station performance, such as frequency ramp-linearity. However, the results of multiple measurements at the same position have a good repeatability and thus the influence of noise in the base station is small.

The positioning accuracy decreases for the strong multipath affected room. This is in accordance to the system simulations with multipaths. The simulations with the UWB channel model (Table 3.11 and Table 3.12) predict a standard error of 25 to 26 cm. In the next chapter, 2D and 3D positioning is studied and multipath simulations in an empty cuboid and a small museum are presented. The simulations with the reflector in an empty cuboid (Section 5.4) has a smaller standard deviation of 17.2 cm and the museum simulations (Section 5.9.1) predict a $\sigma_{all\Delta d}$ of 39.6 cm. In these simulations, the start-up of the reflector is correctly modeled, but the phase noise and the SNR are neglected, because previous simulations revealed that multipath propagation affects the accuracy the most.

The measurement results for an indoor environment with a 14 dBi antenna showed a standard deviation of 26.6 cm, which is almost identical to the simulation with the UWB channel model. The simulation does not take the phase noise of both the reflector and the base station into account and also does not model non-linearity of the frequency ramp generation and thus it is expected that the simulation results are

more optimistic than the measurement results. However, the influence of multipath propagation is reduced because of the directional antenna. These two phenomenas seem to cancel each other out. The measurement results with omni-directional antennas are worse than simulated in the museum environment. An explanation for this is that the measurement lab is smaller than the simulated museum environment and a large part of the walls and doors consist of metal and thus the multipath reflections are stronger. However, the filtered simulated results in the museum environment and the filtered measured results with omni-directional antenna have almost the same accuracy ($\sigma_{all\Delta d} = 39.6$ cm for the museum and $\sigma_{all\Delta d} = 33.4$ cm in the measurement).

For 2D localization, at least three base stations are needed. Unfortunately, only one base station was available and thus no 3D positioning could be measured. The more base stations are deployed, the better is the positioning accuracy. A higher space diversity is better than averaging multiple measurements from the same base station, because the multipath components at one point do not change significantly between subsequent measurements, but they are different for different base stations. Because of the not available base stations, the positioning accuracy of a complete system has to be simulated. In the next chapter, a small museum environment is simulated in Section 5.9 and the positioning accuracy of a tracked visitor is evaluated. The positioning accuracy $\sigma_{x,y}$ is below 20 cm in horizontal direction, even though the distance accuracy $\sigma_{all\Delta d}$ is 39.6 cm.

However, there is still room for improvement. For example, the positioning system could be further improved by including a multi-antenna receiver. Then the angle-of-arrival can be measured in addition to the distance. The addition of angle-of-arrival measurements for the tag solution (Section 1.5.2) improved the accuracy $\sigma_{all\Delta d}$ from 2.31 m to 0.42 m [110].

For non-static environments, the positioning accuracy can be further improved by applying Kalman filtering [109] instead of a sliding window weighted average. The active pulsed reflector generates a phase coherent output signal to the interrogating signal and thus inverse synthetic aperture secondary radar technique could in principle also be applied [111], [112], if the relative movement of the reflector is measured by an additional inertia sensor.

4.5. Comparison with State-of-the-Art

The comparison of the achieved detection accuracy with the state-of-the art is difficult, because most papers present measurement results in an idealized environment and only with directional antennas. Most vendors of commercially available systems only publish best case accuracy (outdoor and LOS). But there exist a few paper that present comparable measurements.

Roehr et al. [113] present a RToF based radar system. A base station transmits a linear frequency ramp (center frequency 5.8 GHz and 150 MHz bandwidth, sweep duration is 1 ms) which is very similar to our base stations frequency ramp. The mobile station receives the delayed frequency ramp and mixes this signal with an internally generated frequency ramp. The time difference between the received frequency ramp and the generated ramp is calculated and the internal frequency ramp is synchronized to the received ramp. In a next step, the mobile station transmits the synchronized ramp back to the base station. The base station then calculates the time difference between the ramp it has transmitted and the delayed ramp from the mobile station. The hardware of the base station and the mobile station are identical. Both have a complete receive and transmit path, digital signal processing and ramp generation with DDS and PLL. The achieved accuracy $\sigma_{all\Delta d}$ in an office environment with 14 dBi antennas is 1.5 cm, but the accuracy decreases in an industrial environment to 8 cm after filtering (multipath mitigation algorithm). This is as accurate as our measurements indoor in a strong multipath environment with sliding window averaging ($\sigma_{all\Delta d}$ =7.17 cm). They achieve the same accuracy, but with a larger and more complex reflector.

An UWB system based on an FMCW radar was presented in [114]. This UWB system uses the same principle as Roehr et al. [113], except that the output signal is chopped in order to make it UWB compliant. The radiated power is lower, because it has to be UWB compliant, but the sweep bandwidth f_{BW} can be increased to 1 GHz. The system was tested with cables (accuracy $\sigma_{\Delta d}(d) = 1.7$ cm) and at one fixed distance $d = 1.56$ m (accuracy $\sigma_{\Delta d}(d) = 2$ cm).

The local position measurement (LPM) system [115] uses the same concept as the tag localization described in Section 1.5.2. A mobile transponder and a reference node transmit a chirp signal, which are received at all base stations. The position is then calculated by TDoA. The presented positioning accuracy σ_{xy} is better than 10 cm, but only

Table 4.5. Comparison of different reflector types based on FMCW radar.

	[114]	[113]	[115]	this work
f_0 [GHz]	7.5	5.8	5.8	5.8
Bandwidth [MHz]	1000	150	150	150
t_{meas} [ms]	37	>2	1	<1
$\sigma_{\Delta d}$ at one position	2 cm	<1 cm	NA	1.4 cm
$\sigma_{all\Delta d}$ for industrial LOS	NA	<8 cm	<10 cm[1]	26/7.2[2] cm
complexity[3]	high	high	medium	low
multiple reflectors[4]	Yes	Yes	No	Yes

outdoor and LOS. No information is given about the accuracy of a single distance measurement.

In the framework of the RESOLUTION project the tag localization concept (Section 1.5.2) was implemented [116], [67]. The tag consists of a fractional N-PLL [117], which generates the frequency ramp. The system was tested under strong multipath conditions with additional heavy metallic reflectors. The accuracy $\sigma_{all\Delta d}$ is 2.31 m if only one receive channel is used and improves to 0.42 m with beam-forming (4 channels) in the digital domain.

Table 4.5 compares the state-of-the art with our work. The simple and elegant active reflector approach delivers comparable measurement accuracies as the more complex reflectors. Our active reflector is the smallest and the only integrated reflector solution.

4.6. Conclusion

In this chapter, the developed hardware and measurement results have been presented. The main focus lies on the circuit design of the active reflector ASIC, which is integrated in a 0.18-μm CMOS technology. One of the biggest challenges is the on-switching of the reflector without influencing the phase synchronous start-up. This could be achieved by shortening a differential signal with a transistor. A fully functional

[1] Only outdoor measurements for positioning available (σ_{xy}).
[2] With sliding window averaging.
[3] Hardware complexity of the mobile station.
[4] Possibility to measure multiple reflectors simultaneously during one measurement.

prototype including power supply, interface and the ASIC was build, demonstrating the possible small form factor.

The presented localization system was tested indoors and outdoors with directional and more important with omnidirectional antennas. The measurements proved that the APR even works under harsh multipath conditions with an omnidirectional antenna ($\sigma_{\Delta d} = 32.88$ cm). The system offers a compact reflector with a positioning accuracy good enough for many applications, such as interactive guiding.

Unfortunately, only one base station was available and thus the 2D or 3D positioning could not be tested. The achievable accuracy can be estimated by multipath simulations which are presented in the next chapter.

5

3D Positioning

5.1. Introduction

The active pulsed positioning system is designed for indoor applications. In indoor environments, the signals are reflected by furnitures, equipment, walls, floor and ceiling. Thus, many multipaths exist which influence the positioning accuracy. The influence of multipath propagation on distance measurements is described in Section 3.5 and could be seen in the measurements presented in Section 4.4.3. However, it is not clear yet, how well the positioning system works in a multipath environment. In the case of 3D or 2D positioning, each base station measures the RToF to the reflector. The propagation channel, which each base station sees, depends on the position of the base station and the reflector. It is possible that the different propagation channels are correlated to each other. For example one base station is strongly affected by strong multipaths while the others, measuring from a different angle, are only slightly affected by multipath propagation. Or two base stations close to each other may be disturbed by similar multipaths. The UWB channel model, which was used in Section 3.5, generates channel impulse responses solely based on a stochastic model of the

environment. The real dimensions of a room are not taken into account and thus the individual channel realizations are not correlated. Stochastic channel models are excellent to simulate the influence of multipath propagation, if only one base station exists. However, the missing room information reduces the applicability for positioning.

The 3D simulation should answer which placement of the base station is advantageous. In addition, the simulation data can be used to evaluate different positioning algorithms, such as least-squares, linear or mass-spring model. For 3D positioning with round-trip time-of-flight measurements, at least 3 base stations are needed. In many situations, the reflector is detected by more than 3 base stations. With the simulation results, the improvement in the positioning accuracy due to spatial diversity can be discussed. Finally, a possible application scenario, a walk through a simple museum, is simulated as a proof of concept.

5.2. Channel Model

As stated in the introduction, wide-band channel models are not useful, because the individual channel realizations are assumed to be uncorrelated. In a 2D or 3D positioning system, it is possible, that two base station see a very similar channel with similar multipaths. In order to investigate the influence of spatial diversity on the positioning accuracy, the exact multipath components have to be calculated.

The multipath components can be calculated by ray-tracing. For example, ray-tracing is successfully applied for the simulation of radio propagation in urban canyons [118], [119] or for the simulation of a MIMO wireless communication system inside an aircraft [120]. There even exist a few commercial software suites that solve the ray-tracing problem in indoor environments for WLAN. These softwares predict the field strength inside a building and help to place the optimal number of WLAN base stations in a building. But there is no specialized solution for indoor positioning and the export of the impulse response from a commercial ray-tracer to Matlab is inconvenient. Nevertheless, in Section 5.9 commercial ray-tracing software is used to calculate the impulse response for a non-empty room.

For the testing of peak detection and positioning algorithms and in order to investigate to optimal placement of the base stations, it is advantageous if many multipath simulations are conducted. Thus, a new channel model had to be developed, which is simple enough for the simulation of many base stations and reflectors. The channel model

assumes a 10 m wide, 10 m long and 3 m high room. For each base station and reflector configuration, the multipaths are calculated by the geometric solution of the connection of two points over a mirror. Multipaths with reflections by 2 or more walls are neglected, because of simplicity. Multipaths which are reflected by more than one wall are weaker than if only one reflection occurs, because reflection factor of walls is generally below 1. The reflection factor for brick walls was measured by [121] and [89]. The measured values for brick walls are between 0.1 and 0.7, but in most cases are around 0.3. Therefore, a value of 0.3 is used in this channel model. The measured values for limestone and brick walls are not strongly dependent on the incident angle, and thus the angular dependency is neglected in this channel model. Scattering occurs when an electromagnetic wave is incident on a non-uniform surface which has dimensions that are small relative to the incident wavelength λ [122]. The Rayleigh criterion states that a surface can be considered electromagnetically flat if the maximum height difference h of the surface satisfies

$$h < \frac{\lambda}{8 \cos \Theta_i} \tag{5.1}$$

with the angle of incidence Θ_i (zero degrees for a normal incidence). For a normal incidence at 5.8 GHz, h is 6.5 mm. For non-normal incident angles Θ_i, the maximum height difference h is even larger. Therefore, a brick, concrete or plastered wall can be considered flat and scattering can be neglected.

Figure 5.1 illustrates the impulse response for 17 realizations of the implemented channel model. The first multipath component (MPC) has a magnitude of roughly 0.3 times the magnitude of the LOS component and the average delay is 2.8 ns. The simulated room is empty and only a few multipaths were simulated.

A comparison between the channel impulse response of the simple multipath model emulating an empty room and the impulse responses of the stochastic indoor channel model from Molisch [123] is shown in Fig. 5.2. For each channel model 10 realizations are plotted. The office LOS scenario emulates an office environment with many small rooms, but also larger rooms like cubicle areas, laboratories and corridors. Each of the offices contains furniture, bookshelves etc.. The Industrial LOS model is characterized by large enclosure filled with a large number of metallic reflectors. Office LOS scenario has many multipath components, while the industrial LOS scenario has only a

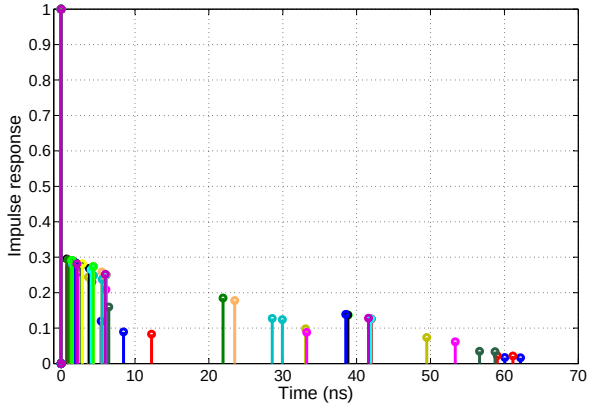

Figure 5.1. Impulse response of our channel model for 17 different positions.

few, but strong multipath components with a larger delay spread. The simple channel model has the shortest mean delay $\tau_m = 0.98$ ns and the shortest RMS delay $\tau_{RMS} = 4.0$ ns.

5.3. Simulation Setup

The multipath simulations were conducted with 200 random reflector positions and 17 fixed base stations. The positions of the 17 simulated base stations are shown in Fig. 5.3. A base station is placed at each corner, in the center of the roof and all 4 walls and also in the middle of the edges between walls. These locations are all well suited for the placement of base stations in real world scenarios. Only a few base stations (>3) are needed to localize a reflector. The reason to simulate 17 base stations is to find the best subset. This will help to find the best positions for the base stations. The simulations should clarify, which is the best place for the base stations. Is it in the corner of the room or in the middle of the walls or a combination of both.

5.4. Simulated Distance Errors

This section compares the simulated distance results with the simple channel model to the results from Section 3.5 with the more complex

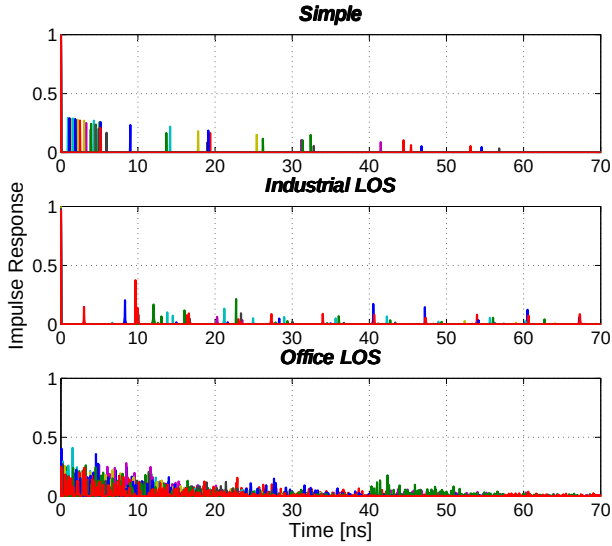

Figure 5.2. Comparison of the impulse responses from our simple model, the Industrial LOS and the Office LOS model from Molisch [123].

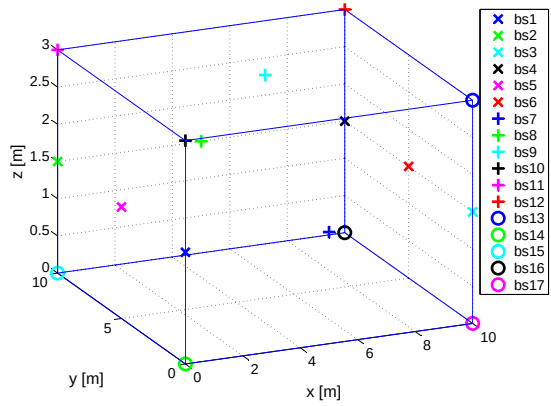

Figure 5.3. Position of the 17 simulated, fixed base stations.

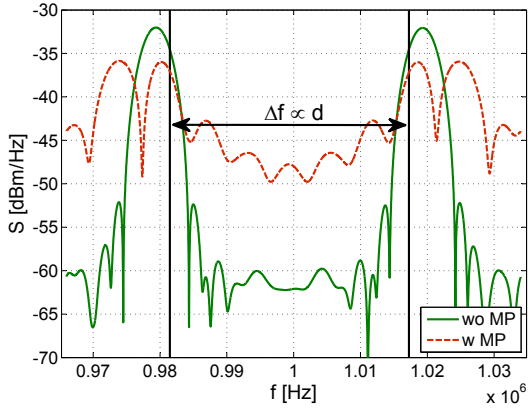

Figure 5.4. Base-band spectrum without and with multipath propagation. The frequency difference between the peaks is proportional to the distance d from the base station to the reflector.

UWB channel model [123]. 200 reflector positions and 17 base station positions were simulated, resulting in 3400 different channel impulse responses. Multipath propagation heavily influences the final base-band spectrum. The spectra with and without multipath propagation are compared in Fig. 5.4. Multipath propagation reduces the peak heights and peaks can be split up into several peaks.

Two different edge detection algorithms are applied to the simulation results: steepest edge and the detection of the 3 dB point. The steepest edge algorithm searches for the maximum in the derivative of the spectrum, while the 3 dB algorithm searches for the innermost points which are 3 dB below the peaks. The histograms of both detection algorithms are plotted in Fig. 5.6. If the spectrum shows strong peaks, the performance of both algorithms is similar. The detection of the steepest edge gives very good results for most cases, except if the peaks are split up into several peaks, as can be seen in Fig. 5.5. In these cases, the detection of the 3 dB point is more accurate. The standard deviation of all 200 reflectors and 17 base stations is 18.46 cm for the detection of the 3 dB point and 21.17 cm for the detection of the steepest edge. Excluding the worst case scenarios, the detection of the steepest edge shows a smaller standard deviation. The results can be improved by combining both detection algorithms. If the edge detection results in a much larger distance (here +0.5 m), the value of the

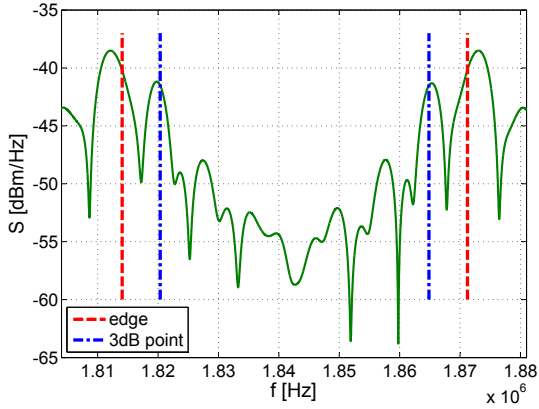

Figure 5.5. Simulated baseband spectrum of the active reflector with the simple multipath model. Severe multipath propagation change the form of the peaks and the peaks are split. The 3 dB detection method detects the correct edge, while the edge detection method detects a multipath component.

3 dB point is chosen. This procedure reduces the standard deviation to 17.19 cm. Figure 5.7 depicts the histogram of the combined algorithm.

Figure 5.8 compares the positioning accuracy of the non-stochastic model with the accuracy of the simulations with the UWB model presented in Section 3.5. The simulations with the complex UWB channel model take more multipath components into account and thus, the simulated standard deviation is with 25 cm larger than with the simple model (17.19 cm). Nevertheless, the simple channel model is valuable, because peak splitting occurs as in free space measurements. In addition, it can help to identify critical reflector positions.

The 200 reflector positions with 17 different base station positions were simulated, leading to a total of 3400 detected distances. If a correlation between the position of the reflector and the distance error can be found, then the different measured distances could be weighted and it could help to identify the optimal positions for the base stations.

One assumption is that the distance error is larger when the reflector is close to a wall, because the path difference between the LOS and the first MPC is small. This assumption can be rejected. As our simulation show, the correlation between the distance error and distance to the closest wall is only 0.01. Thus, there is no correla-

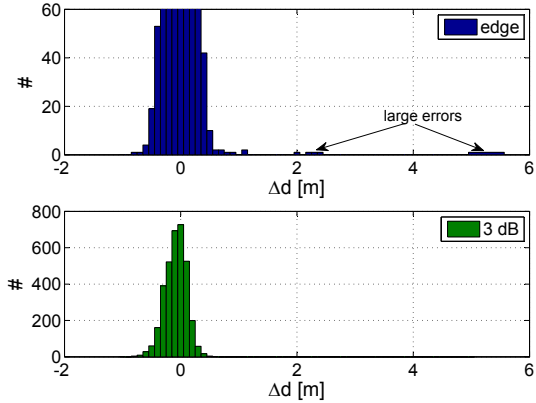

Figure 5.6. Comparison of the two edge detection methods. Detecting the 3 dB point is overall more robust, but the steepest edge detection is more accurate if the correct edge is detected.

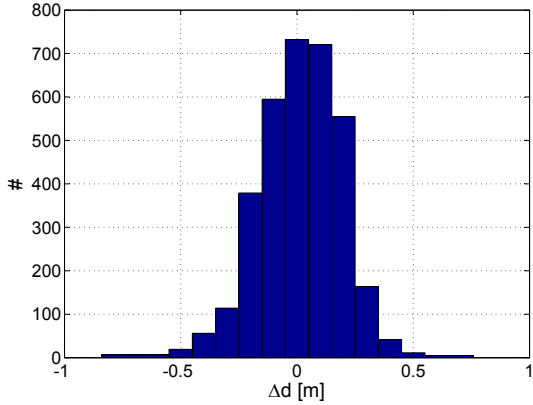

Figure 5.7. Histogram of the combined algorithm of 3 dB point and steepest edge.

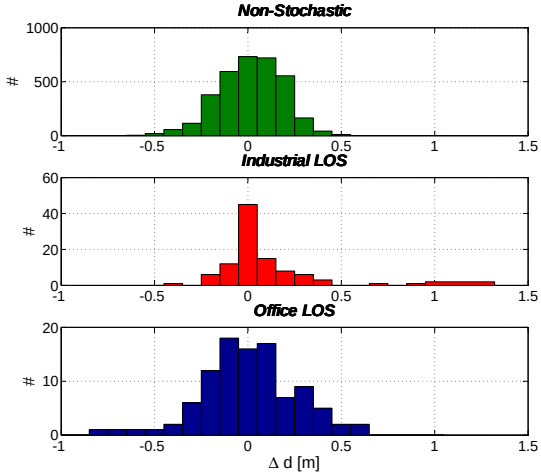

Figure 5.8. Comparison of the non-stochastic model with the results from the IEEE 802.15.4a channel model.

tion. The next hypothesis is that the distance error is correlated to the path difference of the LOS signal and the first multipath component ($\Delta d_{LOS,MP} = d_{LOS} - d_{MP}$), because the additional fading due to the path difference is small. But the distance error is not significantly correlated to the distance difference between the direct LOS and the shortest multipath $\Delta d_{LOS,MP} = d_{LOS} - d_{MP}$. The correlation factor is -0.0898.

However, the detection error is correlated to the damping factor α_{LOS} of the LOS component with a correlation factor of -0.2013. Without multipath propagation, the detected distance error is directly proportional to the damping factor in dB as shown in Section 3.3.3. A damping of 10 dB results in an detection error of 3.6 cm. The difference in signal strength between a distance of 1 m and 14 m is 22 dB, thus resulting in an error of almost 7 cm.

Another effect that could have a large influence on the positioning accuracy is destructive and constructive interference in the presence of multipath propagation. In this paragraph, the possible severity of destructive interference with only one multipath is discussed. In the simplest case of only one multipath component as illustrated in Fig. 5.9, the received signal can be strongly damped over the complete bandwidth. In the worst case, the LOS component and the MPC interfere

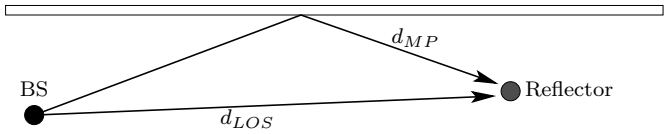

Figure 5.9. Reflector and base station with LOS and one MPC.

destructively at the center frequency f_0 of the reflector, which is ideally equal to the center frequency f_B of the linear frequency ramp. The distance difference between the LOS and the multipath component has to be a multiple of half the wavelength

$$\Delta d_{LOS,MP} = d_{MPC} - d_{LOS} = (k + 0.5)\,\frac{c}{f_B}. \tag{5.2}$$

The shortest $\Delta d_{LOS,MP}$ occurs for $k = 0$. Assuming a distance of 10 m and a complete reflection ($\Gamma_r = 1$), the channel damping can be calculated with the Friis transmission equation.

$$\alpha_{LOS} = 20\log\left(\frac{\lambda}{4\pi d_{LOS}}\right) = -67.7103 \text{ dB} \tag{5.3}$$

$$\alpha_{MPC} = 20\log\left(\frac{\lambda}{4\pi d_{MPC}}\right) = -67.7328 \text{ dB} \tag{5.4}$$

If the wall on which the MPC is reflected has a high reflection factor Γ_r, the signal power from the LOS component and the MPC are almost equally strong. The MPC travels for a longer time, leading to a larger phase at the reflector. The additional phase can be written as

$$\phi_{MPC}(f) = \frac{\lambda_0}{2}\frac{f}{c}2\pi = \frac{f}{f_B}\pi \tag{5.5}$$

The resulting phase change and attenuation due to the superposition of the LOS component and the MPC can be written as

$$H_{channel}(f) = 1 + \left(\frac{d_{LOS}}{d_{MPC}}\right)^2 e^{i\phi_{MPC}} \tag{5.6}$$

In the case of a path difference of $\lambda_B/2$, destructive interference occurs. This worst case attenuation of the channel due to one single multipath is illustrated in Fig. 5.10. The best case has a multipath component, which is λ_B longer than LOS, which leads to constructive interference

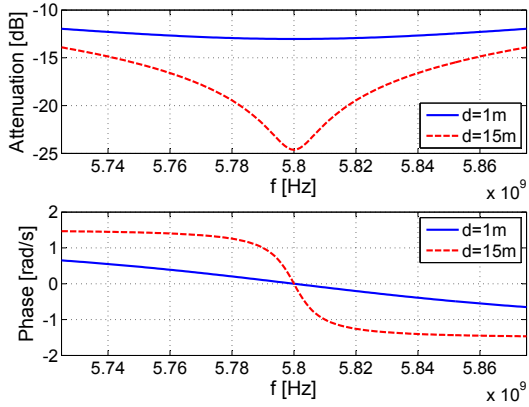

Figure 5.10. Attenuation due to one multipath, which is $\lambda_B/2$ longer than the LOS component.

leading to a channel gain of almost 3 dB. For a distance of 1 m, the mean channel gain difference due to one MPC is 16 dB and for 15 m even up to 20.7 dB. In the worst case, the reflector moves by $\lambda_B/2$ and moves from a zone with constructive interference to a zone with destructive interference. The received signal's power level changes by 20.7 dB which adds an error of 7 cm.

In the simulated 3D case up to 5 MPC occur, because only single reflections are taken into account and all base stations are mounted on a wall. Constructive and destructive interference leads to a channel gain and attenuation. This attenuation depending on the frequency is

$$\alpha_{MP}(f) = 1 + \sum_{k=1}^{5} \left(\frac{d_{LOS}}{d_{MPC,k}} \right)^2 e^{2\pi i (d_{MPC,k} - d_{LOS}) \frac{f}{c}} \tag{5.7}$$

The simulation results show a correlation between the channel attenuation $\alpha_{MP}(f)$ at the center frequency $f_0 = 5.8$ GHz and the detected distance error. The correlation factor is 0.5946. Thus, the influence of the multipaths is larger than the influence due to free space damping. Figure 5.11 illustrates the correlation between the distance error Δd and the damping factor $10 \log(\alpha_{MP}(f))$. The highest correlation occurs at the center frequency f_0. The further away from the center frequency, the lower is the correlation.

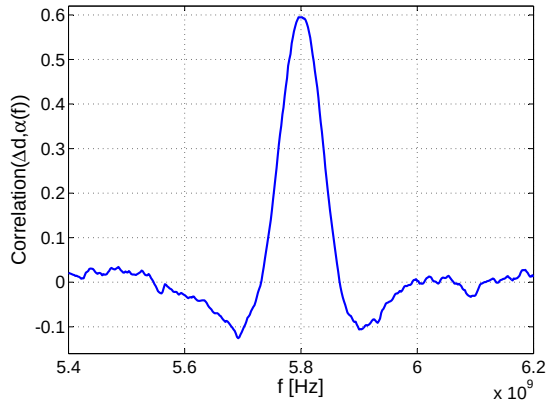

Figure 5.11. Correlation between the channel damping due to multipath propagation $\alpha_{MP}(f)$ (in dB) and the distance error Δd versus f.

The error distance error Δd is not correlated to the distance to the wall, only the standard deviation of the distance errors of one reflector $\sigma_{\Delta d_{refn}}$ measured from several base stations is. Figure 5.12 illustrates the 60 reflector positions with the highest standard deviations. All of these reflectors are less than 2 m away from the closest wall. The standard deviation of the distance error ($\sigma_{\Delta d}$) of each reflector is correlated to the distance to the wall by a correlation factor of -0.3759. This means that the closer a reflector is to a wall, the less reliable are the measurements. This knowledge can be helpful for the design of positioning algorithms and filters. For example positions close to walls could have a lower weight in a filter as positions close to the center of the room. The measurements are even less reliable, if the sum of the distances to the next two closest walls is small (correlation=-0.4687). This means that positions close to an edge of the room have a higher $\sigma_{\Delta d}$.

The position of the base stations has a smaller influence on the detection error than the position of the reflector. By comparing all 200 simulations from one base station, the standard deviation changes only from 15.28 cm for the best base station to 19.9 cm. Also the correlation between the base stations is small. The highest correlation between two base stations is 0.16. The two base stations are on the same edge, one is in 1.5 m height, the other one is on the ceiling 3 m above ground. They are close to each other and thus see similar MPCs. That the base

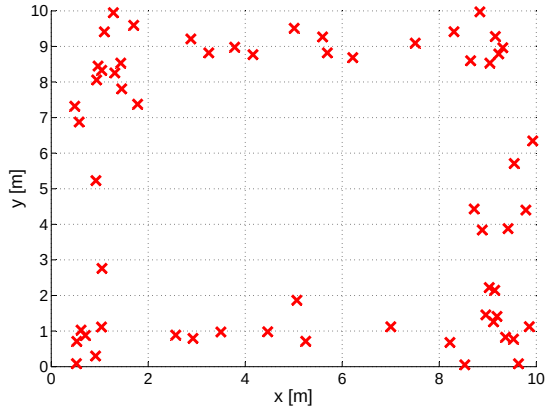

Figure 5.12. Plot of the 60 reflector positions with the highest standard deviation of the distance error ($\sigma(\Delta d)$).

stations are only weakly correlated is an advantage, because each additional base station holds additional information and thus improves the positioning accuracy. From the simulated distances, it is not possible to decide which base station positions are the best and which ones are inferior. For this, the 3D position has to be calculated for different base station subsets. Therefore, different positioning algorithms are introduced and compared in the next section.

5.5. Positioning algorithms

It is assumed that all the positions of the base stations $\vec{x}_{BS,i}$ are known a priori, and each base station i measures the distance to the reflector as ρ_i. By knowing the distance to a base station, the possible reflector positions lie on a sphere with the base station at the center. The intersection of the spheres of all base stations gives the correct position of the reflector. This triangulation approach only works, if all the distance measurements are correct. Otherwise, the spheres do not intersect at a specific point. Thus the approach with the intersection of spheres is not an optimal solution in an environment with multipath propagation.

5.5.1. Least-Squares

The simplest solution to estimate the position of the reflector $\vec{x}_{ref,det}$, based on the measurement data, is by using an unweighted minimum least-squares algorithm. The least-squares algorithm minimizes the sum of the quadratic error between the measured distances ρ_i and the distances between the base stations i and a possible unknown reflector position $\vec{x}_{ref}$. The least-squares problem can be written as:

$$\vec{x}_{ref,det} = \arg\min_{\vec{x}_{ref}} \sum_i \left(||\vec{x}_{ref} - \vec{x}_{BS,i}|| - \rho_i\right)^2 . \tag{5.8}$$

where $\vec{x}_{ref}$ are all possible positions of the reflector. This optimization problem can be solved numerically with the aid of Matlab's optimization toolbox. The interior trust region approach [124], [125] is selected to solve the problem, because this approach is orders of magnitude faster than the brute force grid search approach.

5.5.2. Linear Minimization

The least-squares algorithm is not optimal, if all measurements ρ_i with the exception of one are correct. Then, the wrong measurement influences the position strongly, because least-squares tries to balance the errors. The linear minimization can reduce this problem. Linear minimization is almost identical to least-squares, but optimizes the 1 norm of all measured distances versus the calculated distances at the point $\vec{x}_{ref}$.

$$\vec{x}_{ref,det} = \arg\min_{\vec{x}_{ref}} \sum_i \left|\left(||\vec{x}_{ref} - \vec{x}_{BS,i}|| - \rho_i\right)\right| . \tag{5.9}$$

One single distance measurement error has a smaller weight on the sum (not squared), and thus influences the detected position less. It could be that often only one distance measurement is wrong in a multipath environment. Hence, we also test linear minimization.

5.5.3. Mass-Spring Model

A popular algorithm used to solve the localization problem in sensor networks is the mass-spring model. It was originally presented by [126] for modeling the drape of clothes and improved by [127]. A cloth object is approximated by a deformable surface composed of masses and springs, the movement of which is evaluated using the numerical integration of the fundamental law of dynamics.

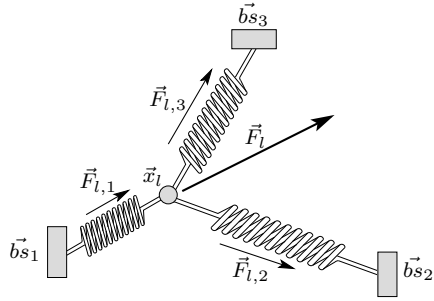

Figure 5.13. Illustration of the mass-spring model for one mobile reflector $\vec{x}$ and three base stations $\vec{bs}_1$, $\vec{bs}_2$ and $\vec{bs}_3$.

A wireless sensor network can also be viewed as a mesh. The sensors measure the distances to the closest neighbors, which is similar to the connection of two points with a thread with known length. If all measurements are corrected then only one solution exists. If one or more measurement exists, then either more than one or no solution exists. By introducing elasticity to the threads, the point is found where the resulting force from all threads is zero, which is equivalent to the solution of the least-squares problem. Thus, the mass-spring model for cloth can be applied for sensor networks [128]. But in contrast to clothes only the final state is of interest in sensor networks. Therefore, a simplified algorithm can be used [129]. The situation with fixed base stations and one movable reflector, as it is the case in our positioning system, is a very simple sensor network. Thus, the mass-spring algorithm can be applied.

Figure 5.13 illustrates the mass-spring model for three base stations and one reflector. The algorithm starts by assuming a position of the reflector $\vec{x}_1$. Usually the middle of the room is chosen, but this depends on the application. In a next step, the distances between the initial position $\vec{x}_1$ (or more generally $\vec{x}_l$ for the lth iteration) and the base stations $\vec{bs}_i$ are calculated by

$$\vec{d}_{l,i} = \vec{bs}_i - \vec{x}_l, \tag{5.10}$$

which can be split up in a direction vector

$$\vec{d}_{l,i,dir} = \frac{\vec{d}_{l,i}}{||\vec{d}_{l,i}||} \tag{5.11}$$

and a length

$$d_{l,i} = ||\vec{d}_{l,i}||. \tag{5.12}$$

A virtual spring is inserted between each base station and the reflector. Each spring i exerts a force $\vec{F}_{l,i}$ on the reflector depending on the difference between the measured distance ρ_i and the estimated distance $d_{l,i}$ between the ith base station and the estimated position $\vec{x}_l$

$$\vec{F}_{l,i} = k\,(d_{l,i} - \rho_i)\,\vec{d}_{l,i,dir} \tag{5.13}$$

where k is the linear spring constant. The total force exerted on the reflector is

$$\vec{F}_l = \sum_i \vec{F}_{l,i}. \tag{5.14}$$

The complete mass-spring model calculates the complete dynamics of the system. The mobile station has a certain mass m and a viscous damping factor C_{vis}. The total force $F_{tot,l}$ in iteration l is the sum of the spring forces and the damping

$$\vec{F}_{tot,l} = \vec{F}_l - C_{vis}\vec{v}_l \tag{5.15}$$

This force $\vec{F}_{tot,l}$ accelerates the mobile station to a new speed $\vec{v}_{l+1}$

$$\vec{v}_{l+1} = \vec{v}_l + \frac{\vec{F}_{tot,l}}{m}\Delta t \tag{5.16}$$

where Δt is the incremental time step. The new estimated position $\vec{x}_{l+1}$ is now calculated by

$$\vec{x}_{l+1} = \vec{x}_l + \vec{v}_l\Delta t \tag{5.17}$$

The algorithm continues with the calculation of the distances $\vec{d}_{l+1,i}$ based on the new estimated position $\vec{x}_{l+1}$. The algorithm stops, when the resulting force F_l is below a certain limit or the estimated position does not change anymore. The parameters m, C_{vis}, k and Δt can be freely chosen. The system can be overdamped, critical damped, under damped or even unstable. The optimal parameter set has to be found by testing different scenarios.

Because we are only interested in the final position, a more efficient way is to minimize the force vector $\vec{F}_l$. The springs drag the mobile station in one direction. We assume that the mobile station moves in the direction of $\vec{F}_l$ with a proportional factor k_2 [s^2/kg]

$$\vec{x}_{l+1} = \vec{x}_l + k_2\vec{F}_l, \tag{5.18}$$

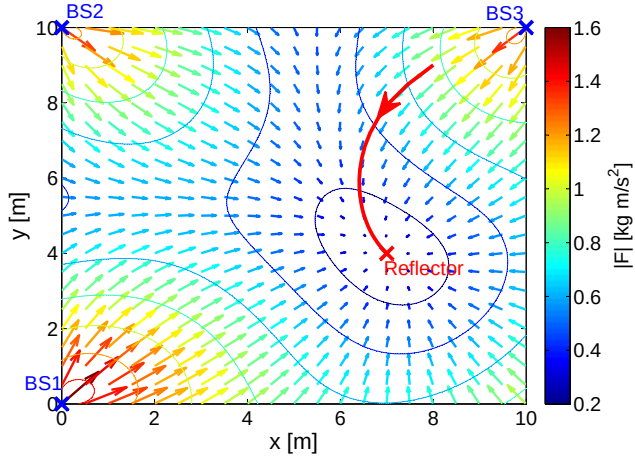

Figure 5.14. The resulting force vector ($\vec{F}$) field for 3 base stations at $\vec{x}_{bs1} = [x, y] = [0, 0]$, $\vec{x}_{bs2} = [0, 10]$ and $\vec{x}_{bs3} = [10, 10]$. The actual position of the reflector is at $\vec{x}_{reflector} = [7, 4]$. The red path illustrates the solution of the mass-spring algorithm for a starting point $\vec{x}_1 = [8, 9]$.

The speed $\vec{v}_l$ and the damping are neglected. Hence, fewer calculation steps are needed for each iteration. The number of parameters is reduced to one ($k_{tot} = k \cdot k_2$). The larger k_{tot} is, the faster the algorithm converges, but if chosen too large, the algorithm gets unstable. We experimentally verified that the algorithm is stable for $k_{tot} \leq 0.3$. A smaller value $k_{tot} = 0.1$ ensures a stable algorithm. The advantages of the mass-spring model are the simple implementation and the fast convergence.

This algorithm is a form of gradient descent, thus it cannot be assured that the found minimum is the global minimum. A typical plot of the strength of the force $\vec{F}_l$ for a 2D localization problem with 3 base stations (at $\vec{x}_{bs1} = [x, y] = [0, 0]$, $\vec{x}_{bs2} = [0, 10]$ and $\vec{x}_{bs3} = [10, 10]$) is depicted in Fig. 5.14. In this case, only one minimum exists. The red line illustrates the solution of the mass-spring algorithm with a starting point at $\vec{x}_1 = [8, 9]$.

In this paragraph, it will be verified that the mass-spring model is a simple method to solve the least-squares problem. The mass-spring optimization minimizes the resulting force on the reflector. By minimizing the force, the algorithm also minimizes the potential energy.

The potential energy of one spring i during the lth iteration can be written as

$$E_{pot,l,i} = -\int \vec{F_{l,i}} \mathrm{d}\vec{x} = \frac{1}{2} k \left(d_{l,i} - \rho_i\right)^2 \tag{5.19}$$

The total potential energy in iteration l is

$$E_{pot,l} = \sum_i E_{pot,l,i} = \frac{1}{2} k \sum_i \left(d_{l,i} - \rho_i\right)^2 . \tag{5.20}$$

In each iteration, the force vector $\vec{F_l}$ decreases, which results in a lower potential energy. Thus, the minimization of the potential energy solves the least-squares problem (5.8). The advantages of the mass-spring model are the fast convergence and its simplicity. The mass-spring algorithm can be implemented on an FPGA. The disadvantage is that the algorithm can converge to a local minimum or not at all.

An interesting question is, how the mass-spring model behaves if the distance measurements are erroneous. Each base station measures the distance to the reflector ρ_i. This measurement has a certain error due to multipath, channel fading and phase noise. The measured distance is modeled as $\rho_i = d_i + \Delta d$. Δd is assumed to be a uncorrelated Gaussian random variable with a mean value and a standard deviation. The simulation results in Section 5.4 showed that the error due to multipath is only very weakly correlated to the position of the reflector. The further apart the base stations are, the lower is the correlation between the simulated results. For the following simulations, the error is assumed to be uncorrelated.

Table 5.1 summarizes the results for a 10x10 m^2 2D room. If the measured distances have standard deviation of 0.5 m and no mean error, then the error of the detected position $\Delta\vec{x} = \vec{x}_{ref,opt} - \vec{x}_{reflector}$ has a smaller standard deviation than each single measurement. However, the variance of $\Delta\vec{x}$ is larger than in the case of two independent Gaussian measurements for the same variable

$$\frac{1}{\sigma^2_{\vec{x}}} < \frac{1}{\sigma^2_{d1}} + \frac{1}{\sigma^2_{d2}}. \tag{5.21}$$

This is the theoretical lowest limit. It occurs, if two base stations measure a reflector, which lies on the direct connection of these two base stations.

The accuracy improves for a higher number of base stations. An interesting observation is that a mean error (mean(Δd)) of -0.5 m results in a smaller positioning error ($\sigma_{\Delta\vec{x}}$ and mean($\Delta\vec{x}$)) then a positive

Table 5.1. Error in a 10x10m 2D positioning scenario due to erroneous distance measurements modeled as $\rho = d + \Delta d$. Δd is assumed to be a uncorrelated Gaussian random variable with a mean value and a standard deviation. The positioning problem is solved with the mass-spring model.

mean(Δd) [m]		0		0.5		-0.5	
$\sigma_{\Delta d}$ [m]		0	0.5	0	0.5	0	0.5
3 BS sym	$\overline{\|\|\Delta\vec{x}\|\|}$	0.08	8.54	55.05	52.00	41.56	42.44
	$\sigma_{\|\|\Delta\vec{x}\|\|}$	0	30.13	0	41.79	0	31.28
4 BS corners	$\overline{\|\|\Delta\vec{x}\|\|}$	0.05	6.53	38.52	38.70	27.77	28.28
	$\sigma_{\|\|\Delta\vec{x}\|\|}$	0	24.10	0	33.16	0	24.81
4 BS edges	$\overline{\|\|\Delta\vec{x}\|\|}$	0.04	4.99	53.54	51.97	42.70	43.49
	$\sigma_{\|\|\Delta\vec{x}\|\|}$	0	24.26	0	33.59	0	26.69

mean error of 0.5 m. Thus, it is favorable to slightly overcompensate systematic offsets.

5.6. Performance Evaluation of the Positioning Algorithms

The previously described four positioning algorithms are implemented in Matlab and compared. The least squares and the linear algorithm use the Matlab functions 'lsqnonlin' and 'fmincon' from the 'Optimization Toolbox'. Two versions of the mass-spring algorithm are programmed: the simple one calculates the position according to (5.18). The complete mass-spring algorithm (ms_c) calculates the complete dynamics of the mass-spring model with Equations (5.15), (5.16) and (5.17). The complete algorithm has the advantage that in some cases, the algorithm will not stop in a local minimum because of the remaining speed. The solution of the complete mass-spring algorithm is comparable to the movement of a marble in the potential well. If only the force is taken into account, the marble can stop in a small local minimum. The complete mass-spring model calculates the dynamics, thus the marble in the local minimum can have enough kinematic energy to get over the potential barrier into the global minimum.

The algorithms are tested on the simulation data with the simple multipath model, 200 reflector positions and 17 base station positions.

Table 5.2. Computation time in [ms] for the various positioning algorithms.

# of bs	t_{lsq} [1]	t_{ms} [2]	t_{ms_c} [3]	t_{lin} [4]
3	31.59	19.50	73.75	71.35
4	32.20	10.71	29.04	75.28
5	33.59	10.55	26.61	78.10
8	32.36	9.18	20.58	74.93

[1] least-squares, [2] mass-spring, [3] complete mass-spring, [4] linear algorithm

5.6.1. Computation Time

Table 5.6.1 summarizes the average computation times of these algorithms. The computation time is averaged over 200 different reflector positions and then 4 different sets of base stations. This leads to a total of 800 executions of each algorithm for a certain number of base stations. The least-square and the linear algorithm are independent of the number of base stations. Both mass-spring algorithms profit from an increasing number of base stations. For 3 base stations, the 3D position is the intersection of three spheres. The intersection of two spheres is a circle or a point (if they intersect). The intersection of the circle with a sphere results in two possible solutions. Hence, the solution is ambiguous. The algorithm can detect the correct position in most cases, because only one of the two solutions is inside the room. However, the force distribution is very flat between the two possible solutions and thus the mass-spring algorithms converge slower. Nevertheless, the simple mass-spring algorithm outperforms all others. For a higher number of base stations, the force which drags the MS to the correct position increases and thus the mass-spring algorithms converge faster. For more than 3 base stations, the complete mass-spring model is the second fastest. The mass-spring model is solved in 9.18 ms for 8 base stations. This is in the same order as the time needed for the 8 base stations to measure the distance to the reflector. Thus, the system is as fast in calculating the position as it is measuring the single distances, which is a prerequisite for real-time application.

5.6.2. Accuracy

Table 5.3 compares the accuracy of these algorithms for different base station subsets. The accuracy is the standard deviation of the position error $\Delta\vec{x} = \vec{x}_{ref,det} - \vec{x}_{reflector}$. Overall, the linear minimization algorithm results in the highest standard deviation and thus is the worst algorithm. However, the difference between the linear algorithm and the other ones is smaller than in the 2D case. The simple (ms) and the complete (ms_c) mass-spring model perform identically for all except one case. The difference between the least-square algorithm and the simple mass-spring model is also marginal. Thus, we can conclude that the simple mass-spring model combines the fastest computation time and one of the best accuracies, which makes this algorithm suitable for real-time indoor positioning.

Table 5.3 also indicates on where the best placements for the base stations are. Only a few of the evaluated base stations subsets are listed. Configurations, where 2 solutions for the same measurement are possible, are neglected. For example this occurs, when all base stations are 1.5 m above the floor, because for every reflector's z-component two solutions exist ($1.5\ m \pm z_{component}$). In Table 5.3, always the best configurations for a certain number of base stations are depicted together with some other configurations. It is obvious that more base stations result in a more accurate position, because the individual distance errors have a smaller weight on the final position. The 2D accuracy (σ_x and σ_y) outperforms the distance measurement accuracy ($\sigma_{\Delta d} = 17.19$ cm), if there are 4 or more base stations. The z-component improves when the base stations are in different heights. Thus, from a theoretical point of view, it would be optimal to place base stations at the ceiling and at the floor. The accuracy is then σ_x=8.9 cm, σ_y=9.9 cm and σ_z=14.5 cm. However, for most applications this will not be feasible, because the base stations on the floor are very likely to be blocked by moving objects (e.g. persons in a museum, AGVs in a factory).

5.7. Results with Random Error

With the multipath simulations, the positioning error in a 3D room for different base station positions was studied. However, it is not clear, how much this error depends on the exact multipath conditions. It would be simpler to assume a normal distributed error with a standard deviation and mean error. If the simulation with a normal distributed

Table 5.3. Comparison of the accuracy of the 4 implemented positioning algorithms. All values are in [cm]. Simulated room is 10 m wide, 10 m long and 3 m high.

		lsq	ms	ms_c	lin
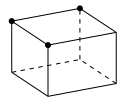	σ_x	18.666	18.964	18.966	18.375
	σ_y	17.955	18.253	18.256	18.253
	σ_z	69.596	66.935	66.956	68.297
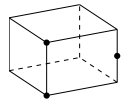	σ_x	18.888	18.902	19.226	20.135
	σ_y	27.684	29.812	27.345	29.197
	σ_z	52.853	52.549	60.437	52.899
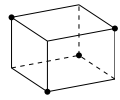	σ_x	14.808	14.889	14.888	16.982
	σ_y	14.089	13.201	13.202	15.819
	σ_z	37.514	31.585	31.584	35.059
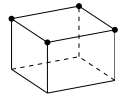	σ_x	12.504	12.486	12.486	14.786
	σ_y	12.756	12.754	12.755	14.864
	σ_z	36.718	35.485	35.482	41.301
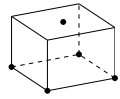	σ_x	11.525	11.389	11.389	13.846
	σ_y	12.290	12.307	12.307	14.072
	σ_z	23.133	23.092	23.096	27.314
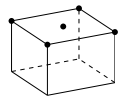	σ_x	11.230	11.043	11.043	13.281
	σ_y	12.274	12.262	12.262	14.193
	σ_z	32.058	31.193	31.193	44.304
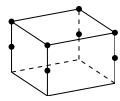	σ_x	9.570	9.559	9.560	11.638
	σ_y	9.938	9.950	9.950	11.861
	σ_z	29.607	29.573	29.580	34.568
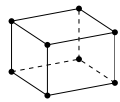	σ_x	8.921	8.916	8.916	11.650
	σ_y	9.861	9.861	9.861	12.037
	σ_z	14.573	14.540	14.539	19.581

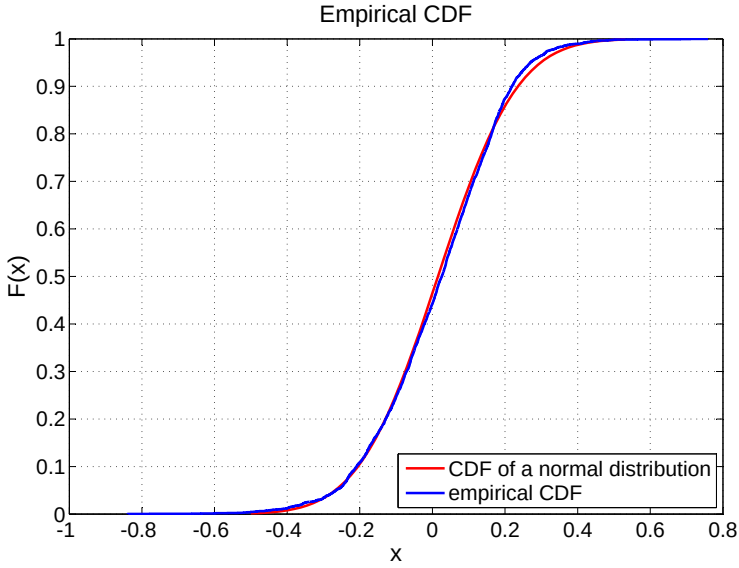

Figure 5.15. Cumulative distribution function (CDF) of the distance errors Δd for a normal distribution and for the multipath simulations.

error leads to the same results, then there is no need to simulate the optimal position with the multipath model and the time consuming Simulink model. In this section, the 3D positioning accuracy is simulated assuming a Gaussian distribution with the mean μ and standard deviation σ found with the simple channel model in Section 5.4.

Figure 5.15 illustrates the empirical cumulative distribution function (CDF) of the distance error based on the simulation results with multipath propagation as presented in Section 5.4. The distribution can be approximated with a normal distribution with mean value $\mu = 0.0153$ m and standard deviation $\sigma = 0.1719$ m. The distance errors from multipath simulations are not exactly normal distributed, but the distribution is very close to a normal distribution. Hence, a normal distributed error is a good approximation.

For the random simulations, 500 reflectors are randomly placed in a 10x10x3 m^3 room. For each position, the distance to the base station is calculated and a random error with normal distribution is added. The noisy distance between base station BS_n and reflector R_m is modeled

as

$$\rho_{BSn,Rm} = d_{BSn,Rm} + d_{random} \tag{5.22}$$

where d_{random} is a normal distributed distance with the mean value $\mu = 0.0153$ m and standard deviation $\sigma = 0.1719$ m. These noisy distances are then fed into the mass-spring positioning algorithm. This is repeated for each position 50 times, hence a standard deviation and a mean error can be calculated at every position. With this information, the critical points in the room can be identified, where the positioning accuracy is the smallest.

Figure 5.16 illustrates statistics of the positioning error of all 500 reflector positions. The error increases if a mean error is introduced. However, this case is special, because 3 base stations are 1.5 m above ground and one is mounted on the ceiling. The three base stations are not symmetrically placed and thus the positioning system is more susceptible. When 4 symmetrically placed base stations are used in addition to the one mounted on the ceiling, the influence of the mean error becomes smaller. In the center of the room, the mean errors compensate each other in xy-direction and only a z-error results.

5.8. Comparison between Multipath and Random Error Simulations

The simulations with a Gaussian distributed random error can be useful to find the optimal position for the base stations, because the simulation time is drastically lower (4 orders of magnitude) than the system simulation with the channel impulse response. However, the applicability has to be verified by the comparison with the multipath simulation results. Table 5.4 compares the accuracy for different base station configurations for both the multipath simulations and the random error simulations. For most cases, the accuracies in the x- and y-direction determined by the random error simulations agree with the multipath simulations. But the error in the z-direction is overestimated in 8 out of 10 cases.

Figure 5.17 to Fig. 5.18 compare the accuracy depending on the place of the reflector. For the random error simulations, the standard deviation $\sigma_{\Delta\vec{x}}$ of a reflector at a certain place is plotted. For the multipath simulations, the absolute error is plotted, because with the non-stochastic multipath model multiple simulations for the same reflector will always hold the same result. Figure 5.17 compares the error in the

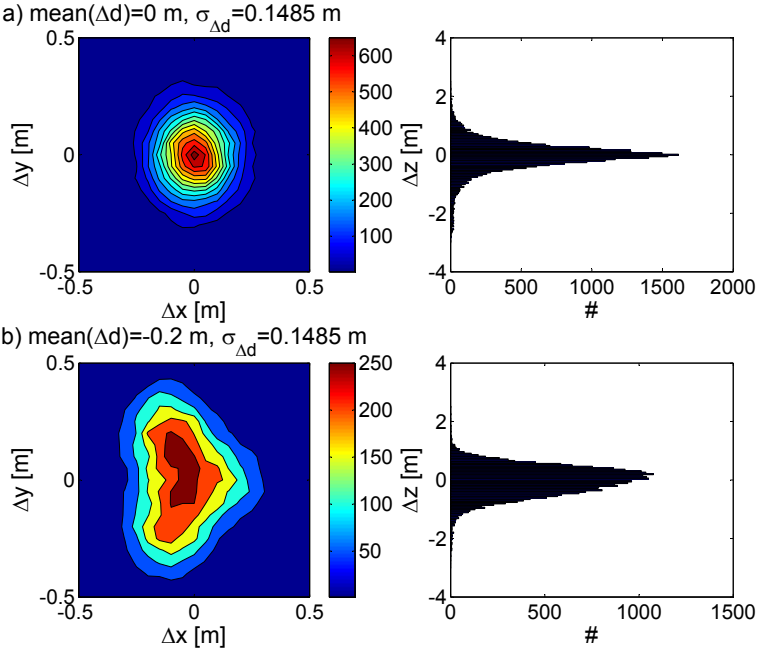

Figure 5.16. The histograms for the simulation with three base stations at 1.5 m height and an additional base station at the center of the ceiling. The upper histograms illustrate the positioning accuracy if no mean error (mean(Δd)) exists. The lower histograms illustrate that a small offset (mean(Δd) = -0.2 m) strongly influences the accuracy.

Table 5.4. Comparison between the positioning accuracy with multipath propagation compared to random error. All values are in [cm]. Simulated room is 10 m wide, 10 m long and 3 m high.

		random	mp
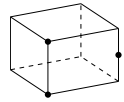	σ_x	17.30	18.90
	σ_y	28.30	29.81
	σ_z	56.62	52.55
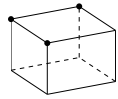	σ_x	18.83	18.96
	σ_y	18.74	18.25
	σ_z	60.52	66.94
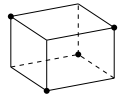	σ_x	13.76	14.89
	σ_y	13.73	13.20
	σ_z	38.17	31.59
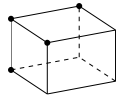	σ_x	15.12	15.83
	σ_y	14.89	16.33
	σ_z	39.53	39.25
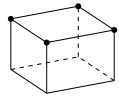	σ_x	12.88	12.49
	σ_y	13.00	12.75
	σ_z	41.28	35.49
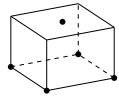	σ_x	12.25	11.39
	σ_y	12.30	12.31
	σ_z	27.25	23.09
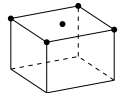	σ_x	12.35	11.04
	σ_y	12.41	12.26
	σ_z	35.79	31.19
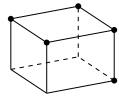	σ_x	12.01	11.87
	σ_y	12.10	12.06
	σ_z	36.02	27.62
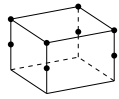	σ_x	9.04	9.56
	σ_y	9.10	9.95
	σ_z	36.84	29.57
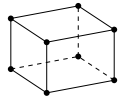	σ_x	6.28	7.01
	σ_y	6.27	7.06
	σ_z	17.79	13.30

z-direction. Here, both simulations lead to similar results. The further away a reflector is from the base stations, the larger is the z-error. This is not the case for the xy-direction as depicted in Fig. 5.18. The simulations with the random error identified reflectors close to one of the two walls, where the base stations are mounted, to be more susceptible to measurement errors, because of how the positioning problem is conditioned. The simulations with multipath propagation show the opposite behavior, because reflectors close to an opposite wall are influenced more by multipath propagation and thus are less accurate. This reveals that the random error simulations are not suited for the exact evaluation of the positioning error. Nevertheless, these simulations are good enough to give a rough estimate of the system performance for different base station configurations.

An interesting observation can be made by comparing the simulations with a random error with 3 base stations, each mounted in a corner on the ceiling, with the simulations with 4 base stations, each in a corner as well. With three base stations, the simulations with random errors predict a higher accuracy than the multipath simulations. If a fourth base station is added, the accuracy improves, because the error is averaged out. But with 4 base stations, the simulation with random errors underestimates the accuracy. The accuracy of the system with multipath propagation is better than one would expect, if the individual distance errors were uncorrelated. The influence of the position of the fourth base station is larger, if the multipaths are calculated. For example, the accuracy in z-direction of the 3 configurations with 4 base stations in Table 5.4 is similar for the simulations with random, uncorrelated distance errors. But, with multipath propagation, the accuracy in z-direction significantly differs for the different placements. Thus, with multipath propagation, it is preferred to have the base stations spread over the room. The positioning improves when the base stations are placed as diverse as possible. This has nothing to do with the positioning algorithm, because then the effect should also be visible with random errors. When the base stations are placed close to each other (grouped around a corner) or are placed in the same plane, it is likely that more than one base stations is affected by multipath propagation at the same time. Hence, multipath propagation has a stronger influence on the positioning accuracy and it is important to simulate the multipath conditions in order to predict the accuracy of a positioning system.

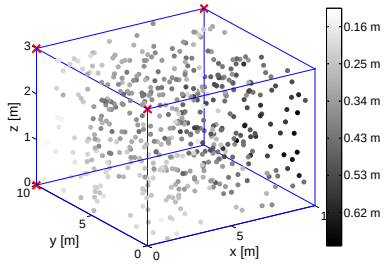

(a) Random error ($\sigma_{||\Delta\vec{x}||}$)

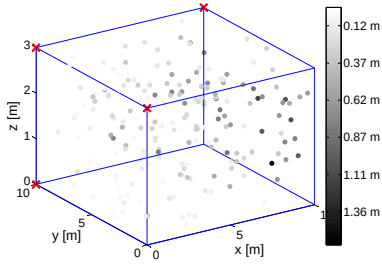

(b) With multipath ($||\Delta\vec{x}||$)

Figure 5.17. (a) illustrates the standard deviation ($\sigma_{||\Delta\vec{x}||}$) of the positioning error in z-direction, if a random error ($\sigma_{\Delta d} = 0.1719$ m) is assumed. (b) shows the positioning error ($||\Delta\vec{x}||$) of the system simulated with multipath propagation. Both simulations identify the same reflector positions as problematic.

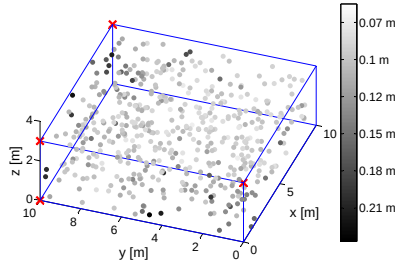

(a) Random error ($\sigma_{||\Delta\vec{x}||}$)

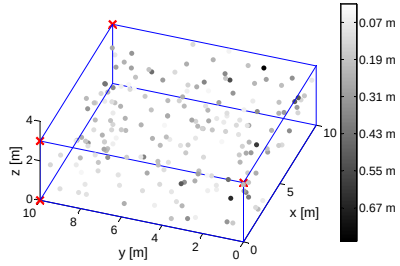

(b) With multipath ($||\Delta\vec{x}||$)

Figure 5.18. (a) illustrates the standard deviation ($\sigma_{||\Delta\vec{x}||}$) of the positioning error in xy-direction, if a random error ($\sigma_{\Delta d} = 0.1719$ m) is assumed. (b) shows the positioning error in xy-direction ($||\Delta\vec{x}||$) of the system simulated with multipath propagation. The multipath simulations revealed that reflector positions close to the opposite wall are critical, which disagrees with the simulations with a random positioning error.

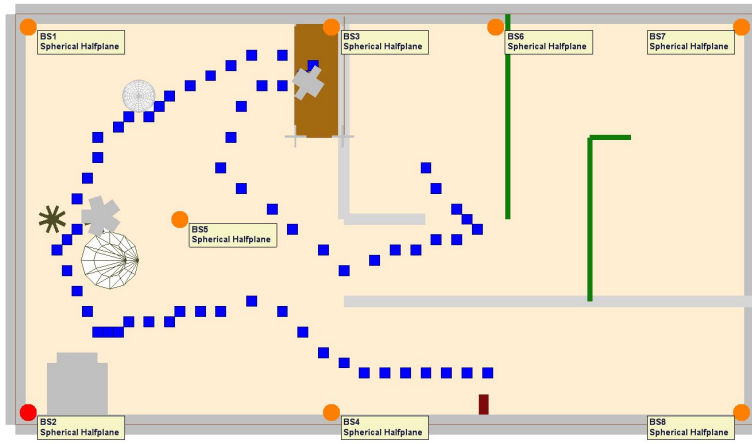

Figure 5.19. Map of a small museum.

5.9. Ray Tracing

The previous simulations showed that multipath propagation influences the positioning error drastically. In this section, the accuracy of the positioning system in a small museum environment is studied. The small museum environment is a prototype application for our system. The multipaths are calculated with the commercial WLAN planning tool Radioplan Simulator (RPS) from Actix. It uses 3D ray tracing to calculate the field strength in a room. For this, the simulator calculates all multipath components and the resulting impulse response of the transmission channel which can be exported to Matlab. This impulse response is then fed into our simulation environment in the same way as with the stochastic UWB channel model depicted in Fig. 3.33. This enables us to simulate complex indoor scenarios. Here, a small museum room is drawn. The floorplan of the museum is depicted in Fig. 5.19. The museum measures 10x18x3 m^3. The outer walls are massive 0.5 m thick walls with a relative permittivity $\epsilon_r = 4 - 0.4i$. This value is taken from the RPS material database for brick walls and the value agrees with other literature values of $\epsilon_r = 3.58$ [130] and $5 - 0.45i$ [131]. Two different types of inner walls are used in the simulation. The thicker and thinner inner walls are 0.28 m and 0.12 m thick, respectively. The main room has two glass windows. Inside the museum, there is a wooden table with metal legs. On the table is a metal block (0.4x0.2x0.4 m^3).

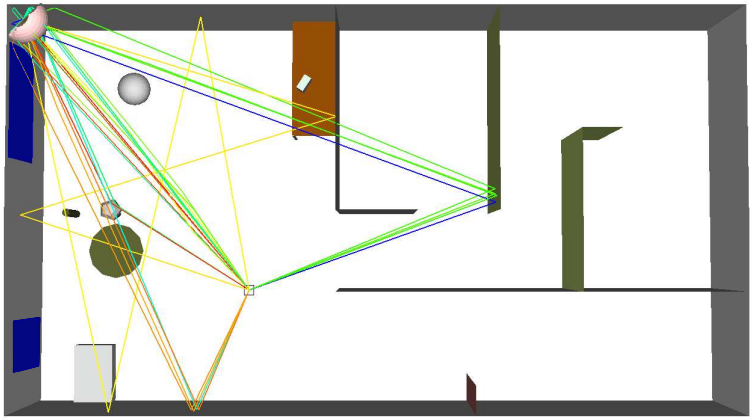

Figure 5.20. Multipath components for 1 reflector and 1 base station.

A metal sphere hangs from the roof, similar to a mirror ball. And a second sphere together with two stone columns and a stone cone are placed inside the museum. These objects represent sculptures. The museum is equipped with 8 base stations. The simulated visitor enters the main room through a corridor, walks around the sculptures towards the table and then leaves the room through another corridor into the next room. The 63 simulated positions are marked in Fig. 5.19.

For each position and each base station, the LOS and multipaths are simulated. The used student version of the Radioplan Simulator only calculates LOS and multipath components with up to 2 reflections. Figure 5.20 illustrates the calculated propagation paths for one position and one BS. The corresponding impulse response is plotted in Fig. 5.21.

5.9.1. Filtering and Position Estimation

In an indoor scenario, there are always some base stations, which have no LOS component or receive only a very weak input signal. Therefore, several base stations are needed. This is especially true for the museum application with multiple rooms. The main problem for such a scenario is to select the correct sub set of all base stations, because at any given position, there are some base stations, which do not see the reflector at all and some with NLOS conditions. The histogram of the distance error Δd is plotted in Fig. 5.22. Most distances are correctly detected,

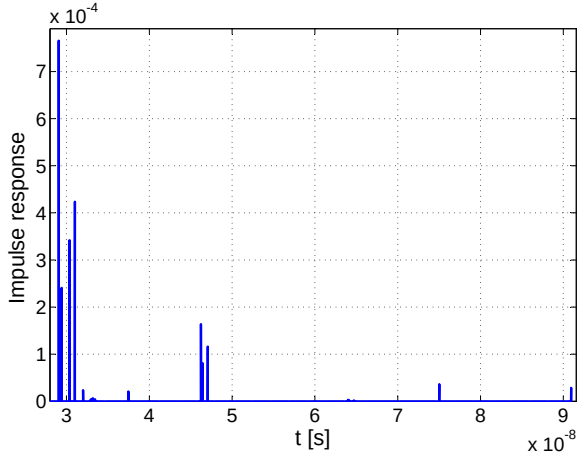

Figure 5.21. Impulse response for 1 reflector and 1 base station (same configuration as in Fig. 5.20).

but a few distances are too short, this happens, if no LOS and no strong multipath exist. In this case a random peak is detected. Too long distances are detected if one multipath component is stronger than the LOS component. This leads to an overall standard deviation of $\sigma_{\Delta d} = 3.07$ m. For most positioning algorithms, such large errors due to NLOS are unacceptable. Hence, they are rarely covered in publications.

It is crucial to filter the largest errors. Our approach to filter the wrong distances from the correct distances is by comparing them to the expected distances. The position of the reflector $\vec{x}_{est,t}$ is estimated based on the previously detected positions $\vec{x}_{det,t-1}$. The position can be estimated based on different heuristics. The simplest heuristic is to estimate the position at the last known position, especially if no information about the target and its dynamics is available or it moves randomly. According to the estimated position $\vec{x}_{est,t} = \vec{x}_{det,t-1}$, the distances between each base station and the reflector are calculated and compared with the measured distances. If the measured distances and the calculated, estimated distances agree ± 1 m, the measured distance is kept. Otherwise, the measured distance is neglected. The histogram after this filtering is depicted in Fig. 5.22. The filtered distances have a standard deviation of $\sigma_{\Delta d} = 39.57$ cm.

At least 3 measured distances are needed for the calculation of the

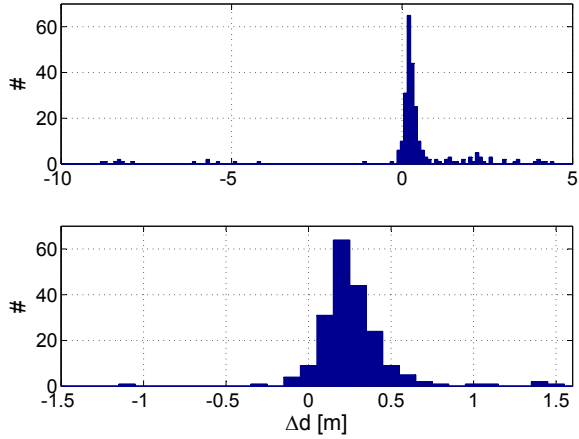

Figure 5.22. Histogram of the distance error: In the upper histogram all distance errors are taken into account. The lower histogram plots only the distance errors after filtering.

position of the reflector. If less than 3 distances remain after filtering the position cannot be calculated. Different possibilities exist for these cases. One could take the estimated distance as the correct distance. This can be a good approach if the behavior of the target is well known (e.g. robots, AGVs). Instead of predicting the position, one could take the 4 best measurements and use these results for the mass-spring algorithm. This is useful when the movement of an object cannot be well predicted (e.g. a person in a museum). The difficult part is to decide which measurements are the best. The best measurements are the ones without multipath propagation. By comparing base band spectra with strong multipath propagation with spectra without multipath propagation (see Fig. 5.4), it can be seen that the height of the peaks reduces if multipath propagation exists. Thus, the best heuristic that could be found for the weighting of the individual distance measurements is

$$weight = \frac{\log\left(\max|S_{zoom}|\right) - \log\left(\text{mean}\,|S_{zoom}|\right)}{5}, \tag{5.23}$$

S_{zoom} is the spectrum of the zoom FFT of the received signal. The correlation factor between the distance error and the weighting factor is 0.42. This heuristic is valid, because in a strong multipath scenario, multiple peaks exist and thus the distance between the main peaks and

Table 5.5. Results for the museum simulations in both directions and with known and unknown starting point.

direction	forward		reverse	
starting point	known	unknown	known	unknown
$\sigma_{\Delta x}$ [cm]	18.72	22.91	19.21	87.39
$\sigma_{\Delta y}$ [cm]	15.90	30.36	14.59	51.90
$\sigma_{\Delta z}$ [cm]	30.12	30.86	29.94	30.46
$\sigma_{\Delta x(10:50)}$ [cm]	10.84	10.84	18.95	18.96
$\sigma_{\Delta y(10:50)}$ [cm]	11.82	11.82	14.38	14.38
$\sigma_{\Delta z(10:50)}$ [cm]	26.53	26.53	27.62	27.62

the average is smaller than in a clean spectrum with only the wanted two peaks. However, if no LOS exists and one multipath is very strong, the spectrum looks as if the strongest multipath is the LOS component.

The computed weight is only used, if the filter rates less than 3 measurements valid. Then, the 4 distance measurements with the highest weights are chosen.

weight according to (5.23). Thus, even when a wrong position is predicted, the right position was detected.

5.9.2. Results

Four different scenarios are simulated: in both directions and with known and unknown starting point. The results are summarized in Table 5.5. The detected paths are depicted in Fig. 5.23 to Fig. 5.26. The paths with a known starting point and with the unknown starting point only differ in the first few position. After the first 10 positions, both scenarios identified the same path. Thus, the algorithm is able to recover from wrong positions. Both end points of the path are in a harsh environment with only a few direct LOS connections. In the lower end, LOS connections to base stations 2, 4 and 8 exist, which are all mounted on the same wall. For the upper end of the path, there is only 1 direct LOS connection to base station 6. Base station 3 and 7 have a direct LOS path, but this path is heavily attenuated by the walls. Even without Kalman or particle filtering, the path through the museum could be accurately detected.

The standard deviation in x- and y-direction for the path through the main room are between 10.8 and 19 cm. The position accuracy in

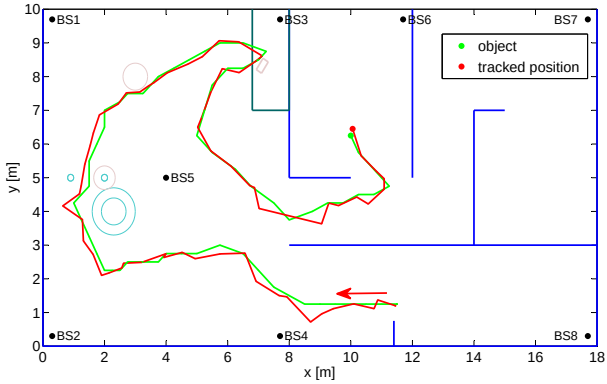

Figure 5.23. The museum visitor enters the museum at position [x,y]=[11.5,1.25] and the localization algorithm knows the starting point. The visitor can be tracked accurately enough for interactive guiding.

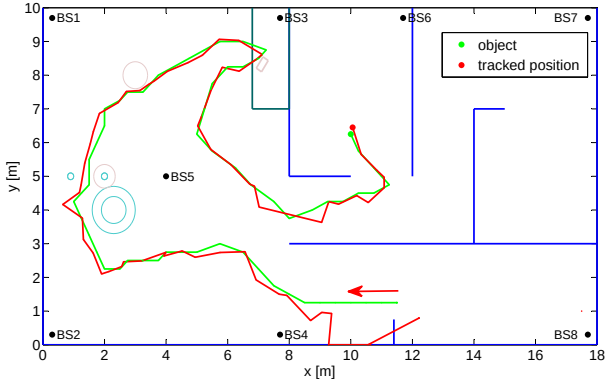

Figure 5.24. The museum visitor enters the museum at position [x,y]=[11.5,1.25], but the localization system has no information about the starting point. The first few localization steps are not accurate, but after 10 steps the exact same path is detected as if the starting point is known.

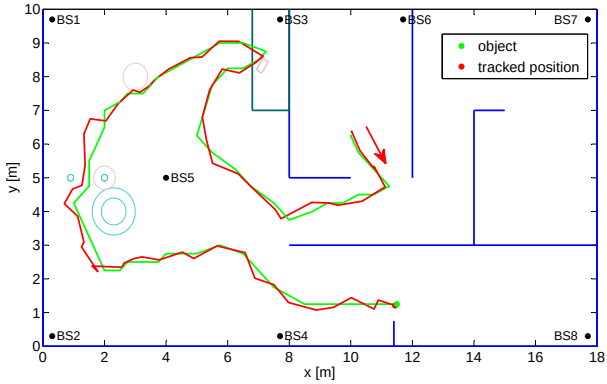

Figure 5.25. The museum visitor starts in the room at position [x,y]=[10,6.25]. The positioning system knows the starting point of the visitor. The positioning accuracy can be further improved by filtering the detected position and if the position is measured more often.

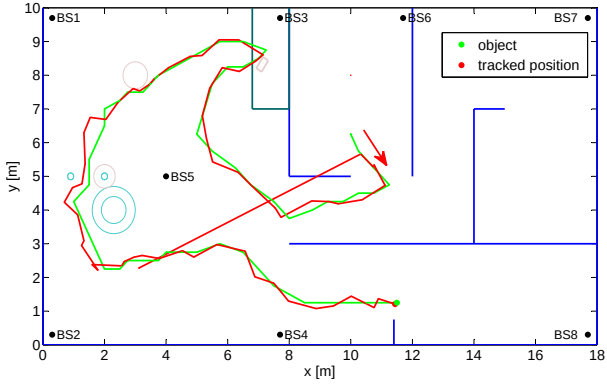

Figure 5.26. The museum visitor starts in the room at position [x,y]=[10,6.25]. The starting point is unknown to the system and thus the first detected position is completely wrong. But the position is correctly detected after the second steps, although only one unattenuated LOS path exists for the first three positions.

the hallway and in the smaller room is worse. This could be improved by adding additional base stations. However, the simulated positioning system detects the x- and y-position pretty well. But, the z-component cannot be resolved accurately enough. In the simulation, the z-position is limited to the range between 1 and 2 m above ground, which is reasonable for a hand-held device. The reason for the unsatisfactory accuracy in the z axis is that all base stations are at the same height. Therefore, a small distance error can result in a large z-error. For example, in a 10x10x3 m^2 room with a base station in each upper corner, the detected z-position can vary from 1.08 to 2.08 m for distance errors between -0.1 and 0.1 m. In the same scenario, the x and y-errors are limited to only ± 0.14 m. The standard deviation in the z-direction is 13.6 cm and in the x- and y- direction only 4.16 cm. The ratio between the standard deviation in z-direction and in the x-direction is equal to the room length (x-direction) to the room height (z).

The applied position filtering and localization algorithm yields good results. The standard deviation of the detected path in x- and y-direction are better than the standard deviation of the distance error $\sigma_{\Delta d} = 39.57$ cm. The quality of the applied algorithms can be illustrated with Table 5.6. This table compares the achieved accuracies with the accuracy without positioning filtering (all 8 BS). The accuracy for all 8 base stations is almost as low as if only the 5 base stations in the main room are used ($\sim$2 m). The system is inaccurate, if always all base stations are taken into account, because there are always some base stations which have only a NLOS path or a strongly attenuated LOS path to the reflector. These wrong distance measurements distort the positioning.

The results for the best 3, best 4 and best 5 are only theoretical values. These are found by calculating all possible points with 3, 4 or 5 base stations, respectively. All these points are then compared to the real position and the closest point is chosen. This is only possible, because the real position is known for the simulations. The achieved accuracy is the lowest limit, which can be reached if always the best 3, 4 or 5 distance measurements are selected. Therefore, it is a good benchmark for the accuracy of the applied filtering mechanism. The accuracy of the positioning with the applied algorithms is similar to the best 4 base stations. With the best 4 base stations, the z-component is more accurate, but the horizontal component is slightly less accurate. Therefore, the presented position filtering based on an estimated position is a good solution for the localization approach. Another advantage is

Table 5.6. Accuracy $\sigma_{x,y,c}$ [cm] of a virtual walk through a museum. The accuracy is low if all base stations (8 BS) or the 5 in the main room are chosen. The filtering of the distances leads to an improved accuracy (forward and reverse direction).

	σ_x [cm]	σ_y [cm]	σ_z [cm]
forward direction	18.72	15.9	30.12
reverse direction	19.21	14.59	29.94
8 BS	192.25	225.58	43.713
5 in the main room	260.69	196.6	40.391
best 3	8.8722	12.478	12.88
best 4	14.459	26.844	15.652
best 5	45.783	39.943	18.366

that the position filtering together with the mass-spring model is very fast and real time positioning is possible. The execution time for all 63 position, including zoom FFT, peak detection, position filtering and position calculation with the mass spring model takes 5.08 s (81 ms per position). The algorithm is implemented in Matlab and is not compiled prior execution. The execution time can be further reduced by doing the FFT and peak detection on the FPGA of each base station. Furthermore, the localization algorithm can be sped up by implementing it in a more hardware based programming language such as C.

The distance filtering and positioning indicate the possible accuracy of the positioning system with an active pulsed reflector. However, it is possible to further improve the accuracy by applying tracking algorithms or Kalman filters. For example [132] uses constrained weighted least square optimization for vehicle position tracking. They applied a Kalman filter on the measured GPS positions. Some use a Markov approach [133] or probability grids [134]. But most of these approaches have the disadvantage that they are computationally expensive.

5.10. Conclusion

The simulations of the system with a simple multipath model, which only takes the LOS and 5 MPCs into account, help to identify the influence of multipath propagation. The comparison of two peak detection methods (3dB point and steepest edge) based on the simulation data revealed that the 3dB point is more reliable, but if the steepest edge method detects the correct edge, then the steepest edge algorithm is

more accurate. Therefore, a combined algorithm is chosen. The distance accuracy $\sigma_{\Delta d}$ is 17.19 cm for the 200 reflectors and 17 simulated base station positions.

Four different positioning algorithms are compared using the simulation data with the multipath model. Linear minimization of the distance error results in the worst accuracy and the slowest execution time. The least-square and the two mass-spring algorithms are equally accurate, but the simple mass-spring model has the shortest execution time. The mass-spring model is simple enough to be executed on an FPGA and is fast enough for real-time positioning.

Multipath propagation leads to a distance error $\sigma_{\Delta d}$. Assuming this error is random and normal distributed leads to different positioning accuracy $\sigma_{x,y,z}$ than the simulation with multipath propagation. With the random simulations, it is possible to see how the error propagates. For example, if all base stations are on the same horizontal plane, the accuracy in vertical direction (z) is bad. But the multipath propagation show that it is as important that the distances are measured from different angles. If one measurement is affected by multipath, the probability that the other measurements are also corrupted by multipath propagation is smaller if a higher spatial diversity can be achieved.

The active pulsed reflector is only tested with one base station, because only one base station was available. Therefore, the 3D performance of the system in a real environment is not known. For an estimation of the possible accuracy, a small museum environment is simulated with ray tracing. The distance error $\sigma_{\Delta d}$ is large (3-07 m) due to multipath propagation and especially NLOS paths. Many wrong measurements can be filtered out by comparing with the distance to an estimated position and thus the distance accuracy increases to $\sigma_{\Delta d} = 0.3957$ m. This is in the same range as the measured accuracy in a small room with strong multipath propagation. The positioning algorithm with filtering predict a positioning accuracy $\sigma_{x,y}$ in the range of 15 to 20 cm.

It is almost impossible to compare this positioning accuracy and the performance of the localization including filtering of NLOS paths. Most papers do not state the accuracy of the positioning system or the improvements due to the localization algorithm or the measurements are conducted outdoors with LOS conditions. One approach to filter NLOS paths is to use power-level surveillance [33]. The power level is estimated and compared to the received power level. If the signal is blocked (e.g. by a wall or a person), the received power level is

much lower than estimated. The power level difference is then used to generate a weighting matrix. Figure 8 from [33] clearly show that the positioning accuracy improves due to power-level surveillance, but the accuracy is not quantified. Furthermore, only outdoor measurements were conducted. It is expected that power-surveillance works less reliable indoors, because there exist more and potentially stronger multipaths. The accuracy can also be improved by constrained weighted least square optimization with Kalman filtering. The improvement is discussed for GPS signals [132], but the algorithm is only tested on artificial noisy data with zero mean and a large standard deviation $\sigma = 150$ m. The accuracy of the filtered data improved to 3.3 m. However, the vehicle has an almost constant velocity and does not change direction. The accuracy of the algorithm in a real life scenario is hard to predict.

The presented algorithm proofed that the system can work in a museum environment with multiple rooms and many NLOS paths. However, the algorithms have to be developed further and additional filtering can improve the accuracy. The development of these algorithms is going to take an additional effort. It makes sense to optimize the positioning filtering on real life, measured data.

6

Conclusion

The start-up of an oscillator with an applied sinusoidal signal was studied. It was shown that the oscillator starts with the same initial phase as the incoming signal ('phase synchronous'). The imperfection of the phase synchronization is the phase error $\Delta\phi$ between ideal start-up and the real start-up. This phase error $\Delta\phi$ depends on three main parameters of the oscillator: the loop gain A, the quality factor Q of the feedback path and the difference between the oscillation frequency f_0 and the incoming FMCW signal's frequency f. The phase synchronous start-up was proven by measurements, both in the time and the frequency domain. Obviously, the synchronization works best for strong input signals. For weak input signals, the SNR becomes small and the phase error increases.

The verified start-up behavior helped to build two different models for system simulations. The optimal reflector parameters were found by systematic simulations.

However, the largest error source in practice is multipath propagation. For this reason multiple scenarios were simulated. The simplest scenario emulates an empty cuboid. Even with this basic model, the accuracy of the distance measurements deteriorated. The standard deviation of the distance error ($\sigma_{all\Delta d}$) is 17 cm. The system was also

simulated with an UWB channel model and with ray-tracing software for a small museum environment. The simulated accuracies ($\sigma_{all\Delta d}$) are 26 and 40 cm respectively. In the latter case, the 3D position was calculated according to the distance simulations. The 3D positioning accuracy is better than the distance accuracy: $\sigma_{\Delta x} = 19$ cm, $\sigma_{\Delta y} = 16$ cm and $\sigma_{\Delta z} = 30$ cm, because the individual distance errors are averaged.

The active reflector integration in CMOS posed a number of challenges. The phase synchronous start-up behavior had to be achieved and the influence of the on-switching transients must be minimized. In addition, the reflector has to be matched to the antenna and the output power must be at least 0 dBm. All these constraints could be fulfilled. The sensitivity of the active reflector is -67 dBm, which is above the required sensitivity of -78 to -73 dBm. But the influence of a deterministic phase due to switching is too low to be detected. Nevertheless, the repeatability of the distance measurements is very high. If the same position is measured several times, the standard deviation of the measured distance $\sigma_{\Delta d}(d)$ is small (only 1.6 cm outdoors, 5.96 cm indoors). Parameters that affect the repeatability are noise (SNR and phase noise), jitter of the modulation signal and the non-linearity of the frequency ramp. The high repeatability proves that the system is well designed, robust and the influence of the mentioned parameters on the positioning accuracy is small. The more important figure of merit is the standard deviation of the error over different distances. In a strong multipath environment, the standard deviation ($\sigma_{all\Delta d}$) for directional and omni-directional antennas are 26.6 cm and 74.2 cm, respectively. These value improve significantly, if a distance filtering is applied. With a simple sliding window averaging, the values improved to 7.2 cm and 32.9 cm. Application specific filtering may improve the results even further. These values are only for distance measurements. As was shown, the 3D accuracy with multiple base stations is normally better than the single distance measurements.

The implemented system verified the feasibility of the active reflector. Integration in CMOS is possible, even with the low Q-factor, the limited gain and the limited output swing. The achieved performance is similar to complexer, more power consuming systems. And as demonstrated, there are ways to further improve the system performance.

6.1. Outlook

The presented prototype system proved that the active reflector can be implemented in CMOS. The system is not yet ready for commercial use. Both the infrastructure, consisting of localization server and base stations, and reflector have to be improved.

6.1.1. Infrastructure

The presented distance measurements were all conducted with only one base station, because only one fully functional base station was available. The signal was processed on a host computer. In a next step, the zoom FFT and the peak detection can be implemented on the FPGA in the base stations. Multiple base stations are needed for 3D positioning and a host computer which coordinates the individual distance measurements.

Until now, only one transmit and one receive channel was used. The base stations offer the possibility to use 4 channels. One possibility is to use one transmit channel and an antenna array with three receive channels. The antenna array allows filtering of unwanted multipath components. This can be achieved with adaptive beam steering or with an estimation technique such as MUSIC [135], [136], [137] or ESPRIT [138], [139]. Independent of the chosen methodology, the angle-of-arrival of the received signal is known. This additional information improves the robustness of the positioning algorithm and improves the accuracy of the system.

6.1.2. Reflector

Although the active reflector already performed as good as comparable, more complex systems, there is still room for improvements. A few ideas are presented here:

The oscillation frequency ω_0 of the active reflector is calibrated manually by a tuning voltage v_{tune}. Although the oscillation frequency did not drift substantially over time, the active reflector has to be calibrated automatically in a production environment. One possibility is to calibrate each reflector when the reflector is charged in a docking station. The reflector is tuned automatically in the charging station and the value is stored digitally. A DAC then converts the control word to a voltage. Another possibility is an FPGA on the active reflector board which compares the reflector's frequency with a reference frequency and

tunes the reflector accordingly. The most complex approach, is the implementation of an all-digital PLL. However, this would be an overkill, because the phase of the reflector is not important.

In applications such as interactive guiding, many reflectors can be in the same room. At the moment, all reflectors are simultaneously active. This limits the number of reflectors for our base stations to 7 because of cross-talk between the simultaneously active reflectors and the limited base-band bandwidth. There are two ways to increase the number of reflectors.

- Each reflector is cycled: every reflector is randomly switched off for a certain amount of time and then switched on for at least the time needed for a complete position measurement. Multiple base stations use the same modulation frequency f_{mod}. Thus, the base stations need an additional way to identify the reflectors. This could be solved by transmitting an identity code at the beginning. The identity code is generated by a specific on-off switching pattern of the reflector.

- In the case of interactive guiding, the reflector is paired with a communication device (e.g. a PDA or smartphone). In this case, the host computer of the positioning system selects the device, which position has to be measured and transmits a message to the communication device. Upon completion of the positioning, a second message is sent to switch off the reflector.

An idea to improve the sensitivity of the active reflector further is to use additional amplifiers: The incoming signal is amplified by a LNA. The output of the LNA is applied to an oscillator, which is periodically switched on and off. As soon as the reflector reaches full swing, the LNA is switched off and the output amplifier is switched on. With the additional LNA, higher sensitivity can be achieved. Furthermore, the LNA filters the incoming signal due to the band-pass characteristic of the LNA. The additional power consumption of the LNA and PA can be compensated by reduced power consumption of the oscillator. The oscillator only has to drive the input of the PA and not the antenna anymore. Further studies are needed to verify that this approach significantly improves the sensitivity.

A

Supplement Information

A.1. Start-up Calculation

A.1.1. Simplification of u and v

The start-up behavior of an oscillator was calculated in Section 2.1. The resulting signal $y_{out}(t \geq 0)$ in the time domain is

$$y_{out}(t \geq 0) = z(x \sin(\omega t + \phi_0) + y \cos(\omega t + \phi_0) + Ae^{\frac{(A-1)t\omega_0}{2Q}} (u(\phi_0) \sin(\omega_0' t) + v(\phi_0) \cos(\omega_0' t))) \tag{A.1}$$

The terms u, v, x, y, z and ω_0' are given by the following expressions:

$$u(\phi_0) = \frac{(A-1)\,Q\omega\omega_0\left(\omega^2+\omega_0^2\right)\cos\phi_0}{\sqrt{\left|(A-1)^2-4Q^2\right|}} + \frac{\omega^2\omega_0^2\,(A-1)^2\sin\phi_0 + 2Q^2\omega_0^2\left(\omega_0^2-\omega^2\right)\sin\phi_0}{\sqrt{\left|(A-1)^2-4Q^2\right|}} \tag{A.2}$$

$$v(\phi_0) = \omega\omega_0\left(Q\cos\phi_0\left(\omega^2-\omega_0^2\right)+(A-1)\,\omega\omega_0\sin\phi_0\right) \tag{A.3}$$

$$x = Q^2\left(\omega^2-\omega_0^2\right)^2-(A-1)\,\omega^2\omega_0^2 \tag{A.4}$$

$$y = AQ\omega\omega_0\left(\omega_0^2-\omega^2\right) \tag{A.5}$$

$$z = \frac{B}{(A-1)^2\,\omega^2\omega_0^2+Q^2\left(\omega^2-\omega_0^2\right)^2} \tag{A.6}$$

$$\omega_0' = \omega_0\frac{\sqrt{\left|(A-1)^2-4Q^2\right|}}{2Q} \tag{A.7}$$

The starting phase ϕ_{ref} of the reflector can be calculated by

$$\phi_{ref} = \angle(u(\phi_0)+iv(\phi_0)). \tag{A.8}$$

The two functions u and v have to be simplified for the analytical calculation of the starting phase. We assume that both the incoming signal and the oscillator have the same frequency ($\omega = \omega_0$). This is true at least once, if the incoming signal is a frequency ramp and the oscillator's frequency is inside the bandwidth of the ramp. The two Equations (A.2) and (A.3) are then

$$u(\phi_0) = \frac{(A-1)\,2Q\omega^4\cos\phi_0+\omega^4\,(A-1)^2\sin\phi_0}{\sqrt{\left|(A-1)^2-4Q^2\right|}} \tag{A.9}$$

$$v(\phi_0) = (A-1)\,\omega^4\sin\phi_0 \tag{A.10}$$

Furthermore, we assume that the quality factor Q of the feedback

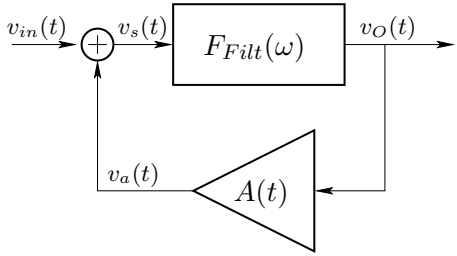

Figure A.1. Block diagram of an active reflector with variable loop gain $A(t)$ and a loop filter F_{Filt}.

filter is much larger than the loop gain A.[1] Equation (A.9) reduces to

$$\begin{aligned} u(\phi_0) &\approx \frac{(A-1)\,\omega^4\,(2Q\cos\phi_0 + (A-1)\sin\phi_0)}{2Q} \\ &\approx (A-1)\,\omega^4\cos\phi_0 \end{aligned} \tag{A.11}$$

The starting phase ϕ_{ref} of the reflector is

$$\begin{aligned} \phi_{ref} &= \angle(u(\phi_0) + iv(\phi_0)) \\ &= \angle\left((A-1)\,\omega^4\,(\cos\phi_0 + i\sin\phi_0)\right) \\ &= \angle\,(\cos\phi_0 + i\sin\phi_0) = \phi_0 \end{aligned} \tag{A.12}$$

The reflector starts exactly phase coherent to the incoming signal, if the assumptions ($Q \gg A$ and $\omega = \omega_0$) are true.

A.2. Sensitivity Curve

The concept of the sensitivity curve was introduced for super-regenerative receivers [80]. The sensitivity curve $s(t)$ determines how sensitive the receiver is to incoming signal over time. The active pulsed reflector is very similar to a super-regenerative receiver. In this Section, the sensitivity curve of the active pulsed reflector is calculated based on [74].

The reflector depicted in Fig. A.1 consists of a time-varying gain $A(t)$ and a band-pass filter F_{Filt}. The transfer function of thesecond

[1] This is a strong simplification. The ratio between Q and $A-1$ is practically in the order of 5 to 15.

order band-pass filter $F_{Filt}(s)$ leads to the differential equation

$$\ddot{v}_O(t) + \frac{\omega_0}{Q}\dot{v}_O(t) + \omega_0^2 v_O(t) = \frac{\omega_0}{Q}\dot{v}_S(t) \tag{A.13}$$

The signal $v_S(t)$ is the sum of the incoming signal and the feedback

$$v_S(t) = v_{in}(t) + A(t)v_O(t). \tag{A.14}$$

Inserting (A.14) into (A.13) gives

$$\ddot{v}_O(t) + \frac{\omega_0}{Q}\left(1 - A(t)\right)\dot{v}_O(t) + \left(\omega_0^2 - \frac{\omega_0}{Q}\dot{A}(t)\right)v_O(t) = \frac{\omega_0}{Q}\dot{v}_{in}(t) \tag{A.15}$$

We can introduce a new function, the damping function $\zeta(t)$

$$\zeta(t) = \zeta_0\left(1 - A(t)\right) \tag{A.16}$$

with $\zeta_0 = 1/(2Q)$. The differential equation with the damping function $\zeta(t)$ is

$$\ddot{v}_O(t) + 2\omega_0\zeta(t)\dot{v}_O(t) + \left(\omega_0^2 - \frac{\omega_0}{Q}\dot{A}(t)\right)v_O(t) = \frac{\omega_0}{Q}\dot{v}_{in}(t) \tag{A.17}$$

The solution can be splitted up in homogeneous solution $v_{Oh}(t)$ and particular solution $v_{Op}(t)$

$$v_O(t) = v_{Oh}(t) + v_{Op}(t) \tag{A.18}$$

A.2.1. Homogeneous Solution

The homogeneous differential equation is the equation without an input signal ($v_{in}(t) = 0$):

$$\ddot{v}_{Oh}(t) + 2\omega_0\zeta(t)\dot{v}_{Oh}(t) + \left(\omega_0^2 - \frac{\omega_0}{Q}\dot{A}(t)\right)v_{Oh}(t) = 0 \tag{A.19}$$

This differential equation can be solved by a change of variable

$$v_{Oh}(t) = y(t)e^{-\omega_0\int_0^t \zeta(x)\mathrm{d}x} \tag{A.20}$$

$$\dot{v}_{Oh}(t) = \left(\dot{y}(t) - \omega_0\zeta(t)y(t)\right)e^{-\omega_0\int_0^t \zeta(x)\mathrm{d}x} \tag{A.21}$$

$$\ddot{v}_{Oh}(t) = \left(\ddot{y}(t) - 2\omega_0\zeta(t)\dot{y}(t) - \omega_0\dot{\zeta}(t)y(t) + \left(\omega_0\zeta(t)\right)^2 y(t)\right) \cdot e^{-\omega_0\int_0^t \zeta(x)\mathrm{d}x} \tag{A.22}$$

which converts the homogeneous equation (A.19) into a differential equation for $y(t)$

$$\ddot{y}(t) + \omega_0^2 \left(1 - \frac{\dot{A}(t)}{\omega_0 Q} - \frac{\dot{\zeta}(t)}{\omega_0} - \zeta(t)^2\right) y(t) = 0. \tag{A.23}$$

The derivative of ζ is

$$\dot{\zeta}(t) = -\zeta_0 \dot{A}(t) = -\frac{\dot{A}(t)}{2Q} \tag{A.24}$$

and thus the differential equation for $y(t)$ is

$$\ddot{y}(t) + \omega_0^2 \left(1 - \frac{\dot{A}(t)}{2\omega_0 Q} - \zeta(t)^2\right) y(t) = 0. \tag{A.25}$$

The on-switching function $A(t)$ is plotted in Fig. A.2. ζ^2 is

$$\zeta^2 = ((A-1)/(2Q))^2 \tag{A.26}$$

for which we can assume

$$\zeta(t)^2 \ll 1. \tag{A.27}$$

$\dot{A}(t)$ is piecewise known

$$\dot{A}(t) = \begin{cases} 0 & \text{if } t < t_0, \\ \frac{A_{max}}{t_{rise}} & \text{if } t_0 \le t \le t_0 + t_{rise}, \\ 0 & \text{if } t > t_0 + t_{rise}. \end{cases} \tag{A.28}$$

The homogeneous differential equation

$$\ddot{y}(t) + \omega_0^2 \left(1 - \frac{\dot{A}(t)}{2\omega_0 Q}\right) y(t) = 0 \tag{A.29}$$

has the known solution

$$y(t) = V_1 e^{j\omega_0 t\sqrt{1-\frac{\dot{A}(t)}{2\omega_0 Q}}} + V_1^* e^{-j\omega_0 t\sqrt{1-\frac{\dot{A}(t)}{2\omega_0 Q}}} \tag{A.30}$$

Undoing the change of variable, the solution of the homogeneous equation is

$$v_{Oh}(t) = \begin{cases} e^{-\omega_0 \int_0^t \zeta(x)\mathrm{d}x} 2\mathrm{Re}[V_{11} e^{j\omega_0 t}] & \text{if } t < t_0, \\ e^{-\omega_0 \int_0^t \zeta(x)\mathrm{d}x} 2\mathrm{Re}[V_{13} e^{j\omega_0 t}] & \text{if } t > t_0 + t_{rise}, \\ e^{-\omega_0 \int_0^t \zeta(x)\mathrm{d}x} 2\mathrm{Re}\left[V_{12} e^{j\omega_0 \sqrt{1-\frac{A_{max}}{2\omega_0 Q t_{rise}}} t}\right] & \text{else.} \end{cases} \tag{A.31}$$

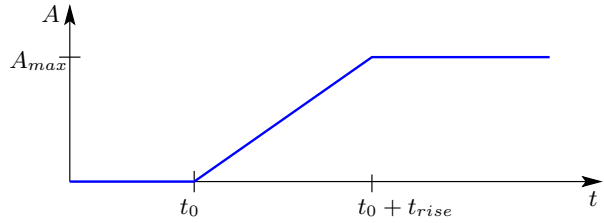

Figure A.2. On-switching function $A(t)$. The reflector is switched on at t_0.

The variables V_{11} can be found from the initial conditions. The solution $v_{Oh}(t)$ must be a continuous function, this sets the conditions for V_{12} and V_{13}.

A.2.2. Particular Solution

The particular solution can be found by the method of variation of parameters [74]. The ansatz function for the particular solution is

$$v_{Op}(t) = V_2(t)b(t) + V_2^*(t)b^*(t) \tag{A.32}$$

where $b(t)$ is the basis of the solution of the homogeneous equation

$$b(t) = e^{-\omega_0 \int_0^t \zeta(x)\mathrm{d}x} e^{j\omega_0 t\sqrt{1-\frac{\dot{A}(t)}{2\omega_0 Q}}} \tag{A.33}$$

The derivative of the ansatz function is

$$\dot{v}_{Op}(t) = V_2(t)\dot{b}(t) + V_2^*(t)\dot{b}^*(t) + \underbrace{\dot{V}_2(t)b(t) + \dot{V}_2^*(t)b^*(t)}_{0} \tag{A.34}$$

The method of variation of parameters assumes $\dot{V}_2(t)b(t)+\dot{V}_2^*(t)b^*(t) = 0$, this assumption gives later one of the equation, which the particular solution has to fulfill. The second derivative is

$$\ddot{v}_{Op}(t) = \dot{V}_2(t)\dot{b}(t) + \dot{V}_2^*(t)\dot{b}^*(t) + V_2(t)\ddot{b}(t) + V_2^*(t)\ddot{b}^*(t) \tag{A.35}$$

Hence, the differential equation for the particular solution is

$$\begin{aligned}\dot{V}_2\dot{b} + \dot{V}_2^*\dot{b}^* + V_2\ddot{b} + V_2^*\ddot{b}^* + \frac{\omega_0}{Q}(1-A)(V_2\dot{b} + V_2^*\dot{b}^*) \\ + \left(\omega_0^2 - \frac{\omega_0}{Q}\dot{A}\right)(V_2 b + V_2^* b^*) = \frac{\omega_0}{Q}\dot{v}_{in}\end{aligned} \tag{A.36}$$

We know that $b(t)$ fulfills the homogeneous equation, which reduces (A.36) to

$$\dot{V}_2\dot{b} + \dot{V}_2^*\dot{b}^* = \frac{\omega_0}{Q}\dot{v}_{in} \tag{A.37}$$

The particular solution has to fulfill

$$\dot{V}_2(t)b(t) + \dot{V}_2^*(t)b^*(t) = 0 \tag{A.38}$$

$$\dot{V}_2(t)\dot{b}(t) + \dot{V}_2^*(t)\dot{b}^*(t) = \frac{\omega_0}{Q}\dot{v}_{in} \tag{A.39}$$

The complex conjugate b^* of $b(t)$ is known

$$b^*(t) = e^{-\omega_0\int_0^t \zeta(x)\mathrm{d}x}e^{-j\omega_0 t\sqrt{1-\frac{\dot{A}(t)}{2\omega_0 Q}}} = b(t)e^{-2j\omega_0 t\sqrt{1-\frac{\dot{A}(t)}{2\omega_0 Q}}} \tag{A.40}$$

and $b(t)$ is not zero. Dividing (A.38) by $b(t)$ and solving for $\dot{V}_2^*(t)$ leads to

$$\dot{V}_2^*(t) = -\dot{V}_2(t)e^{2j\omega_0 t\sqrt{1-\frac{\dot{A}(t)}{2\omega_0 Q}}} \tag{A.41}$$

Inserting (A.41) and (A.40) into (A.39) leads to

$$2j\omega_0 b(t)\dot{V}_2(t) = \frac{\omega_0}{Q}\dot{v}_{in}(t) \tag{A.42}$$

which, after integration, results in

$$V_2(t) = -\frac{j}{2Q}\int_0^t \frac{\dot{v}_{in}(\tau)}{b(\tau)}\mathrm{d}\tau \tag{A.43}$$

$$= -\frac{j}{2Q}\int_0^t \dot{v}_{in}(\tau)e^{\omega_0\int_0^\tau \zeta(x)\mathrm{d}x}e^{-j\tau\omega_0\sqrt{1-\frac{\dot{A}(\tau)}{2\omega_0 Q}}}\mathrm{d}\tau \tag{A.44}$$

Finally, the particular solution is

$$v_{Op}(t) = b(t)V_2(t) + V_2^*(t)b^*(t) = 2\mathrm{Re}[b(t)V_2(t)] \tag{A.45}$$

$$= -\frac{e^{-\omega_0\int_0^t \zeta(x)\mathrm{d}x}}{Q}\mathrm{Re}\left[je^{j\omega_0 t\sqrt{1-\frac{\dot{A}(t)}{2\omega_0 Q}}}\right.$$

$$\left.\cdot\int_0^t \dot{v}_{in}(\tau)e^{\omega_0\int_0^\tau \zeta(x)\mathrm{d}x}e^{-j\tau\omega_0\sqrt{1-\frac{\dot{A}(\tau)}{2\omega_0 Q}}}\mathrm{d}\tau\right]. \tag{A.46}$$

For a compacter form, the receiver gain $G(t)$ and the sensitivity curve $s(t)$ are defined

$$G(t) = \frac{e^{-\omega_0\int_0^t \zeta(x)\mathrm{d}x}}{Q} \tag{A.47}$$

$$s(t) = e^{\omega_0\int_0^t \zeta(x)\mathrm{d}x} \tag{A.48}$$

The particular solution is then

$$v_{Op}(t) = -G(t)\mathrm{Im}\left[e^{j\omega_0 t\sqrt{1-\frac{\dot{A}(t)}{2\omega_0 Q}}}\int_0^t \dot{v}_{in}(\tau)s(\tau)e^{-j\tau\omega_0\sqrt{1-\frac{\dot{A}(\tau)}{2\omega_0 Q}}}\mathrm{d}\tau\right]. \tag{A.49}$$

The sensitivity function $s(t)$ weights the incoming signal $\dot{v}_{in}(t)$. The larger $s(t)$ is, the stronger is the influence of the incoming signal on the output signal, hence the name sensitivity function. The $\zeta(t)$ function is known

$$\zeta(t) = \frac{1-A(t)}{2Q} = \begin{cases} \frac{1}{2Q} & \text{if } t < t_0, \\ \frac{1}{2Q}\left(1-(t-t_0)\frac{A_{max}}{t_{rise}}\right) & \text{if } t_0 \le t \le t_0 + t_{rise}, \\ \frac{1}{2Q}\left(1-A_{max}\right) & \text{if } t > t_0 + t_{rise} \end{cases} \tag{A.50}$$

and the sensitivity curve for this $\zeta(t)$ is

$$s(t) = \begin{cases} e^{\frac{\omega_0}{2Q}t} & \text{if } t < t_0, \\ e^{\frac{\omega_0}{2Q}\left(t-\frac{A_{max}}{2t_{rise}}(t-t_0)^2\right)} & \text{if } t_0 \le t \le t_0 + t_{rise}, \\ e^{\frac{\omega_0 t}{2Q}(1-A_{max})} & \text{if } t > t_0 + t_{rise}. \end{cases} \tag{A.51}$$

The normalized sensitivity curve $(s(t)/\max|s(t)|)$, $\zeta(t)$ and the numerical solution of $v_{Op}(t)$ are plotted in Fig. A.3. The higher the maximum gain A_{max} is, the narrower is the sensitivity function. The time during which the reflector is sensitive to incoming signals, called sampling window, decreases. But the sampling window widens for higher Q-factors. The sampling window also decreases for a faster on-switching (smaller t_{rise}) as illustrated in Fig. A.4.

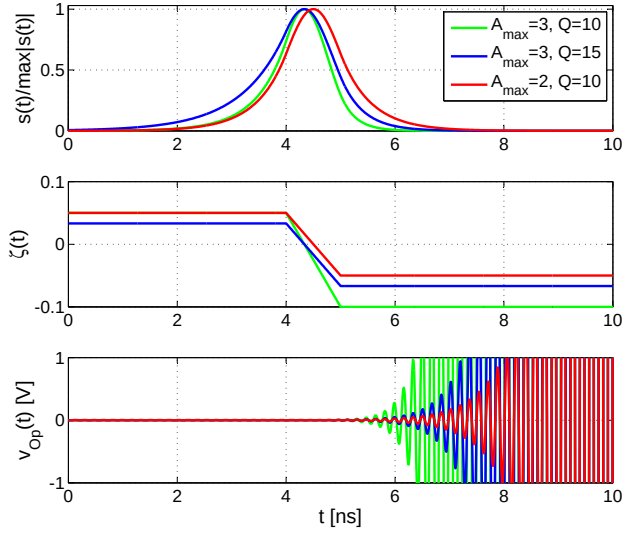

Figure A.3. The normalized sensitivity curve $(s(t)/\max|s(t)|)$, the damping function $\zeta(t)$ and the numerical solution of $v_{Op}(t)$ are plotted for $t_0 = 4$ ns, $t_{rise} = 1$ ns, $v_{in} = B\sin(\omega t)$ with $B = 1$ mV and $\omega = \omega_0 = 2\pi \cdot 5.8$ GHz.

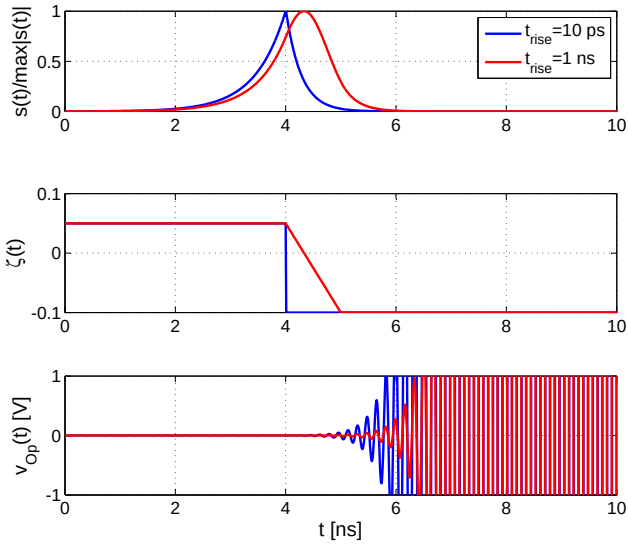

Figure A.4. Comparison of the normalized sensitivity curve $(s(t)/\max|s(t)|)$, the damping function $\zeta(t)$ and the numerical solution of $v_{Op}(t)$ with a fast on-switching process ($t_{rise} = 10$ ps) and a slow on-switching process ($t_{rise} = 1$ ns) respectively. The simulation parameters are $t_0 = 4$ ns, $A_{max} = 3$, $Q = 10$, $v_{in} = B\sin(\omega t)$ with $B = 1$ mV and $\omega = \omega_0 = 2\pi \cdot 5.8$ GHz.

A.3. Q-factor of Loaded LC Tank

The bandpass filter $F_{Filt}(s)$ is modeled in Chapter 2 as

$$F_{Filt}(s) = \frac{v_{out}}{v_{in}} = \frac{sL}{s^2LCR + sL + R} = \frac{s\frac{\omega_0}{Q}}{s^2 + s\frac{\omega_0}{Q} + \omega_0^2}. \tag{A.52}$$

The circuit implementation consists of two differential pairs with parallel LC loads, as depicted in Fig. 4.4. This LC load has a slightly different characteristic than the ideal bandpass filter. The small signal, single ended equivalent of one differential pair with LC load is plotted in Fig. A.5. The inductance has a quality factor Q_L

$$Q_L = \frac{\omega_0 L}{R_L} \tag{A.53}$$

which is according to the model guide less than 25 [83] for the 0.18-μm CMOS technology. The quality factor Q_C of the capacitor is defined as

$$Q_C = \frac{1}{\omega_0 C R_C}. \tag{A.54}$$

The metal insulator metal (MIM) capacitors have a Q_C factor of around 150 at 5.8 GHz. The hyper-abrupt varactors have a much lower Q-factor. The extracted simulation of the varactor revealed that the Q_C factor is as low as 16, if all interconnects and vias are taken into account.

The transfer function of the small signal equivalent from Fig. A.5 is

$$F_{LC}(s) = \frac{v_{out}}{v_{in}} = g_m \cdot \left(\frac{1}{\frac{1}{sL+R_L} + \frac{sC}{sCR_C+1} + \frac{1}{r_{ds}}} \right). \tag{A.55}$$

The reflector consists of two differential pairs, but the second differential pair has a lower r_{ds} as the first differential pair, because the second differential pair drives the antenna and thus consists of wider transistors. The overall transfer function is

$$F_{tot}(s) = F_{LC,r_{dsO}}(s) \cdot F_{LC,r_{dsI}}(s). \tag{A.56}$$

The transfer functions $F_{LC,r_{dsI}}$, F_{Filt} and F_{tot} are compared in Fig. A.6. The Q factor of the overall transfer function F_{tot} is 8.1.

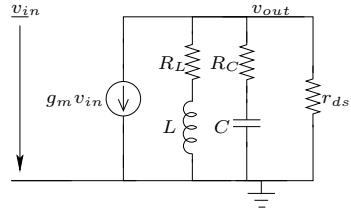

Figure A.5. Single ended small signal equivalent of a loaded LC tank.

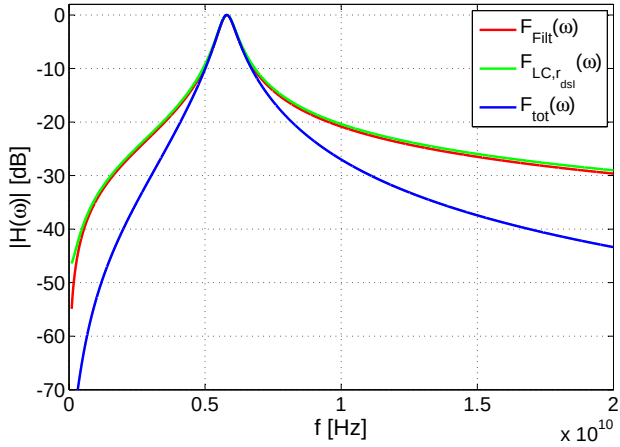

Figure A.6. Comparison of the transfer function of a second order band-pass filter F_{Filt}, a single loaded LC-tank $F_{LC,r_{dsI}}$ and the complete transfer function of the active reflector F_{tot}.

A.4. Oscillation Frequency vs Temperature

An LC tank is temperature dependent. The inductor depends on temperature. The inductor is made of aluminium, the temperature dependence of the resistance of aluminium is

$$R_L(T) = R_{L,ref} \cdot (1 + \alpha(T - T_{ref})) \tag{A.57}$$

with the temperature coefficient of resistance $\alpha = 0.004308$. With higher temperature, the resistance of the inductor increases and thus the quality factor Q_L decreases. In addition, the inductance slightly increases because of thermal expansion of the inductor.

Varactors are also temperature dependent. The temperature coefficient of a MOS capacitor can be resolved into three components [140]. Firstly, the capacitance changes due to thermal expansion, mainly the gate. Secondly, the space charge capacitance is temperature dependent and lastly, the dielectric constant of the oxide k_{ox} depends on the temperature.

The influence of the temperature on the resonance frequency f_0 and the quality factor Q_{LC} can be simulated with the available BSIM3.3 models. The schematic of the simulated LC tank is depicted in Fig. A.7. The quality factor Q_{LC} decreases almost linearly with increasing temperature (Fig. A.8). The oscillation frequency f_0 decreases by approximately 1.2 MHz per 1°C temperature increase. This is 201 ppm/°C. Figure A.9 illustrates the temperature dependence of the resonance frequency f_0.

A.5. Confidence Interval for Standard Deviation

The confidence interval for standard deviation σ of a normal distribution is presented in [141]. Suppose the variable X is normal distributed with mean μ and σ. The variable is n times sampled. The sample has a variance s^2 and a mean $\overline{x}$. The $1 - \alpha$ confidence interval for σ is

$$\left[\sqrt{\frac{(n-1)s^2}{\chi^2_{\alpha/2,n-1}}}, \sqrt{\frac{(n-1)s^2}{\chi^2_{1-\alpha/2,n-1}}} \right], \tag{A.58}$$

As an example, we can take the data from the SNR simulations in Section 3.3.7. 20 simulations are carried out for each SNR ($n = 20$). The sampled standard deviation s for a SNR of 3 dB is 3.083 cm. the

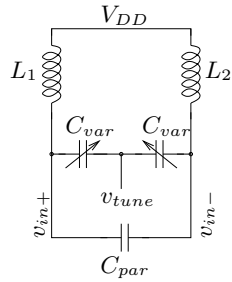

Figure A.7. Simulated LC tank consisting of two HA varactor diodes, a symmetrical inductance (here drawn as two inductances L_1 and L_2) and a parasitic capacitance C_{par}.

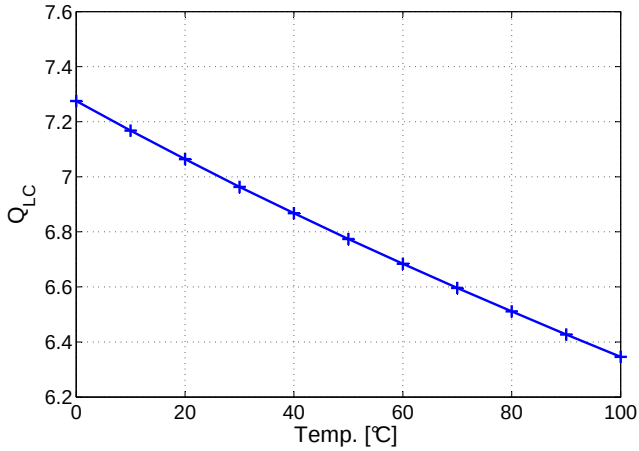

Figure A.8. Temperature dependence of the quality factor Q_{LC}.

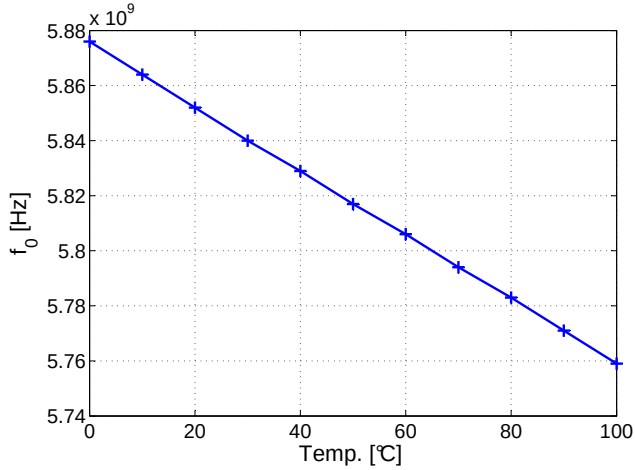

Figure A.9. Temperature dependence of the resonance frequency f_{LC} of an LC tank.

95% $(1-\alpha)$ confidence interval for σ is

$$\left[\sqrt{\frac{19\cdot 3.08^2}{\chi^2_{0.025,19}}}, \sqrt{\frac{19\cdot 3.08^2}{\chi^2_{0.975,19}}}\right]. \tag{A.59}$$

$\chi^2_{0.975,19}$ is 32.8524 and $\chi^2_{0.975,19}$ is 8.9066, thus the 95% confidence interval of σ is

$$[s\cdot 0.7605, s\cdot 1.4606] = [2.342, 4.499], \tag{A.60}$$

where s is the measured standard deviation.

A.6. Varactor Diode

A hyper-abrupt junction varactor is used for the tuning capability of the active reflector [142], [143]. The capacitance of the varactor diode

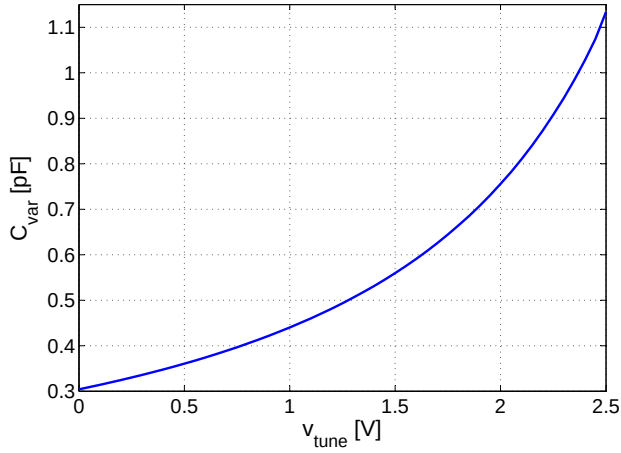

Figure A.10. HA Varactor tuning behavior.

is

$$C_{nom}(V) = C_A(V)\, LWN + C_P(V)\, 2N(W+L) \tag{A.61}$$

$$C_A(V) = \frac{C_{A0}}{\left(1 - \frac{V}{pb}\right)^{ma}} \tag{A.62}$$

$$C_P(V) = \frac{C_{P0}}{\left(1 - \frac{V}{php}\right)^{mp}}, \tag{A.63}$$

where N is the number of anodes, W is the anode width and L is the length of the varactor's anode. The other parameters can be found in the design manual [102].

Glossary

$\alpha(d)$ free space loss for a distance d. 68

$\overline{\Delta d}$ mean distance error. 93

Δd_{min} is the minimal range resolution. 24

$F_{Filt}(\omega)$ transfer function of the band-pass feedback. 30

Δf_{min} is the minimal frequency resolution. 24

f_{mod} is the modulation frequency of the active pulsed reflector. 46

F_{Osz} closed loop transfer function of the oscillator. 31

G_{pr} pathloss. 104

$\mathcal{L}(\Delta\omega)$ phase noise characteristic described by the Leeson formula. 90

ω_{BW} sweep bandwidth of the linear frequency ramp. 12

ω_{SW} time dependent part of the linear frequency ramp. 63

ϕ_{rec} received phase at the antenna of the reflector. 23

ϕ_{refl} output phase of the reflector. 23

ϕ_{rx} phase of the received signal s_{rx} at the base station. 23

ϕ_{tx} phase of the base station's output signal. 23

S_{11} reflection coefficient. 127

s_{bb} the resulting base-band signal. 67

s_{filt} the filtered, down-converted signal at the base station without the periodic modulation. 66

$\sigma_{\Delta d}$ standard deviation of the distance error. 93

SR slew rate. 129

s_{rec} received signal at the reflector. 63

s_{ref} output signal of the reflector. 65

s_{rx} received signal at the base station. 20

s_{tx} signal, which the base station transmits. 20

T sweep duration of the linear frequency ramp. 12

τ Time-of-flight. 13

t_{on} time during which the reflector is switched on. 46

$y_{out}(t)$ output signal of the reflector. 53

Z_{in} input impedance of the reflector. 127

Acronyms

ADC analog-to-digital converter. 15, 68, 95

AGV autonomous guided vehicles. 2, 9, 16

AM amplitude modulated. 30

AoA angle-of-arrival. 6

APR active pulsed reflector. 66

ASIC application-specific integrated circuit. 27

AWGN Additive white Gaussian noise. 91

BS base station. 17, 19, 68

CMM coordinate measuring machine. 8

CW continuous wave. 10, 11, 47

DDS direct digital synthesizer. 146, 165

DFT discrete Fourier transform. 146

DSO digital sampling oscilloscope. 47

EIRP equivalent isotropically radiated power. 6, 25

FDMA frequency division multiple access. 23

FFT fast Fourier transform. 20, 211

FMCW frequency modulated continuous wave. 11, 13

FPGA field-programmable gate array. 15

GNSS global navigation satellite system. 3, 7

GPS global positioning system. 1

IMU inertial measurement unit. 3

ISM industrial, scientific and medical. 15, 54, 69

LAN local area network. 19

LNA low-noise amplifier. 15, 146

LOS line-of-sight. 6, 68, 104, 106

MIM metal insulator metal. 223

MPC multipath component. 102, 105

MS mobile station. 2, 14, 19

NLOS non-line-of-sight. 25, 104

PA power amplifier. 146

PLL phase locked loop. 29, 165

RFID radio frequency identification. 4

RS reference station. 17, 19

RSS received signal strength. 3, 4

RTK real time kinematic. 7

RToF round-trip time-of-flight. 13, 19, 20, 96, 165

SNR signal-to-noise ratio. 47, 70, 80, 91

TDMA time division multiple access. 20

TDoA time difference of arrival. 3, 17, 165

ToF time-of-flight. 4

UWB ultra-wideband. 6, 29, 104

VCO voltage-controlled oscillator. 29

VGA variable gain amplifier. 15

WLAN wireless local area network. 4

XO quartz oscillator. 146

Bibliography

[1] S. Beyer, "Bulk solids picking robot for plant automation." http://www.bulk-solids-handling.com/conveying_transportation/mechanical_coveyor_systems_belt_conveyor_systems/articles/255339/, Nov. 2009. [Online; accessed Mar. 8, 2011]. 1.1

[2] SICK AG, *Application: Safe travel path monitoring and navigation support for mobile robots*, 2011. 1.1

[3] G. P. Technology, "Automated guided vehicles." http://www.gottwald.com/gottwald/site/gottwald/en/products/agv.html. [Online; accessed Mar. 8, 2011]. 1.1

[4] M. Scholz, T. Riedel, and C. Decker, "A flexible architecture for a robust indoor navigation support device for firefighters," in *Networked Sensing Systems (INSS), 2010 Seventh International Conference on*, pp. 227 –232, June 2010. 1.1

[5] S. Gandhi, A. Ganz, and G. Mullett, "FIREGUIDE: Firefighter guide and tracker," in *Engineering in Medicine and Biology Society (EMBC), 2010 Annual International Conference of the IEEE*, pp. 2037 –2040, Sep. 2010. 1.1

[6] H. Gellersen, P. Lukowicz, M. Beigl, and T. Riedel, "Cooperative relative positioning," *Pervasive Computing, IEEE*, vol. 9, pp. 78 –89, Oct. 2010. 1.1, 1.2

[7] C. Guo, J. Wang, R. Prasad, and M. Jacobsson, "Improving the accuracy of person localization with body area sensor networks: An experimental study," in *Consumer Communications and Networking Conference, 2009. CCNC 2009. 6th IEEE*, pp. 1 –5, Jan. 2009. 1.1

[8] A. L. Liu, H. Hile, G. Borriello, H. Kautz, B. Ferris, P. A. Brown, M. Harniss, and K. Johnson, "Implications for location systems in indoor wayfinding for individuals with cognitive impairments," in *Pervasive Health Conference and Workshops, 2006*, pp. 1 –5, Dec. 2006. 1.1

[9] Y.-J. Chang, C.-N. Chen, L.-D. Chou, and T.-Y. Wang, "A novel indoor wayfinding system based on passive RFID for individuals with cognitive impairments," in *Pervasive Computing Technologies for Healthcare, 2008. PervasiveHealth 2008. Second International Conference on*, pp. 108 –111, Feb. 2008. 1.1

[10] R. Mautz, M. Kunz, and H. Ingensand, eds., *Indoor Positioning and Indoor Navigation (IPIN), 2010 International Conference on*, Sep. 2010. 1.2, 1.2

[11] G. Hein, M. Paonni, V. Kropp, and A. Teuber, "GNSS indoors fighting the fading, part 1," in *Working Paper, Inside GNSS*, pp. 43–52, Apr. 2008. 1.2

[12] S. Schon and O. Bielenberg, "On the capability of high sensitivity GPS for precise indoor positioning," in *Positioning, Navigation and Communication, 2008. WPNC 2008. 5th Workshop on*, pp. 121 –127, march 2008. 1.2

[13] M. Monnerat, "AGNSS standardization: The path to success in location-based services," in *Inside GNSS*, Aug. 2008. 1.2

[14] M. Kjrgaard, H. Blunck, T. Godsk, T. Toftkjr, D. Christensen, and K. Grnbk, "Indoor positioning using GPS revisited," *Lecture Notes in Computer Science*, vol. 6030, pp. 38–56, 2010. Title of the vol.: Pervasive Computing. Proceedings. / Patrik Floren, Antonio Krger and Mirjana Spasojevic (eds.) ISBN: 978-3-642-12653-6. 1.2

[15] J. Barnes, C. Rizos, J. Wang, D. Small, G. Voigt, and N. Gambale, "LocataNet: Intelligent time-synchronised pseudolite transceivers for cm-level stand-alone positioning," 2003. 1.2

[16] A. Vervisch-Picois and N. Samama, "Interference mitigation in a repeater and pseudolite indoor positioning system," *Selected Topics in Signal Processing, IEEE Journal of*, vol. 3, pp. 810 –820, Oct. 2009. 1.2

[17] A. Vervisch-Picois, I. Selmi, Y. Gottesman, and N. Samama, "Current status of the repealite based approach: A sub-meter indoor positioning system," in *Satellite Navigation Technologies and European Workshop on GNSS Signals and Signal Processing (NAVITEC), 2010 5th ESA Workshop on*, pp. 1 –6, Dec. 2010. 1.2

[18] A. Fluerasu, A. Vervisch-Picois, G. Boiero, G. Ghinamo, P. Lovisolo, and N. Samama, "Indoor positioning using GPS transmitters: Experimental results," in *Indoor Positioning and Indoor Navigation (IPIN), 2010 International Conference on*, pp. 1 –9, Sep. 2010. 1.2

[19] D. Gusenbauer, C. Isert, and J. Kro andsche, "Self-contained indoor positioning on off-the-shelf mobile devices," in *Indoor Positioning and Indoor Navigation (IPIN), 2010 International Conference on*, pp. 1 –9, Sep. 2010. 1.2

[20] Q. Ladetto and B. Merminod, "Digital magnetic compass and gyroscope integration for pedestrian navigation," in *9th Saint Petersburg International Conference on Integrated Navigation Systems*, (Saint Petersburg, Russia), May 2002. 1.2

[21] Q. Ladetto, J. van Seeters, S. Sokolowski, Z. Sagan, and B. Merminod, "Digital magnetic compass and gyroscope for dismounted soldier position & navigation," in *Military Capabilities enabled by Advances in Navigation Sensors, Sensors & Electronics Technology Panel, NATO-RTO meetings*, (Istanbul, Turkey), Oct. 2002. 1.2

[22] Q. Ladetto and B. Merminod, "In step with INS navigation for the blind, tracking emergency crews," *GPS World*, vol. 13, pp. 30–38, Oct. 2002. 1.2

[23] P. Bahl and V. Padmanabhan, "RADAR: an in-building RF-based user location and tracking system," in *INFOCOM 2000. Nineteenth Annual Joint Conference of the IEEE Computer and Communications Societies. Proceedings. IEEE*, vol. 2, pp. 775 – 784 vol.2, 2000. 1.2

[24] F. Tappero, B. Merminod, and M. Ciurana, "IEEE 802.11 ranging and multi-lateration for software-defined positioning receiver," in *Indoor Positioning and Indoor Navigation (IPIN), 2010 International Conference on*, pp. 1 –6, Sep. 2010. 1.2

[25] L. Ni, Y. Liu, Y. C. Lau, and A. Patil, "LANDMARC: indoor location sensing using active RFID," in *Pervasive Computing and Communications, 2003. (PerCom 2003). Proceedings of the First IEEE International Conference on*, pp. 407 – 415, Mar. 2003. 1.2

[26] F. Seco, C. Plagemann, A. Jime andnez, and W. Burgard, "Improving RFID-based indoor positioning accuracy using Gaussian processes," in *Indoor Positioning and Indoor Navigation (IPIN), 2010 International Conference on*, pp. 1 –8, Sep. 2010. 1.2

[27] N. B. Priyantha, *The Cricket Indoor Location System*. PhD thesis, Massachusetts Institute of Technology (MIT), 2005. 1.2

[28] A. Ward, A. Jones, and A. Hopper, "A new location technique for the active office," *Personal Communications, IEEE*, vol. 4, pp. 42 –47, Oct. 1997. 1.2

[29] G. Oberholzer, P. Sommer, and R. Wattenhofer, "SpiderBat: Augmenting wireless sensor networks with distance and angle information," in *10th ACM/IEEE International Conference on Information Processing in Sensor Networks (IPSN), Chicago, IL, USA*, Apr. 2011. 1.2

[30] Y. Fukuju, M. Minami, H. Morikawa, and T. Aoyama, "DOLPHIN: an autonomous indoor positioning system in ubiquitous computing environment," in *Software Technologies for Future Embedded Systems, 2003. IEEE Workshop on*, pp. 53 – 56, May 2003. 1.2

[31] "LPR-2D: Position detection of cranes and vehicles for tracking of goods," tech. rep., Symeo GmbH, 2009. 1.2

[32] A. Stelzer, A. Fischer, and M. Vossiek, "A new technology for precise local position measurement - LPM," in *Microwave Symposium Digest, 2004 IEEE MTT-S International*, vol. 2, pp. 655 – 658 Vol.2, June 2004. 1.2

[33] R. Pfeil, M. Pichler, P. Scherz, A. Stelzer, and G. Stelzhammer, "Power-level surveillance for an fmcw-based local positioning system," in *Indoor Positioning and Indoor Navigation (IPIN), 2010 International Conference on*, pp. 1 –10, Sep. 2010. 1.2, 5.10

[34] A. Stelzer, K. Pourvoyeur, A. Fischer, and G. Gassenbauer, "A local position measurement system with integrated telemetry channel," in *Radio and Wireless Symposium, 2006 IEEE*, pp. 91 – 94, Jan. 2006. 1.2

[35] A. E. AG, "Lpm - the technology - specification." `http://www.abatec-ag.com/index_html?sc=46328500`. [Online; accessed Mar. 24, 2011]. 1.2

[36] "First report and order (revision of part 15 of the commissions rules regarding ultra-wideband transmission systems)," tech. rep., Federal Communication Commission, Feb. 2002. ET Docket 98-153. 1.2

[37] "Ubisense series 9000 compact tag," tech. rep., Ubisense, 2011. 1.2

[38] "3D guidance trakSTAR," tech. rep., Ascension Technology Corporation, 2010. 1.2

[39] "FASTRAK - product brochure," tech. rep., Polhemus, 2008. 1.2

[40] J. Blankenbach and A. Norrdine, "Position estimation using artificial generated magnetic fields," in *Indoor Positioning and Indoor Navigation (IPIN), 2010 International Conference on*, pp. 1 –5, sept. 2010. 1.2

[41] "LEA-6: u-blox 6 GPS modules (data sheet)," tech. rep., uBlox, 2010. 1.2

[42] D. Manandhar, K. Honda, and S. Murai, "Accuracy assessment and improvement for level survey using real time kinematic (rtk) gps," in *Geoscience and Remote Sensing Symposium, 1999. IGARSS '99 Proceedings. IEEE 1999 International*, vol. 2, pp. 882 –884 vol.2, 1999. 1.2

[43] L. S. Monteiro, T. Moore, and C. Hill, "What is the accuracy of DGPS?," *The Journal of Navigation*, vol. 58, no. 2, pp. 207–225, 2005. 1.2

[44] N. Mir-Nasiri, "Camera-based 3D object tracking and following mobile robot," in *Robotics, Automation and Mechatronics, 2006 IEEE Conference on*, pp. 1 –6, June 2006. 1.2

[45] D. Aufderheide and W. Krybus, "Towards real-time camera egomotion estimation and three-dimensional scene acquisition from monocular image streams," in *Indoor Positioning and Indoor Navigation (IPIN), 2010 International Conference on*, pp. 1 –10, Sep. 2010. 1.2

[46] "ProCam — DPS: Optical 3D metrology for vehicle safety testing," tech. rep., AICON 3D Systems —. 1.2

[47] J. E. Muelaner, Z. Wang, O. Martin, J. Jamshidi, and P. G. Maropoulos, "Estimation of uncertainty in three-dimensional coordinate measurement by comparison with calibrated points," *Measurement Science and Technology*, vol. 21, no. 2, p. 025106, 2010. 1.2

[48] R. Mautz, "Opening session," in *Indoor Positioning and Indoor Navigation (IPIN), 2010 International Conference on*, Sep. 2010. 1.1

[49] D. K. Allison, *New Eye for the Navy: The Origin of Radar at the Naval Research Laboratory.* Washington D.C.: Naval Research Laboratory, 1981. NRL Report 8466. 1.3

[50] C. Hlsmeyer, "Verfahren, um entfernte metallische Gegenstnde mittels elektrischer Wellen einem Beobachter zu melden.." Patent DE 165546, Apr. 1904. 1.3

[51] G. Marconi, "Radio telegraphy," *Proceedings of the Institute of Radio Engineers*, vol. 10, pp. 215 – 238, Aug. 1922. 1.3

[52] I. Amato, *Seventy-Five Years of High Stakes Science and Technology at the Naval Research Laboratory.* Naval Research Laboratory, 1998. 1.3

[53] E. V. Appleton and M. A. F. Barnett, "On some direct evidence for downward atmospheric reflection of electric rays," *Proceedings of the Royal Society of London. Series A, Containing Papers of a Mathematical and Physical Character*, vol. 109, pp. pp. 621–641, Dec. 1925. 1.3

[54] G. Breit and M. A. Tuve, "A test of the existence of the conducting layer," *Phys. Rev.*, vol. 28, pp. 554–575, Sep. 1926. 1.3

[55] Wikipedia, "Continuous wave — Wikipedia, the free encyclopedia." `http://en.wikipedia.org/wiki/Continuous_wave`, 2010. [Online; accessed Feb. 28, 2011]. 1.3.1

[56] F. Ellinger, J. Carls, S. Wehrli, H. Jäckel, C. Kromer, L. Wiebking, A. Dabek, J. Hüttner, R. Roskosch, R. Gierlich, C. Seisenberger, M. Huemer, R. Mosshammer, T. Ußmüller,

R. Weigel, V. Subramanian, M. Krcmar, G. Böck, D. Doumenis, A. Kounoudes, K. Kurek, Y. Yashchyshyn, R. Szumny, A. Kalis, E. Avatagelou, A. Garbi, and S. Spiegel, "EU PROJECT RESOLUTION: Reconfigurable Systems for Mobile Local Communication and Positioning," in *Proceedings of the International Conference on Wireless Information Networks and Systems*, (Lisbon), 7-10 August 2006. 1.5

[57] F. Ellinger, R. Eickhoff, R. Gierlich, J. Huttner, A. Ziroff, S. Wehrli, T. Ussmuller, J. Carls, V. Subramanian, M. Krcmar, R. Mosshammer, S. Spiegel, D. Doumenis, A. Kounoudes, K. Kurek, Y. Yashchyshyn, C. Papadias, P. Tragas, A. Kalis, and E. Avatagelou, "Local positioning for wireless sensor networks," in *Globecom Workshops, 2007 IEEE*, pp. 1 –6, Nov. 2007. 1.5

[58] F. Ellinger and H. Jaeckel, "RESOLUTION: Annex I - 'description of work'." SIXTH FRAMEWORK PROGRAMME Information Society Technologies, 2.4.5 Mobile and wireless systems beyond 3G, 2005. 1.5

[59] R. Mosshammer, M. Huemer, R. Szumny, K. Kurek, J. Huttner, and R. Gierlich, "A 5.8 GHz local positioning and communication system," in *Microwave Symposium, 2007. IEEE/MTT-S International*, pp. 1237 –1240, June 2007. 1.5

[60] V. Subramanian, M. Krcmar, and G. Boeck, "A high performance low IF receiver for wireless local positioning applications," in *Proceedings of 38th European Microwave Conference (EuMC)*, (Amsterdam, Netherlands), 27-31 October 2008. 1.5

[61] M. Krcmar, V. Subramanian, and G. Boeck, "Low noise, high gain low-IF CMOS receiver for wireless local positioning applications," in *Proceeding of the EEEfCOM 2008*, (Ulm, Germany), May 2008. 1.5

[62] M. Krcmar, V. Subramanian, G. Boeck, and S. Spiegel, "Digitally controlled VGA for low power low-IF receivers," in *Proc. IEEE Germany Microelectronics 2009*, 2009. 1.5

[63] T. Ußmüller, R. Weigel, and R. Eickhoff, "Highly integrated fractional-n synthesizer for locatable wireless sensor nodes," in *ICC 2009 Signal Processing for Communications Symposium*, (Dresden, Germany), June 2009. 1.5

[64] A. Ziroff, J. Hüttner, R. Gierlich, and S. Wehrli, "D17 - redesign of system and testing," resolution project deliverable, Siemens and ETH Zurich, Jan. 2009. 1.5

[65] R. Mosshammer, R. Eickhoff, M. Huemer, and R. Weigel, "System topologies and performance evaluation of the RESOLUTION embedded local positioning system," *e & i Elektrotechnik und Informationstechnik*, vol. 125, pp. 347–352, 2008. 10.1007/s00502-008-0572-6. 1.5

[66] A. Ziroff, J. Huttner, R. Gierlich, R. Eickhoff, and F. Ellinger, "A wireless sensor network with radiolocation subsystem," in *GLOBECOM Workshops, 2008 IEEE*, pp. 1 –5, Dec. 2008. 1.5.2

[67] R. Gierlich, J. Huttner, A. Ziroff, and M. Huemer, "Indoor positioning utilizing fractional-N PLL synthesizer and multi-channel base stations," in *Wireless Technology, 2008. EuWiT 2008. European Conference on*, pp. 49 –52, Oct. 2008. 1.5.2, 4.5

[68] L. Wiebking, *Entwicklung eines zentimetergenauen mehrdimensionalen Nahbereichs-Navigations-Systems.* VDI Verlag, 2003. 1.5.3

[69] M. Vossiek, L. Wiebking, P. Gulden, J. Wieghardt, C. Hoffmann, and P. Heide, "Wireless local positioning," *Microwave Magazine, IEEE*, vol. 4, pp. 77 – 86, Dec. 2003. 1.5.3

[70] S. Piper, "Homodyne FMCW radar range resolution effects with sinusoidal nonlinearities in the frequency sweep," in *Radar Conference, 1995., Record of the IEEE 1995 International*, pp. 563 –567, May 1995. 1.6, 4.3

[71] D. Barras, F. Ellinger, H. Jackel, and W. Hirt, "Low-power ultra-wideband wavelets generator with fast start-up circuit," *Microwave Theory and Techniques, IEEE Transactions on*, vol. 54, pp. 2138 – 2145, May 2006. 2, 2.1.2

[72] J. Ryckaert, G. Van der Plas, V. De Heyn, C. Desset, B. Van Poucke, and J. Craninckx, "A 0.65-to-1.4 nJ/Burst 3-to-10 Ghz UWB all-digital TX in 90 nm CMOS for IEEE 802.15.4a," *Solid-State Circuits, IEEE Journal of*, vol. 42, pp. 2860 –2869, Dec. 2007. 2

[73] E. Armstrong, "Some recent developments of regenerative circuits," *Proceedings of the Institute of Radio Engineers*, vol. 10, pp. 244 – 260, Aug. 1922. 2

[74] F. Moncunill-Geniz, P. Pala-Schonwalder, and O. Mas-Casals, "A generic approach to the theory of superregenerative reception," *Circuits and Systems I: Regular Papers, IEEE Transactions on*, vol. 52, pp. 54 – 70, Jan. 2005. 2, 2.1.3, A.2, A.2.2

[75] J.-Y. Chen, M. Flynn, and J. Hayes, "A fully integrated auto-calibrated super-regenerative receiver in 0.13- μm CMOS," *Solid-State Circuits, IEEE Journal of*, vol. 42, pp. 1976 –1985, Sep. 2007. 2

[76] E. David, "RF phase control in pulsed magnetrons," *Proceedings of the IRE*, vol. 40, pp. 669–685, June 1952. 2

[77] M. Vossiek and P. Gulden, "The switched injection-locked oscillator: a novel versatile concept for wireless transponder and localization systems," *IEEE Trans. Microwave Theory Tech.*, vol. 56, pp. 859–866, apr 2008. 2

[78] L. Dai and R. Harjani, "Design of low-phase-noise CMOS ring oscillators," *Circuits and Systems II: Analog and Digital Signal Processing, IEEE Transactions on*, vol. 49, pp. 328–338, May 2002. 2.1

[79] Q. Huang, "Phase noise to carrier ratio in LC oscillators," *Circuits and Systems I: Fundamental Theory and Applications, IEEE Transactions on*, vol. 47, pp. 965 –980, jul 2000. 2.1.2

[80] G. MacFarlane and J. Whitehead, "The theory of the super-regenerative receiver operated in the linear mode," *Electrical Engineers - Part III: Radio and Communication Engineering, Journal of the Institution of*, vol. 95, pp. 143 –157, May 1948. 2.1.3, A.2

[81] ETSI, "Electromagnetic compatibility and radio spectrum matters (ERM); short range devices; radio equipment to be used in the 1 GHz to 40 GHz frequency range; part 1: Technical characteristics and test methods (ETSI EN 300 440-1 V1.3.1)," tech. rep., European Telecommunications Standards Institute, 2001. 2.3

[82] M. Vossiek and P. Gulden, "The switched injection-locked oscillator: a novel versatile concept for wireless transponder and localization systems," *IEEE Trans. Microwave Theory Tech.*, vol. 56, pp. 859–866, Apr. 2008. 3.1

[83] IBM Microelectronics Division, *BiCMOS-7WL Model Reference Guide*, v1.5.1.3 ed., Sep. 2007. 3.3.1, 4.1.2, A.3

[84] T. Bushby, "Thermal-frequency-drift compensation," *Proceedings of the IRE*, vol. 30, pp. 546 – 553, Dec. 1942. 3.3.5

[85] I. Zamek and S. Zamek, "Crystal oscillators jitter measurements and its estimation of phase noise," in *Frequency Control Symposium and PDA Exhibition Jointly with the 17th European Frequency and Time Forum, 2003. Proceedings of the 2003 IEEE International*, pp. 547 – 555, 4-8 2003. 3.3.6

[86] C. Zhang, X. Wang, and L. Forbes, "Simulation technique for noise and timing jitter in electronic oscillators," *IEE Proceedings - Circuits, Devices and Systems*, vol. 151, no. 2, p. 184, 2004. 3.3.6

[87] T. Lee and A. Hajimiri, "Oscillator phase noise: a tutorial," *Solid-State Circuits, IEEE Journal of*, vol. 35, pp. 326 –336, mar 2000. 3.3.9

[88] A. Bar-Guy, "Phase noise." `http://www.mathworks.com/matlabcentral/fileexchange/8844-phase-noise`, 2005. [Online, accessed: July 31, 2008]. 3.3.9

[89] O. Landron, M. Feuerstein, and T. Rappaport, "In situ microwave reflection coefficient measurements for smooth and rough exterior wall surfaces," in *Vehicular Technology Conference, 1993 IEEE 43rd*, pp. 77–80, May 1993. 3.4.2, 5.2

[90] Z. Irahhauten, H. Nikookar, and G. Janssen, "An overview of ultra wide band indoor channel measurements and modeling," *IEEE Microwave and Wireless Components Letters*, vol. 14, no. 8, p. 386, 2004. 3.5.1

[91] C.-C. Chong, C.-M. Tan, D. Laurenson, S. McLaughlin, M. Beach, and A. Nix, "A novel wideband dynamic directional

indoor channel model based on a markov process," *IEEE Transactions on Wireless Communications*, vol. 4, no. 4, p. 1539, 2005. 3.5.1

[92] Z. Irahhauten, A. Yarovoy, G. Janssen, H. Nikookar, and L. Ligthart, "Ultra-wideband indoor propagation channel: Measurements, analysis and modeling," in *Antennas and Propagation, 2006. EuCAP 2006. First European Conference on*, pp. 1 –6, 6-10 2006. 3.5.1

[93] A. F. Molisch, "Ultrawideband propagation channels-theory, measurement, and modeling," *IEEE Trans. Veh. Technol.*, vol. 54, pp. 1528–1545, Sep. 2005. 3.5.1

[94] A. F. Molisch, K. Balakrishnan, C. chin Chong, S. Emami, A. Fort, J. Karedal, J. Kunisch, H. Schantz, U. Schuster, and K. Siwiak, "IEEE 802.15.4a channel model - final report," in *Converging: Technology, work and learning. Australian Government Printing Service*, Online Available, 2004. 3.5.1

[95] J. Karedal, S. Wyne, P. Almers, F. Tufvesson, and A. Molisch, "Statistical analysis of the UWB channel in an industrial environment," in *Vehicular Technology Conference, 2004. VTC2004-Fall. 2004 IEEE 60th*, vol. 1, pp. 81 – 85 Vol. 1, Sep. 2004. 3.5.3

[96] Y. Eo and K. Lee, "A fully integrated 24-dBm CMOS power amplifier for 802.11a WLAN applications," *Microwave and Wireless Components Letters, IEEE*, vol. 14, pp. 504 – 506, Nov. 2004. 4.1

[97] W. Zhang, E.-S. Khoo, and T. Tear, "A low voltage fully integrated 0.18um CMOS power amplifier for 5GHz WLAN," in *Solid-State Circuits Conference, 2002. ESSCIRC 2002. Proceedings of the 28th European*, pp. 215 – 218, Sep. 2002. 4.1

[98] A. Behzad, Z. M. Shi, S. Anand, L. Lin, K. Carter, M. Kappes, T.-H. Lin, T. Nguyen, D. Yuan, S. Wu, Y. Wong, V. Fong, and A. Rofougaran, "A 5-GHz direct-conversion CMOS transceiver utilizing automatic frequency control for the IEEE 802.11a wireless LAN standard," *Solid-State Circuits, IEEE Journal of*, vol. 38, pp. 2209 – 2220, Dec. 2003. 4.1

[99] Y.-J. Chan, C.-F. Huang, C.-C. Wu, C.-H. Chen, and C.-P. Chao, "Performance consideration of mos and junction diodes

for varactor application," *Electron Devices, IEEE Transactions on*, vol. 54, pp. 2570 –2573, sept. 2007. 4.1.2

[100] Q. Zhang, J. Liou, J. McMacken, J. Thomson, and P. Layman, "SPICE modeling and quick estimation of MOSFET mismatch based on BSIM3 model and parametric tests," *Solid-State Circuits, IEEE Journal of*, vol. 36, pp. 1592 –1595, Oct. 2001. 4.1.2

[101] S. Lovett, M. Welten, A. Mathewson, and B. Mason, "Optimizing MOS transistor mismatch," *Solid-State Circuits, IEEE Journal of*, vol. 33, pp. 147 –150, Jan. 1998. 4.1.2

[102] IBM Microelectronics Division, *BiCMOS7WL Design Manual*, Sep. 2006. 4.1.2, A.6

[103] S. Wehrli, D. Barras, F. Ellinger, and H. Jäckel, "Integrated active pulsed reflector for fmcw radar localization," in *Microwave Symposium Digest, 2009. MTT '09. IEEE MTT-S International*, pp. 81–84, June 2009. 4.2

[104] S. Wehrli, R. Gierlich, J. Huttner, D. Barras, F. Ellinger, and H. Jackel, "Integrated active pulsed reflector for an indoor local positioning system," *Microwave Theory and Techniques, IEEE Transactions on*, vol. 58, pp. 267 –276, Feb. 2010. 4.2

[105] B. Sporrer, "Active reflector PCB integration," semester thesis, ETH Zürich, June 2010. 4.2

[106] S. Scheiblhofer, S. Schuster, and A. Stelzer, "Effects of systematic FMCW radar sweep nonlinearity on bias and variance of target range estimation," in *Microwave Symposium Digest, 2006. IEEE MTT-S International*, pp. 1418 –1421, June 2006. 4.3

[107] M. Pichler, A. Stelzer, P. Gulden, C. Seisenberger, and M. Vossiek, "Phase-error measurement and compensation in PLL frequency synthesizers for FMCW sensors - I: Context and application," *Circuits and Systems I: Regular Papers, IEEE Transactions on*, vol. 54, pp. 1006 –1017, May 2007. 4.3

[108] M. Pichler, A. Stelzer, P. Gulden, C. Seisenberger, and M. Vossiek, "Phase-error measurement and compensation in PLL frequency synthesizers for FMCW sensors - II: Theory," *Circuits and Systems I: Regular Papers, IEEE Transactions on*, vol. 54, pp. 1224 –1235, June 2007. 4.3

[109] M. Navarro and M. Najar, "Toa and doa estimation for positioning and tracking in ir-uwb," in *2007 IEEE International Conference on Ultra-Wideband*, pp. 574 – 579, Sept. 2007. 4.4.5, 4.4.6

[110] J. Huettner, R. Gierlich, A. Ziroff, and R. Weigel, "A low cost ultra-wide-band pulse radar in a guided wave gauging application," in *Radar Conference, 2009. EuRAD 2009. European*, pp. 101 –104, Oct. 2009. 4.4.6

[111] M. Vossiek, A. Urban, S. Max, and P. Gulden, "Inverse synthetic aperture secondary radar concept for precise wireless positioning," *IEEE Trans. Microwave Theory Tech.*, vol. 55, pp. 2447 – 2453, Nov. 2007. 4.4.6

[112] S. Max, P. Gulden, and M. Vossiek, "Localization of backscatter transponders based on a synthetic aperture secondary radar imaging approach," in *5th IEEE Sensor Array and Multichannel Signal Processing Workshop*, pp. 437 – 440, July 2008. 4.4.6

[113] S. Roehr, P. Gulden, and M. Vossiek, "Precise distance and velocity measurement for real time locating in multipath environments using a frequency-modulated continuous-wave secondary radar approach," *Microwave Theory and Techniques, IEEE Transactions on*, vol. 56, pp. 2329–2339, Oct. 2008. 4.5, 4.5

[114] B. Waldmann, R. Weigel, P. Gulden, and M. Vossiek, "Pulsed frequency modulation techniques for high-precision ultra wideband ranging and positioning," in *Ultra-Wideband, 2008. ICUWB 2008. IEEE International Conference on*, vol. 2, pp. 133 –136, Sep. 2008. 4.5, 4.5

[115] A. Stelzer, K. Pourvoyeur, and A. Fischer, "Concept and application of LPM - a novel 3-D local position measurement system," *Microwave Theory and Techniques, IEEE Transactions on*, vol. 52, pp. 2664 – 2669, Dec. 2004. 4.5, 4.5

[116] R. Gierlich, J. Huttner, A. Dabek, and M. Huemer, "Performance analysis of FMCW synchronization techniques for indoor radiolocation," in *Wireless Technologies, 2007 European Conference on*, pp. 24 –27, Oct. 2007. 4.5

[117] T. Ussmuller, R. Weigel, and R. Eickhoff, "Highly integrated fractional-n synthesizer for locatable wireless sensor nodes," in

Communications, 2009. ICC '09. IEEE International Conference on, pp. 1 –5, June 2009. 4.5

[118] D. Schettino, F. Moreira, and C. Rego, "Efficient ray tracing for radio channel characterization of urban scenarios," *Magnetics, IEEE Transactions on*, vol. 43, pp. 1305 –1308, Apr. 2007. 5.2

[119] F. Fuschini, H. El-Sallabi, V. Degli-Esposti, L. Vuokko, D. Guiducci, and P. Vainikainen, "Analysis of multipath propagation in urban environment through multidimensional measurements and advanced ray tracing simulation," *Antennas and Propagation, IEEE Transactions on*, vol. 56, pp. 848 –857, Mar. 2008. 5.2

[120] A. Magleby, C. Furse, and Z. Yun, "3d ray-tracing for intra-vehicle environments," in *Antennas and Propagation Society International Symposium, 2009. APSURSI '09. IEEE*, pp. 1 –4, June 2009. 5.2

[121] O. Landron, M. Feuerstein, and T. Rappaport, "A comparison of theoretical and empirical reflection coefficients for typical exterior wall surfaces in a mobile radio environment," *Antennas and Propagation, IEEE Transactions on*, vol. 44, pp. 341–351, Mar. 1996. 5.2

[122] J. McDonnell, "Characteristics of the indoor wireless propagation environment at microwave and millimetre frequencies," in *Radio Communications at Microwave and Millimetre Wave Frequencies (Digest No. 1996/239), IEE Colloquium on*, pp. 13/1 –13/6, 16 1996. 5.2

[123] A. Molisch, D. Cassioli, C.-C. Chong, S. Emami, A. Fort, B. Kannan, J. Karedal, J. Kunisch, H. Schantz, K. Siwiak, and M. Win, "A comprehensive standardized model for ultrawideband propagation channels," *IEEE Transactions on Antennas and Propagation*, vol. 54, pp. 3151–3166, Nov. 2006. 5.2, 5.2, 5.4, A.6

[124] T. F. Coleman and Y. Li, "An interior trust region approach for nonlinear minimization subject to bounds," *SIAM Journal on Optimization*, vol. 6, no. 2, pp. 418–445, 1996. 5.5.1

[125] T. F. Coleman and Y. Li, "On the convergence of interior-reflective Newton methods for nonlinear minimization subject to bounds," *Math. Program.*, vol. 67, no. 2, pp. 189–224, 1994. 5.5.1

[126] D. Terzopoulos, J. Platt, A. Barr, and K. Fleischer, "Elastically deformable models," in *SIGGRAPH '87: Proceedings of the 14th annual conference on Computer graphics and interactive techniques*, vol. 21, (New York, NY, USA), pp. 205–214, ACM Press, July 1987. 5.5.3

[127] X. Provot, "Deformation constraints in a mass-spring model to describe rigid cloth behavior," in *Graphics Interface*, pp. 147–154, 1995. 5.5.3

[128] W. Chen, T. Mei, M. Q.-H. Meng, H. Liang, Y. Liu, Y. Li, and S. Li, "Localization algorithm based on a spring model (LASM) for large scale wireless sensor networks," *Sensors*, vol. 8, no. 3, pp. 1797–1818, 2008. 5.5.3

[129] A. Howard, M. Mataric, and G. Sukhatme, "Relaxation on a mesh: a formalism for generalized localization," in *Intelligent Robots and Systems, 2001. Proceedings. 2001 IEEE/RSJ International Conference on*, vol. 2, pp. 1055–1060 vol.2, 2001. 5.5.3

[130] I. Cuias and M. G. Snchez, "Permittivity and conductivity measurements of building materials at 5.8 GHz and 41.5 GHz," *Wireless Personal Communications*, vol. 20, pp. 93–100, 2002. 10.1023/A:1013886209664. 5.9

[131] N. Maaref, P. Millot, C. Pichot, and O. Picon, "A study of UWB FM-CW radar for the detection of human beings in motion inside a building," *Geoscience and Remote Sensing, IEEE Transactions on*, vol. 47, pp. 1297 –1300, May 2009. 5.9

[132] L. Farhi, L. Zhao, and Z. Liao, "Constrained weighted least square optimization for vehicle position tracking," in *Global Telecommunications Conference, 2009. GLOBECOM 2009. IEEE*, pp. 1 –6, Nov. 2009. 5.9.2, 5.10

[133] W. Burgard, A. Derr, D. Fox, and A. Cremers, "Integrating global position estimation and position tracking for mobile robots: the dynamic markov localization approach," in *Intelligent Robots and Systems, 1998. Proceedings., 1998 IEEE/RSJ International Conference on*, vol. 2, pp. 730 –735 vol.2, 13-17 1998. 5.9.2

[134] W. Burgard, D. Fox, D. Hennig, and T. Schmidt, "Position tracking with position probability grids," in *Advanced Mobile Robot,*

1996., Proceedings of the First Euromicro Workshop on, pp. 2 –9, 9-11 1996. 5.9.2

[135] T.-J. Shan, M. Wax, and T. Kailath, "On spatial smoothing for direction-of-arrival estimation of coherent signals," *Acoustics, Speech and Signal Processing, IEEE Transactions on*, vol. 33, pp. 806 – 811, Aug. 1985. 6.1.1

[136] R. Schmidt, "Multiple emitter location and signal parameter estimation," *Antennas and Propagation, IEEE Transactions on*, vol. 34, pp. 276 – 280, Mar. 1986. 6.1.1

[137] P. Stoica and T. Soderstrom, "Statistical analysis of music and subspace rotation estimates of sinusoidal frequencies," *Signal Processing, IEEE Transactions on*, vol. 39, pp. 1836 –1847, Aug. 1991. 6.1.1

[138] A. Paulraj, R. Roy, and T. Kailath, "Estimation of signal parameters via rotational invariance techniques1- esprit," in *Circuits, Systems and Computers, 1985. Nineteeth Asilomar Conference on*, pp. 83 – 89, Nov. 1985. 6.1.1

[139] R. Roy, A. Paulraj, and T. Kailath, "Esprit–a subspace rotation approach to estimation of parameters of cisoids in noise," *Acoustics, Speech and Signal Processing, IEEE Transactions on*, vol. 34, pp. 1340 – 1342, Oct. 1986. 6.1.1

[140] J. McCreary, "Matching properties, and voltage and temperature dependence of mos capacitors," *Solid-State Circuits, IEEE Journal of*, vol. 16, pp. 608 – 616, Dec. 1981. A.4

[141] T. Zhang, "Statistical methods - lecture notes." online, accessed 20. Apr. 2011, 2011. A.5

[142] Y.-J. Chan, C.-F. Huang, C.-C. Wu, C.-H. Chen, and C.-P. Chao, "Performance consideration of MOS and junction diodes for varactor application," *Electron Devices, IEEE Transactions on*, vol. 54, pp. 2570 –2573, Sep. 2007. A.6

[143] W. Abadeer, R. Rassel, and J. Johnson, "A capacitance reliability degradation mechanism in hyper-abrupt junction varactors," in *Reliability Physics Symposium, 2008. IRPS 2008. IEEE International*, pp. 310 –314, Apr. 2008. A.6

List of Tables

List of Figures